

Radiation Behaviour of High-Entropy Alloys for Fusion Reactor Environments

Antonio Fernández Caballero
Department of Mechanical Aerospace and Civil
Engineering, School of Engineering

*A thesis submitted to the University of Manchester for the degree
of Doctor of Philosophy in the Faculty of Science and Engineering
2019*

Contents

1 Introduction	14
1.1 The challenges to fusion power	14
1.2 Scope	16
1.3 Aims and Objectives	20
1.4 Thesis Structure	22
1.5 Publications arising from thesis	24
2 Irradiation damage to structural materials in the blanket of fusion reactors and the role of HEAs	27
2.1 Fusion basics and nuclear aspects	28
2.2 Physics of radiation damage in metals	37
2.2.1 Elementary neutron matter interactions	39
2.2.2 Elementary charged particle matter interactions	40
2.2.3 Defect cascades at elevated temperatures	44
2.3 Fusion reactor structural materials	54
2.3.1 Ferritic/Martensitic steels	56
2.3.2 ODS steels	57
2.3.3 Austenitic steels and other materials	58
2.4 High entropy alloys	59
2.4.1 Phase stability	61
2.4.2 Mechanical and physical properties	66
2.4.3 Radiation performance	68
2.5 Conclusion	75
3 Modelling methods	78
3.1 Ab initio electronic structure calculations	79

3.2	From ab initio electronic structure to coarse-graining: the cluster expansion	86
3.3	CVM and Monte Carlo mean field theories	93
3.4	Computational details	97
3.5	Crystallographic space group theory	98
3.6	Conclusion	101
4	Experimental methods, and conduction of experiment	103
4.1	Sample preparation	103
4.2	Self-ion irradiation experiment	107
4.3	Structure and composition with X-ray and electron spectroscopies	114
4.4	Defect characterisation with TEM	122
4.5	Mechanical properties	125
5	Short-Range Order in High Entropy Alloys: Theoretical Formulation and Application to Mo-Nb-Ta-V-W System	129
5.1	Introduction	131
5.2	Cluster Expansion Hamiltonian for Multicomponent Alloys . .	133
5.3	Short Range Order Parameters for Multicomponent Alloy . .	143
5.4	Application High Entropy Alloy Mo-Nb-Ta-V-W	146
5.5	Second Nearest-Neighbor SRO Effects	153
5.6	Conclusion	155
5.7	Acknowledgements	158
6	Configurational Entropy in Multicomponent Alloys: Matrix Formulation from ab initio based Hamiltonian and Application to FCC Cr-Fe-Mn-Ni Alloys	160
6.1	Introduction	162
6.2	Methods	166
6.2.1	Matrix formulation of cluster expansion	167
6.2.2	Configuration entropy in the matrix formulation	173
6.2.3	Computational details	177
6.3	Cluster probability functions in fcc Cr-Fe-Mn-Ni alloys	178

6.3.1	Cluster Expansion Hamiltonian for FCC CrFeMnNi . . .	179
6.3.2	Full set of cluster decorations	180
6.3.3	Four-body probability functions from Monte Carlo simulations	186
6.4	Configuration entropy in Cr-Fe-Mn-Ni system	193
6.5	Conclusions	197
6.6	Acknowledgements	198
7	High-dose ion irradiation damage in $\text{Fe}_{27}\text{Ni}_{28}\text{Mn}_{27}\text{Cr}_{18}$ HEA characterised by TEM and nanoindentation	200
7.1	Introduction	202
7.2	Experimental methods	204
7.2.1	Thermo-mechanical processing and sample preparation	204
7.2.2	Self-ion irradiation experiment	207
7.2.3	Nanoindentation methods	208
7.2.4	TEM sample preparation	214
7.3	Results and discussion	215
7.3.1	Microstructural characterization in the non-irradiated condition	215
7.3.2	Microstructural characterization in the irradiated condition	221
7.3.3	Irradiation hardening from nanoindentation tests . . .	223
7.4	Conclusion	225
8	Conclusion and future work	227
8.1	Conclusion	227
8.2	Experimental future work	229
8.3	Modelling future work	230
A	Appendix	233
A.1	Principles of superlattice structure construction for HEAs. . . .	233
B	Appendix	241

B.1 Ergodicity, broken-ergodicity and configuration entropy in high-entropy alloys	241
C Appendix	244
C.1 Kinematics of two-body scattering	244
D Appendix	247
D.1 Derivation of the ABVI model hamiltonian from cluster expansion in the pair interaction	247
D.2 Two-body Hamiltonian interaction	250
Bibliography	253

Word count: 69,044

Abstract

The world is hungry for energy with an estimated need of 20 TW-year at present. The demand of electrical power (approximately 1/4) could be supplied by the construction of a few 1,000 nuclear fusion power plants each providing 1 GW of clean electrical energy. After achieving the main challenge of producing and confining a deuterium-tritium plasma, the economic, safety, and environmental impact factors will have to be considered for the development of advanced reactor structural materials. These materials will have to withstand demanding heat and radiation flux environments during an estimated 30-40 years of device lifetime with doses of 200 dpa and temperatures of 1,000 °C. Current fusion structural candidate materials such as bcc ferritic/martensitic, fcc austenitic stainless steels, or ODS steels have serious limitations after exposure to radiation and heat fields in terms of their induced brittleness at room temperatures, or fracture by creep at high temperatures.

HEA (high entropy alloys) are a new type of complex metallic material that are fabricated on the basis that the alloy contains multiple principal elements. HEAs have come to attention after their intrinsic radiation resistance, and excellent mechanical properties both at low and intermediate temperatures. The chemical complexity is at present the source of many hypotheses about their properties, in particular their phase stability at temperature and irradiation resistance.

In this thesis, a novel formulation of short-range order based on electronic structure methods is developed for predicting phase stability in bcc HEAs. This was used to predict the formation of a bcc phase, associated with a Cr-Cr-Cr-Cr tetrahedron cluster, in an fcc lattice. In experimental work, in contrast to previous studies, but in agreement with the modelling results, a bcc phase enriched in Cr was observed in the fcc HEA CrMnFeNi following a recrystallisation heat treatment. This phase was also present after irradiating with Ni ions up to 20 dpa at temperatures of 300 and 450 °C, although no significant increase in volume fraction was measured, indicating that matrix stability was maintained. The mechanical properties after the ion irradiation were investigated by nanoindentation. There was a significant increase in hardness with irradiation dose. The associated changes in microstructure were examined by transmission electron microscopy.

Acronyms

- JET - Joint European Torus
- ITER - International Thermonuclear Experimental Reactor
- DEMO - Demonstration Power Plant
- PPCS - Power Plant Conceptual Studies
- HEA - High entropy alloys
- DFT - Density functional theory
- PP - Pseudopotential for electronic structure calculations
- CE - Cluster Expansion Hamiltonian for coarse grained statistical physics model
- $E[\vec{\sigma}]$, total binding energy of the electronic system in configuration given by spin-like variables, $\vec{\sigma}$, that refer to the chemical species occupying each lattice site of the system
- \mathcal{R} - Crystallographic space group with \mathcal{T} elements.

- dpa - Displacement per atom
- PKA - Primary Knock on Atom
- TEM - Transmission Electron Microscope.
- SEM - Scanning Electron Microscope
- XRD - X-ray diffraction
- CIF - Crystallographic Information File

Declaration

I, Antonio Fernández Caballero, declare that no portion of the work referred to in the thesis has been submitted in support of an application for another degree or qualification of this or any other university or other institute of learning.

The following peer reviewed articles were published or will be submitted as a consequence of the research conducted by the author of this thesis:

1. A. Fernández-Caballero, J.S. Wróbel, P.M. Mummary, and D. Nguyen-Manh. *Short-Range Order in High Entropy Alloys: Theoretical Formulation and Application to Mo-Nb-Ta-V-W System..* J. Phase Equilibria Diffus. 38, 391 (2017). (Special Issue on The Thermodynamics and Kinetics of High-Entropy Alloys, included in Chapter 5)
2. A. Fernández-Caballero, M. Fedorov, J. Wróbel, P. Mummary, and D. Nguyen-Manh. *Configuration Entropy in High-Entropy Alloys beyond Solid Solution: Theoretical Formulation from Cluster Expansion Hamiltonian and Application to fcc CrFeMnNi Alloys.* Entropy 21, 68 (2019). (Feature paper in Special Issue on New Advances in High-Entropy Alloys, included in Chapter 6)
3. A. Fernández-Caballero, E. J. Pickering, E. Bousser, S.M. Shubeita, P.T. Wady, Y. Gu, R. Krishna, O. Ciucă, M. Gorley, D. Nguyen-Manh, M. G. Burke, P. M. Mummary. *High-dose ion irradiation damage in Fe₂₇Ni₂₈Mn₂₇Cr₁₈ HEA characterised by TEM and nanoindentation* (included in this thesis in Chapter 7)

..... Signature of Antonio Fernández Caballero Date

Copyright statement

- I. The author of this thesis (including any appendices and/or schedules to this thesis) owns certain copyright or related rights in it (the “Copyright”) and s/he has given The University of Manchester certain rights to use such Copyright, including for administrative purposes.
- II. Copies of this thesis, either in full or in extracts and whether in hard or electronic copy, may be made only in accordance with the Copyright, Designs and Patents Act 1988 (as amended) and regulations issued under it or, where appropriate, in accordance with licensing agreements which the University has from time to time. This page must form part of any such copies made.
- III. The ownership of certain Copyright, patents, designs, trade marks and other intellectual property (the “Intellectual Property”) and any reproductions of copyright works in the thesis, for example graphs and tables (“Reproductions”), which may be described in this thesis, may not be owned by the author and may be owned by third parties. Such Intellectual Property and Reproductions cannot and must not be made available for use without the prior written permission of the owner(s) of the relevant Intellectual Property and/or Reproductions.
- IV. Further information on the conditions under which disclosure, publication and commercialisation of this thesis, the Copyright and any Intellectual Property University IP Policy (see <http://documents.manchester.ac.uk/display.aspx?DocID=24420>), in any relevant Thesis restriction declarations deposited in the University Library, The University Library’s regulations (see <http://www.library.manchester.ac.uk/about/regulations/>) and in The University’s policy on Presentation of Theses

Acknowledgement

Firstly, I wish to express gratitude to Dr Porton and Dr Surrey from UKAEA or Culham for the considerable trust they deposited in me for undertaking a very ambitious project and for making financially possible to come to Manchester. I also wish to thank financial support from EPSRC (EP/L01680X/1) through the Materials for Demanding Environments Centre for Doctoral Training. I only hope that this work can get us all a little bit closer to fusion. Secondly, I thank my supervisory team: Dr Pickering for his efficient approach in getting experimental work done with great patience with me, and also for considerable aid in the TEM training (in particular with his practical teaching on simple but important task of loading correctly a TEM holder); Dr Gorley for accepting to co-supervise me in the experimental work by contributing into the discussion of experimental results and in the choice of next steps; Prof Burke for her practical teachings in the use of the TEM CM20 dark and bright field imaging and diffraction and for contributing part of her funding in the aid of my irradiation experiments at DCF; Prof Mummery for taking me as PhD student and advising in both the modelling and experimental works initially during the fusion group meetings with Aneeqa, Luke, and Assad, and later in one-to-one meetings; and Dr Nguyen-Manh in the modelling work, an excellent senior academic, who probably understood me better than anyone and knew when to add the extra pressure required to achieve excellence, and whose judgement ultimately lead me to publish my work for the first time in my life as first author in the 2017 Short-range order paper (and 2 more would come later). I wish to thank the Technology department at CCFE (Dr Gorley and Dr Nguyen-Manh) for offering super computer facility Eric cluster, and also for office work during my several visits to Culham. I am especially grateful to Culham for having given me the opportunity to present my experimental work at the 2018 PhD showcase event.

Upon reflection of the experimental work in the PhD, I look back and remember the significant challenges involving most notably the Charged particle Accelerator in the Dalton Cumbrian Facility from making a proposal, to organising a whole team of people to take over night shifts for days long irradiations, and having the privilege of operating a million pound machine basically on myself for a few late hours at night. To a lesser degree, but

nonetheless challenging tasks involving the training on the TEM, SEM, FIB, and XRD, for which I have to thank greatly the technicians in particular Mr. Smith, Mr. Faulkner, Dr. Gholinia, and Dr. Warren. I apologize in advance if I have forgotten to thank anyone not mentioned here.

I wish to thank both examiners for their comments for improving the coherence, critical content and quantitative data discussion of this work. Upon reflection on the difficult years that I am leaving behind, I think that I have learnt to value the importance of academic writing. In my opinion, knowing how to do the work is just 40 % of the effort and writing research work properly is in my estimation 60 % of the effort.

I am grateful to Paul Mummery, Abbie Jones, Barry Marsden, James Wade, Ram Krishna, and Zhoutong He for their financial support in letting me collaborate with the nuclear graphite research group by undertaking synchrotron radiation diffraction work and contributing to the development of analysis tools for undertaking texture analysis from pole figure maps from data taken specifically at SLAC, USA in 2,017 and at Diamond, UK in 2,018. The experience in California was really awesome.

During my days at Manchester, I could have never had imagined to meet so many people from so many different nationalities, almost from every intermediate cardinal direction. I am grateful for having crossed paths with them, in particular I thank my CDT friends Andy (Spain), and Sándor (South East, Hungary); Andrea (South East, Italy) for his willing to share wisdom on the TEM by providing some of his Vanadium TEM specimens before I could produce my TEM samples due to the lengthy training required, and also on a personal level for being the best wingman in Manchester; and Tapio (North East, Finland) for many lunches at Café du Nord and for interesting political discussions after bad days in the office, Miguel and Paloma (South, Spain) for keeping my Spanish well trained during coffee breaks in Café du Nord. Finally I thank my friends of the Pariser football group: Vasco (South West, Portugal), Ilias, Elisa and so many others thanks for giving me an excuse to escape from the office and release some Adrenalin.

This near 5 year long project would not have reached an end if it wasn't for the support of my parents Conchi and Jose, my brother Miguel, my sister Inma, my godfather Antonio, and my grandfather Antonio. I wish to dedicate this work to the memory of my grandmother, Concepcion Caballero Giner, who passed away days before I embarked in this adventure in 2014.

Introduction

“ If you wish to make an apple pie from scratch, you must first invent the universe.

— Carl Sagan

Cosmos - Ep 9: The Lives Of The Stars

1.1 The challenges to fusion power

Nuclear energy is released from fission or fusion processes that occur among interacting nuclei. In our sun, helium and hydrogen nuclei interact by fusion processes to release radiation (radiation is just energy that travels in space, in the case of the sun electromagnetic radiation). The specific energy content in fusion processes is superior to any existing technology: in chemical reactions (Methane chemical bonds) is approximately 0.05 GJ/kg, in uranium for nuclear fission is approximately 28,000 GJ/kg (as can be seen at [1]), and for deuterium-tritium nuclear fusion reaction the energy content is 360,000 GJ/kg [2]. At present, the main candidate fusion technologies include magnetic confinement, and inertial confinement of hot fusion plasmas (high temperature - homogeneous mix of fully ionised atoms and electrons). For the human species to be able to extract the nuclear energy from fusion processes by nuclear fusion power plants necessary technology developments need be overcome:

Fusion power Approximately 1 GW of net electrical power production (comparable to current pressurised water reactor power plants) from the

nuclear fusion processes by a pulsed (pulse of about 1 day) or steady-state burning fusion plasma depending on local energy needs or storage technology. The plasma will have to be confined with magnetic fields of approximately 10 Tesla generated by approximately 20 D-shaped toroidal and poloidal superconducting coils made of Nb₃Sn and requiring active cooling to cancel heat generation by γ -rays and also requiring neutron shielding for irradiation damage.

Materials The plasma in a fusion power plant is surrounded by blankets as shown in Fig. 1.1. The fusion reactor analogue of the cladding of a fission reactor fuel element is the first wall separable panel, a several cm barrier between the near-vacuum plasma and the high-pressure coolant. The blankets are made of several materials: the tritium breeding material, the structural material, the neutron multiplier, and the coolant. Bombardment of the blanket materials with intense neutron fluxes produced from fusion processes in the plasma is believed to be the limiting technological issue for the lifetime of fusion power plants. The radiation damage is quantified by dpa (displacements per atom), which is proportional to the neutron fluence. During the lifetime of the ITER device, the neutron damage could accumulate to 1.6 dpa. In a commercial fusion power plant, the neutron damage over a lifetime could reach 120 dpa. An optimum combination of wall materials will have to ensure high lifetime and power plant availability with a minimum of radioactive waste.

Heat extraction The approximate 3 GW of fusion energy is deposited as heat in the blanket modules. Conventional cooling systems (cycle of steam generators, turbines and electric generators) could be used to extract the heat to produce an estimated net electrical output of 1 GW. Cooling systems may be single or dual loop depending on whether the coolant directly drives the turbine or includes a heat exchanger and

then the turbine. These turbines are expected to be standard off the shelf technologies.

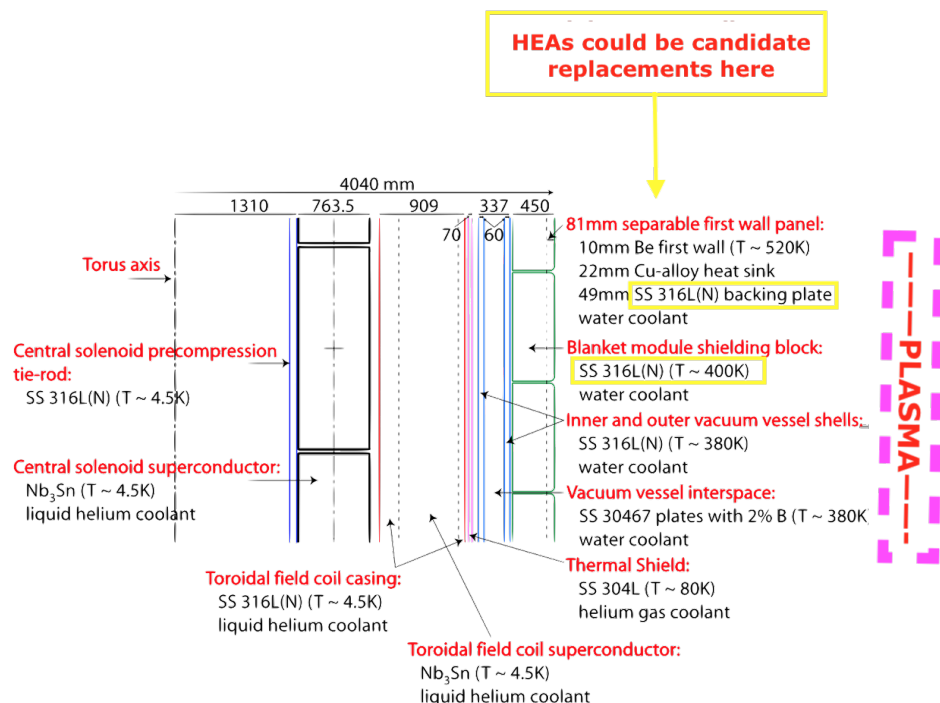
Tritium re-fueling Annual fuel requirements for 1 GW electric fusion power plant have been estimated to 110 kg of deuterium and 380 kg of tritium [3]. These quantities may be compared to the approximate of fuel demands with 35,000 kg of uranium (enriched with 1,100 kg of ^{235}U , and remaining being ^{239}U) for a typical 1 GW electric light water reactor [4]. Tritium is scarce on earth due to its short half-life of only 12.3 years; consequently, it must be bred from neutron nuclear reactions with Li compounds (salt brines, minerals, and seawater); examples of Lithium compounds are Li_2ZrO_3 , Li_2TiO_3 , or Li_4SiO_4 . ITER technology will address tritium production commonly measured in terms of the tritium breeding ratio (i.e. the ratio of tritium atoms produced to neutrons emitted from the plasma).

Costs Fabrication costs of fusion power plants are likely to be the dominating factor for the cost of selling electricity at a competitive price (more than the fuel cost). Reserves of neutron multiplier materials such as beryllium (see Fig. 1.1 in the blanket of the ITER device) remain largely unexplored [3]. Lead, the other multiplier material with an annual production (3 million tonnes) and worldwide estimated reserves of 70 million tonnes [3] is at risk of running out even before fusion power plants are built.

1.2 Scope

The scope of this work is focused on the development of radiation-resistant first wall materials for nuclear power plants of the magnetic confinement technology. Specifically on high-entropy alloys as a structural material in the

Fig. 1.1.: Depiction of proposed location of structural material high-entropy alloys in a nuclear fusion power plant of the magnetic confinement technology. The reactor dimensions as well as local conditions of temperature are referred to the ITER machine in the range 400-520 K. Length units are in mm. The neutron wall load in ITER will be 1 MW. Figure modified from [5].

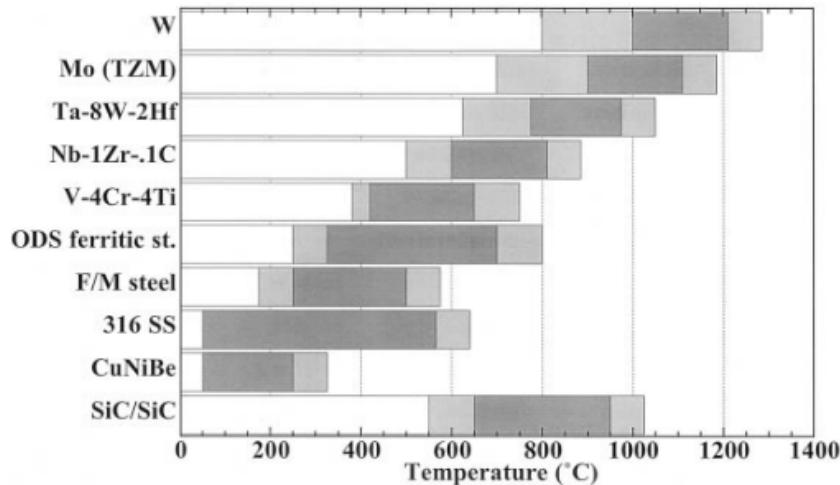


blanket structure of fusion power plants (see Fig. 1.1 for the proposed use in ITER device). In the case of the ITER machine, the structural material will be austenitic stainless steels 316 L(Nitrogen controlled). In the austenitic stainless steel of first wall structure, the surface heat load will reach 1 MW/m^2 , and the neutron damage 1.6 dpa over the lifetime of the ITER device. The temperature of the 316L(N) will range in 400-520 K. Furthermore, major plasma instabilities induce eddy currents inside the blanket structure which interact with the magnetic field resulting in high forces. These forces in combination with the thermal stresses resulting from thermal gradients in structural materials may generate mechanical stresses up to a few hundred MPa. The frequency of these varying stresses could potentially limit the lifetime of the blanket structure by mechanical fatigue.

Future magnetically confined fusion reactor power plants will convert the energy from high energy neutrons emerging from a deuterium-tritium plasma into useful electrical power and additional tritium fuel for self-sustaining the plasma fuel. The energy of the neutrons will be deposited in a region called the blanket module, that is to be isolated from the exterior by a neutron shield wall. In the blanket module, the materials will be exposed to unprecedented conditions of magnetic fields, irradiation fields (due to 14 MeV neutrons), and heat fluxes.

The economic viability of fusion reactors will require the development of materials that can withstand these demanding heat and radiation fluxes during their operational lifetime. The potential application to fusion of a wide range of materials has been studied in terms of a so-called temperature window and an estimated 30 years of device lifetime [7]. The lower limit for the operational temperature was set by irradiation hardening, by void swelling at intermediate temperatures, and the higher temperature limit was set by helium embrittlement of the grain boundaries, or thermal creep [6]. Detailed consideration (see figure 1.2) of all of these effects and power plant

Fig. 1.2.: Temperature window for some proposed fusion materials based on the degradation of the limiting property. The limiting property can be thermal properties for SiC/SiC ceramic composites or by mechanical properties for metallic materials such as ductility for stainless steel. Figure reproduced from [6]



thermodynamic efficiency considerations led to the conclusion that fusion materials would have to be exposed to operational temperatures as low as 300 and as a high as 1000 °C and displacements per atom (dpa) between 150 and 200 [8, see Fig. 5]. These proposed materials included vanadium alloys, oxide dispersion strengthened steels (ODS), and ferritic/martensitic steels as can be seen from the same table 1.2.

Stainless steel is a key structural material for the advanced fusion prototype ITER partly attributed to the built-up experience of these alloys in commercial fission reactors [9]. In these steels improvements of strength and thermal creep are obtained by controlling impurity amounts of elements such as Ti or Nb [10]. Since 2004, where publications on the topic of HEA first started [11], their interest has kept increasing [12]. HEAs offer an alternative concept to modifying commercial alloys for improving mechanical properties by using multiple principal elements [13] instead of being based around small additions to a base element.

HEAs can be considered as relevant fusion materials for the following reasons:

Ductility and Fracture Toughness HEAs have potential to overcome the strength-ductility trade-off in conventional alloys i.e. the decrease in ductility as yield strength (see high-entropy steels in Fig. 1.3 with elongation ranging from 50-100% and corresponding to UTS in the range 600-1100 MPa) is increased by exploiting lack of phase stability of some known HEAs such as in the FeMnCoCr HEA [14]. Similarly for CrMnFeCoNi and CrFeCoNi [15]. The increased ductility of the HEAs could compensate for the loss of ductility or embrittlement during irradiation hardening at low temperatures. The fracture toughness also has been proved to be superior to conventional alloys ($>200 \text{ MPa}\cdot\text{m}^{1/2}$) as shown in Fig. 1.3.

Intrinsic radiation resistance Enhanced vacancy-interstitial recombination of point defects in the cascade during the thermal spike [16, 17, 18, 19]. Practically this has been observed for void swelling [20]

Low activation HEAs have potential for designing compositionally tailored systems to minimise activation due to transmutation induced by neutron irradiations, for example W, Ta, V and Cr [21]. The Co-free FeNiMnCr HEA [20] is better fitted for nuclear applications than the five component CrMnFeCoNi [20]. Co is a γ -ray emitter under neutron exposure:

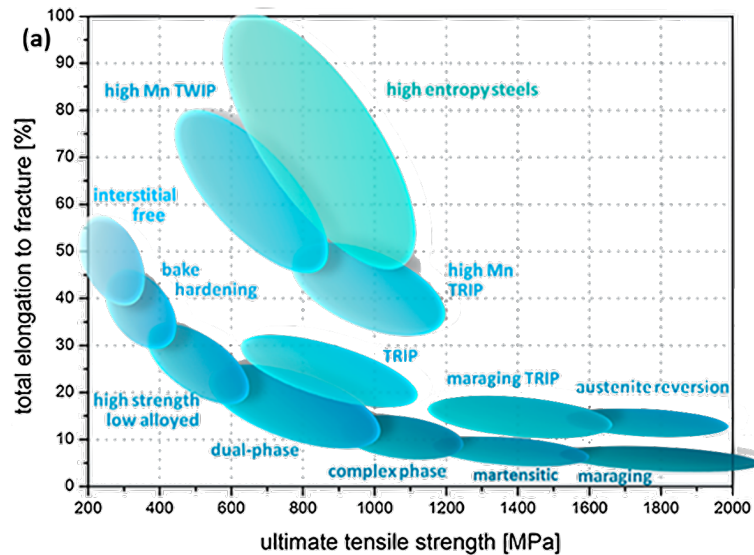
$$^{59}\text{Co} + \text{n} \longrightarrow ^{60}\text{Co}^* \longrightarrow ^{60}\text{Co} + \gamma$$

1.3 Aims and Objectives

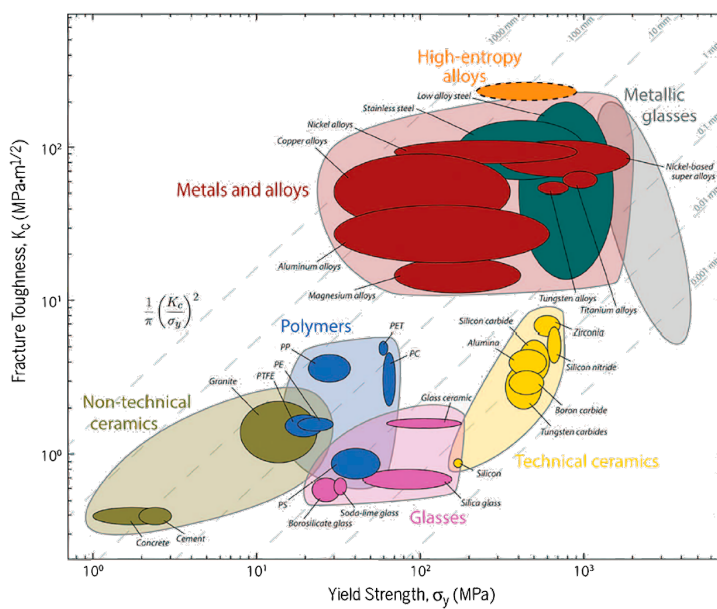
The aim of the research was to find if HEAs in particular CrFeMnNi HEAs are likely to be resistant to high dpa to neutron irradiation for structural

Fig. 1.3.: Superior mechanical properties of high-entropy alloys depicted in an Ashby chart. Figures adapted from [22]

(a)



(b)



materials in fusion reactor blanket or divertor components. The research was undertaken by a combined experimental and modelling approach.

For the experimental work, HEAs for examination were chosen based on two criteria: feasibility of their formation in the laboratories from Sheffield Universities (due to collaboration through the Accelerated Metallurgy Project) and good radiological properties. Specimens were to be irradiated at Dalton Cumbrian Facility by ionic species already present in the alloy under different irradiation dose rates and irradiation temperatures to simulate neutron irradiation damage. The microstructure of the irradiated material was to be examined on the transmission electron microscope (TEM) in order to observe most prominent radiation-induced features which could include amorphisation, radiation-induced segregation (RIS), dislocation loops or voids. Wherever possible radiation-induced effects were to be quantified i.e. counting cluster number densities.

The modelling work was aimed at predicting phases in equilibrium with Cr-FeMnNi HEAs from ab initio electronic structure calculations (first-principles density functional theory); in particular to challenge the findings of phase stability of this alloy composition following work from [20].

1.4 Thesis Structure

In chapters 2, 3, and 4 the background for the thesis is set in terms of a review of the field and a detailed description of both the theoretical and experimental methods used to produce the remaining chapters. In each of the result chapters 5, 6, and 7 there is a brief preamble at the beginning for explaining the purpose and the contributions coming from the different authors that took part in the work. Below there is a description for the purpose of each of the paper chapters appearing in this thesis.

Chapter 5

The purpose of this chapter is to show how first-principles modelling can be used to predict chemical ordering or segregation tendencies in HEAs at low temperatures, where entropy is not expected to stabilize the disordered random solid solution. Short-range order can indicate the existence of ordered domains in a microstructure. The general formalism is applied to the MoNbTaVW system, and in particular, it is predicted Mo-Ta ordering, which may derive into B2 phase precipitation.

Chapter 6

The purpose of this chapter is to generalize the formulation found in the previous chapter 5 for multi-body probabilities which can hint at the precipitation of equilibrium structures consisting on more than require more than 2 lattice sites that SRO employs. These multi-body probabilities are also used to compute temperature-dependent configuration entropies, this is done to complement another methodology to evaluate configuration entropy, namely the thermodynamic integration, that generally is more computationally demanding due to the need to evaluate thermodynamic equilibrium configurations in a finer temperature grid. The general formalism is applied in particular to the FCC Cr-Fe-Mn-Ni with composition 18% Cr to show that $L1_2\text{CrFe}_3$ and $L1_0\text{-MnNi}$ are particularly stable at low temperatures.

Chapter 7

The purpose of this chapter was to characterize the microstructures of recrystallised and irradiated FeNiMnCr HEAs. For the non-irradiated condition, specimens are prepared by electropolishing, and it is found that Cr-rich BCC phase precipitates in the FCC matrix of FeNiMnCr. Irradiation experiments performed at Dalton Cumbrian Facility with Nickel ions to 20 dpa resulted in an irradiated microstructure consisting of dislocation loops. Finally, mechanical behaviour in the irradiated condition was tested using nanoindentation to show irradiation hardening levels as high as 4 GPa for 20 dpa.

Finally, concluding remarks and the scope for future work are provided in Chapter 8

1.5 Publications arising from thesis

Journal publications:

1. A. Fernández-Caballero, J.S. Wróbel, P.M. Mummery, and D. Nguyen-Manh. *Short-Range Order in High Entropy Alloys: Theoretical Formulation and Application to Mo-Nb-Ta-V-W System..* J. Phase Equilibria Diffus. 38, 391 (2017). (Special Issue on The Thermodynamics and Kinetics of High-Entropy Alloys, included in Chapter 5)
2. A. Fernández-Caballero, M. Fedorov, J. Wróbel, P. Mummery, and D. Nguyen-Manh. *Configuration Entropy in High-Entropy Alloys beyond Solid Solution: Theoretical Formulation from Cluster Expansion Hamiltonian and Application to fcc CrFeMnNi Alloys.* Entropy 21, 68 (2019). (Feature paper in Special Issue on New Advances in High-Entropy Alloys, included in Chapter 6)
3. M. Fedorov, J. S. Wróbel, A. Fernández-Caballero, J. K. Krzysztof, D. Nguyen-Manh. *Phase stability and magnetic properties in fcc Fe-Cr-Mn-Ni alloys from first-principles modeling* (submitted to Physical Review B)

Journal publications to be submitted:

- A. Fernández-Caballero, D. Nguyen-Manh. *Theoretical derivation of ABVI model from cluster expansion Hamiltonian*

- A. Fernández-Caballero, E. J. Pickering, E. Bousser, S.M. Shubeita, P.T. Wady, Y. Gu, R. Krishna, O. Ciucă, M. Gorley, D. Nguyen-Manh, M. G. Burke, P. M. Mummery. *High-dose ion irradiation damage in Fe₂₇Ni₂₈Mn₂₇Cr₁₈ HEA characterised by TEM and nanoindentation* (included in this thesis in Chapter 7)

Conference papers and posters:

- A. Fernández Caballero, M. Fedorov, J. Wróbel, P. Mummery, and D. Nguyen-Manh. *Configuration Entropy in High-Entropy Alloys beyond Solid Solution: Theoretical Formulation from Cluster Expansion Hamiltonian and Application to fcc CrFeMnNi Alloys*. EUROMAT (2019). Stockholm, Sweden
- A. Fernández Caballero, J. S. Wróbel, D. Nguyen-Manh, and P. M. Mummery. *Theoretical derivation of the ABVI model from cluster expansion Hamiltonian*. (2018) Multiscale Materials Modeling. Osaka, Japan.
- A. Fernández-Caballero, J.S. Wróbel, P.M. Mummery and D. Nguyen-Manh. *Short-range order in HEAs: theoretical formulation and application to W-V-Ta-Mo-Nb HEA*. EUROMAT (2017), Thessaloniki, Greece.
- A. Fernández Caballero, E. Pickering, G. Burke, S. M. Shubeita, P. Wady, R. Krishna, Y. Gu, O. Ciucă, M. Gorley, D. Nguyen-Manh, P. Mummery. *Precipitation behaviour of CrMnFeNi HEA under heavy ion irradiation*. EUROMAT (2017), Thessaloniki, Greece.
- M. Fedorov, J. S. Wróbel, A. Fernández-Caballero, J. K. Krzysztof, D. Nguyen-Manh. *Phase stability and magnetic properties in fcc Fe-Cr-Mn-Ni alloys from first-principles modeling*.EUROMAT (2019). Stockholm, Sweden

- D. Nguyen-Manh, J.S. Wróbel, A. Fernández Caballero, S.L. Dudarev. *Constrained thermodynamic model for multi-component alloys under irradiation: A matrix formulation from first-principles Hamiltonian.* (2018) Multiscale Materials Modeling. Osaka, Japan.
- J. Wróbel, D. Nguyen-Manh, S. Dudarev, I. Toda-Caraballo, P. Rivera Díaz del Castillo, Z. Leong, R. Goodall, I. Todd, A. Fernández Caballero, K. Kurzydlowski. *Phase composition and thermodynamic properties of high-entropy alloys from first-principles modelling.* EUROMAT (2017), Thessaloniki, Greece.
- M. Fedorov, J.S. Wrobel, A. Fernandez-Caballero, K.J. Kurzydlowski, and D. Nguyen-Manh. *Phase stability and magnetic properties of Fe-Cr-Ni-Mn high entropy alloys from first-principles and Monte-Carlo simulations.* 2019. TMS Annual Meeting & Exhibition, San Antonio, USA

Irradiation damage to structural materials in the blanket of fusion reactors and the role of HEAs

“ Materials is the queen technology of any advanced technical system. The economics eventually depend upon the materials, the reliability depends upon the materials, and safety depends upon the materials.

— Edwin E. Kintner

(U.S Navy captain)

Before the 21st century ends, nuclear fusion is likely to succeed in fulfilling the human need for the development of environmentally sustainable and cost-effective energy sources while continuously improving the standard of living with technological advances.

In this chapter, the principles and materials being considered for magnetically confined fusion devices are reviewed, in particular for the models or prototypes under the considerations of the European Union (JET, ITER, and DEMO). The role of HEAs as a potential candidate fusion material is outlined by the currently known properties of these relatively new alloy systems (research in these alloys started in 2004 by [11]).

2.1 Fusion basics and nuclear aspects

Energy is required for many industrial, transportation, commercial or residential activities in 21st century. According to a 2018 report on electricity gross production and consumption worldwide by the International Energy Agency (IEA) [23], from 1974 until 2016 the world's annual quantity of electrical energy consumption increased from 5,335 to 20,863 TW-hr at an approximate annual rate 3.3%. The approximate electrical energy consumption will be given by the expression, $(1+0.033)^{\text{year}-2016}$ 20,863 TW-hr. At the 3.3 % rate, by the year 2,100, the annual electrical energy consumption could reach up to 319,010 TW-hr. Therefore, the annual world's average electric power consumption amounts to approximately 2.4 TW-yr now and could rise to 36.4 TW-yr by 2100. The world total energy consumption in 2016 was 12.7 TW-yr as shown in Table 2.1. The total world energy consumption includes oil, gas, coal, electricity, and renewables with a prediction for the year 2,100 of approximately 41.9 TW-yr (assuming average annual energy increase of 0.3 TW-yr estimated from data between 1973 and 2016 obtain from [23]). Electricity consumption in the U.K. is currently expensive. The development of nuclear fusion power plants could help overcome both the high price and the reduction of CO₂ emissions to the atmosphere.

If the human race fails to save planet earth from threats such as climate change, humanity may be pushed to outer space to search for other habitable planets. To reach other planets, advanced interstellar propulsion systems will be required for long flight times and with high-efficiency light-weight energy conversion equipment. The role of fuel mass will be critical for such missions. Primary energy sources for propulsion systems include chemical, nuclear fission, nuclear fusion, and matter annihilation. In the 21st century, human species has only unravelled nuclear fission energy sources and chemical energy sources. The exhaust velocity of rocket propulsion has been formulated in terms of the specific energy (per unit mass) stored in the fuel (chemical,

Table 2.1.: Total final energy consumption (TFC) for the year 2016. UK energy prices: 1-refers to automobile diesel oil, 2- refers to electricity price for households, 3- refers to natural gas for households. Data retrieved from [23]

	TFC (TW-yr)	Sectors Main (TW-yr)	CO ₂ emissions (Mt)	Price (USD/unit)
Oil	5.2	Road (2.6)	11,180	1.44 ¹ (litre)
Electricity	2.4	Industry (1.1)	-	202.41 ² (MWh)
Gas	1.9	Industry (0.7)	6,590	55.62 ³ (MWh)
Coal	1.4	Iron and steel (0.4)	14,250	102.58 (tonne)
Total	12.7	4.8	32,316	-

nuclear, or matter annihilation technology) [2]. For the case of nuclear fusion, the theoretical maximum exhaust speed would be greater than chemical or nuclear fission sources of energy with 30,000 km/s compared to 5 km/s from chemical or 12 km/s from fission energy sources [2, 24]

Primary energy sources on earth are broadly categorised into renewables and nonrenewable. Renewables are limited by the amount of power they can provide and they include solar energy with an estimated plausible harnessable power of 50 TW as the most powerful, and wind as the least powerful with an estimated harnessable power of 1 TW [25]. On the other hand, nonrenewables are limited by the availability of their stock resources, in this category there is fusion with total earth reserves of lithium and deuterium leading to a harnessable electrical energy of 140,000,000 and 250,000,000,000 TW-year respectively as the most resourceful option (fusion requires lithium and deuterium, see later in this subsection) and petroleum as the least resourceful option with 600 TW-years [25]. Uranium resources, required for nuclear fission reactors either conventional technology or for Generation IV reactors (Gas-cooled and sodium-cooled fast reactors - GFR and SFR respectively; supercritical water-cooled reactors-SCWR; very high-temperature gas reactors - VHTR; lead-cooled fast reactors - LFR; and molten salt reactors - MSR) are estimated to be 2,500 and 3,000,000 TW-year respectively.

As the most plentiful energy source, nuclear fusion makes sense as a solution to cope with the increasing energy demand. Furthermore, fusion energy offers advantages over fossil fuels, nuclear fission reactors and renewables (see [26]): fossil fuels for no carbon emissions, fission for no long-lived radioactive waste (<100 years half-life), and renewables for the ability to provide a constant base-load of power. Fusion reactors are intrinsically safe so that a large-scale nuclear accident is not possible based on the amount of radioactive fuel it contains (for example for the Joint European Torus (JET) plasma experiments, tritium was merely 0.2 g [27])

Nuclear fusion reactions occur when light nuclei react to transform the net available nuclear binding energy and release it as kinetic energy shared by the products of the fusion reaction. The binding energy, E_B , for a given nucleus can be calculated approximately by using the liquid-drop nuclear model (see Eq. 2.5 from any graduate-level nuclear physics book for example [28]). The binding energy is formulated in terms of the atomic mass $A = N + Z$, where N is the number of neutrons, and Z is the number of protons; mass represented by M , and pairing term δ . Examples of binding energies obtained from accurate sources (the live chart of nuclides at [29]) that can be calculated from Eq. 2.5 are 0 MeV for neutron or protons; 2.22 MeV for deuterium; 8.48 MeV for tritium; 28.30 MeV for an α -particle. For fusion energy production, interest is put into exothermic reactions, which can be shown to be possible by combining light nuclei into a heavier one up to the fusion isotope ^{56}Fe (most stable nuclei). Several nuclear fusion reactions have been reported: $\text{D} + \text{T} \longrightarrow \text{n} + \alpha\text{-particle}$ ($Q=17.60$ MeV; 100% branch ratio); $\text{D} + \text{D} \longrightarrow \text{T} + \text{p}$ ($Q=4.1$ MeV; 50% branch ratio); $\text{D} + \text{D} \longrightarrow {}^3\text{He} + \text{n}$ ($Q=3.3$ MeV; 50% branch ratio). The Q -value for the D-T reaction can be calculated as the difference of binding energies between the products and reactants giving $28.30 - 2.22 - 8.48 = 17.60$ MeV. For other fusion reactions and their Q -value, the reader can consult Table 2.3. The Q -value gives the available kinetic energy for the products, in this case, α -particle and a neutron. The branching ratio refers

to the probability of the decay mode when several are active. Endothermic nuclear reactions ($Q < 0$) may occur when the projectile particle reaches threshold energy given by $E_{th} = -Q(1 + A_i/A_l)$ for the generic nuclear reaction $I(i,j)J$ for the target nuclide I, projectile i, emitted particles j and product nuclide J.

$$\frac{E_B}{A} = (Z \cdot M_P + N \cdot M_N - M_A) \cdot c^2 \quad (2.1)$$

$$\frac{E_B}{A} \left(\frac{\text{MeV}}{\text{Nucleon}} \right) = 14 - \frac{13}{A^{1/3}} - \frac{0.585 \cdot Z^2}{A^{4/3}} - \frac{19.3(A - 2Z)^2}{A^2} + \delta \quad (2.2)$$

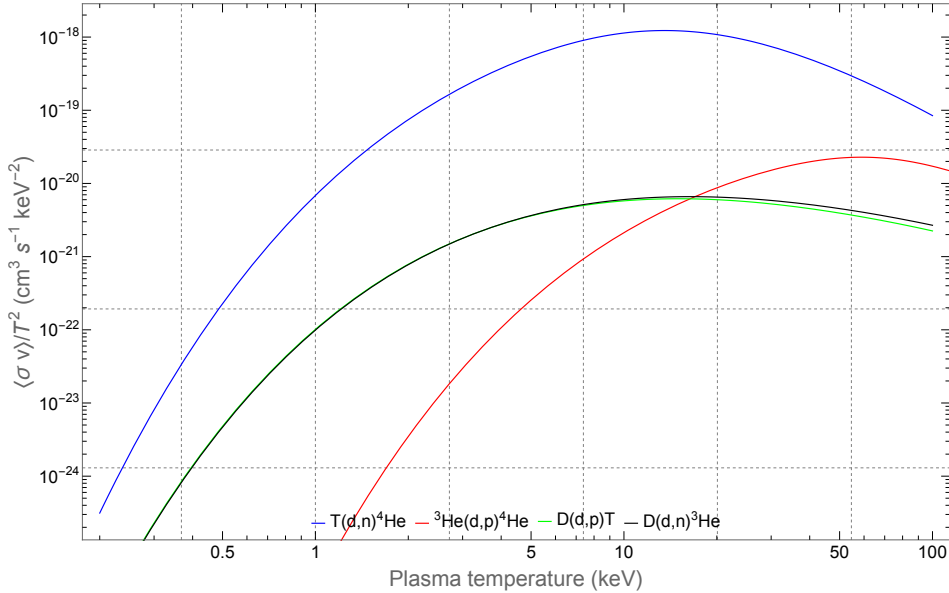
$$\delta = \frac{33}{A^{4/7}} \text{ (when } Z \text{ even, } N \text{ even)} \quad (2.3)$$

$$\delta = -\frac{33}{A^{4/7}} \text{ (when } Z \text{ odd, } N \text{ odd)} \quad (2.4)$$

$$\delta = 0 \text{ (when } Z \text{ and } N \text{ differing in parity)} \quad (2.5)$$

The rate of the nuclear fusion reaction between nuclides i and j per unit plasma volume, dR/dV , (for example $i=D$, and $j=T$) depends on the fusion reaction cross section, σ_f (measured in millibarns), and the distribution of velocities of the nuclei i and j (described by Maxwell distribution in a thermal plasma at temperature T as described by the normalised distribution of relative nuclei speeds and reduced mass $\mu = m_i m_j / (m_i + m_j)$): $f(v) = \left(\frac{\mu}{2\pi k_B T} \right)^{3/2} e^{-\mu v^2 / (2k_B T)}$. The fusion rate per unit volume is obtained from $dR/dV = n_i n_j / (1 + \delta_{ij}) \langle \sigma_f v \rangle$, where $\langle \sigma_f v \rangle$ is known as the fusion reactivity and only depends on the temperature of the plasma, T . The reactivities divided by the square of plasma temperature for several fusion reactions are illustrated in Fig. 2.1, in particular the D-T fusion reactivity is shown to be the most probable at approximately $5500 \text{ cm}^3/\text{s}$ for plasma temperatures near 50 keV. For 50 keV of kinetic energy, atoms ($Z < 17$) are stripped of their electrons because total atomic binding energies are much lower (the atomic binding energies are approximately given by $21Z^{7/3} \text{ eV}$ (see 3.1 for a

Fig. 2.1.: Nuclear fusion reactivities in thermal plasmas, $\langle \sigma_f v \rangle / T^2$. Parametrisations obtained from experimental data as reported in tables IV and VII obtained from reference [30].



discussion on the binding energies of atoms), where Z is the atomic number. Consequently fusion reactors require a plasma phase formed by a hot gas of electrons and ions.

As an energy system, a fusion reactor requires the output energy to be larger than the input power required to maintain the plasma at the plasma temperature. The fusion power from the plasma is defined by the product of the reaction rate and the Q-value of the fusion reaction integrated over the entire plasma volume, V , thus giving $P_F = V \left(\frac{dR}{dV} \right) Q$. Values for different plasma scenarios have been evaluated in Table 2.3, all assuming that the magnetic field pressure $B^2/(2\mu_0)$ is evaluated at 5 Tesla, and the ratio of the plasma pressure to the magnetic field pressure is 0.1 (also known as β -ratio). The fusion power from a D-T plasma can be written in terms of pressure and reactivities as $P_F = 1/4 p^2 \frac{\langle \sigma_f v \rangle}{T^2} Q$. The plasma volume can be estimated by considering the tokamak as a cylinder with radius r , and height $2\pi R$, where r is the minor tokamak radius, and R is the major radius. The deviation from the circular shape of the cylinder is accounted by the parameter κ ; thus resulting a volume formula $2\pi^2 r^2 R \kappa$. Similarly, the surface surrounding

Table 2.2.: Magnetic confinement parameters relevant for thermonuclear fusion reactor experiment JET, and expected values for ITER (*), and DEMO. All data are taken from <http://www.tokamak.info>, except where indicated. The volume of the plasma and the wall area are estimated from the major, minor radius and the elongation. For more accuracy, the flux profile of the plasma is required. The neutron flux at the first wall has been estimated assuming a neutron energy of 14.08 MeV.

Parameter	JET(divertor configuration)	ITER	HCPB DEMO
Major radius (m)	2.96	6.2	8.5 ([31])
Minor radius (m)	0.96	2.0	2.83 ([31])
Elongation	1.7	1.7	1.66 ([31])
Plasma volume (m^3)	90	830	2,230
1 st wall area (m^2)	146	638	1,238
Max plasma current (MA)	6.0	15.0	-
Toroidal magnetic field (T)	4.0	5.3	-
Fusion power (MW)	16.1([32])	500*	2,700 ([31])
Neutron 1 st wall load (MW/m^2)	0.09	0.63	1.74
Neutron 1 st wall flux ($\text{m}^{-2}\text{s}^{-1}$)	3.9×10^{16}	2.7×10^{17}	7.7×10^{17}
Pulse length (s)	5([32])	3,000*	-

the plasma can be estimated by the formula $4\pi^2 r \sqrt{\kappa} R$. Taking the parameters from Table 2.2, and assuming an elongation for ITER of $\kappa=1.7$, the plasma volume is 830 m^3 . Fusion power can be lost from the reaction. Plasma can lose power due to end of confinement duration or plasma lifetime, τ , of the homogeneous mix of ions, n_i and electrons, n_e resulting in power loss given by $P_\tau = \frac{3/2n_i kT + 3/2n_j kT + 3/2n_e kT}{\tau}$; and from braking radiation power loss (Bremsstrahlung) P_B . Two criteria measuring the viability of fusion power are of interest: breakeven condition when fusion power is greater than the power required to maintain the plasma temperature ($P_F > P_\tau$); and ignition condition when the heating power from α -particles produced in the D-T fusion reaction is greater than the power loss by radiation ($P_\alpha > P_\tau + P_B$). The application of the two criteria for breakeven, and for ignition result in two functions of plasma temperature of $nkT\tau$, known as the triple product function. Current progress on the triple product is measured with respect to reactor-grade values of approximately $10^{22} \text{ m}^{-3} \text{ s keV}$ [5, 28].

Plasma stability by magnetic fields in tokamaks can be achieved by confining ions and electrons from the plasma to closed orbits using helix-like magnetic

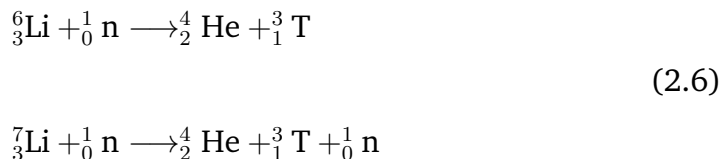
Table 2.3.: Parameters of common nuclear fusion reactions and their optimal plasma temperature, T , derived from maximum of $\langle\sigma_f v\rangle/T^2$ (data for reactivities taken from [30]). The notation for fusion reactions is $I(i,j)J$, where I represents the target nuclide, projectile i , outgoing/emitted particle j , and product nuclide, J , respectively. K.E. is short for Kinetic Energy. The plasma temperature, T , and the reactivity are evaluated at the maximum value found for $\langle\sigma v\rangle/T^2$.

	Q-value (MeV)	K. E. (j) (MeV)	K.E (J) (MeV)	T (keV)	$\langle\sigma v\rangle/T^2$ $\text{cm}^3\text{s}^{-1}\text{keV}^{-2}$	P_f (MW/m ³)
D(T,n) ⁴ He	17.6	14.0	3.5	13.6	1.23×10^{-18}	10.53
³ He(d,p) ⁴ He	18.4	14.7	3.7	59.0	2.28×10^{-20}	0.21
D(d,p)T	4.0	3.0	1.0	15.0	6.17×10^{-21}	0.02
D(d,n) ³ He	3.3	2.4	0.8	16.4	6.60×10^{-21}	0.02

field lines. The magnetic field lines, which are generated by winding superconducting coils around the tokamak, are of maximum quantity magnitude of 5 Tesla (see Table 2.2), and of two configurations for a tokamak: toroidal, and poloidal. Other confinement modes exist including spherical (MAST in the UK), and stellarator (W7-X in Germany) magnetic configuration.

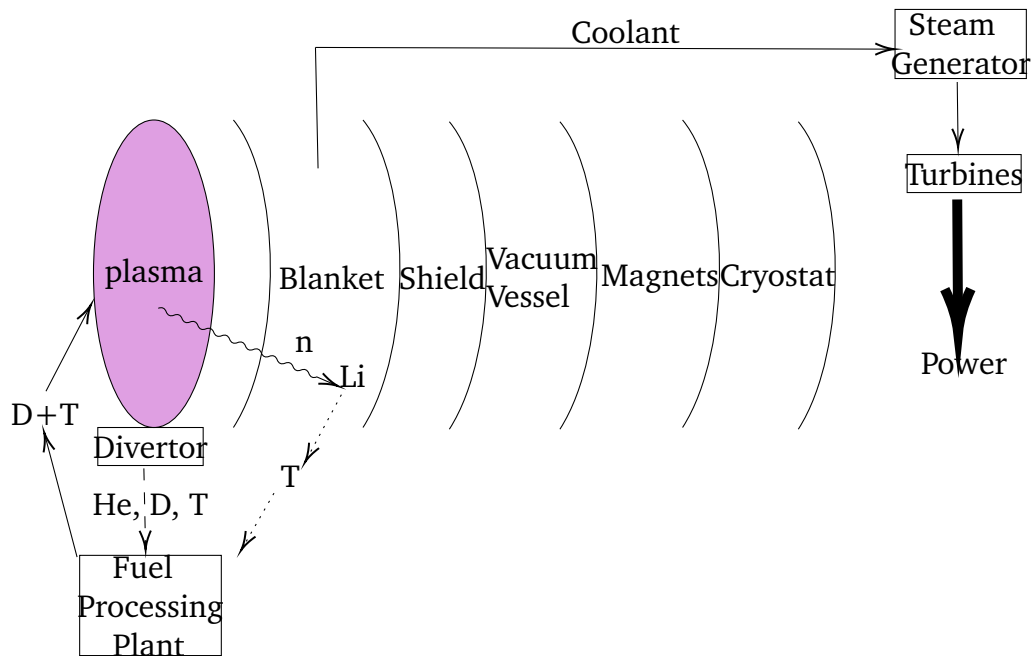
The following key components of a tokamak power plant can be distinguished based on the radial schematic shown in Fig. 2.2: plasma, feeding system, blanket, biological shield, magnets, cryostat, and heat-to-electricity conversion systems. The plasma could be a 50-50 mixture of deuterium and tritium in an ultra-high vacuum (<1 mPa) chamber. Tritium has a half-life of approximately 12.3 years, and it can not be found in nature, therefore tritium must be artificially bred to the plasma for maintaining the fusion reaction. Lithium has been proposed for that purpose since it can yield tritium upon reacting with neutrons by either of the two reactions in Eq. 2.6. Fortunately, lithium is an abundant element with approximately 0.2 g per ton of seawater [33] (see Table 2.4 for a total estimated amount worldwide). The divertor removes impurities from the plasma and He, and T, and it will have to resist high heat fluxes and neutron damage levels (10 MW/m² peak heat flux and neutron wall peak load of 0.5 MW/m² ITER). The blanket, where Li is meant to be contained, serves as a multi-purpose region: recover and transport heat, breed

and recover tritium, and survive neutron bombardment. ITER programme will carry out tests of several blanket concepts for testing the generation of tritium above the consumption rate (needing tritium breeding ratio above 1) including He-cooled Li-Pb, He-cooled pebble bed, water-cooled pebble bed, dual-coolant Li-Pb, and LiPb ceramic breeder [34]. The structural material of these blankets is stainless steels, and the blanket tests will be undertaken by the several parties involved in the ITER project, namely EU, China, Japan, US, Korea, and India. The blanket test modules also include a neutron multiplier material either Pb or Be. The magnetic field in ITER would be generated by approximately 20 D-shaped superconducting Nb₃Sn magnets, encapsulated inside the cryostat region where low vacuum is maintained to keep cryogenic conditions for the operation of the superconducting magnets. The cryostat structure is made of stainless steel and will contain many ports for services of plasma diagnostics, and plasma heating devices (ITER Radio-frequency and Neutral Beam Injection heating systems). The fusion energy deposited as heat in the blanket would have to be extracted through steam generators, turbines and electricity generators.



The electrical power demand worldwide at present amounts to roughly 3 TW. Based on this rough estimate, current energy electricity demands worldwide could be provided by approximately 3,000 nuclear fusion power plants each operating at 1 GWe. 3,000 power plants is a significant number when compared to currently operating nuclear fission power plants with 449 (as can be seen at [35]). For harnessing the fusion power with thousands of reactors in service for 40 years each, a large and wide variety of materials are required to construct and to operate fusion power plants. Leaving aside basic

Fig. 2.2.: Conceptual fusion reactor for illustrating the journey of the neutrons from the core to the blanket. Neutrons deposit their kinetic energy as heat and at the same time, they serve to breed new tritium for sustaining the D-T reaction.



construction materials such as concrete, the world reserves of the following fusion elements D, Li, Nb, Be, and Pb were 5×10^{13} t in seawater, 2.2×10^{11} t in seawater, 3,500,000 t inland, 18,000 t inland, 64,000,000 t inland respectively [3]. The material demand of D, T, Li, Nb, Be, and Pb for a fusion power plant operating during 40 years would be: 4.4 t, 15.2 t, 29.2 t, 100 t, 3000 t, and 35,000 (Pb will be required for neutron multiplication in the Li-Pb blanket design) [36]. The materials demand when multiplied by 3,000 fusion power plants indicate that either Be or Pb are insufficient quantity in currently known worldwide reserve to serve to build future nuclear fusion power plants and that these material demand issues will have to be addressed with alternative neutron multiplication materials. See table 2.4 for a summary of the fusion resources.

Table 2.4.: Fusion resources for a 40 year lifetime 1 GW electric fusion power plant. Five replacements of the blanket have been assumed, and that both D, and T have to be replenished every year during the lifetime. Note that T will have to be bred from Lithium, and fueled into the plasma. Nb will be required for the superconducting magnets. Data retrieved from [36] and [3].

	D	T	Li	Nb	Be	Pb
Mass per plant (Tonnes)	4.4	15.2	29.2	100	3,000	35,000
Worldwide reserves (Tonnes)	4.6×10^{13}	-	2.2×10^{11}	3.8×10^8	18,000	70,000,000

2.2 Physics of radiation damage in metals

The application of alloy materials in nuclear reactors, particularly in the first wall of fusion power plants with its high neutron flux density, causes radiation damage to be a technological problem. When ionizing radiation penetrates matter, displacement and rearrangement of charges in the atoms and molecules along the path of the ionising radiation may lead to chemical changes and changes in crystal configurations, and may on the nuclear level affect both the chemical and physical properties of the material. Atomic defects in metals form endothermically. The required energy can be supplied athermally which is possible by the kinetic energy of irradiation. Important property changes such as swelling, radiation-induced creep, embrittlement, and radiation-induced atom redistribution can have a drastic influence on the lifetime of reactor components

The ionising species considered here are neutrons, electrons, light ions (electron charge, e ; mass, M_1 ; speed, v ; and kinetic energy, E_1), and heavier ions (electron charge number, $2 < Z_1 < 20$; mass, M_1 ; speed, v_1 ; and kinetic energy, E_1). The particle radiation interactions are with matter, in particular in the condensed solid state. Charged particle radiations mainly lose energy to the matter through inelastic scattering collisions with the atomic electrons

Table 2.5.: Penetration of radiation in matter is quantified by the particle range. Typical examples of radiation and their ranges in air. Table adapted from [37]. Thermal neutrons refer to the energy range 0.02 to 0.05 eV.

Particle	Mass (MeV/c ²)	Charge (e)	Speed	Interaction	Range (in air)
Fission product	10s-100s	+10s-100s	Slow	Coulomb	Few μm
α -particle	37200	+2	10 % c	Coulomb	Few cm
Electron	0.511	-1	90 % c	Coulomb	Few m
Positron	0.511	+1	90 % c	Coulomb	Few m
Photon	0	0	c	Coulomb	100s m
Neutron	940	0	thermal	Strong nuclear	100s m
Neutrino	0	0	c	Weak nuclear	1000s km

in the matter, exciting them and resulting in ionisation of the matter (atomic number density, n_2 ; atomic number, Z_2 ; and atomic mass M_2). Charged particle species can also interact with the nuclei of the matter by the elastic scattering collisions, which is important for displacement damage. On the other hand, neutrons interact mainly by elastic and inelastic scattering collisions with the nuclei of the matter, and also with the nuclei of matter by nuclear forces in nuclear reactions, which results in activation. Atomic ionisation energies are of the order of several, eV, can be approximated by the mean ionisation potential $I = 11Z$ (eV) [37].

A sharp contrast exhibits between charged particle (electrons, positrons, α -particles, heavy ions), and uncharged particle (neutrons, γ -rays) radiations. Charged particle radiation interact through the long-range Coulomb force with a large number of small interactions, making it very difficult to study the scattering on a collision by collision basis. The implications of the number of these interactions are reflected partially in Table. 2.5. For example, the slowing down of neutron, γ -rays, and electron radiation from 0.5 MeV to 0.0625 eV in Al is resulted after 30, 10, and 10^5 collisions respectively.

2.2.1 Elementary neutron matter interactions

The interactions of neutrons with matter are the most complex as they cover all four fundamental interactions (strong and weak nuclear, electromagnetic, and gravitational). As first demonstrated experimentally by Alvarez and Bloch in 1940 [38], the neutron has a magnetic moment in nuclear magneton of $-1.91 \mu_N$ [39], which allows for electromagnetic interactions. Three interactions of neutrons and matter are relevant for nuclear fusion materials: elastic collisions, inelastic collisions (nucleus excitation followed by emission of γ -rays), and neutron capture i.e. (n,p) for production of hydrogen gas, and (n,α) for production of helium gas within the material. Other neutron capture nuclear reactions include $(n, 2n)$, $(n, n'p)$, (n, d) , and fission, where the ejected particles are two neutrons, a neutron and a proton, a deuteron, and for fission the ejected products are Ba, Kr, and 2 two neutrons. Altogether, these interactions need to be taken into account to track the change in energy of the 14 MeV neutrons, as they are transported through the blanket interacting with the materials. The transport of neutrons is formulated in terms of flux variation across phase space in position, energy, and angular orientation ($\vec{r}, E, \vec{\Omega}$ respectively), which under steady-state conditions follows the Boltzmann transport equation [40] as shown in Eq. 2.9. In Eq. 2.9 the LHS term is the streaming of neutrons; the terms on the RHS represent the neutron capture Σ_t ; the next term represents the scattering term, Σ_s ; and the final term corresponds to the source/sink for neutrons, S .

$$\vec{\Omega} \cdot \nabla \Phi(\vec{r}, E, \vec{\Omega}) = -\Sigma_t(\vec{r}, E, \vec{\Omega}) \cdot \Phi(\vec{r}, E, \vec{\Omega}) \quad (2.7)$$

$$+ S(\vec{r}, E, \vec{\Omega}) \quad (2.8)$$

$$+ \int_{\vec{\Omega}'} \int_{E'} \Sigma_s(\vec{r}, E' \rightarrow E, \vec{\Omega}' \rightarrow \vec{\Omega}) \Phi(\vec{r}, E', \vec{\Omega}') dE' d\vec{\Omega}' \quad (2.9)$$

Table 2.6.: Main decay modes in radioactive nuclei and the emitted radiation (e^+ for positrons, e^- for electrons), $\bar{\nu}_e$ for antineutrinos, ν_e for neutrinos, and γ for photons).

Symbol	α	β^+	β^-	γ
Radiation emitted	He^{2+}	$e^+ + \bar{\nu}_e$	$e^- + \nu_e$	γ
Parent nucleus	(Z,A)	(Z,A)	(Z,A)	(Z,A)
Daughtet nucleus	(Z-2,A-4)	(Z-1,A)	(Z+1,A)	(Z,A)

Nuclei are characterised by their number of protons or atomic number, Z, and neutrons, N, totalling a given unique number of nucleons, A=N+Z. Nuclei can be stable or unstable, and they seek stability by decaying. The activity is the rate of radioactive nuclei decaying, and it is given by λN , where λ is the decay constant, and N is the number of nuclei at any given time. The units of decay rate are Becquerel (Bq) or Curie (Ci), where 1 Ci = 3.7×10^{10} Bq. The half-life of a nucleus, $T_{1/2}$, is the required time to halve the activity, and it is related to the decay constant by $T = \ln(2)/\lambda$. For example, the half-life of tritium is 12.3 years.

The following are examples of neutron transmutation reactions that result in the production of helium ${}_{Z}^A M + n \rightarrow {}_{Z-2}^{A-4} M + {}_2^4 He + n$, and ${}_{Z}^A M + n \rightarrow {}_{Z-2}^{A-3} M + {}_2^4 He$ [41]

2.2.2 Elementary charged particle matter interactions

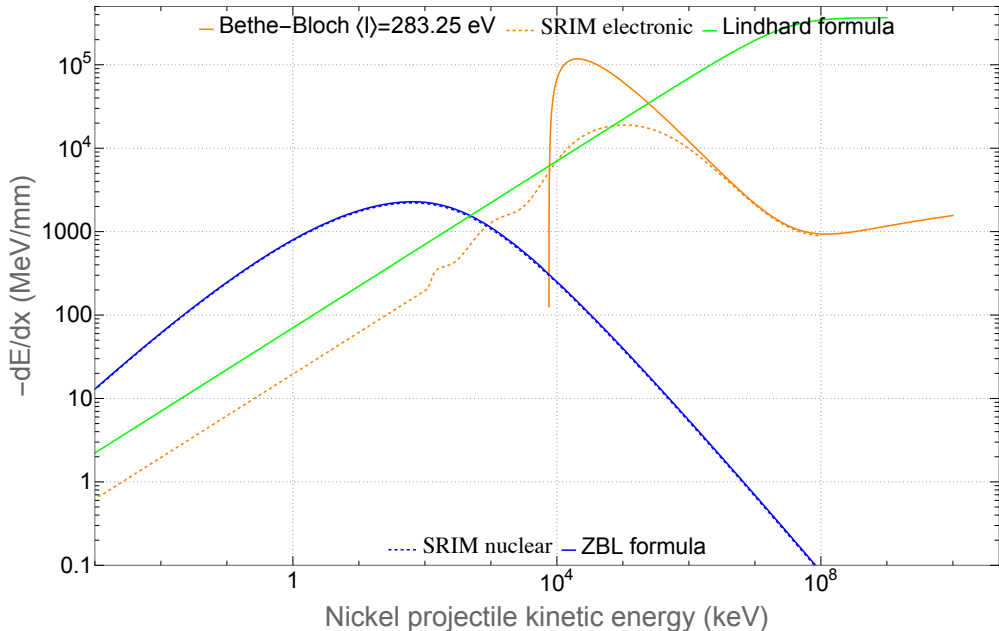
When incident charged energetic ions penetrate a solid, they are deflected by collisions to atoms, and also lose kinetic energy by collisions to the electrons and atoms approximately at a rate of 100 eV per nm of track length. The quantity of energy lost depends parametrically on energy, mass, and the atomic number of the charged ion, and also on the atomic mass, atomic number, and density of the target atom. For heavy ions, an approximate

formula [42] for the range of penetration into solids is given by Eq. 2.10. The range of charged particles in matter at moderate energy of MeVs is typically measured in μm , and this makes challenging the preparation of specimens for microscopy analysis [43, 44]. Consider the penetration of a fission product ^{137}Ba in the bulk of Uranium after fission occurs: $^{235}_{92}\text{U} + \text{n} \rightarrow ^{137}_{56}\text{Ba} + ^{97}_{36}\text{Kr} + 2\text{n}$, where the kinetic energy of the fission products Ba and Kr is 174 MeV. The range of Ba in pure U (density 19 g/cm³) results in 11 μm . Another example is the 1.5 μm penetration of a 5 MeV Nickel ion into bulk Ni with density 8.9 g/cm³. The track length R is related to the projected path along the direction of the incident ion by the expression $R_p = R/(1 + M_2/3M_1)$. The implantation of charged ion particle is distributed about the projected track length value due to straggling [42]. More values for the range of several incident radiations into air are provided in Table 2.5.

$$R(\text{nm}) = \frac{13E_1(\text{keV})}{\rho(\text{g/cm}^3)} \frac{1 + M_2/M_1}{Z_1^{2/3}} \quad (2.10)$$

Nuclear stopping for arbitrary projectile/target combination (atomic number less than 92 i.e. from hydrogen to uranium) is well established. It has been formulated by Ziegler, Biersack, and Littmark in a so-called "Magic formula" which is used in TRIM software is explicitly formulated in Eq. 2.11 in units of cm² MeV/g [45]. To convert the nuclear stopping power to units of MeV/mm, multiply Eq. 2.11 by the 1000 times the density in g/cm³. The reduced projectile energy, ϵ , is related to the projectile's energy in the laboratory system, E_1 , by the expression $\epsilon = \frac{32.53M_1M_2E_1/M_1}{Z_1Z_2(M_1 + M_2)(Z_1^{0.23} + Z_2^{0.23})}$, and $\kappa = \frac{0.6022}{M_2} \frac{8.462Z_1Z_2M_1}{(M_1 + M_2)(Z_1^{0.23} + Z_2^{0.23})}$ is prefactor to the energy dependent part in

Fig. 2.3.: Ni irradiation into CrMnFeNi HEA (density calculated 7.904 g/cm³ from the rule of mixtures at compositions 0.18, 0.27, 0.27, and 0.28 respectively for Cr, Mn, Fe, and Ni) in terms of stopping powers for nuclear and electronic stopping power. The Bragg-Kleeman additive rule was used for the continuous curves. SRIM includes electronic stopping tables until the threshold of 10 GeV/amu (approximately 10⁸ keV), this is the rightmost endpoint of the orange curve.



Eq. 2.11. Other values for range of several particles in air are provided in Table 2.12

$$-\left(\frac{dE}{dx}\right)_{nuclear} = \begin{cases} \frac{\kappa \ln(1 + 1.1383\epsilon)}{2(\epsilon + 0.01321\epsilon^{0.21226} + 0.19593\epsilon^{0.5})}, & \epsilon < 30 \\ \frac{\kappa \ln(\epsilon)}{2\epsilon}, & \epsilon > 30 \end{cases} \quad (2.11)$$

Interaction of charged particles with electrons results in slowing down, but no deflection of trajectory. At low speeds, the Linhard stopping formula proportional to projectile speed is correct Eq. 2.12. The factor $\frac{8\pi h^2}{m_e}$ has a practical value of 19.1511 MeV/mm if the atomic number density is put into 10²² cm³ units. This regime describes the electron pickup region by the projectile from the target atoms. The value of β_0 is given by the speed of an

electronic in the first Bohr orbit of atomic hydrogen $\frac{e^2}{4\pi\epsilon_0\hbar c}$. The Linhard stopping is compared to the SRIM electronic stopping in Fig. 2.3.

$$-\left(\frac{dE}{dx}\right)_{electronic,\beta \ll 1} = n \frac{8\pi h^2}{m_e} \frac{Z_2^{7/6} Z_1}{(Z_1^{2/3} + Z_2^{2/3})^{3/2}} \frac{\beta}{\beta_0} \quad (2.12)$$

At projectile energies approximately above 100 keV/amu (roughly 10 MeV for Ni ions), the moving ion is fully stripped of electrons and does not change its charge state. The Bethe-Bloch formula describes the stopping power quantum-mechanically for a charged particle moving in a homogeneous electron gas i.e. consisting of all electrons of the material as if they were evenly distributed. Thus the atomic structure of the sample becomes meaningless. For a comprehensive quantum mechanical derivation of the Bethe-Bloch formula, the reader is referred to the review paper by Inokuti et al. [46]. Bethe-Bloch formula for the electronic stopping power expressed in Eq. 2.13. The particle properties are the charge or atomic number, z ; and velocity normalised to the speed of light, $\beta = v/c$. The properties for the target are: n is the number density of the target atom in the solid, liquid, or gas; Z is the number of electrons in the target atom i.e. 28 for Ni; I is the mean ionisation potential for which we can use the rough approximation of $I = 11Z$ i.e. 172 eV compared to 154 eV for the case of Silicon. In working with the Bethe-Bloch formula it is useful to remember the relativistic expression that relates the kinetic energy per unit mass in atomic mass units of the projectile, E/m , with the velocity, $\beta = \sqrt{E/m(2c^2 + E/m)}/\sqrt{c^4 + 2c^2E/m + (E/m)^2}$.

$$-\left(\frac{dE}{dx}\right)_{electronic,\beta \gg 1} = \left(\frac{e^2}{4\pi\epsilon_0}\right)^2 \frac{4\pi z^2 Z n}{m_e c^2 \beta^2} \left(\ln\left(\frac{2m_e c^2 \beta^2}{I}\right) - \ln(1 - \beta^2) - \beta^2 \right) \quad (2.13)$$

For compounds, for example, alloys, where several elements, i (with the atomic number Z_i , and the molar volume v_i), are mixed with composition c_i , the stopping power can be approximated by the Bragg-Kleeman additive rule with an error 10-20 %.

$$\left(\frac{dE}{dx} \right)_{alloy} = \sum_i \frac{c_i v_i}{Z_i} \frac{\sum_j Z_j c_j}{\sum_j Z_j c_j v_j} \left(\frac{dE}{dx} \right)_{i-th-element} \quad (2.14)$$

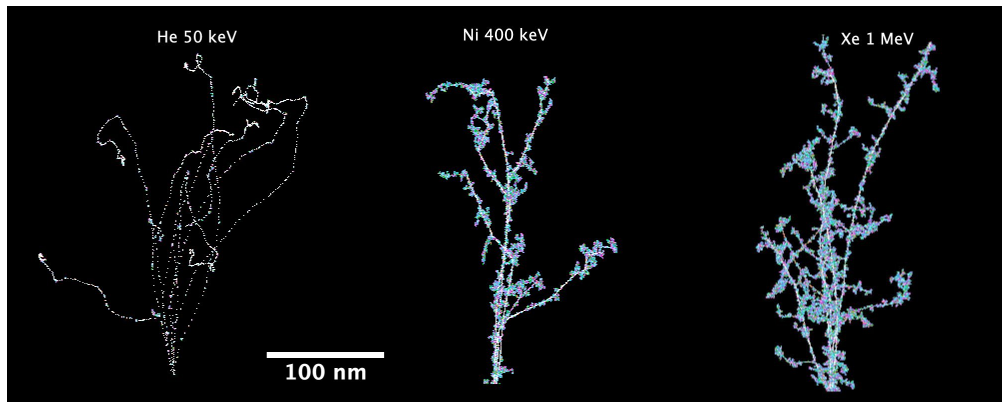
Nuclear interactions can also occur between charged particle radiation and nuclei, but these occur at much higher energies of 10s of MeV (see threshold energy from Section 2.1)

2.2.3 Defect cascades at elevated temperatures

The production of atomic defects by irradiation of neutrons or charged particle radiations involves roughly four processes distributed across time from 10^{-21} s (1 zeptosecond) to 10^9 s (40 years) and length scales of 0.1 nm (atomic spacing) to 100s μm (grain size) [47]. The first process corresponds to an energy transfer from radiation particle to the nucleus (10^{-21} - 10^{-14} s, and length scales of 0.03nm) which result in the transfer of kinetic energy to the struck nucleus (see Appendix C for a description of two-body kinematics), becoming the PKA - primary knock-on atom. During the next stage, interatomic collisions occur resulting in collision damage cascades (10^{-13} - 10^{-12} s, and length scales of 5nm); the third stage the displacement cascade dissipates excitation energy resulting in the displacement cascade with stable atomic defects and clusters. The final stage of radiation damage is the thermal migration of the atomic defects by diffusion, resulting in growth and formation of other clusters of defects (10^{-11} - 10^9 s, and length scales of μm 's).

The primary knock-on atom (PKA) gains recoil energy, T , from its collision with the incident particle radiation with energy, E_1 . The minimum recoil energy of a lattice atom for being displaced from the lattice site is the displacement energy, T_d , and the maximum recoil energy, T_m , that the incident radiation can transfer is given by $T_{max} = 4M_1M_2/(M_1 + M_2)^2E$ or by $T_{max} = \frac{2M_2E(E + 2M_1c^2)}{(M_1 + M_2)^2c^2 + 2M_2E}$ (conservation of energy formula in the classical and relativistic limit), see the appendix A and [48] for a comprehensive formulation of kinematics of recoil for classical and relativistic particles. Where M_1 and M_2 are the atomic masses of the incident and recoil particles, and E is the energy of the M_1 particle. A simple calculation for a Fe lattice bombarded by fusion radiation is depicted in table 2.7; the PKA recoil energy is well within the keV region, and therefore Lindhard electronic stopping formula is more appropriate than Bethe-Bloch. The distribution probability of recoil energies can be understood in terms of the recoil differential cross-section, $d\sigma[E, T]/dT$. The median recoil energy, which can be calculated from the recoil differential cross-section produced by ions by using the analytical formula reported in [49]; specifically $\langle T \rangle = \int_{T_d}^{T_{max}} T \frac{d\sigma[E, T]}{dT} dT / \int_{T_d}^{T_{max}} \frac{d\sigma[E, T]}{dT} dT$. The reader is recommended to read the comprehensive discussion on cross-sections (Chapter 4) from the monograph [42]. The energy imparted to the PKA depends on the atomic mass of the incident radiation: light incident radiation favours low energy transfers, and an atomic mass increases so does the average recoil energy. An approximate expression of the recoil energy is given by $\langle T \rangle = T_d \ln \left(\frac{4M_1M_2}{(M_1 + M_2)^2} \right)$. On the other hand, for neutrons, energetic recoils are equally favoured (this behaviour is illustrated in Fig. 2.5), with approximate average recoil energy given by $\langle T \rangle = E_1 \frac{2M_1M_2}{(M_1 + M_2)^2}$. Energetic recoils create dense and large displacement cascades (DC), as shown in Fig. 2.4 after performing a Monte Carlo simulation with 3 different radiations different in mass and energy, and the effect is enhanced with the mass of the projectile or heavy-ion. The energy transferred to a PKA, T , is not entirely available to cause more displacement damage. The fraction of PKA energy available to cause displacement energy, T_{dam} has been calculated

Fig. 2.4.: TRIM calculation displaying projected trajectories of 3 different incident ions as well as the location where primary, secondary, tertiary, and higher-order knock-on atoms in $\text{Cr}_{18}\text{Fe}_{27}\text{Mn}_{27}\text{Ni}_{28}$ with recoil energies $T > E_d$ were produced. Furthermore to the trajectories, the collision cascade with the sub-cascades is also visible in red and blue for vacancies or interstitials. The incident radiation energy and mass increase from left to right depicting.



in various ways including a formulation in terms of the ratio of nuclear and electronic stopping powers [50]. The current standard is the so-called NRT model [51] (see Table 2.8) which has been implemented in Monte Carlo radiation transport codes such as MCNP [52].

Displacement cascades are formed when the PKA carries recoil energy, T of keV order, which is much higher than the displacement energy, E_d . The PKA generates many recoils with energies slightly higher than the displacement threshold T_d , resulting in cascade damage. The energy losses of the PKA or secondary ions to the electronic excitations result in the deposition of deposit heat, a process known as a thermal spike. The duration of the Displacement cascade caused by the PKA in its slowing down can be estimated from the range expression 2.10 and the speed of the PKA ion, $v = \sqrt{2E/m}$, by $\Delta t = 2vR$; for example for a 0.5 keV PKA in pure Ni, the displacement cascade time to form is approximately 8×10^{-15} s. After the displacement collision, the radiation-damaged volume is known as a thermal spike due to the kinetic energy deposited by the atomic collisions. During the thermal spike, an amorphous phase (collision cascade) forms as the energy of the PKA or the secondary ions is partitioned among the surrounding lattice atoms.

Table 2.7.: Calculation of maximum and the averaged recoil energy of a PKA in solid Fe and W from bombardment by typical energetic neutrons (energy spectrum of fusion neutrons [53]), α -particles, and electrons. The average PKA energy from α -particle bombardment has been calculated using the differential energy transfer in analytical form from [49]. The recoil energy of the PKA after the electron bombardment is negligible.

	14 MeV-neutron	3.5 MeV α -particle	200 keV electron
T_{\max} (Fe-PKA)	980 keV	870 keV	10 eV
$\langle T \rangle$ (Fe-PKA)	18.8 keV [53]	0.4 keV	-
T_{\max} (W-PKA)	306 keV	292 keV	3 eV
$\langle T \rangle$ (W-PKA)	3.2 keV [53]	0.5 keV	-

Fig. 2.5.: Differential energy transfer cross section from several energetic radiations to a Ni-PKA recoil atom. The units are in Bohr radius squared per keV energy ($a_0 = 5.29 \times 10^{-9} \text{ cm}$). For ion radiations, the differential cross section is reported of Mueller [49]. For neutrons, $\sigma(E=14 \text{ MeV}) = 1.207 \text{ b}$ ($1 \text{ b} = 10^{-24} \text{ cm}^2$), and that $d\sigma/dT$ is uniformly distributed across T_d , and T_{\max} .

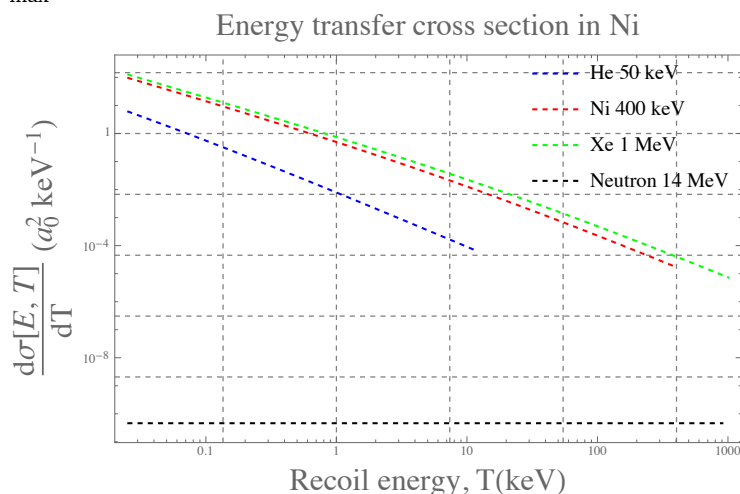


Table 2.8.: The average number of displacements produced as a function of the PKA energy according to two models NRT [51], and TW [50].

	ν_{NRT}	ν_{TW}
$T_{\text{dam}} > 2.5T_d$	$\frac{0.8T_{\text{dam}}(T)}{2T_d}$	$\frac{1}{2T_d} \int_0^T \frac{(dT'/dx)_{\text{nuc}}}{(dT'/dx)_{\text{nuc}} + (dT'/dx)_{\text{elec}}} dT'$
$T_d < T < 2.5T_d$	1	-
$T < T_d$	0	-

Subsequently, the cascade affected region relaxes, leaving behind a residual number of vacancies and interstitials (Frenkel pairs). The radius of the cascade region, r , has been estimated to be several Å, resulting in a thermal spike duration, $t = r^2/D$, of several 10's of ps, where the thermal diffusivity at the melting temperature has been assumed to be approximately given by $D = 0.001$ cm/s.

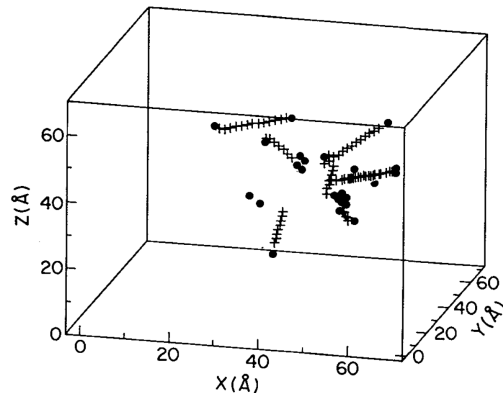
Interstitials are produced during the cooling down of the thermal spike cascade region. During the cooling phase, interstitials are ejected beyond shock wave by a process of replacement collision sequences leaving a vacancy in the spike. The end result is a stable Frenkel Defect (FD). Another process by which interstitials in FCC metals are produced occurs at the shock front when platelets of perfect interstitials loop on {111} planes glide along their burgers vector. On the other hand, vacancies are produced by direct ejection of the lattice atom. Figure 2.6 illustrates the process of interstitial emission by replacement collision sequences.

The displacement per atom (dpa) [55] is a commonly used quantity to report a measure of particle fluence independently of the type of incident radiation (neutron or from simulation experiments with light or heavy ions). The dpa, ϕ is calculated from the radiation flux, φ , the irradiation duration, t ,

Table 2.9.: The implications of the nature of incident radiation into the formation of atomistic defects in solids. The values have been estimated from the formula 2.15, and Ni number density of $9.1 \times 10^{22} \text{ cm}^{-3}$, and $T_d = 40 \text{ eV}$

Radiation type	Schematic	$\text{PKA} - \langle T \rangle / T_{\max} (\text{keV}/\text{keV})$	Dpa along range ($\text{Dpa} \cdot \text{cm}^2/\text{Ion}$)	Dominant Damage
200 keV Electron		0.007/0.004	6×10^{-21}	Frenkel pairs
1 MeV Proton		0.3/66	10^{-17}	
5 MeV Nickel		0.5/5000	3×10^{-15}	Cascade and sub-cascades
14 MeV Neutron		465/930	2×10^{-21}	Cascade and sub-cascades

Fig. 2.6.: Molecular dynamics simulation of a displacement cascade generated by a 5 keV Ni PKA in Ni. Interstitials (filled) and several replacements (+) are depicted. The length of the replacement collisions is roughly 20 Å. The depleted zone of vacancies (omitted for clarity) is located at position (40,20,20) Å of the coordinate system. Figure reproduced from [54]



and the displacement cross section, σ_d measured in barns or cm². The displacement cross section, $\sigma_d[E_i] = \int_{T_d}^{T_{max}} \frac{d\sigma}{dT}[T; E_i] \nu_{NRT}[T] dT$ is calculated in turn from the recoil differential cross section, $d\sigma/dT[T; E_i]$ (see figure [53] for a depiction of the recoil differential cross section), and from the total number of lattice displacements that a PKA (caused from direct bombardment by neutrons or ion irradiations but not electrons) with given recoil energy, T , produces, $\nu_{NRT}[T; E_i]$. The formulation of the average number of displacements for an energetic PKA is provided in Table 2.8. Here the number of lattice displacements per PKA is typically taken to be that from the so-called NRT model [55] that accounts for an analytical formulation of the electronic stopping power of the PKA to the electrons in the lattice. In practice, the dpa from simulation experiments involving ion irradiations can be approximated from SRIM software after taken consideration in the settings of the simulation, following [56]; this will be shown in Fig. 4.

In Table 2.9, the effect of incident particle radiation into types of atomistic damage in solids are illustrated. The estimations of displacements per atom refer to the integrated number displacements generated along the track of the radiation (the range given by R) in the bulk of a solid with number density N,

and for a unit dose 1 particle-cm⁻² (see [42] for a more detailed derivation of Eq. 2.15). The recoil energy transferred from the incident radiation to the PKA increases from electrons, protons, Ni ions, to neutrons. The implications of Table 2.9 are relevant for ion beam acceleration experiments in materials science to mimic neutron damage from fusion reactors. Heavy-ion irradiations such as Nickel generate energetic recoils which lead to more abundant cascade damage than for light ion irradiation such as protons. Electrons on the other extreme generate mainly point defects.

$$Dpa/Fluence = \frac{N_d(E)}{NR} = \frac{0.64E_1}{2NRT_d} \quad (2.15)$$

For charged particle radiations of 1 MeV He and 5 MeV Ni ions, a simple analytical formula for the scattering cross-section and mean free path (average distance between atomic collisions) can be derived using a screened Coulomb interatomic potential. The formula 2.16 can be derived by straightforward integration of the $d\sigma/dT=C_1/(E_1 T^2)$ expression, which has been reported for screened Coulomb collisions (the value for the constant C_1 may be found at [42]). The units of the cross-section σ in Eq. 2.16 are in squared Bohr radius units ($1 a_0=0.529 \text{ \AA}$). A calculation for 1 MeV He, and 5 MeV Ni ions into solid Ni gives $0.012 a_0^2$, and $7.15 a_0^2$. Therefore, Nickel ions interact more strongly in the solid than He ions. The mean free path at these energies can be obtained from the expression $1/(N \sigma)$ where N is the number density of bulk atoms in the solid, which for pure Ni is $9.1 \times 10^{22} \text{ cm}^{-3}$. The mean free path for 1 MeV He solid Ni collisions is $0.3 \mu\text{m}$, and that for 5 MeV Ni solid Ni collisions is 0.5 nm , a factor of 1,000 difference. Finally, regarding neutron radiation, the scattering cross-section for a 14 MeV neutron interaction with Ni nucleus is approximately $3.6 \times 10^{-8} a_0^2$ (see Fig. 2.5), much weaker than for charged particle radiation. In consequence, the mean free path for neutron

collisions with Ni nuclei is 10.9 cm. The mean free path is illustrated in schematic form in the Table. 2.9.

$$\sigma(E_1, T_d) = \left(-\frac{5.81 \cdot 10^{-10}}{(E_1(\text{in MeV}))^2} \frac{Z_1^2 Z_2^2 (M_1 + M_2)^2}{M_2^2} + \frac{0.0023}{E_1(\text{in MeV}) T_d(\text{in eV})} \frac{M_1 Z_1^2 Z_2^2}{M_2} \right) a_0^2 \quad (2.16)$$

Atomic defects such as vacancies, interstitials, and their clusters disappear by annealing to a sufficiently high temperature by several defect reactions. Each defect reaction affects the macroscopic properties of the alloy system. These reactions are detailed in Table 2.10. For example, interstitial point defects are mobile at low temperatures, and vacancies become mobile at room temperatures. Interstitial point defects cause distortions of the crystal structure, and vacancy point defects lead to thermally activated atomic transport.

The identification of the defect reaction mechanisms is understood from the so-called resistivity recovery curves. In these experiments, a metal is irradiated at temperatures near 0 K, and then the sample is annealed at a given temperature for several minutes, and the electrical resistivity is measured. When the experiment is repeated for different temperatures, the result is a curve where the resistivity recovers its non-irradiated quantity only at the highest temperature isochronal annealing heat treatments.

The recovery of resistivity can be analysed into stages. Each stage is associated with a defect reaction. The recovery of resistivity in the prototype Cu can be found in [57] . The following temperature sub-stages are found A, B, C, D, and E. Stage I is associated to spontaneous recombination of nearby Frenkel pairs, or recombination produced after interstitials migration (either correlated or uncorrelated depending on the migration distance). Stage II:

Table 2.10.: The categorisation of radiation damage effects (Low-temperature embrittlement, irradiation growth, void swelling, RIS - radiation-induced segregation, and helium embrittlement at high temperature) occurring as a consequence of fundamental defect reactions as a fraction of homologous temperature (melting temperature T_m). Adapted from [58]

Defect Reaction		Temperature range	Effect
Recombination	$I_1 + V_1 \rightarrow 0$	$T/T_m > 0.05$	none
	$I_m + V_i \rightarrow V_{i-m}$		
	$I_g + V_i \rightarrow V_{i-g}$	$T/T_m > 0.1$	
	$V_m + I_i \rightarrow I_{i-m}$	$T/T_m > 0.2$	
Agglomeration of interstitials and vacancies	$I_m + I_{m'} \rightarrow I_{m+m'}$	$T/T_m > 0.05$	Embrittlement
	$I_m + I_i \rightarrow I_{m+i}$		Embrittlement
	$I_g + I_g \rightarrow I_i = I_{g+g'}$	$T/T_m > 0.01$	Embrittlement
	$I_g + I_i \rightarrow I_i = I_{g+i'}$		Irradiation growth
	$V_m + V_{m'} \rightarrow V_{m+m'}$	$T/T_m > 0.2$	Irradiation growth
	$V_m + V_i \rightarrow V_i = V_{m+i'}$		Irradiation growth
Vacancy emission	$V_i \rightarrow V_{i-1} + V_1$	$T/T_m > 0.3$	
Annihilation at sinks	$V_m + S \rightarrow S$	$T/T_m > 0.2$	Void swelling
	$I_m + S \rightarrow S$		Irradiation creep
	$I_g + S \rightarrow S$	$T/T_m > 0.1$	Irradiation creep
Interaction with foreign atoms	$V_m + A \leftrightarrow (A V_m)$	$T/T_m > 0.2$	RIS, He embrittlement
	$n(AV_m) + S \rightarrow S + A_n$		RIS, He embrittlement
	$I_m + A \leftrightarrow (AI_m)$		RIS, He embrittlement
	$n(AI_m) + S \rightarrow S + A_n$		RIS, He embrittlement

Growth of interstitial clusters into the formation of dislocation loops, and migration of SIA-solute complexes, and the formation or dissociation of SIA-solute complexes. Stage III: Defect reactions associated with this stage are linked to single vacancy migration and its annihilation at interstitial clusters, and secondly to the formation of small vacancy clusters. Stage IV: Growth of vacancy clusters. In some metals like Al, Pt, or Au rapid single vacancy migration results in efficient annihilation at dislocation loops, so that growth of vacancy clusters in these metals does not occur. Stage V: Dissociation of vacancies and interstitial clusters. Vacancies annihilate at dislocation loops

A wide variety of phases have been reported in steels depending on composition, and thermomechanical treatment. Under irradiation, the kinetics of phase alterations are the result of three thermodynamically driven forces

[59]: 1) supersaturation of point defects (vacancies and interstitials) which can bind to solute atoms (see Table 2.10) that drag the solute atoms upon concentration gradients of point defects. 2) Inverse Kirkendall effect resulting in segregation of slowest self-diffusing species at sinks where vacancies are diffusing into. 3) Driving forces caused by the presence of radiation-induced point defect clusters (Frank loops, He bubbles, and voids).

2.3 Fusion reactor structural materials

The European Union plans for harnessing fusion power included the already built JET which demonstrated how deuterium-tritium plasmas can produce a peak of 16.1 MW and under quasi-stationary conditions more than 4 MW of fusion power [27]. More recently, ITER (Cadarache, France) fusion experiment which is expected to begin operations for its first plasma by 2025 ([60]), and the definitive reactor DEMO, intended for assessment of commercial viability of fusion reactors. A plan for DEMO is not yet clear as it depends on some of the findings from the ITER experiment (namely proving the feasibility of producing 500 MW from 50 MW of input power [61]), but there exist the so-called conceptual power plant designs (PPCS) [62]. Based on plant efficiency arguments, the PPCS studies have resulted in a set of 4 concepts (as seen in Fig. 2.7) differing from each other by the type of coolant for the heat extraction, the composition of the tritium breeder containing lithium, and by the inlet or outlet temperatures of the coolant into the blanket [62].

The selection of a candidate structural material for fusion reactors is complex because it depends on many factors. However, to maximise power generation of future fusion reactors by optimising the plant efficiency and considering economical factors, it would be required to widen the window of operational temperatures for structural fusion material candidates. Some of

Fig. 2.7.: The four power plant conceptual studies. Figure reproduced from [63]

	Model A or WCLL	Model AB or HCLL	Model B or HCPB	Model C or Dual-Coola.	Model D or Self-cooled
Structural material	EUROFER	EUROFER	EUROFER	EUROFER	SiC/SiC
Coolant	H ₂ O	He	He	LiPb/ He	LiPb
Coolant I/O T(°C)	285 / 325	300 / 500	300 / 500	480 / 700 300 / 480	700 / 1100
Breeder	LiPb	LiPb	Li ₄ SiO ₄	LiPb	LiPb
TBR	1.06	1.13	1.12	1.15	1.12
Structural material	CuCrZr	W alloy	W alloy	W alloy	SiC/SiC
Armour material	W	W	W	W	W
Coolant	H ₂ O	He	He	He	LiPb
Coolant I/O T(°C)	140/167	~ 540/720	~ 540/720	~ 540/720	~ 600/990
Net efficiency	0.31	0.35	0.36	0.42	0.60

blanket
divertor

these factors that influence the temperature window of structural materials include: material fabricability and welding technology for full reactor implementation; mechanical and thermophysical properties in the nonirradiated microstructure; the mechanical and thermophysical properties in the irradiated microstructure; corrosion considerations between the material and the coolant; nuclear properties (activation, and tritium breeding considerations) [6]. The importance of each of these factors in the selection of suitability of a given material for fusion depends on each particular material, but previous experience has shown that irradiation embrittlement (loss of ductility with irradiation), thermal conductivity, helium embrittlement, thermal creep, and corrosion compatibilities with coolants at high temperatures are the most important material properties determining the potential applicability of a material alloy or ceramic to fusion [6].

At present, there is no dedicated 14 MeV neutron source for experimental tests of the first wall and blanket material structures and their behaviour under irradiation. The fusion community has relied on fission reactors with fast neutron spectrum (<5 MeV), electrostatic accelerators in single, dual or triple beam configurations, neutron spallation sources, cyclotrons [64]. A suitable neutron spectrum can be in principle obtained both from plasma-based or accelerators based facilities with either gas, liquid or solids target

Table 2.11.: Ion beam facilities for irradiation of materials in the energy range kV to MV. Note that some facilities can do in situ TEM characterization. Adapted from [64]

Ion beam facility	Accelerator voltage	Details
Michigan Ion Beam (USA)	1.7-3.0 MV	
Sandia's Ion Beam (USA)	3.0-6.0 MV	
Los Alamos Ion Beam (USA)	3 MV	
Argonne Ion Beam (USA)	2 MV	In situ TEM
ORNL Ion Beam (USA)	3 MV	
JANNUS Saclay (France)	3 MV	
JANNUS Orsay (France)	2 MV	In situ TEM
FZ Dresden (Germany)	3 MV	
FSU Jena (Germany)	3 MV	
Surrey Ion Beam Centre (UK)	0.2 kV	
Dalton Cumbrian Facility (UK)	5 MV	

and proposals have been made for accelerator-driven neutron sources for a future closer mimicking of the fusion neutrons including IFMIF, and FAFNIR [65, 66]. See Table 2.11 for a listing of some ion beam facilities currently in use for studying fusion materials after radiation damage. Note that Dalton Cumbrian Facility at the University of Manchester has among the highest acceleration voltages.

2.3.1 Ferritic/Martensitic steels

The European Union has put the focus on the development of structural materials for two of the models in particular [67]: the helium-cooled pebble bed (HCPB); and the helium-cooled lithium lead (HCLL). Both of these models use EUROFER as structural material at operating temperatures between 300 and 500 °C. The motivations for EUROFER reside in the fact Cr (in the range 9-12 atomic %), W, Mn, V, Ta, and the remaining elements of EUROFER (see [67] for detailed composition values of EUROFER alloys) are all classified as reduced activation elements upon neutron radiation exposure. Activation

of materials exposed to fusion radiation is an issue from the radiological waste point of view. Simulations of neutron activation and decay heat have been performed [68] to reveal that only a few primary elements are safe from the induced residual radioactivity levels - namely C, Si, Ti, Fe, and Cr. The parameter that dictates how safely can a material be disposed of is the clearance index, which needs be below 1 in order to be handled as non-radioactive by IAEA (International Atomic Energy Authority) guidelines [68]. Furthermore, EUROFER has radiation resistance in terms of low swelling. Swelling is a complex phenomenon by which irradiation-induced point defect cluster into voids, increasing the macroscopic volume (several per cent increase have been observed in FeCrNi austenitic alloys [69]) and leading to deformed materials. Swelling is dependent among other parameters on the crystal structure. EUROFER being BCC appears to reduce void swelling with respect to FCC crystal structures (see [70, p. 78] for a detailed description of the effect of crystal structure on void swelling). The risks for EUROFER as fusion material were summarised by [9]: the low temperature limit of 300 °C was found from irradiation hardening and embrittlement associated to a significant increase (from -100 °C to a values between 100-200 °C) of the ductile-brittle transition temperature (see [71, Fig. 3]) after 70 dpa irradiation; and at high temperature for the decline in strength (less than 400 MPa after 500 °C) and the decline in thermal creep performance after 500 °C with time to rupture failure dropping below 1 yr for creep stresses of 100 MPa. The temperature window limits questions over the applicability of EUROFER to the 700 °C coolant temperature for model C of the PPCS (see Fig. 2.7)

2.3.2 ODS steels

Oxide dispersion strengthened steels (ODS) are intended to be an advanced version of EUROFER, in the sense of extending the operation temperature window of EUROFER by 100 °C from the limit of 500 °C of EUROFER due to

thermal creep [67] improvements and the low-temperature limit by improving the irradiation hardening properties. ODS-EUROFER steels manufactured by producing a fine-grained structure with densely populated Y–Ti–O 5 nm-sized nanoclusters in the matrix, showed that the ductile to brittle transition temperature after small level of irradiation of 1.5 dpa maintained the ductile to brittle transition temperatures at cryogenic temperatures [72, Fig. 9]. The potential improvement of ODS-EUROFER alloys with respect to EUROFER has been rationalised in terms of the increased effective irradiation point defects bias strength to sinks [9], allowing for more point defect recombination with cluster defects of irradiation-induced dislocation loops (as observed in EUROFER [71, Fig. 2]); thus improving the low-temperature irradiation-induced hardening behaviour. With regards to the high-temperature creep and strength performance, it has been rationalised that it is the grain size reduction that by reduction of dislocation movement can improve yield strength and creep performance [73, see Fig. 3] with respect to ferritic martensitic steels. Despite the positive improvements of ODS steels with respect to ferritic martensitic, further research is required to improve upscale production of ODS steels and joining [74].

2.3.3 Austenitic steels and other materials

Austenitic stainless steels are known from their extensive use in commercial pressurised water fission reactors [10]. The temperature window for austenitic stainless steels appears to be limited by loss of ductility and fracture toughness after irradiation at the low-temperature limit of 300°C and 10 dpa [75, see sec. 2.3.4]; and for void swelling due to the FCC crystal structure ([70, p. 78]), and helium embrittlement at the high temperature limit of approximately 500 °C at 20 dpa [9].

Vanadium alloys have also been reported as fusion materials for structural applications. The details of the physical properties of austenitic, ferritic/martensitic, vanadium alloys, and a high entropy alloy are reported in Table 2.12.

2.4 High entropy alloys

According to materials science, the performance of a material is determined by its microstructure. Other approaches, such as Edisonian testing or trial and error, are not materials science because they do not try to control the microstructure through changing composition, or processing. The microstructure of metallic materials includes a hierarchy of structural features from atoms in a crystal structure (5 Å), individual dislocation (10 nm), dislocation cells (0.2 μm), single grains (10 μm), grain structure (0.1 mm), and to the macro-structure of forgings (10 cm). In this section, the phase stability, mechanical properties and irradiation performance of high entropy alloys for assessing their suitability as structural materials in fusion reactors are reviewed. The atomistic nature of radiation damage caused by fusion neutrons narrows this review to microstructural instead of macroscopic properties. The scope of the review of HEAs is greatly limited to a few selected pieces of work because of the early stage [11, 83] of development of these alloys in fields such as fabrication, heat treatments and thermo-mechanical processing, phase diagrams, mechanical properties.

The terminology of High-entropy alloys (HEAs), and multi-principal element alloys (MPEAs) were used to refer to investigations of structural or functional properties of multicomponent alloys with compositions near the equiatomic region from the compositional space [84]. One of the earliest papers on these alloys [11] defined HEAs by the requirement of having 5 or more distinct chemical elements in concentrations ranging from 5 at. % to at.

Table 2.12.: Physical properties of some fusion materials without irradiation. The temperature limits on F/M steels, VCr₄Ti₄, and Austenitic steel refer to a minimum corrosion rate of 5 $\mu\text{m}/\text{year}$ at coolant speeds of 1.5 m/s. The electrical resistivity for the CoCrFeMnNi is an estimation from the corresponding room temperature value for CoCrFeNi alloy. The elongation at fracture for austenitic steels corresponds to solution annealed samples and tensile test performed at room temperature. Most data of properties were taken from [76, Table.10-5]. The Young's and Shear modulus are reported from room temperature tensile experiments. Note that the shear modulus(G) has been estimated from Young's modulus(E) and the Poisson ratio ($\nu=0.3$) by $G=E/2(1+\nu)$.

	F/M steel	VCr ₄ Ti ₄	Austenitic steel	CoCrFeMnNi
Melting temperature (°C)	1,420-1,800	1,890-2,170	1,400-	1280-1350[15]
Density (g/cm ³)	7.8-7.90	6.05	8.00	7.83 (ROM)
Young's modulus (GPa)	190	120	170	200 [77]
Shear modulus (GPa)	73	46	65	80 [77]
Elongation RT (%)	20 [67, Fig.3] 35 [78, Fig.24D4]	35	35	60 [79]
Yield Strength (MPa)	450	440	560	200 [80]
UTS (MPa)	630	680	600	570 [80]
Thermal stress parameter (kW/m)	9.5	18.5	5.1	1.1
Thermal expansion (10^{-6} K^{-1})	11.5	10	18	15 [81]
Thermal conductivity (W/m-K)	33	36	20	12 [82]
Max temp comp with PbLi (°C)	410*	650*	370*	
Electrical resistivity ($\Omega\text{-m}$)	7.0×10^{-7}	7.1×10^{-7}	1.01×10^{-6}	1.4×10^{-4} [82]

35 % in a single phase. In terms of configuration entropy of mixing of a disordered solid solution, the compositional definition of Yeh et al. translates into $1.36R$ and $1.61R$ (where $R = 8.31\text{J/mol} - \text{K}$) for a mol of a quinary alloy [84]. Complex, Concentrated Alloys (CCAs) encompasses HEAs and MPEAs by including multiphase microstructures made of 3 or more concentrated elements [85].

2.4.1 Phase stability

Approximately 30 % (or 45 % of the 81 nonradioactive elements) from the 118 elements of the periodic table, specifically 37 different chemical elements ranging from the alkali metal lithium (Li) to the lanthanide Thulium (Tm) have been reported in the literature as constituents of 408 different HEAs [84]. The number of explored HEAs is almost negligible when compared to the metals known by mankind, which is approximately 17,000 (7,000 ferrous metals, and 9,000 non-ferrous metals) [86].

The HEAs currently studied are divided into four distinct families according to the location of their conforming elements in the periodic table [85]: light metals CCAs, 3d transition metal CCAs, refractory metal CCAs, and bronzes and brasses CCAs. These CCAs form crystals with face-centred cubic (FCC), body-centred cubic (BCC), and hexagonal close-packed (HCP) structures, which are detailed in table 2.13. The constituent elements of the 3d transition metal CCAs were Ti, V, Cr, Mn, Fe, Co, Ni, and Cu [84]. Additions of Al have also been reported in combination with 3d transition metal elements forming CCAs into FCC, BCC, FCC+BCC, and FCC or BCC phases in combination with intermetallic phases (IM). The refractory metal CCAs constituents included Cr, Hf, Mo, Nb, Re, Ta, V, W, and Zr forming CCAs into primarily BCC phase, and BCC in combination with intermetallic phases (B2 and/or Laves) [87]. Additions with Al, Ti, Si, Co, Ni, C, and N have also been reported [87]. The

light metal CCAs constituents included Al, Li, Mg, Sn, Zn, Sc, Ti, and Cu forming into the FCC phase primarily, FCC+HCP, and combinations with intermetallic phases [85]. CCAs bronzes and brasses constituent elements were Cu, Mn, and Ni with additions of Al, Sn, and Zn forming into FCC and intermetallic crystal structures [88, 85].

The search for new HEAs can be aided by phase diagram screening of subsystems [89]. The process consists of looking for a wide range of system compositions in the solid solution phase of interest (see Table 2.13 and Fig. 2.8 for typical binary phase diagrams). Wide ranges of composition values can be found in phase diagrams with isomorphous solid solutions, non-isomorphous but with large terminal solubilities, and with large homogeneity range for intermediate solid solution phase. For example, the set of five chemical elements Mo, Nb, Ta, V, W have all pairwise isomorphous binary phase diagrams. A simple calculation of the number of subsets containing between four and five elements i.e. new HEAs results in 6. Furthermore, by adding Ti to the set of elements Mo, Nb, Ta, V, W, the number of subsets containing between four and six elements results in 22 new HEAs.

Application of phase diagram screening technique to 3d-forming transition metal element based HEA results in 46 (37% of 126 possible quaternary alloys) potential candidates of forming single-phase structure. Some of these 46 quaternary alloys include equiatomic TiVCrAl, VCrMnFe, VCrMnCo, VCrMnNi, VCrMnAl, VCrFeCo, CrMnFeCo, and CrMnFeNi. For each of these 46 alloys, the corresponding 6 pair-wise phase diagrams display extensive regions of terminal solubility (>20%) in a single phase. This small calculation shows the tremendous room for exploration of compositional alloy space in CCAs.

The Gibbs phase rule is the fundamental equation relating the number of coexisting phases at thermodynamic equilibrium (P), the number of compo-

nents (C), and the number of independent variables (F) such as temperature, and pressure: $P = C - F + 2$ [90]. When the Gibbs phase rule is applied to HEAs with 1, 2, and up to 6 components, the simple calculation of the maximum number of phases at equilibrium gives 3, 4, and up to 8 phases respectively. The single-phase stabilisation of HEAs against the formation of intermetallic phases has been generally attributed to high configurational entropy of mixing, however, it has been shown that the formation of secondary phases can often not be completely avoided. In CrMnFeCoNi precipitation of two phases (σ -phase, and $M_{23}C_6$) has been observed [13], so the principle of high configuration entropy does not universally apply.

Empirical rules for prediction of predominant phases as in the CrMnFeCoNi HEAs have failed after experimental determination of the secondary phase precipitates [13]. Ab initio methods of electronic structure simulations based on DFT - Density Functional Theory has been suggested as a means to improve the accuracy of the phase stability predictions from empirical models [91]. Some of these ab initio methods will be discussed in more detail in Chapter 3.

X-Ray Diffraction (XRD) characterisation has been used to study the characterisation of the crystal structure of the CCAs to reveal simple BCC or FCC solid solution phases [91]. The so-called valence electron concentration model (VEC) was proposed as a physical parameter for determining the CCAs crystal structure of the solid solution [92]. Specifically, FCC phases were proposed to be stable at higher VEC (>8) and BCC phases stable for VEC (<6.87). The valence electron for each atomic species for typical transition metals can be found from [92] or from the configuration of occupied electrons in the atomic shells reported in the periodic table of chemical elements. The concentration of valence electrons for a given CCA composition is determined by adding the compositionally weighted valence electron numbers for all the

Table 2.13.: Description of the lattice as expressed in terms of their lattice constants (a, c) typically measured in fractions of nm. Lattice vectors are in the Cartesian coordinate system. Notation for simple cubic (SC); face-centred cubic (FCC); body-centred cubic (BCC); and hexagonal close-packed (HCP). These lattices are commonly reported structures for CCAs. Full figures of the lattices can be found at standard references, see for example [93].

Structure	a	b	c	t	c/a
SC	$(a, 0, 0)$	$(0, a, 0)$	$(0, 0, a)$		
FCC	$\frac{a}{2} (0, 1, 1)$	$\frac{a}{2} (1, 0, 1)$	$\frac{a}{2} (1, 1, 0)$		
BCC	$\frac{a}{2} (-1, 1, 1)$	$\frac{a}{2} (1, -1, 1)$	$\frac{a}{2} (1, 1, -1)$		
HCP	$\frac{a}{2} (\sqrt{3}, -1, 0)$	$a (0, 1, 0)$	$c (0, 0, 1)$	$a \left(\frac{1}{\sqrt{3}}, 0, \frac{c}{2a} \right)$	$\frac{\sqrt{8}}{3}$

elements conforming the CCA. The rule has been verified for approximately 20 CCA reported in [92].

Configuration entropy has been proposed to be a key ingredient in favouring solid solution in CCA phases against intermetallic compounds. Specifically, the relative difference of configuration entropy between parent and product intermetallic phases has been shown to dominate over vibrational and magnetic entropies [84].

Suppressed substitutional diffusion (sluggish self-diffusion) due to high activation diffusion energy barriers have been attributed to HEAs by Tsai [82] after studying CrMnFeCoNi HEA. In this HEA, ratio of activation energies to melting temperature T_m reached maximum of 0.2 kJ/mol-K (24 $k_B T_m$), where typically they are around 0.15 kJ/mol-K (18 $k_B T_m$). On the other hand, precipitation of Ni-Al B2 phase has been observed in as-cast Al_{0.5}CrFeCoNiCu after rapid cooling/quenching [94]. To resolve the apparent dispute around sluggish diffusion more work has been proposed; specifically relating to the pre-exponential factor in the self-diffusion coefficient [84, p.484]. Chemical short-range order, atomic size, and vibrational frequencies near vacancy

mediated diffusion could result in non-constant pre-exponential self-diffusion coefficient.

Short-range order can be a precursor of precipitation of secondary phases in alloy systems, which require long-range order (this is depicted in the schematic binary phase diagram in Fig. 2.8). Short-range order has been observed in concentrated CuPd alloys in the temperature range 500-650 °C at Pd compositions ranging between 10 and 30 at. %. Below 500 °C the transition from short-range order to long-range order occurs by precipitation into the Cu₃Pd phases [95]. Short-range order in the nearest and next-nearest in the BCC lattice, and four-body nearest FCC shell clustering in the FCC lattice have been predicted in Mo-Nb-Ta-V-W and FeNiMnCr HEAs [96], and [97] respectively. Further experimental work of equilibrium phase diagram determination will be required to determine the validity of these predictions. Research that is part of this thesis (see Chapters 5, and 6).

Recently Varvenne et al. [98] have developed a strengthening theory that indicates that strengthening of HEAs is a consequence of the interactions that dislocations experience concerning local fluctuations for the average bulk composition due to ordering or segregation [98]. Furthermore, short-range order in concentrated NiCoCr solid solution alloys has been reported to enhance short-range order after Ni self-ion irradiation [99]. In austenitic FeCrNi alloys, the neutron diffuse scattering technique has been used to examine the degree of short-range ordering [100] to reveal Ni-Cr ordering. The effect of electron irradiation into austenitic FeCrNi has also been studied by the neutron diffuse scattering technique to reveal that the degree of Ni-Cr ordering was higher than by thermal treatments [101].

Each atom has a different atomic number, which in turn leads to different shell and subshell electronic structure. As a consequence, the atomic size is seen to depend on the atomic number, Z . In CCAs, the mixing of different sized

atoms has been associated with lattice distortions. Distortions in the crystal lattice have been linked to abnormal electrical and thermal conductivities [84].

The "cocktail" effect refers to possible non-linear material property values associated with CCAs, that arise from the chemical complexity in the combinations of elements and microstructures of CCAs [84].

2.4.2 Mechanical and physical properties

For a comprehensive reading of the basics of mechanical properties of metals and alloys such as stress, strain, yield strength, ultimate tensile strength, elongation at fracture, ductility the reader is referred to one of the many textbooks [102].

Generally, HEAs have yield strengths between 300 MPa to 3,000 MPa, fracture toughness as high as 200 MPa m^{1/2}, and Vickers hardness values of 900 [84]. The range of mechanical properties depends on composition, crystal structure FCC, BCC or HCP, the heat treatment history [84].

Despite the complex structure of HEAs, the intrinsic of strengthening of solid solution HEAs were shown to be consistent with solid-solution, forest dislocation, and grain boundary strengthening mechanisms [103]. The strength of HEAs can be assumed to be additive in the contributions from grain-size Hall-Petch strengthening (length scale of grain diameter d), solid-solution strengthening (length scale of atomic spacing, ξ), and dislocation-dislocation forest strengthening (length scale of dislocation forest spacing

l). Generally, the HEA strength after a tensile experiment at temperature T , pre-strained to level ε_P , and strain rate $\dot{\varepsilon}$.

$$\sigma_{Y,HEA} = \sigma_{H-P}[d] + \sigma_{SS}[T, \dot{\varepsilon}, \xi] + \sigma_{Forest}[T, \dot{\varepsilon}, \varepsilon_P, l] \quad (2.17)$$

The dislocation-dislocation strengthening mechanisms can be explicitly shown to be $M\alpha G b \rho^{1/2}$, where M is an orientation parameter known as Taylor factor that takes a value M=3.06 in equiaxed FCC alloys [104], α -parameter ranges between 0.123 and 0.0625 depending on twinning, G is the shear modulus, and ρ is just the density of dislocations in the forest. The Burgers vector modulus refers to the perfect dislocation, which in the FCC lattice is given the shortest lattice vector, which for FCC is $a/2(110)$ as indicated in Table 2.13, for Ni ($a=0.35$ nm) $b=0.25$ nm.

The thermal stress parameter is a desirable parameter to maximise to reduce thermal stresses that build up in heat transfer processes; thermal stresses add up to the mechanical stresses such as the hoop stress in coolant pipes which may lead to failure by creep rupture. The thermal stress parameter has been estimated from a formulation by Dolan [105, Eq.8.8] $M=2(1-\nu)\sigma_y k / \alpha E$; where ν is the Poisson ratio approximately equal to 0.3, σ_y is the yield strength, k is the thermal conductivity, α is the thermal expansion, and E is the Young's modulus. Table 2.12 thermal stress parameter for Ferritic/Martensitic steels is optimal, and the worst parameter is the corresponding to CoCrFeMnNi alloy, caused by the poor thermal conductivity of this alloy. The electrical resistivity of CoCrFeMnNi is also notoriously low by two orders of magnitude in comparison to Ferritic/Martensitic steels, Vanadium alloys, and austenitic stainless steels. The thermal conductivity, and electrical resistivity are interrelated by the Wiedemann-Franz law $k=L_0 T/\rho$, where ρ is the electrical resistivity, and L_0 is the Lorenz ratio approximately given by $2.45 \times 10^{-8} \text{ V}^2/\text{K}^2$ (Sommerfeld value). Since the values of the product of electrical resistivity and thermal

conductivity divided by room temperature in Kelvins are $3.2 L_0$, $3.6 L_0$, $2.8 L_0$, and $233 L_0$ reported in Table 2.12 correspond to room temperature, we conclude that CoCrFeMnNi do not follow well the Wiedemann-Franz law by a two orders of quantity magnitude. The Wiedemann-Franz law implicitly assumes that the lattice conductivity is negligible, and it is due to only the electronic component due to electrical resistivity [106], it may be that lattice conductivity may not be a negligible component in HEAs.

The mechanical and physical properties of fusion materials and Cantor alloy are detailed in Table 2.12. Note that the estimated electrical resistivity for Cantor alloy is approximately 100 times less than the remaining candidate materials. The temperature limits due to corrosion in PbLi coolants strongly depend on coolant speeds and grain size [105], and as far as concerned no data has been reported for Cantor alloy.

2.4.3 Radiation performance

As far as the author knows, the radiation performance of HEAs has been reported in the literature by experimental works using transmission electron microscopy after several types of ion irradiations: α -particles ([142, 104, 143, 144]), and heavy ions irradiations ([20, 145, 99, 146, 147, 148]). Therefore an effort must be made to estimate the impact of the microscopical features reported into the mechanical performance of HEAs after exposure to radiation doses. The interested reader is recommended to consult one of the many textbooks on the fundamentals of radiation damage theories in metals such as [149].

The characterisation of irradiation damage in fusion materials can be achieved by three main experimental techniques. The most common one is TEM - Transmission electron microscopy, which is used for imaging the atomistic

Table 2.14.: Screening of 36 phase diagram corresponding to pairwise combinations of elements Al, Co, Cr, Cu, Fe, Mn, Ni, Ti, V belonging to the 3d transition metals class of CCAs. There are a total of 126 Quaternary system associated, from which only 46 are potential single-phase systems (see text). Phase diagrams references indicated inside the cell.

	Al	Co	Cr	Cu	Fe	Mn	Ni	Ti	V
Al	X								
Co	80-100% Co in γ (Al,Co) [107]								
Cr	0-40% Al in α (Al,Cr) [108]	0-70% Cr in Co [109]	X						
Cu	0-20% Al in γ (Al,Cu) [110]	0-30% Cu in (Co,Cu) [111]	Not soluble [112]	X					
Fe	80-100% Fe in α (Al,Fe) [113]	15-100% Fe in α (Co,Fe) [114]	Isomorphous [115]	70-100% Fe in γ (Cu,Fe) [116]	X				
Mn	55-90% Mn in β -(Al,Mn) [117]	0-60% Mn in α -(Co,Mn) [118]	0-70% Mn in α -(Cr,Mn) [119]	0-80% Mn in γ -(Cu,Mn) [120]	10-95% Mn in γ -(Fe,Mn) [121]	X			
Ni	44-60% Ni in CsCl(Al,Ni) [122]	Solid solution in α -(Co,Ni) [123]	0-30% Ni in α -(Cr,Ni) [124]	Isomorphous [125]	25-90% Ni in γ -(Fe,Ni) [126]	Isomorphous [127]	X		
Ti	0-40% Al in Ti [128]	Not soluble [129]	Isomorphous [130]	Not soluble [131]	Not soluble [132]	Not soluble [133]	Not soluble [134]	X	
V	0-50% Al in V [135]	20-30% solubility [107]	Isomorphous [136]	Not soluble [137]	Soluble in α -(Mn,V) [138]	Mn soluble in δ -(Mn,V) [139]	20-40% sol in γ - α -(Ni,V) [140]	Soluble in β -(Ti) [141]	X

Fig. 2.8.: Relevant binary phase diagrams for the formation of HEAs

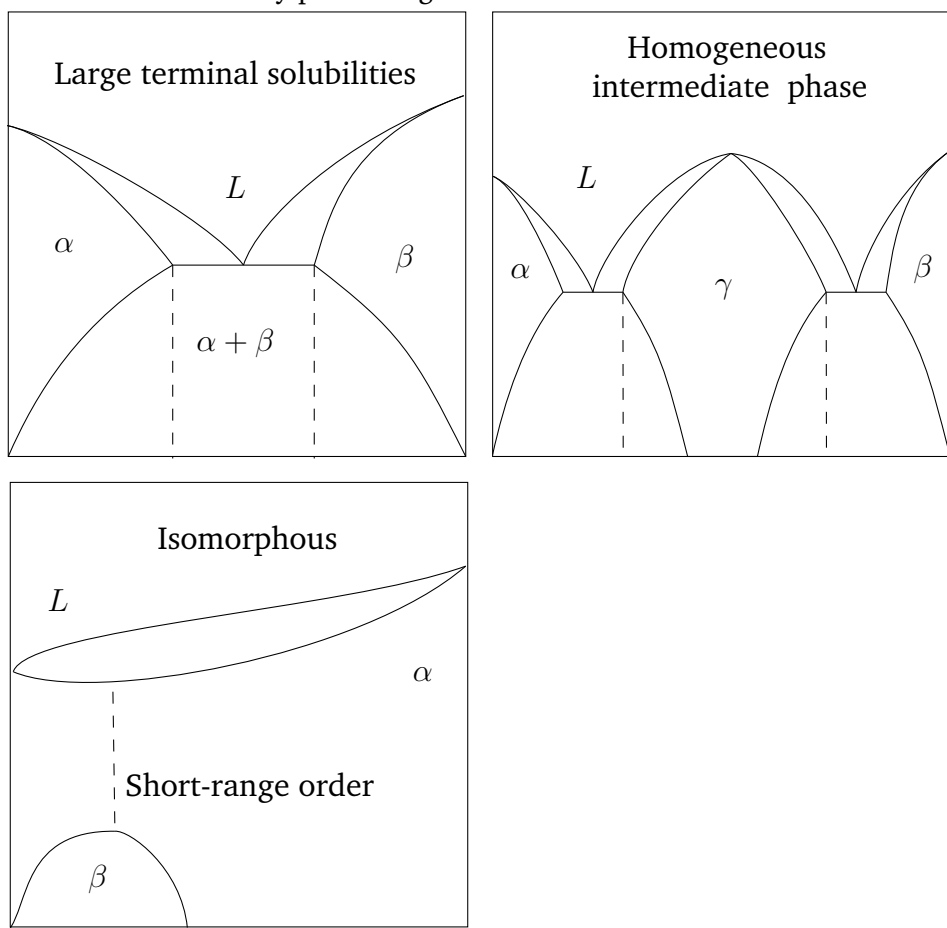
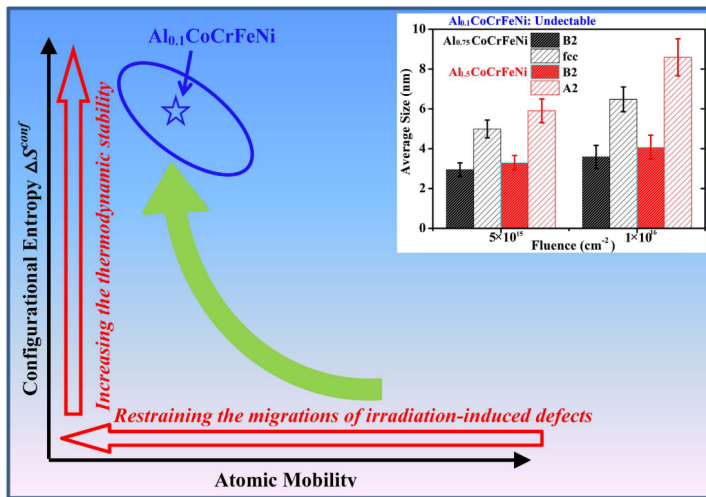


Fig. 2.9.: Depiction of phase stability under ion irradiation attributed to high configuration entropy of mixing and sluggish diffusion in single-phase Al_{0.1}CoCrFeNi. Figure adapted from [146]



defects created by radiation damage. The detection limit is 1 nm, which is roughly equal to 100 point defects per cluster. The TEM will be described in more detail in Chapter 4. Other techniques that can be applied to investigate the arrangement of atomistic defects in materials include the Field ion microscopy (atomic resolution), and diffuse X-ray scattering.

Three HEAs with varying Al composition (Al_xCoCrFeNi) were Au ion irradiated to a maximum of 43 dpa [146]. The two MPEAs enriched with Al resulted in multiphase systems. The lowest Al content MPEA that was also single-phase resulted in great structure stability under irradiation. The phase stability was attributed to high configuration entropy and low atomic mobilities, this is illustrated in Fig. 2.9. The low atomic mobilities for HEAs have been discussed earlier in this Chapter as a controversial topic.

The accumulation of knowledge in the nuclear materials community has resulted in generally 3 strategies to design materials resistant to irradiation [8]: materials with intrinsic radiation resistance such as BCC vs FCC regarding void swelling; design materials for operation at temperature ranges within which vacancy defects are not mobile so that interstitial defects can recombine

and reduce damage; and design materials with high density, small and high sink strength for irradiation-induced point defects such as ODS EUROFER steels. HEAs have been reported to inhibit the growth of defects induced by radiation, a phenomenon attributed to their characteristic sluggish diffusion or slow energy dissipation dynamics, and understood from first principles modelling of their thermal and electrical conductivity [150, 16]. Furthermore, alloys within the compositional space spanned by W, Ta, V and Cr look promising due to their low activation materials properties (nuclear waste classification <100 years of half-life) [21].

In particular, the HEA with composition FeMnNiCr_{18} , has been reported as having violated the so-called strength-ductility trade-off i.e. for decreasing strength, ductility should increase. It appears that the trade-off effect is complex deformation mechanism interrelating dislocation motion and twinning due to the observed presence of twin features in the microstructure of the HEA, according to [151]. It is interesting to compare the mechanical properties of the HEA with an ODS steel in non-irradiated condition, it is seen that the HEA is more ductile at all temperatures, however not so strong as the ODS steel. Therefore, the extra ductility of the HEA may be able to compensate for irradiation hardening when a hypothetical HEA is irradiated and tested for elongation and yield strength performance.

Yield stress can increase due to the presence of dislocation loops introduced by irradiation in the metal. The fundamental reason for the yield strength is due to the shear resistance generated by the loops to the glide of the network dislocations gliding along a plane that intersects the loops. If the mobile dislocation has a Burgers vector of modulus b gliding along a slip plane with shear modulus G in the presence of a number density of dislocation loops N_{loop} , each with average loop diameter d_{loop} , the increase in yield

stress is given by Eq. 2.18, that can be obtained from the forest dislocation strengthening mechanism by taking $\rho \rightarrow \pi N_{\text{loop}} d_{\text{loop}}$.

$$\Delta\sigma_{Y,\text{loop}} = M\alpha G b \rho^{1/2} = M\alpha G b \sqrt{\pi d_{\text{loop}} N_{\text{loop}}} \quad (2.18)$$

The embrittlement can be increased due to the presence of helium bubbles produced by transmutation [149, Eq.18.103]. The elongation at fracture is inversely proportional to the number density of the helium bubbles as expressed in Eq. 2.19.

$$\varepsilon_{\text{Fracture}} = \sqrt{\frac{\pi^2}{12N_{\text{bubble}} d_{\text{bubble}}^3}} \quad (2.19)$$

Dislocation loop is a common irradiation defect reported in the literature. In table 2.15 a simple estimate of the resulting hardening is quantified by yield strength due to the presence of these defects in NiCoFeCrMn representative HEA and austenitic stainless steels. The higher yield stress increase in austenitic stainless steels is approximately greater by a factor of 4.2 that corresponds to the ratio of values for the intrinsic parameter α .

Heat dissipation is important for avoiding heterogeneous temperature profiles across materials, which can lead to oxidation or local melting and strain distribution. More importantly low thermal conductivities can result in poor heat transfer from the nuclear fusion device to the heat exchangers. Thermal conductivities describe the heat dissipation. For HEAs, the majority of the literature has focused on their mechanical properties and not on physical properties such as thermal conductivities [82]. In Tab. 2.16 a summary of findings for a CoCrFeNi HEA are reported 2.16. Further work is required to study how thermal conductivities behave for more temperature values and

Table 2.15.: Prediction of irradiation hardening due intersitial dislocation loops formed in HEAs after several ion irradiations (references indicated in cell). Note that for austenitic stainless steels, I take $\alpha=0.41$ [104] [152], and for all the HEAs I take $\alpha=0.123$ [104]. The formula used to calculate the yield stress increase is $\Delta\sigma_{Y,\text{loop}} = M\alpha Gb\sqrt{\pi d_{\text{loop}} N_{\text{loop}}}$ (Eq. 2.18).

HEAs Name	Defect type	N(10^{21}m^{-3})	d(nm)	Dose (Dpa)	Temperature (K)	$\Delta\sigma_Y$ (MPa)	$\Delta\sigma_Y$ (MPa) (SS 316)
NiCoFeCrMn [153]	I-Loop ($1/3\langle 111 \rangle$)	10	20	38	773	189	629
NiFeCrMn [20]	I-Loop ($1/3\langle 111 \rangle$)	73	2.98	0.03	298	196	655
NiFeCrMn [20]	I-Loop ($1/3\langle 111 \rangle$)	150	3.23	0.3	298	293	978
NiFeCrMn [20]	I-Loop ($1/3\langle 111 \rangle$)	19	4.66	10	673	125	419
NiFeCrMn [20]	I-Loop ($1/3\langle 111 \rangle$)	7.1	4.13	3	1,073	72	241
NiFeCrMn [20]	I-Loop ($1/3\langle 111 \rangle$)	9.4	4.32	10	773	85	283
NiFeCrMn [20]	I-Loop ($1/3\langle 111 \rangle$)	6.7	5.21	10	873	78	262
NiFeCrMn [20]	I-Loop ($1/3\langle 111 \rangle$)	4.3	5.45	10	973	64	215
NiCoFeCrPd [154]	I-Loop ($1/3\langle 111 \rangle$)	35	11.5	38	873	268	892
NiCoFeCrMn [153]	I-Loop ($1/2\langle 110 \rangle$)	10	20	38	773	189	629

Table 2.16.: Thermal conductivities for one HEA in comparison to its pure elements and an austenitic stainless steel. The temperature assumed were 373 K.

Material	Composition	Thermal conductivity (W/m-K)	Reference
HEA	CoCrFeNi	12	[82, Tab. 2]
Pure element	Co	89	[155]
	Cr	92	[155]
	Fe	72	[155]
	Ni	83	[155]
316 L	CrFeNi (see [10, Tab. 3])	16.3	[10, Tab. 2]

compositions. Recent studies have argued by molecular dynamics simulations that low thermal conductivity in HEAs may be due to phonon transport anomalies and that they may be related to radiation-resistant properties of these alloys [150]. In Tab. 2.16 however, it is clear that thermal conductivities for at least one HEA is not negligible when compared to conventional alloys, that are not radiation-resistant such as void swelling as seen before.

2.5 Conclusion

The world needs the development of nuclear fusion technology to match the ever-increasing energy demands. One of the critical technological challenges of fusion is the area of structural materials and their radiation behaviour, which may limit the lifetime of the reactor. The blanket of the ITER fusion device will be made of stainless steels structural material. For commercial reactors, the material selection is underway with strong candidates such as Reduced Activation Ferritic/Martensitic Steels and ODS steels. These candidate materials present severe limitations in their chemical and mechanical properties by exposure to radiation fields, heat fluxes and coolants. Because

of the limitations, new materials such as high entropy alloys may play a role due to enhanced radiation resistance in their mechanical properties.

HEAs are promising metallic materials for nuclear applications for their intrinsic radiation resistance to embrittlement, swelling, and excellent mechanical properties such as ductility, strength and fracture toughness, but with poor functional properties of high electrical resistivity. The complex composition of HEAs leading to high configuration entropy of mixing. The pioneer HEA NiCoFeCrMn [156] can not be used for fusion materials due to Co content and its radiological properties. In previous work [20] considered removing Co to study the irradiation properties of CrFeMnNi HEA to Ni self-ion irradiations of 10 dpa, and maximum irradiation temperatures of 1,073 K. Fusion materials will be exposed to doses of 100s of dpa and maximum temperatures of 1000s of °C. Similarly, W-based BCC HEAs could revolutionise the fusion materials community by improving the mechanical properties of brittle Tungsten. During the work of this thesis, studies of the chemical complexity of Mo-Nb-Ta-V-W system remain unexplored.

To mimic radiation damage from neutrons in a fusion reactor, the research community has recurred to using light ion and heavy-ion accelerators. Heavy-ion ($z > 2$) irradiation has the advantage of producing more energetic recoils than light ions (H ions, and α -particles), and the recoil energy of the PKA is very important for the formation of radiation damage cascades produced in neutron radiations. Another benefit from using heavy ion irradiations instead of neutrons irradiations is the much higher dose rate achievable [149]. The main drawback from using heavy ion irradiations is that their range into solids is few μm 's, making very challenging the preparation of specimens for microscopy examination of radiation produced atomic defects.

Studying chemical complexity due to configuration entropy of mixing and phase stability appears to be a potential threat and at the same time the key

to unravelling the unknown mechanisms behind the radiation performance of the HEAs performance under radiation fields and heat fluxes. Many potential metastable phases could become active by radiation-induced phase alterations. Short-range order and atomic ordering over the first few nearest neighbour shells in the lattices of metals can be used as indicators of long-range ordering, thus resulting in precipitation.

Electron microscopy, in particular, transmission electron microscopy, can be used to cross-check the presence of precipitated phases predicted from modelling studies of short-range order and atomic ordering.

Modelling methods

“ Il suffit, pour cela, de choisir une fonction symétrique des diverses valeurs que prend, par toutes les permutations de l'un des groupes partiels, une fonction qui n'est invariable pour aucune substitution.

— Évariste Galois

(Journal de mathématiques pures et appliquées, 11, 417–444, (1846))

In this chapter the methods to model structural phase transitions between spatially periodic structures from first principles i.e. electronic structure calculations are introduced. These methods will be used later in chapters 5 and 6 for understanding the thermodynamical equilibrium of HEAs at temperature and radiation fields from first principles. Methods based on electronic structure calculations are characterized by requiring no experimental input parameters and appear to be quantitatively accurate when compared to experiments, in particular phase equilibrium diagrams. We will see that once the interactions energies for a given system are derived from electronic structure calculations, the free energies and other thermodynamical properties (including ordering or chemical segregation tendencies) of a system in an arbitrary average composition can be rapidly explored with the aid of powerful Monte Carlo algorithms. Generally, at low temperatures alloys tend to form ordered or partially ordered structures due to the loss of influence of the entropy contribution to the free energy, therefore it is important to understand how HEAs, characterized by maximum configuration entropy behave in the low-temperature region. The implications of phase transitions

and precipitation are critical for the mechanical properties of alloys, for example, the formation of σ phase in CrMnFeCoNi HEAs, precipitates which are known to be very hard and brittle.

The structure of this chapter is as follows: in section 3.1 the principles and main parameters for performing total electronic structure energy calculations are introduced; in sections 3.2 and 3.3 the coarse graining models for obtaining thermodynamical properties by means of computer crystals or supercells are introduced by extending the applicability of electronic structure calculations to non-zero temperatures. Finally in section 3.5, the theory of symmetries is briefly illustrated to interpret the intricate structures arising in equilibrium computer crystal from Monte Carlo with thousands of sites.

3.1 Ab initio electronic structure calculations

Electronic structure calculations based on electron density functional theories (DFT), were initially developed by Thomas [157] and Fermi[158] to investigate the binding energy of non-hydrogenic non-relativistically atoms with a large number of electrons and large nuclear charge (Z-electron system for neutral atoms). In the Thomas-Fermi theory, the electronic density of the Z-electron system, is formulated in terms of a 2nd order, non-linear differential equation for a universal function $\chi[x]$ [159] subject to boundary conditions $\chi[0] = 1$ and $\chi[\infty] = 0$. The universal function $\chi[x]$ is related to the screened Coulomb potential V by an atom with atomic number Z:

$$\sqrt{x} \frac{d^2}{dx^2} \chi[x] = [\chi[x]]^{3/2} \quad (3.1)$$

$$V = \frac{Ze}{4\pi\epsilon_0} \chi[x] \quad (3.2)$$

$$x = \frac{2Z^{1/3}r}{(3\pi/4)^{2/3}a_0} \quad (3.3)$$

The solution $\chi[x]$ can be obtained approximately from the differential equation and boundary conditions by numerical methods, and once found, it can be used to construct the total binding energy of the Z-electron neutral system. The total binding energy is formally expressed as a functional of the dimensionless function $\chi[x]$, from where one can recover the electronic density, with contributions from electronic kinetic energies, electron-nucleus potential energies and electron-electron potential energies. Due to the universality of the $\chi[x]$ function, the total binding energy of the Z-electron system results $E = -CZ^{7/3}$, where C is a universal constant, that can be calculated numerically [159], and it is approximately given by 21 eV (where we have used the value of $R_y = 13.61$ eV for the Rydberg constant and $b = 1/2(3\pi/4^{2/3})$). The total binding energy from the Thomas-Fermi theory generally overestimates the binding energy with respect to the measured values [160]. The causes of the discrepancies concerning experimental values lay on the semi-classical nature of the formulation and the electron-electron self-interaction effect that is reduced with increasing Z. Nevertheless, the Thomas-Fermi theory appears to be remarkably close to the actual experimental values seen in Table 3.1

$$E[\chi[x]] = -Z^{7/3} \frac{R_y}{b} \left(\int_0^\infty \frac{\chi[x]^{3/2}}{\sqrt{x}} - \frac{1}{5} \int_0^\infty \frac{\chi[x]^{5/2}}{\sqrt{x}} \right) \quad (3.4)$$

Table 3.1.: All ionisation energies for C, Al and Fe are in eV and have been taken from experimental values reported in [160]. The addition of all ionization energies divided by the $Z^{7/3}$ factor gives the same order of magnitude as the Thomas-Fermi theoretical predictions, 21 eV

Ion	C(Z=6)	Al(Z=13)	Fe(Z=26)	Ion	Fe(Z=26)
Neutral	11.3	6.0	7.9	13	404.0
1	24.4	18.8	15.7	14	472.0
2	47.9	28.4	32.7	15	506.0
3	64.5	120.0	57.4	16	1168.0
4	392.0	154.0	83.0	17	1283.0
5	490.0	190.0	108.0	18	1399.0
6		241.0	133.0	19	1514.0
7		284.0	158.0	20	1644.0
8		330.0	240.0	21	1760.0
9		399.0	272.0	22	1923.0
10		442.0	303.0	23	2025.0
11		2086.0	335.0	24	8503.0
12		2304.0	372.0	25	8969.0
<i>Total/Z^{7/3}</i>	15.74	16.62			16.62

The Thomas-Fermi theory was generalised to investigate the spatial distribution of the electronic density due to the presence of an arbitrary amount of nuclei and electrons. The general theory seeks to minimize the total electronic energy functional, $E_{TF}[\rho[\mathbf{r}]]$, subject to constraints, $N = \int_0^\infty \rho[\mathbf{r}] d\mathbf{r}$, where N , is the total number of electrons in the system [161, 162]. The minimization of the total energy upon application of the Euler-Lagrange equations results in a partial differential equation. The kinetic energy of the electrons in the Thomas-Fermi theory is approximated by assuming the non-interacting electron approximation and γ_p is a numerical factor involving π . Note that we have used atomic units throughout Hartrees (Ha) for energy, a_0 Bohr for the unit of distances, e for electron charge and m_e for the unit of mass [163].

$$T[\rho[\mathbf{r}]] = \int \frac{3}{5} \frac{(3\pi^2\rho[\mathbf{r}])^{2/3}}{2} \rho[\mathbf{r}] d\mathbf{r} = \frac{3}{5} \gamma_p \int \rho[\mathbf{r}]^{5/3} d\mathbf{r} \quad (3.5)$$

The other terms of the total energy functional in the generalised Thomas-Fermi theory, $E_{TF}[\rho[\mathbf{r}]]$ include the external potential energy due to nuclei interacting with the electrons, $\int \mathcal{V}[\mathbf{r}]\rho[\mathbf{r}]$, and the so-called Hartree term, that accounts for the electron-electron interaction, $\int \int \frac{\rho[\mathbf{r}]\rho[\mathbf{r}']}{| \mathbf{r} - \mathbf{r}' |} d\mathbf{r} d\mathbf{r}'$; this last term is one of the main reasons why the Thomas-Fermi theory overestimates binding energy in table 3.1, because the term includes self-interaction between electrons. The error is specially seen to decrease with increasing number of electrons, as can be seen from the binding energy of Fe compared to Al in the same table.

$$E_{TF}[\rho[\mathbf{r}]] = \frac{3}{5}\gamma_p \int \rho[\mathbf{r}]^{5/3} d\mathbf{r} + \int \mathcal{V}[\mathbf{r}]\rho[\mathbf{r}] d\mathbf{r} + \int \int \frac{\rho[\mathbf{r}]\rho[\mathbf{r}']}{| \mathbf{r} - \mathbf{r}' |} d\mathbf{r} d\mathbf{r}' \quad (3.6)$$

More recent density functional theories are based on the Hohenberg-Kohn theorem [164]. Hohenberg and Kohn proved that the ground state energy of a quantum-mechanical N-electron system moving in this external potential, $\mathcal{V}[\mathbf{r}]$, can be found from minimization of the total energy functional consisting in two contributions: a universal functional, $\mathcal{F}[\rho[\mathbf{r}]]$, and an external potential energy functional due to nuclei-electron interactions, $\int \mathcal{V}[\mathbf{r}]\rho[\mathbf{r}] d\mathbf{r}$. From the ground state electronic density, Harriman showed how to solve for the many-body wave function, the so-called n -representability problem [165]; the coefficients of the expansion of the ground state density functional into a basis of orthonormal orbital functions constructed from the $\rho[\mathbf{r}]$. To date, the universal functional, $\mathcal{F}[\mathbf{r}]$, is only approximately known [166].

Based on the Hohenberg-Kohn theorem, Kohn and Sham later formulated a variational principle to develop a procedure for accurate calculations of the electronic structure of solids [167] by taking the nonlocal exchange term in the Hartree–Fock equations and replacing it by an exchange-correlation

potential. The exchange-correlation potential, $E_{xc}[\rho[\mathbf{r}]]$, is defined in terms of the universal functional from Hohenberg and Kohn theorem, $\mathcal{F}[\rho[\mathbf{r}]]$, by substrating the electron kinetic energy and electron-electron potential energy functionals from the generalised Thomas-Fermi theory.

$$E_{xc}[\rho[\mathbf{r}]] \equiv \mathcal{F}[\rho[\mathbf{r}]] - \frac{3}{5}\gamma_p \int \rho[\mathbf{r}]^{5/3} d\mathbf{r} - \int \int \frac{\rho[\mathbf{r}]\rho[\mathbf{r}']}{|\mathbf{r} - \mathbf{r}'|} d\mathbf{r} d\mathbf{r}' \quad (3.7)$$

The exchange-correlation functional remains unknown, and so is the universal functional, $\mathcal{F}[\rho[\mathbf{r}]]$ derived from it. Nevertheless, various approximated forms have been adopted for the exchange-correlation functional, we report here the parametrization of [168] obtained for the homogeneous electron gas, known as LDA (Local Density Approximation) calculated by the more advanced quantum Monte Carlo methods [169]. In the LDA approximation, we use the dimensionless parameter, r_s , defined locally at position \mathbf{r} by $\rho[\mathbf{r}] = \frac{4\pi}{3}(r_s[\mathbf{r}]a_0)^3$, the exchange functional is given by $\epsilon_e[r_s] = -0.4582/r_s$ and the correlation functional is given by $\epsilon_c[r_s] = -0.1423/(1 + 1.0529\sqrt{r_s} + 0.3334r_s)$ for $r_s \geq 1$ or by $\epsilon_c[r_s] = -0.0480 + 0.0311\ln(r_s) - 0.0116r_s + 0.0020r_s\ln(r_s)$ for $r_s \leq 1$. The exchange and the correlation functions, ϵ_c and ϵ_x , are combined into the so-called exchange-correlation functional expression, $E_{xc}[\rho[\mathbf{r}]]$

$$E_{xc}[n[\mathbf{r}]] = E_X[n[\mathbf{r}]] + E_C[n[\mathbf{r}]] = \int \epsilon_x[n[\mathbf{r}]]n[\mathbf{r}]d\mathbf{r} + \int \epsilon_c[n[\mathbf{r}]]n[\mathbf{r}]d\mathbf{r} \quad (3.8)$$

When the Euler-Lagrange equations are used to find the minimum total energy functional for a N electron system with an approximated exchange-correlation functional, we find the Kohn-Sham equations. The problem is reduced to finding self-consistently the electronic density from orthonormal orbitals of lowest energy eigenvalues ϵ_i (where $i = 1, 2, \dots, N$), $\phi_i[\mathbf{r}]$, by

$n[\mathbf{r}] = \sum_i |\phi_i[\mathbf{r}]|^2$, upon solving the set of coupled (by the total potential) one-particle Schrödinger like equations, $-1/2 \nabla^2 \phi_i[\mathbf{r}] + V_{total}[\mathbf{r}] \phi_i[\mathbf{r}] = \epsilon_i \phi_i[\mathbf{r}]$, where the total potential includes the external potential due to the nuclei, the electro-electron potential energy and the exchange-correlation potential. The self-consistent solution to the Kohn-Sham equation is obtained through a cycle of iterations where the electronic density function is evaluated and compared to initial ansatz, multiple times from the solution of one-particle like Schrödinger equations

Furthermore, in crystalline solids, characterized by a given space group symmetry, the total potential energy of the Kohn-Sham equations must be symmetric under the operations of the space group (see section 3.5 later in this chapter), $\mathcal{T}[V_{total}[\mathbf{r}]] = V_{total}[\mathbf{r}] \quad \forall \mathcal{T} \in \mathcal{R}$. The solutions to the one-particle Schrödinger like equations, due to the symmetry of the periodic structure, are usually studied by decomposition of the Kohn-Sham orbitals, $\phi_i[\mathbf{r}]$, into linear combinations of basis functions, in particular, Bloch functions [170]. In the new basis representation, the set of coupled differential equations are transformed into a matrix eigenvalue problem. The matrix approach is particularly simplified by use of space group representation theory, where expansion of the $\phi_i[\mathbf{r}]$ into symmetrized plane waves [171] by means of projection operators can be used to block diagonalize (Jordan canonical form, [172]) the full Hamiltonian, as a result, the full matrix eigenvalue problem is reduced to finding the eigenvalues of the sub-blocks of the Hamiltonian, which is a more tractable problem with known matrix diagonalization algorithms.

A further simplification to finding the solution of the Kohn-Sham equations is based on the pseudopotential (PP) method. The pseudopotential method re-formulates the potential into the Kohn-Sham equations for treating only valence electrons and correcting for the effects of core electrons. The pseudopotential method is especially useful for heavy atoms, such as W, where the

valence electrons are only 6 compared to the total number of electrons, 74. The essence of the pseudopotential method lies in the principle that chemical binding is achieved by valence electrons only, a result established earlier in the last century by Lewis [173]. Most DFT codes provide PPs for all isolated atoms in the periodic table in a tabulated format. The pseudopotentials are generated to be both transferable and to be able to combine with different sets of elements; in practice, this means that pseudopotentials can be added up, regardless of their use: for an atom, molecule, or bulk solid [163].

The accuracy of the DFT ground state energies can be improved by more accurate exchange-correlation functionals than LDA. In particular by formulating the exchange and correlation functional in terms of both the gradient electronic density and electronic density itself; the approximation receives the name of generalised gradient approximation (GGA) and has been developed by [166]. Another improvement of the Kohn-Sham theory has been made for treating magnetic materials by reformulating the variational problem of minimization of total electronic energy as a functional of both the electronic density and the spin density functions. The theory has been developed by [174].

So far, we have only discussed the equilibration dynamics for electrons at the ground state, but not about the dynamics of nuclei (characterized by charge Z_I at positions \mathbf{R}_I). The reason is that we have decoupled the nuclei from the electrons in the so-called clamped nuclei approximation, due to the much higher mass of the nuclei compared to the electrons (approximately 1000 times), the nuclei are considered as frozen during the equilibration of electrons. Nevertheless, each nucleus interacts with the electronic density and from the surrounding nuclei through a force, \mathbf{F}_I . Hellmann [175] and

Feynman [176] have developed the formulation of the forces exerted on the nuclei.

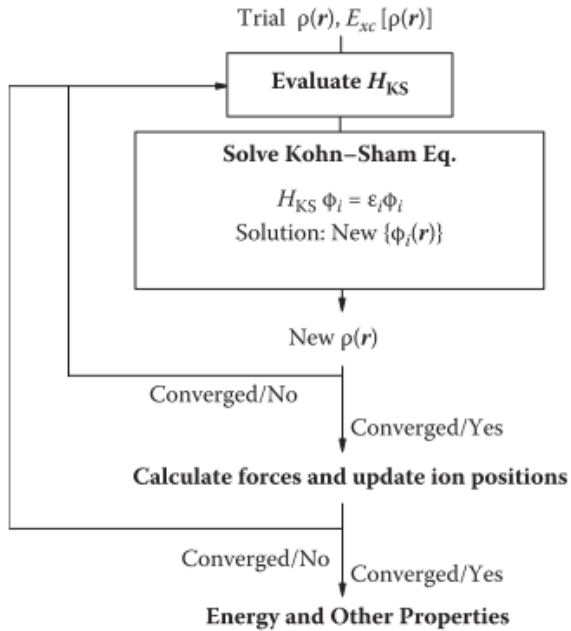
$$\mathbf{F}_I = Z_I \left[\int \frac{\mathbf{r} - \mathbf{R}_I}{|\mathbf{r} - \mathbf{R}_I|^3} \rho[\mathbf{r}] d\mathbf{r} - \sum_{J \neq I} Z_J \frac{\mathbf{R}_J - \mathbf{R}_I}{|\mathbf{R}_J - \mathbf{R}_I|^3} \right] \quad (3.9)$$

Nowadays, density functional theory for finding the electronic ground state total energy of atomistic structures has been implemented algorithmically in computer codes to run even in parallel threads in supercomputers; the algorithm can be generally sketched as illustrated in Fig. 3.1 with the electronic iterations for achieving self-consistency in the Kohn-Sham equations and then for the calculation of the ionic forces to find the equilibrium structure. Some of the most popular numerical implementations include VASP, ABINIT and Quantum Espresso [177]. In particular, VASP (Vienna Ab initio Simulation Package), has proven to be fast and accurate with atomic structures containing up to a hundred atoms efficiently and calculated with tens of CPUs in parallel mode [178]. Furthermore, the Austrian school of VASP traces its origin back to Kohn and Schrödinger.

3.2 From ab initio electronic structure to coarse-graining: the cluster expansion

To predict thermodynamic properties of alloy systems from first principles, we need to link the DFT electronic structure calculations with statistical physics. A common approach to studying temperature-dependent properties in alloy systems is the coarse-graining approximation within mean-field theories of statistical physics. Here the 10^{23} electronic, vibrational, and occupational

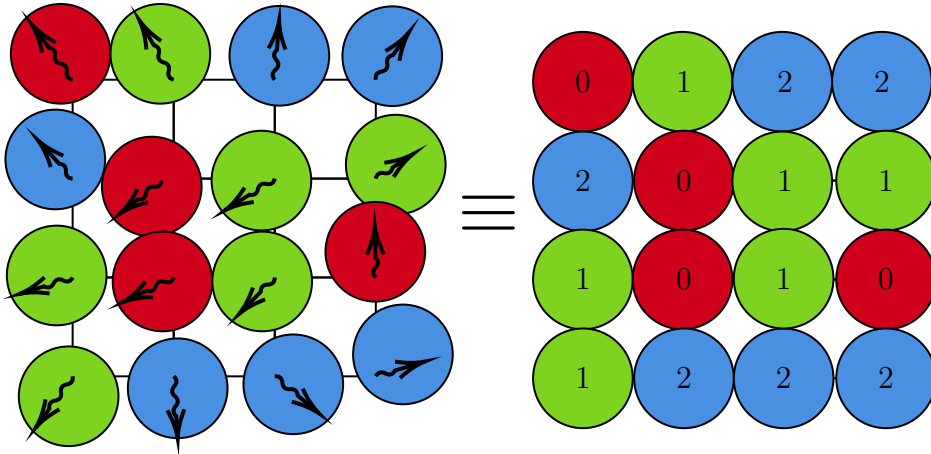
Fig. 3.1.: Schematic of the self-consistent cycle for achieving the electronic density function that minimizes the total electronic energy functional in the theory of Kohn-Sham. Figure adapted from [178]



degrees of freedom are reduced to a number that can be handled by modern-day computers. In alloy thermodynamics, a typical reduced set of degrees of freedom is the fluctuation of chemical species at a given lattice from a disordered crystal lattice [179]. These fluctuations are considered slow, being diffusion-driven (hrs), as compared to other faster degrees of freedom such as thermal vibration (ns). The dynamical evolution of the slow degrees of freedom evolve slower than the faster degrees of freedom and this facilitates their comparison with experiment, say for phase stability study, and the precipitation of phases.

The selection of the reduced degrees of freedom or variables in the coarse-graining approximation for a particular system is important. In theory, the minimum number of variables selected should be simple enough to describe the major features of the dynamical evolution of the system. For alloy thermodynamics, these features include short-range order (SRO), precipitation of secondary phases. The variables for the description of the alloy system

Fig. 3.2.: Coarse graining approximation, where all the degrees of freedom depicted on the LHS including displacement, vibration are collapsed into the configuration of species (represented by colours or number 0-2) sit at perfect lattice sites. Figure adapted from [179]



in the coarse-graining approximation are commonly spin-like variables as in the popular Ising model. The connection [180] between DFT and coarse-graining statistical physics coarse-graining model is then, done by importing the DFT electron structure calculations of a set of alloy system configurations into the construction of an effective Ising-like Hamiltonian, \mathcal{H} , that contains adjustable parameters, J , optimized in accordance to DFT total energy values [181]. Internal energies, configuration entropies, heat capacities, can be predicted once the Ising-like Hamiltonian of the alloy system is known by means of the partition function, Z , which is a summation of terms $e^{-\mathcal{H}_{\vec{\sigma}}/\|_{\mathcal{B}}T}$ over all variables or degrees of freedom (spin-like variables for the Ising-like Hamiltonian).

$$Z = \sum_{\{\vec{\sigma}\}} e^{-\frac{H[\vec{\sigma}]}{k_B T}} \quad (3.10)$$

In the coarse graining approximation, each lattice site is occupied by a chemical species, we use occupation variables to define which species is sitting at the i^{th} lattice site by $\sigma_i = \{0, 1, \dots, K - 1\}$, taking K different values for a K -component alloy system. Therefore, we need at least K point functions [182]

to build an complete basis $\{f_1[\sigma_i], f_2[\sigma_i], \dots, f_K[\sigma_i]\}$ for spanning the vector space of functions of σ_i . For binary alloys, the set of basis functions used in previous works [183] included $\{1, \sigma_i\}$ and for ternary alloys $\{1, \sigma_i, \sigma_i^2\}$. In the vector space of functions of σ_i , we define the scalar product of point functions by $\sum_{\sigma_i=0,1,\dots,K-1} f[\sigma_i]g[\sigma_i]$. In order to consider, clusters of points, we need to introduce the cluster functions, which are defined as products of point functions $f_1[\sigma_{i_1}]f_2[\sigma_{i_2}] \cdots f_\omega[\sigma_{i_\omega}]$ or the orthonormal basis constructed from the sets by applying Gramm-Schmidt method. In general, for arbitrary number of components in alloy system, K, the point functions can be constructed [184] according to:

$$\gamma_{j,K}[\sigma_i] = \begin{cases} 1 & \text{if } j = 0, \\ -\cos(2\pi \lceil \frac{j}{2} \rceil \frac{\sigma_i}{K}) & \text{if } j > 0 \text{ and odd,} \\ -\sin(2\pi \lceil \frac{j}{2} \rceil \frac{\sigma_i}{K}) & \text{if } j > 0 \text{ and even,} \end{cases} \quad (3.11)$$

We define the arbitrary cluster function, $\Gamma_{\omega,n}^{(s)}$, by giving the size of the cluster, i.e. the number of sites, ω , and an array, (s) , of ω integers, each taking values from the set $\{0, 1, \dots, K-1\}$. Sometimes it is necessary to distinguish between geometrically different clusters having the same size, and for this purpose we introduce an auxiliary index, n , that refers to the maximum coordination shell included in the cluster ($n=1$ for a four-body cluster whose sites are never beyond the nearest neighbour, $n=2$ if there is at least one two-body sub-cluster in 2nd nearest neighbour). The array of ω integers is known as the cluster decoration, and it is in effect, a label for the point function defined at a particular cluster site. The scalar product between two arbitrary cluster functions, $\Gamma_{\omega,n}^{(s)}$ and $\Gamma_{\omega',n'}^{(s')}$, is $\langle \Gamma_{\omega,n}^{(s)} \Gamma_{\omega',n'}^{(s')} \rangle = \prod_i \delta_{\omega_i, \omega'_i}$; therefore the set of $\Gamma_{\omega,n}^s$ for all possible decorations (s) is a complete set of orthonormal functions [185] in the vector space of cluster functions for the lattice sites $\{1, 2, \dots, \omega\}$ and any arbitrary function of cluster sites, in particular electronic energy of structure with sites arbitrarily decorated by

chemical species, can be expanded into a linear combination of these cluster functions. This is in essence, the cluster expansion (CE) [186, 187]

$$\Delta H_{CE}^{Mixing}[\vec{\sigma} \equiv \{\sigma_1, \sigma_2, \dots\}] = \sum_{\omega, n, (s)} m_{\omega, n}^{(s)} J_{\omega, n}^{(s)} \langle \Gamma_{\omega, n}^{(s)} [\vec{\sigma} \equiv \{\sigma_1, \sigma_2, \dots\}] \rangle_{\omega}$$
(3.12)

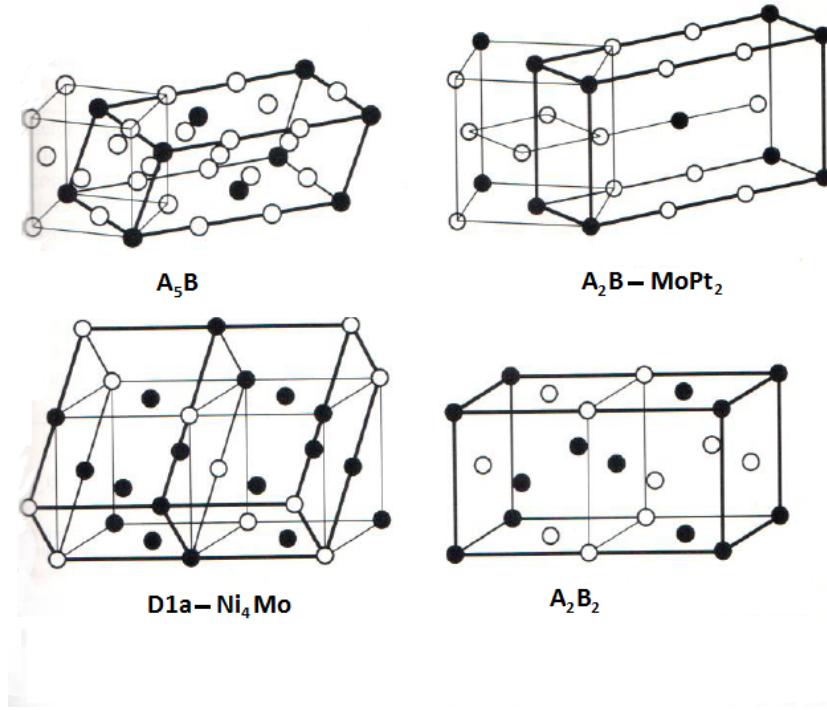
In the cluster expansion in particular, we can find an expression in terms of configuration dependent weighted cluster functions for the enthalpies of mixing in the sense of the coarse graining approximation of mean field statistical physics. The weights of the cluster expansion are the site multiplicity, $m_{\omega, n}^{(s)}$, of the cluster ω, n , and the effective cluster interactions, $J_{\omega, n}^{(s)}$. To obtain temperature dependent enthalpies of mixing, we perform the thermodynamic average of cluster functions $\langle \Gamma_{\omega, n}^{(s)} \rangle = \sum_{\forall(s)} y_{\omega, n}^s \Gamma_{\omega, n}^{(s)}$, where we have introduced $y_{\omega, n}^s$ as the probability of cluster configuration ω, n in decoration (s) at temperature.

The cluster site multiplicities, $m_{\omega, n}^{(s)}$, can be found by the cluster normalizer method, $\mathcal{N}_{\omega, n, (s)} = \{g \in G; g \circ sites \in (\omega, n, (s)) \subseteq sites \in (\omega, n, (s))\}$, by the expression $N_{\omega, n, (s)} = |G| / |\mathcal{N}_{\omega, n, (s)}|$, where $|G|$ is the number of symmetry elements in the class of the space group G of the crystal structure and the ECI, or coupling constants for the Ising-like Hamiltonian, can be found by the Connolly-Williams inversion [181] from the DFT calculated enthalpies of mixing of derivative superlattice structures. Then we can guarantee that the constructed CE is good and consistent with the DFT enthalpies of mixing by the criteria of the cross-validation.

The cluster expansion method is restricted to the prediction of enthalpies of mixing from superlattice structures [188], and can not, therefore, be used for studying arbitrary intermetallic structures. A derivative superlattice structure

is formed by lattice vectors which are multiples of the disordered parent structure lattice vectors and whose atomic basis vectors correspond to lattice points from the parent structure [189]. In contrast to disordered phases, superlattice structures are ordered, i.e. the atomic basis vectors are preferably occupied by only one type of chemical species. Algorithms to enumerate these superlattice structures for all possible combinations of chemical species from an arbitrary K-component alloy system have been developed [189].

Fig. 3.3.: Some common FCC (Face-centered Cubic) derivative structures or superlattices. We use AB notation to indicate stoichiometry and chemical elements for well-known structures in phase diagrams. Note that in the superlattice structures, the coordination of the FCC lattice is maintained. Figure adapted from [190]. See appendix A.1 for a more detailed listing of FCC superstructures.



The convergence of the cluster expansion is dependent on the number of structures composing the database of derivative superlattice structures and on the maximal size of the clusters that are used to expand the enthalpy of mixing. Eventually, the cluster expansion must be truncated. If we truncate the expansion into few terms then the effective Hamiltonian may become imprecise when determining enthalpies of mixing of structures not included in the database (with N structures), but if we include too many terms in the

expansion, the enthalpy of mixing might become noisy. The usual criteria to stop adding new structures or considering bigger clusters is the cross-validation criteria, which is a measure of the distance between enthalpies of mixing by DFT and by the effective Hamiltonian, and for an optimal cluster expansion, the cross-validation should be minimised.

$$CV = \frac{1}{N} \sum_i^{Database} (\Delta\mathcal{H}_{DFT,i}^{Mixing} - \Delta\mathcal{H}_{CE,i}^{Mixing})^2 \quad (3.13)$$

We have defined the spin-like occupation variables indicating which atomic species sit at each lattice site by integers taking values $0, 1, \dots, K - 1$. It is reasonable to question, whether the cluster expansion, in particular, the effective cluster interactions, are invariant over an alternative choice of spin-like occupation variables, i.e. for K even choose the integer values ranging from $-K/2, \dots, 0, \dots, K/2$. It has been proven [191] that cluster expansion is invariant scalar quantity, under linear transformations of the spin-like occupation variables.

The theorem of invariance of the cluster expansion under similarity transformations of the spin-like occupation variables, requires, as a lemma, that all subclusters of a given cluster must be included into the cluster expansion for improving accurate prediction of thermodynamic quantities. Furthermore, it has been suggested as guidance to perform cluster expansions ensuring the following conditions [192]: If an n -body cluster is included, then include all n -body clusters of smaller spatial extent, if a cluster is included, including all its subclusters. And finally to prevent both underfitting and overfitting, minimize the cross-validation (CV) error

Magnetism is not explicitly treated in the cluster expansion formalism [193]. The magnetic properties of alloys between 3d elements and group 4B elements have been studied especially for Mn, Cr, Ni and Fe intermetallic

compounds [194]. They show almost all strong magnetic behaviour such as ferromagnetism, ferrimagnetism, antiferromagnetism and helimagnetism. Furthermore, intermetallic compounds that are observed in phase diagrams and do not correspond to a superlattice structure can not be treated explicitly in the cluster expansion, which is essentially restricted to structures having the same coordination of atoms as the parent structure i.e. FCC(Face Centered Cubic) or BCC(body-centred Cubic). In conclusion, the predictive capabilities of the CE approach remain limited.

An alternative method to the cluster expansion is the cluster variation method (CVM). In the CVM, the enthalpy of mixing is expanded into clusters consisting of a single maximal cluster and its subclusters. Thus, for example, can not expand the enthalpy of mixing into non-overlapping sets of clusters such as the two-body first and second nearest neighbours. The entropy is similarly formulated to the enthalpy of mixing in terms of cluster correlation functions, and the free energy, expressed in an analytical form is minimised by variation principles.

3.3 CVM and Monte Carlo mean field theories

The cluster expansion provides an effective Hamiltonian for an arbitrary computer crystal or supercell structure coordinated in the same way as the parent structure (FCC or BCC) that can be used to study the system configurations at equilibrium i.e. the phase equilibrium at arbitrary temperatures. There are two main techniques to study the equilibrium structures at temperature: the Cluster Variation Method (CVM) and the Monte Carlo method. Each method evaluates differently, the same quantities, thermodynamic ensemble averages, $\sum_{\{\vec{\sigma}\}} P[\vec{\sigma}] e^{-\Delta H_{CE}^{Mixing}[\vec{\sigma}]/k_B T}$. Depending on the system variables (for

example for parametrizing the chemical potential of particle i in the computer cell, μ_i) we can use the semi-grand canonical ensemble (to minimise the semi-grand potential $\Omega = F - \sum_i \mu_i N_i$) or if the number of particles is fixed we can use the canonical ensemble (to minimise Helmholtz free energy, $F = \Delta H_{CE}^{Mixing} - TS$), where T is the equilibrium temperature and S is the configuration entropy. For the semi-grand canonical ensemble the thermodynamic averages are calculated from an expression incorporating the chemical potentials μ_i , $\sum_{\{\vec{\sigma}\}} P[\vec{\sigma}] e^{-(\Delta H_{CE}^{Mixing}[\vec{\sigma}] - \sum_i \mu_i N_i)/k_B T}$

The CVM, developed by Kikuchi [195], uses the constrained cluster expansion of a given maximal cluster and its subclusters contained in the maximal cluster combined with an analytical expression for the configuration entropy to build the free energy functional. The free energy functional is expressed in terms of correlation functions, which is then minimized for finding equilibrium configuration [196]. Configuration entropy is determined from the Boltzmann expression, $S[\vec{\sigma}] = k_B \ln W[\vec{\sigma}]$, where $W[\vec{\sigma}]$ is the number of arrangements for a given cluster of all the possible species in the equilibrium configuration of the maximal cluster. Kikuchi [195] and Barker [197] have worked out in detail the formulation of configuration entropy from the theory of regular mixtures. The general expression for configuration entropy of a maximal cluster ω, n containing $s[\omega, n]$ subclusters (ω_i, n_i) is given by the set of integers $\eta_{\omega_1, n_1}, \eta_{\omega_2, n_2} \dots, \eta_{\omega_s[\omega, n], n_s[\omega, n]}$ are the mean field integer coefficients associated to the geometry of the lattice. In the theory of regular mixtures, the coefficients can be found from the recursive expression after [197].

$$S_{\omega, n}[\vec{\sigma}] \equiv \sum_{i=1}^{s[\omega, n]} \eta_{\omega_i, n_i} \sum_{\forall(s)_{\omega_i}}^{K^{\omega_i}} k_B y_{\omega_i, n_i}^{(s)_{\omega_i, n_i}} [\vec{\sigma}] \ln(y_{\omega_i, n_i}^{(s)_{\omega_i, n_i}} [\vec{\sigma}]) \quad (3.14)$$

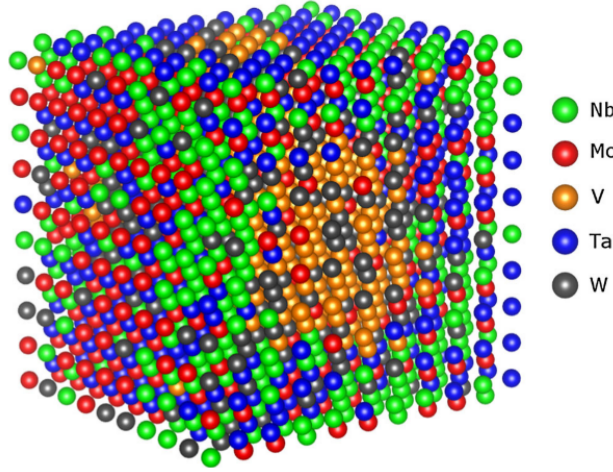
Monte Carlo methods serve to probe thermodynamic properties by direct evaluation of ensemble averages by statistical sampling [198]. The Monte Carlo method was devised in the 1940s at Los Alamos, USA. It requires the

evaluation of a thermodynamic property by averaging its value over the set of all possible system configurations. In theory the list of all configurations is infinite or extremely large (for an alloy system of 5 elements and 2000 sites, the number of possible configurations $5^{2000} = 10^{1400}$), and many configurations are not probable due to the law of large numbers, thus in practice there is a small set of configurations that weight most for evaluating the ensemble average. This essentially means that we can treat approximately the ensemble averages by statistical sampling, in particular truncating the set of configurations to a finite list of configurations over which, we evaluate thermodynamic averages.

The partition function, Z , cannot be evaluated in practice due to a large number of possible configurations. Instead, a trajectory is formed from a finite set of configurations that correctly have their probability distribution approximately equal as if we were to evaluate the full partition function. Metropolis devised an algorithm [198] to reject or accept a configuration based on the relative probabilities of the initial and trial new computer crystal configuration; the set of accepted trial configurations would then form the trajectory. In lattice gas models, we start with a computer crystal or supercell 3.4 with an initial distribution of chemical species among the sites. New configurations are produced by flipping the spin-like i variable for different spin-like variable j at a given site n . The trial configuration is accepted on basis of the outcome of the relative probabilities of exchanging i by j in the computer crystal, denoted by $w_n^{i \rightarrow j}$ in comparison to a random number generated between 0 and 1.

$$w_n^{i \rightarrow j} = \frac{e^{-(\Omega_{j,n} - \Omega_{i,n})/k_B T}}{\sum_{j=1, \dots, K} e^{-(\Omega_{j,n} - \Omega_{i,n})/k_B T}} \quad (3.15)$$

Fig. 3.4.: Computer crystal or supercell with 2048 lattice sites each colour or spin-like variable represents an atomic species of the five component Mo-Nb-Ta-V-W system. Figure adapted from [96]



In the expression for the transition probabilities, $w_n^{i \rightarrow j}$, we have used the difference between grand-canonical energies by using the cluster expansion Hamiltonian $\Omega_{j,n} - \Omega_{i,n} = \Delta H_{CE}^{Mixing}[\sigma_j] - \Delta H_{CE}^{Mixing}[\sigma_i] + \mu_i - \mu_j$ corresponding to the flipping of spin-like variable $i \rightarrow j$ at site n and we have used μ_i for the chemical potentials (which are constraints to account for the fixed average concentration of species i in the computer crystal). The transition probabilities for site n , $w_n^{i \rightarrow j}$, must fulfill the detailed balance equation and be a normalised probability distribution in order to achieve convergence [199] i.e. that the algorithm reaches equilibrium from a given initial configuration. The detailed balance is expressed as $y_{1,1}^i w_n^{i \rightarrow j} = y_{1,1}^j w_n^{j \rightarrow i}$, where $y_{1,1}^i$ represents the average concentration of species i in the computer crystal or supercell. Similarly the normalisation condition for the transition probabilities is expressed as $\sum_{j=1, \dots, K} w_n^{i \rightarrow j} = 1$.

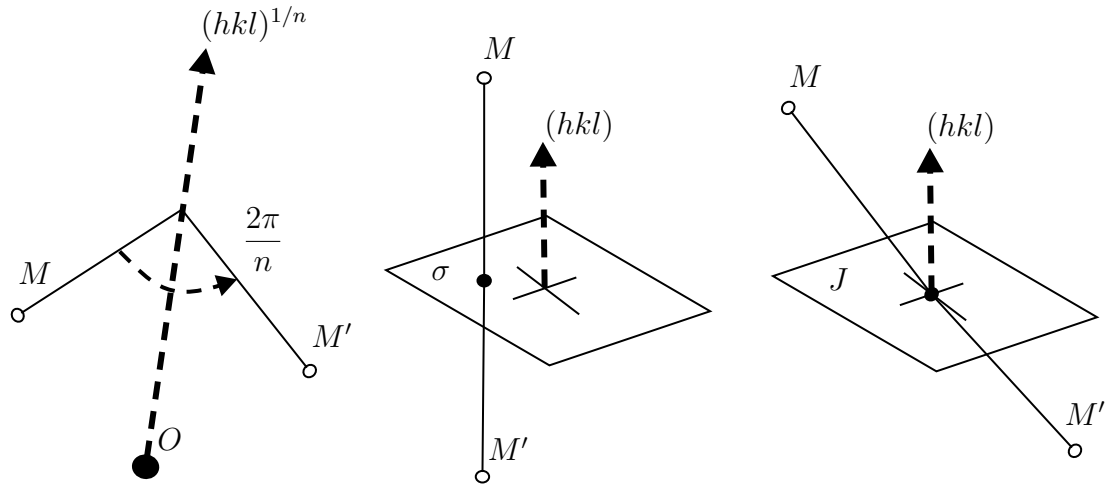
Monte Carlo based algorithms linked with effective cluster expansion Hamiltonians have been implemented in computer codes as in ATAT [200]. In the ATAT simulation code, one typically analyzes the thermodynamic equilibrium of a computer crystal with a fixed total number of atoms of several thousand and fixed atomic concentrations. The thermodynamic potential that mini-

mizes at equilibrium under the control of thermodynamic variables including the total number of atoms, chemical potential of species, pressure and temperature is the semi-grand canonical ensemble, (N, μ_i, P, T) [200]. The value of the chemical potentials, μ_i , are found at each temperature, T , to maintain the fixed atomic concentrations, $y_{1,1}^{(i)}$, at each of temperatures studied. The temperature-dependent Helmholtz or the semi-grand canonical potential free energy calculations are found by integrating from the high-temperature disordered state along a temperature-chemical potential multi-dimensional path that does not experience an energetic fluctuation associated with a phase transition [200].

3.4 Computational details

DFT calculations were performed using the projector augmented wave (PAW) method implemented in Vienna Ab-initio Simulation Package (VASP) [201, 202, 203, 204, 205, 206]. Exchange and correlation interactions were treated in the generalized gradient approximation GGA-PBE [166]. The DFT enthalpies of mixing for the FCC CrFeMnNi system were used to map iteratively into the cluster expansion Hamiltonian given by Eq. 6.2 using the ATAT package [184]. The database of structures for the cluster expansion consisted of 835 structures categorized by the difference of local environments in binaries (structures with two chemical elements: 58 CrFe, 55 CrMn, 77 CrNi, 58 FeMn, 54 FeNi and 52 MnNi), ternaries (structures with three chemical elements: 89 CrFeMn, 85 CrFeNi, 46 FeMnNi, and 66 CrMnNi); and 191 quaternaries CrFeMnNi. More information about the type of binary and ternary structures used in our DFT database has been detailed in Appendix A. Their structures are typically ordered ones with their composition ranged for each constituent element from 5% to 95%. For the Mo-Nb-Ta-V-W BCC system, the ECI $J_{(\omega,n)}^{(s)}$ parameters were obtained by mapping DFT energies calculated for 428 BCC-like structures from different binaries, ternaries, quaternaries into the CE

Fig. 3.5.: Rotation, reflection and inversion point group operations (leaving point O fixed). These operations in combination with translations form the symmorphic space groups such as FCC (O_h^5) or BCC (O_h^9)



Hamiltonian in Eq. 5.8 by using the structure inversion method (SIM) [186, 181].

3.5 Crystallographic space group theory

The key idea for describing and characterizing periodic solid state phases is to use group theoretical arguments to systematically identify the complete system of geometric operations that when acted upon the infinite periodic solid leave it unchanged. A group of elements $\mathcal{T} \in \{\mathcal{R}\}$ is defined by the properties that the \mathcal{T} group elements must obey between themselves under multiplication \circ [207]: 1) the property of closure $\mathcal{T} \circ \mathcal{P} = \mathcal{Q}$, where $\mathcal{T}, \mathcal{P}, \mathcal{Q} \in \{\mathcal{R}\}$; 2) the associative property $(\mathcal{T} \circ (\mathcal{P} \circ \mathcal{Q})) = ((\mathcal{T} \circ \mathcal{P}) \circ \mathcal{Q})$; 3) the identity element, $\mathcal{T} \circ \mathcal{E} = \mathcal{E} \circ \mathcal{T}$ for any $\mathcal{T} \in \{\mathcal{R}\}$; and the existence of the inverse element, $\mathcal{T} \circ \mathcal{T}^{-1} = \mathcal{E}$.

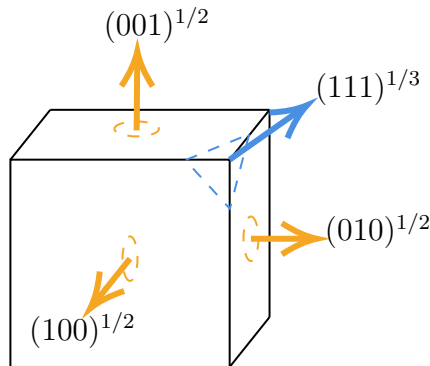
The type of group for particular application to three dimensional periodic structures are the crystallographic space groups, in particular the 73 symmorphic space groups (in total there are 230 space groups) that describe

FCC or BCC crystal structures. These groups have been studied and treated extensively in many works [208], but in particular we follow the clean notation style from [209]. The symmorphic space groups are constructed from operations consisting of rotations, inversions and translations as well as their combination, to form a discrete infinite set of operations. Each operation acts on the vector space of three dimensional Euclidean space formed by vectors \mathbf{r} : 1) Translation transformation, $\mathcal{A}^\lambda \mathcal{B}^\mu \mathcal{C}^\nu [\mathbf{r}] = \mathbf{r} + \lambda \mathbf{a} + \mu \mathbf{b} + \nu \mathbf{c}$, of the vector \mathbf{r} by arbitrary lattice vector $\lambda \mathbf{a} + \mu \mathbf{b} + \nu \mathbf{c}$; 2) Rotation transformation, $(hkl)^{m/n} = [\mathbf{r}] = \mathbf{r}'$ given by an angle $2\pi m/n$ about axis $[hkl]$. where $s = \sin(2\pi m/n)$ and $c = \sin^2(\pi m/n)$. 3) Inversion, $J\mathbf{r} = -\mathbf{r}$.

$$(hkl)^{m/n} = \frac{1}{\sqrt{h^2 + k^2 + l^2}} \begin{pmatrix} 1 - 2(k^2 + l^2) & -ls + 2hkc & ks + 2hlc \\ ls + 2hkc & 1 - 2(h^2 + l^2) & -hs + 2klc \\ -ks + 2hlc & hs + 2klc & 1 - 2(h^2 + k^2) \end{pmatrix} \quad (3.16)$$

The space group associated to the FCC crystal structure is denoted by O_h^5 in Schoenflies notation or in the international notation by 225. The space group associated to the BCC crystal structure is denoted by O_h^9 or 229. The two space groups can be constructed by the combination, \otimes , of the O_h point group (see figure 3.5 for cubic point groups) and the group of translations by the integer linear combinations of Bravais lattice vectors, $\mathcal{A}^\lambda \mathcal{B}^\mu \mathcal{C}^\nu \in \mathcal{T}$, corresponding to the structures: $\mathbf{a}_{FCC} = a/2[011]$, $\mathbf{b}_{FCC} = a/2[101]$, $\mathbf{c}_{FCC} = a/2[110]$ or

Fig. 3.6.: Operations for building the point group $\{222\}$ are $(100)^{1/2}, (010)^{1/2}, (001)^{1/2}$; by adding the operations $(111)^{1/3}, (111)^{2/3}$ we build the group of rotations $\{23\}$ leaving invariant the tetrahedron with vertices $[1, 1, 1] \rightarrow 1, [1, -1, -1] \rightarrow 2, [-1, 1, -1] \rightarrow 3$, and $[-1, -1, 1] \rightarrow 4$ by substituting the twofold axes for four-fold axes we build the point group $\{432\}$, and finally by adding inversion operation J we arrive at, $\left\{\frac{4}{m}3\frac{2}{m}\right\}$ point group, which is also denoted by O_h in Schöenflies notation



$\mathbf{a}_{BCC} = a/2[\bar{1}\bar{1}1], \mathbf{b}_{BCC} = a/2[1\bar{1}\bar{1}], \mathbf{c}_{BCC} = a/2[11\bar{1}]$ for the BCC. The necessary point group operations are illustrated in figure 3.6

$$\begin{aligned}
 \{222\} &= I + (100)^{1/2} + (010)^{1/2} + (001)^{1/2} \\
 \{23\} &= \{222\} + (111)^{1/3} \{222\} + (111)^{2/3} \{222\} \\
 \{432\} &= \{23\} + (100)^{1/4} \{23\} \\
 \left\{\frac{4}{m}3\frac{2}{m}\right\} &= \{432\} + J\{432\}
 \end{aligned} \tag{3.17}$$

$$\begin{aligned}
 \mathcal{T} \otimes \left\{\frac{4}{m}3\frac{2}{m}\right\} &= I \left\{\frac{4}{m}3\frac{2}{m}\right\} + \mathcal{A} \left\{\frac{4}{m}3\frac{2}{m}\right\} + \mathcal{B} \left\{\frac{4}{m}3\frac{2}{m}\right\} \\
 &\quad + \mathcal{C} \left\{\frac{4}{m}3\frac{2}{m}\right\} + \dots + \mathcal{A}^{\pm\infty} \mathcal{B}^{\pm\infty} \mathcal{C}^{\pm\infty} \left\{\frac{4}{m}3\frac{2}{m}\right\}
 \end{aligned}$$

Permutation operations can be regarded as group elements that rearrange a reference listing of objects, which in particular can be positioned in a vector space. We illustrate the point group $\{23\}$ of rotations for the tetrahedron in the representation of permutations of vertices, $[1, 1, 1] \rightarrow 1, [1, -1, -1] \rightarrow 2, [-1, 1, -1] \rightarrow 3$, and $[-1, -1, 1] \rightarrow 4$. The matrix representation of the

Table 3.2.: Isomorphism (a one to one mapping of elements in two representations) between the symmetry operations that act upon the vertices of the tetrahedron, $[1, 1, 1] \rightarrow 1$, $[1, -1, -1] \rightarrow 2$, $[-1, 1, -1] \rightarrow 3$, and $[-1, -1, 1] \rightarrow 4$, and the permutation operators that exchange labels at the vertices upon action of the equivalent symmetry operation.

Rotation representation	Permutation representation
E	$(1,2,3,4)$
$(0, 0, 1)^{1/2}$	$(1,2,3,4)$
$(0, 1, 0)^{1/2}$	$(4,3,2,1)$
$(\bar{1}, 1, \bar{1})^{1/3}$	$(1,2,3,4)$
$(1, 1, \bar{1})^{1/3}$	$(3,4,1,2)$
$(1, 0, 0)^{1/2}$	$(1,2,3,4)$
$(\bar{1}, \bar{1}, 1)^{1/3}$	$(2,4,3,1)$
$(\bar{1}, 1, 1)^{1/3}$	$(1,2,3,4)$
$(1, \bar{1}, \bar{1})^{1/3}$	$(2,3,1,4)$
$(1, \bar{1}, 1)^{1/3}$	$(1,2,3,4)$
$(\bar{1}, \bar{1}, \bar{1})^{1/3}$	$(2,1,4,3)$
$(1, \bar{1}, \bar{1})^{1/3}$	$(1,2,3,4)$
$(\bar{1}, \bar{1}, \bar{1})^{1/3}$	$(3,1,2,4)$
$(1, 1, 1)^{1/3}$	$(1,2,3,4)$
$(1, 1, 1)^{1/3}$	$(3,2,4,1)$
$(1, 1, 1)^{1/3}$	$(1,2,3,4)$
$(1, 1, 1)^{1/3}$	$(4,2,1,3)$
$(1, 1, 1)^{1/3}$	$(1,2,3,4)$
$(1, 1, 1)^{1/3}$	$(4,1,3,2)$
$(1, 1, 1)^{1/3}$	$(1,2,3,4)$
$(1, 1, 1)^{1/3}$	$(1,4,2,3)$
$(1, 1, 1)^{1/3}$	$(1,2,3,4)$
$(1, 1, 1)^{1/3}$	$(1,3,4,2)$

rotation operators permutes the vertices. The detailed equivalence between symbols and the representation of permutations is provided in table 3.2.

3.6 Conclusion

Methods based on electronic structure calculations are characterized by requiring no experimental input parameters. Electronic structure calculations have been proven to be accurate despite their limitations due to not yet formulated exchange-correlation functional. Electronic structure calculations combined with statistical physics model allow rapid exploration of thermodynamic properties of systems with arbitrary composition. The thermodynamic properties of HEAs, in particular, the phase stability is relevant at low temperatures, where the configuration entropy contribution to free energy ceases to stabilize the disordered random solid solution phase.

Monte Carlo methods make use of the entities known computer crystals or supercells containing thousands of lattice sites to find thermodynamic equilibrium configurations with a set average chemical composition. It is important to analyse in detail the sub-structures in these computer crystals as they can indicate the presence of preferred bonding of chemical species i.e. chemical ordering or segregation. Crystallographic space group symmetries are an essential tool in the investigation of these sub-structures, namely pair-sites for chemical short-ranger order or in terms of bigger clusters that can hint into precipitation of phases. These symmetry operators will be exploited first in Chapter 5 and then in Chapter 6 to hint at most probable chemical binding calculations as a function of temperature and HEA alloy composition.

Experimental methods, and conduction of experiment

“ Quality is never an accident. It is always the result of intelligent effort. There must be a will to produce a superior thing ”

— John Ruskin (1819-1900)

In this Chapter, the methods for preparing HEA specimens for electron microscopy characterization are explained in subsection 4.1. There is a detailed description of the effects that irradiation plays in the microstructure 4.2 and how the irradiation defects are geometrically configured and can be imaged by TEM 4.3. The final subsection 4.5 of the chapter concerns the characterization of mechanical properties, namely hardness by a technique known as nanoindentation, which is suitable for ion irradiated specimens.

4.1 Sample preparation

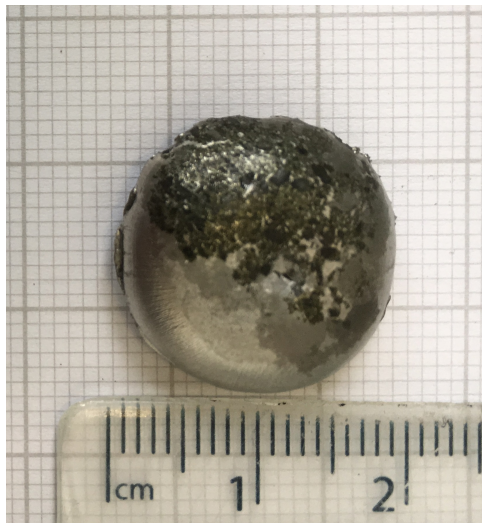
The HEAs with composition $\text{Fe}_{27}\text{Ni}_{28}\text{Mn}_{27}\text{Cr}_{18}$ in atomic percent were manufactured at the University of Sheffield by Dr C. McCaughey and Prof R. Goodall through the Accelerated Metallurgy Program. The arc melter from figure 4.2(a) was used to produce four button-shaped castings with approximately 10 g dry weight and dimensions of 15 mm diameter and 3 mm height (see figure 4.2(b)). The 10 g ingots were produced by mixing high purity

Fig. 4.1.: As cast samples produced at the University of Sheffield by R. Goodall and C. McCaughey from the University of Sheffield. These manufacturing of these samples was financially supported through the Accelerated Metallurgy Project. 4.2(a) for the arc melter located at the University of Sheffield used to cast HEAs. Image reproduced with permission from the University of Sheffield; 4.2(b) for Typical geometry of as-cast HEA buttons. The approximate weight of each button was 10 g.

(a)



(b)



(99.9 %) Cr, Fe, Mn and Ni in the weight proportions 1.68 g, 2.70 g, 2.66 g and 2.95 g respectively.

Arc melting followed by drop-casting processes generally produce microstructures that contain only the primary solidified phase from the liquid metal phase, which is not necessarily the equilibrium phase at standard room temperature conditions. Furthermore, castings generally result in non-uniform distribution of chemical elements within the individual dendrites (microsegregation), and can also contain entrained oxide inclusions; this has been particularly highlighted for $\text{Fe}_{27}\text{Ni}_{28}\text{Mn}_{27}\text{Cr}_{18}$ Cantor's HEAs [13] since a num-

ber of works have focused mainly on this alloy or its derivatives in the as cast state [210, 211, 212, 213, 214]. Homogenisation, cold working and recrystallization heat treatments were performed on the $\text{Fe}_{27}\text{Ni}_{28}\text{Mn}_{27}\text{Cr}_{18}$ specimens in order to erase microsegregation and produce an equiaxed grain microstructure (see Figs. 7.1 later in Chapter 7). The particular temperatures and quenching rates following the heat treatments for the alloy $\text{Fe}_{27}\text{Ni}_{28}\text{Mn}_{27}\text{Cr}_{18}$ were reported in earlier work [20], which are very similar to the conditions used for this work.

Based on the dendrite to dendrite distance approximately being $20 \mu\text{m}$ (as shown in Fig. 7.1), a near-rapid cooling rate between 1 and 10^3 K/s is estimated [215].

The quantitative identification of microstructural features is key for correlating the microstructure with properties in any material. In this thesis, the interest is in the microstructure and mechanical property changes after irradiation of HEAs. The preparation of the thermomechanically processed $\text{Fe}_{27}\text{Ni}_{28}\text{Mn}_{27}\text{Cr}_{18}$ HEA microstructure starts with the sectioning of a small piece of 10 mm by 10 mm size suitable for observing grain structure in an optical microscope or scanning electron microscope and for irradiating at uniform penetrations the HEAs. Preliminary machining of the buttons to remove round edges was undertaken with an automatic SiC cutting wheel with continuous feeding of coolant. High precision machining to obtain 10 mm by 10 mm by 1 mm thick slices from the casting was performed by technicians with the electro-discharge machining from the School of Mechanical, Aerospace and Civil Engineering.

Following the electro-discharge machining, the specimens were mechanically ground with coarse SiC abrasive grit paper (P800 with median particle diameter $25 \mu\text{m}$) for the variable duration to remove oil residues and other deposits materials from the heat-affected zone. Ultrasonic bath cleaning was

carried out in all the ground samples to remove any last remains of foreign impregnated oils.

Generally, specimens are mounted in compressive granular media such as Bakelite or castable resins for easily grinding and polishing planar surfaces. The mounting process always involves some degree of heating (minimum temperatures 170 °C for castable resins). In this work, the specimens were mounted in Bakelite granular media and cured for 2 minutes.

Grinding was conducted starting with coarse grit size paper of P800, and then continued to P1200, P2400 and ended with fine P4000 paper, where the median particle diameter of the SiC is approximately given by $2.5 \mu\text{m}$. An automatic spinner wheel platter was programmed to run for a default time of 5 min duration on each grit paper until scratch-free surfaces were resolved under X500 magnification in the Zeiss Axio optical microscope. Polishing was undertaken subsequently with diamond paste polycrystalline suspension in distilled water for 10 min duration at $3 \mu\text{m}$ and $1 \mu\text{m}$ and then finalised with 10 % vol OPS in distilled water for 15 min, until grain boundaries were slightly visible under the optical microscope.

In this work, transmission electron microscopy (TEM) was used to study the microstructure of both non-irradiated and irradiated HEAs. The preparation of specimens for TEM was performed by two techniques namely: electropolishing and focused ion beam lift out. The electropolishing method has the advantages of being able to sample several grains, the samples are durable, on the other hand, the disadvantages include difficulties in controlling the area of interest for producing the samples and strong smells. The focused ion beam lift out method has as main advantage the fact it allows to probe exactly the area of interest. As for disadvantages from the lift-out method one can find the processing time consuming (it can take 1 entire day to produce 1 specimen), and the fact that Ga ions can introduce damage in the samples.

The damage has described as consisting of ripples and black dot contrast [216].

4.2 Self-ion irradiation experiment

Direct experiments of in reactor performance of structural materials under the extreme environment of a fusion reactor are not possible in 2019. In practice, the prediction of materials performance can be achieved by the rapid introduction of radiation damage in materials by simulation experiments with electron, proton or heavy ion irradiations. The purpose of irradiation simulation experiments in materials is to study the microscopic irradiation effects in materials (defect production types, their spatial arrangement into cascade, their concentration, and their annealing evolution) for a broad range of parameters (type of radiation, radiation energy spectrum, microstructure of the material in its pre-irradiation condition, radiation fluence, material temperature, exposure, radiation flux) . The expectations are that the microscopic irradiation effects are extrapolated for the prediction of potential macroscopic radiation effects (creep, hardening, fatigue).

In this work, the materials end station at Dalton Cumbrian Facility (beamline 6) 15SDH-4 (DAFNE, supplied by National Electrostatics Corp., Middleton, Wi, USA) was used for irradiation experiments. DAFNE is a 5 MV negative ion 2 acceleration stage electrostatic field-based (tandem pelletron) with a metallic powder loaded MC-SNICS ion source (in this case with Ni). MC-SNICS is a negative ion sputter source, which generates ion current from a 6mm solid cathode; commonly MC-SNICS cathodes are made from elemental metallic powder, in this work Ni was used due to its higher current yield for other metallic powders. With location in Whiteheaven, Cumbria, Dalton Cumbrian Facility also houses a second accelerator BABY 2.5 MV. Acknowledgement for work at the Dalton Cumbrian Facility (DCF) goes to the experimental base of

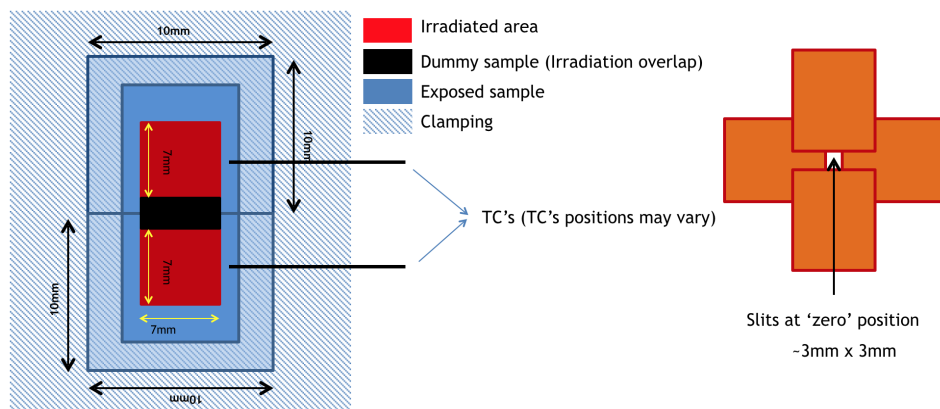
The University of Manchester's Dalton Nuclear Institute and a partner in the National Nuclear User Facility, the EPSRC UK National Ion Beam Centre and the Henry Royce Institute. Mr N.J.S. Mason, Dr A. Smith, Dr S.M. Shubeita, and Dr P. Wady assisted during the experiment.

The materials end station (beamline 6) is for general purpose ion implantation experiments in solid materials. It has additional features to control specimen temperature (heaters, chiller, IR Camera, thermocouples for temperature monitoring) but it is limited to approximately 600 °C at the specimen due to Cu structural material support having low melting point (Cu melting temperature is 1080 °C, and it is in contact with the heaters). The station also has a Beryllium window to allow for gamma spectrometer monitoring, and linear manipulator to adjust the area of irradiation. The sample stage requires a specimen geometry with minimal size given by 3 mm by 3 mm, that is determined from the closest separation between the slits (slits at zero position). Attached to the specimen are the thermouple wires for reading temperature, and the Ta shim to clamp in place the specimen to the stage. On the back of the specimen, there is melted Indium that provides thermal contact for heat conduction from the heaters, and cooling from the chillers. A schematic of the sample set up for a dual specimen is depicted in Fig. 4.2. Dual loading is advantageous because it can save time from mounting, and dedicate it for extending the beam time. The stage has implemented in it an electronic interface of a data acquisition system, known as DAQ DCF/D/0156.

The temperature on the non-irradiated regions of the sample can be measured by spot-welded thermocouples. However, during the irradiation experiment, the energetic beam on the surface of the sample can increase the surface temperature (Power comes from the product of the Beam current by the Beam energy). For reading correctly the temperature on the sample surface an infrared camera was used. The infrared camera readings were calibrated by

Fig. 4.2.: Set up for a dual specimen loading into the sample stage used for this work. The irradiated area on each of the samples was approximately 7 mm by 7 mm. The minimum irradiated area possible is determined by the slits distance 3 mm by 3 mm approximately 7.14(a). Photograph illustrating the components of the beamline at Dalton Cumbrian Facility, Cumbria, UK [217] 7.14(b)

(a)



(b)

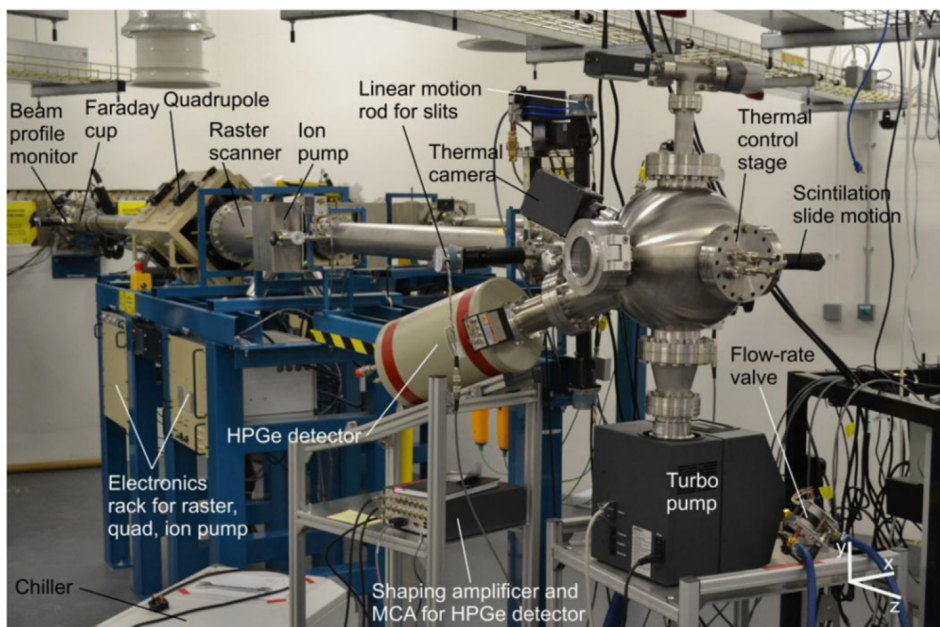
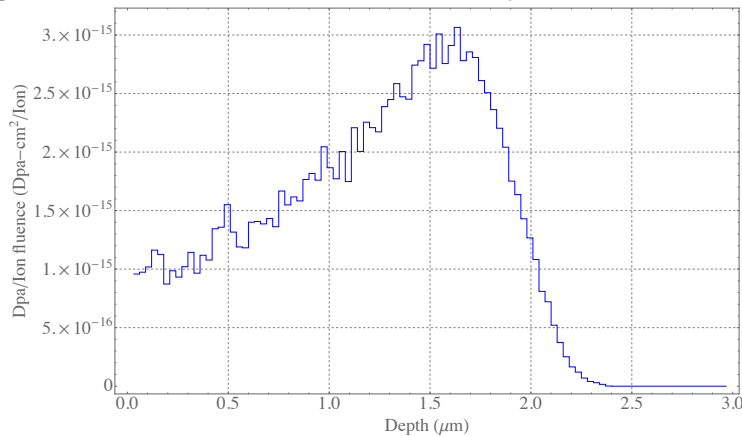


Fig. 4.3.: Dpa per fluence for Ni irradiation at 5 MeV into CrMnFeNi with density 7.9 g/cm³ calculated with SRIM using the methodology described by quick Kinchin-Pease mode as described by Stoller in [56].



comparison to thermocouple readings in the absence of irradiation. During the irradiation experiment, minor adjustments in temperature can be made by varying the power of the heaters. A particularly common scenario occurs when the beam is lost due to a problem in the accelerator. Then, the operator must be swift in turning off the power of the heaters to not annealing the irradiation damage introduced earlier!

$$I(\mu\text{A}) = q \cdot e(\mu\text{C}) \cdot A(\text{cm}^2) \cdot \frac{\text{Dpa rate(Dpa/s)}}{\text{Dpa/Fluence}(\frac{\text{Dpa}}{\text{Ion}/\text{cm}^2})} \quad (4.1)$$

Ion fluence, F measured in Ions/cm², can be estimated from charge, Q measured in C accumulated at the sample, the area under irradiation, A (cm²), and the charge state of the heavy charged particle radiation, q . The charge accumulated on the sample is read by a data acquisition system programmed in Labview. The area under irradiation is planned before the irradiation experiment, and during the sample mounting stage by the positioning of quartz scintillating window with pen marks. The slits are adjusted to trim the beam raster to fit the area of irradiation. In conclusion, $Fq = Q/A$

The bombardment of heavy charged particles on surfaces can result in sputtering of heavy particles, emission of electromagnetic radiation, and in the potential ejection of secondary electrons from the conduction band of the bulk solid. As the heavy charged particle reaches the surface of the solid, the ion becomes neutral by direct Auger neutralization. The electron makes a transition from the conduction band to the potential well of the approaching ion, leaving the remaining electrons in the conduction band excited. The remaining excitation energy of the bulk solid can be released by the ejection of a secondary conduction band electron into the continuum (effectively escaping the bulk) if $E_i > \varphi$, where E_i is the ionization energy of the incident atomic species, and φ is the work function of the metal. The yield of secondary electrons per ion is symbolized by γ_i , known as the secondary electron emission coefficient. These secondary electrons can lead to erroneous beam current measurements unless a sample stage reader is equipped with a Faraday cup. For example, a heavy positively charged particle beam with current $10\mu\text{A}$ impacts on a surface with $\gamma_i = 0.5$; if the secondary electrons are not returned to the surface, the current reader will detect $15\mu\text{A}$. For this work, the emission coefficient is plotted in Fig. 4.4. Similarly in Fig. 4.5, the stability of the temperature, and current for depositing charge are illustrated. In the figure, the cut-off point corresponds to the shut down of the beam on the sample, and subsequent cooling.

The charge and temperature data from the Dalton Cumbrian Facility experiment are plotted in Fig. 4.5. The temperature measured was approximately 50°C higher than the objective 300, and 450°C . The dose also varied with respect to the objective values.

For calculating the dpa profile with depth from the SRIM output files "e2recoils.txt" the damage energy method from [56] was used, and for the implantation profile the "range.txt" file. Eqs. 4.2 and 4.3 were used to produce the profiles from SRIM output. The density of the CCAs for SRIM computed from the

Fig. 4.4.: Secondary electron emission coefficient after calibration.

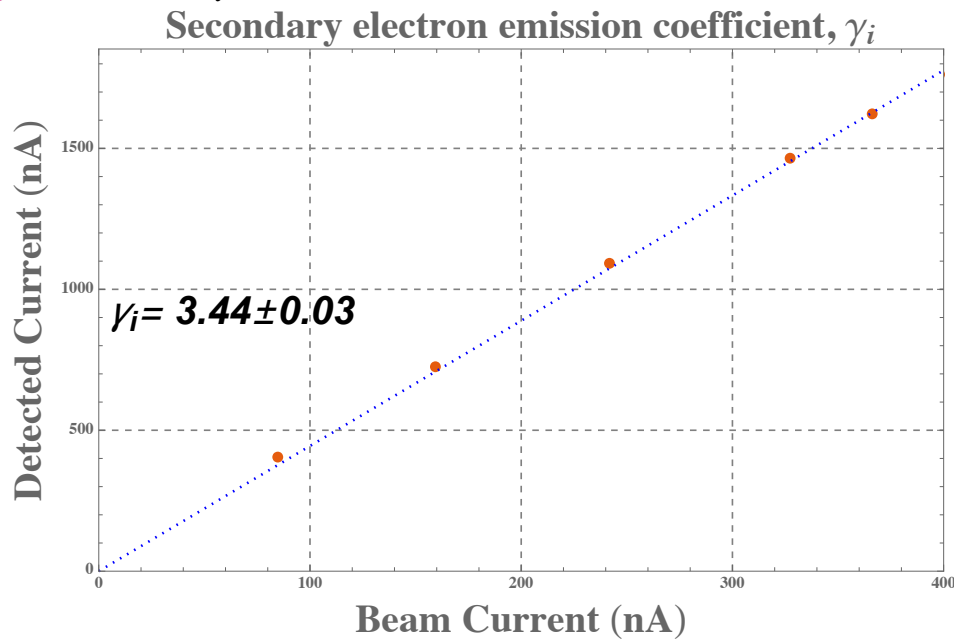
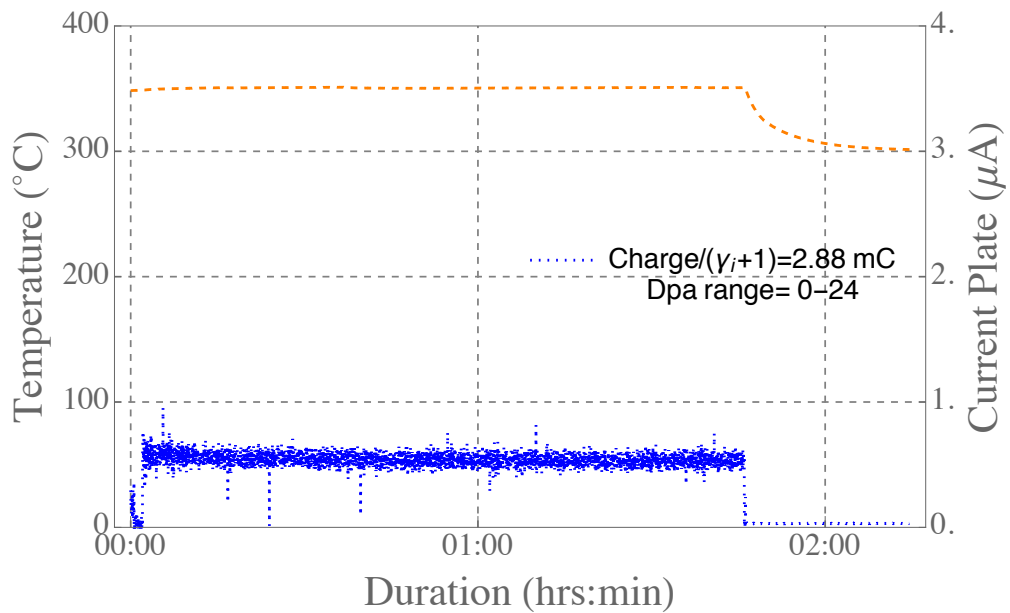


Fig. 4.5.: Temperature and current readings from the Infrared camera, and the Data adquisition system.



molar masses of the atomic elements, and their atomic fraction by the expression: $\rho_{at} = \frac{1}{\sum_{i=1}^N c_i v_i}$. More generally, the alloy mass density can be estimated from the molar mass and volume of elements in the CCA by using the rule of mixtures: $\rho_{mass} = \frac{\sum_1^N c_i m_i}{\sum_{i=1}^N c_i v_i}$, where c_i is the element i atomic fraction of N elements in the mixture, m_i its atomic mass; and v_i the molar volume. For the CCA with atomic composition Cr₁₈Mn₂₇Fe₂₇Ni₂₈, the molar volumes of Fe, Ni, Mn, and Cr were taken as $7.092 \cdot 10^{-6} \text{ m}^3/\text{mol}$, $6.589 \cdot 10^{-6} \text{ m}^3/\text{mol}$, $7.354 \cdot 10^{-6} \text{ m}^3/\text{mol}$, and $7.232 \cdot 10^{-6} \text{ m}^3/\text{mol}$ respectively. Similarly, the molar masses of Fe, Ni, Mn, and Cr were taken as 55.845 g/mol, 58.6934 g/mol, 54.9380 g/mol, and 51.9961 g/mol respectively. In brief, the atomic and mass densities of Cr₁₈Mn₂₇Fe₂₇Ni₂₈ CCA calculated by the formulas above were found to be $8.5454 \cdot 10^{22} \text{ 1/cm}^3$ and 7.9045 g/cm^3 . Other parameters required for SRIM calculation of dpa are the displacement energies, E_d , for which 40 eV for Cr, Mn, Fe, Ni were taken (the recommended values by [218, Table 2.4]), and no lattice binding energy.

$$Dpa = \frac{0.8}{2E_d(\text{eV})} \overbrace{\left(\frac{\text{eV}}{\text{Ions} - \text{\AA}} \right)}^{"E2recoil.txt"} \left(\frac{10^8(\text{\AA}/\text{cm})}{\rho(\text{atoms}/\text{cm}^3)} \right) Fluence(\text{Ions}/\text{cm}^2) \quad (4.2)$$

$$At \% Ion = \overbrace{\left(\frac{\text{atoms}/\text{cm}^3}{\text{atoms}/\text{cm}^2} \right)}^{"Range.txt"} \left(\frac{100}{\rho(\text{atoms}/\text{cm}^3)} \right) Fluence(\text{Ions}/\text{cm}^2) \quad (4.3)$$

4.3 Structure and composition with X-ray and electron spectroscopies

The characterization of the structure of matter at the atomic scale can be achieved by suitable X-ray, electron, ion and neutron radiations. In particular, we place interest in the low mobility, long-lived, and non-equilibrium microstructural features relevant for the mechanical properties of solids such as elastic modulus, strength, hardness, fracture toughness, and fatigue strength. Some features of interest include dislocations, grain boundaries, phase boundaries, stacking faults, antiphase boundaries, magnetic or ferroelectric domain boundaries, cracks, porosity, inclusions, precipitate particles, to cite a few. The capacity of resolving the geometry of the microstructural features utilizing radiation is determined by the approximate optical criteria that the wavelength, λ , of radiation must be equal or smaller (typically less than the atomic size, 1 Å) that the minimum spatial separation between the features of interest. The interaction between radiation and the microstructural features by diffraction carries the geometrical information of the feature. In practice, imaging the features for an unambiguous geometrical description can be achieved by focusing or deflecting the diffracted radiation, a process that is significantly easier by applying electric or magnetic fields for electrons (charged particles) over X-rays and neutrons.

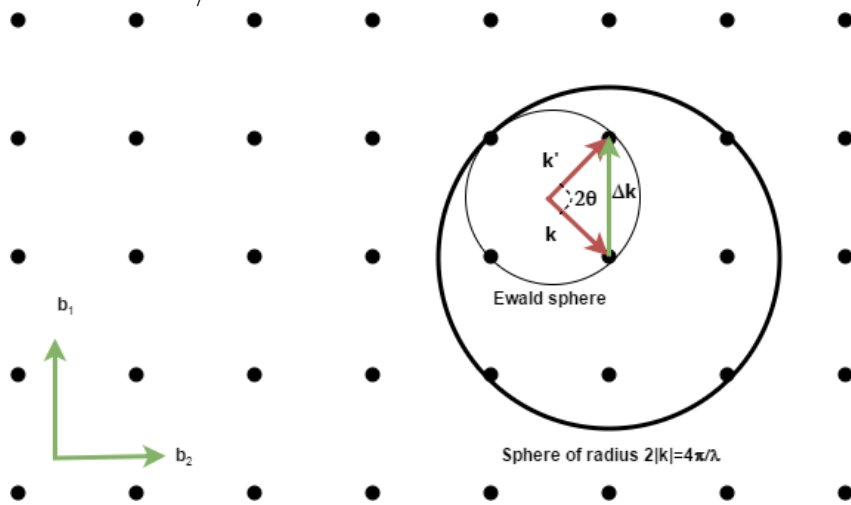
Let us consider a monochromatic beam of X-ray radiation with wavelength, λ , and incident wave vector, \mathbf{k} , into a single crystal. The X-ray radiation is diffracted into a set of different directions, \mathbf{k}' , due to the elastic scattering of each photon by the periodic spatial distribution from the outermost electrons inside each of the $n = 1, \dots, \infty$, unit cells of the crystal, $\rho_{total}[\mathbf{r}] = \sum_n \rho_{cell}[\mathbf{r} - \frac{2\pi}{\lambda} \mathbf{R}_n]$. The wavelength of the incident photon is conserved, $|\mathbf{k}'| = |\mathbf{k}| = \frac{2\pi}{\lambda}$ because in elastic scattering the energy, $h\frac{c}{\lambda}$, is constant. The probability amplitude, A , for the photon to be scattered coherently into direction \mathbf{k}' , is

described by the Fourier transform of the electronic density in the whole solid [219, 220]; as a consequence, the probability amplitude is zero for photons scattered coherently by other entities different from crystallographic planes described by reciprocal lattice vectors, $\Delta\mathbf{k} = h\mathbf{b}_1 + k\mathbf{b}_2 + l\mathbf{b}_3$. Due to the point group symmetry of the reciprocal lattice and Bragg's law for diffraction, $\sin(\theta)/\lambda = |\Delta\mathbf{k}|/4\pi = |h\mathbf{b}_1 + k\mathbf{b}_2 + l\mathbf{b}_3|/4\pi$, we find that in general a given diffraction angle, $\theta = \widehat{(\mathbf{k}, \mathbf{k}')}$, can be associated to a multiplicity, m , of reciprocal lattice vectors; for example the planes (111) and ($\bar{1}\bar{1}\bar{1}$) result in the same diffraction angle, θ . Furthermore, the intensity of the coherently scattered photon from the crystal plane (hkl) depends on the factor ($\int \rho[\mathbf{r}]e^{-i\Delta\mathbf{k}\cdot\mathbf{r}}d\mathbf{r}$), which sums the modulated contributions of atomic scattering factors over the unit cell (for FCC lattice, the crystallographic plane Miller indexes are all odd or all even; for BCC lattice $h+k+l$ is odd integer). The atomic scattering factors are complicated quantities that depend on the electronic structure of the atoms, data tables have been published for most elements in the periodic table [221].

$$A[\mathbf{k}'] = \int \left(\sum_n \rho[\mathbf{r} - \mathbf{R}_n] e^{-i\Delta\mathbf{k}\cdot\mathbf{r}} \right) d\mathbf{r} = \left(\sum_n e^{-i\Delta\mathbf{k}\cdot\mathbf{R}_n} \right) \left(\int_{cell} \rho[\mathbf{r}] e^{-i\Delta\mathbf{k}\cdot\mathbf{r}} d\mathbf{r} \right) \quad (4.4)$$

Alloys are made up of an agglomerate of single crystals. For each grain, in particular, for a given crystallographic plane, (hkl), we find that its orientation with respect to an external laboratory coordinate system will vary from one grain to another for the same chosen crystallographic plane. If the combined set of crystallographic planes from all the grains in the alloy cover all directions in the external laboratory coordinate system, the relative intensities, $I[\theta']/I[\theta]$, of one diffracted beam to another, will be given by the ratio of their multiplicities, m/m' because the incident radiation is probing all possible $\Delta\mathbf{k}$ vectors inside the volume of the limiting diffraction sphere

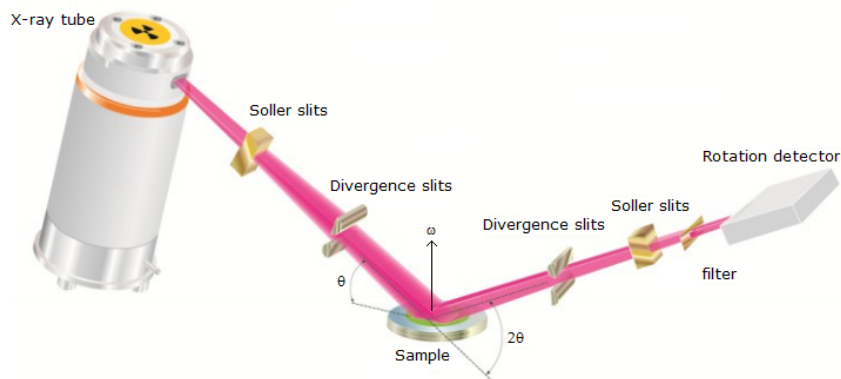
Fig. 4.6.: Reciprocal space construction for illustrating the diffraction condition when the vector Δk coincides with a reciprocal space vector. When all the grains in the alloy are randomly distributed, the incident radiation with wavevector k probes the entire region contained in the limited sphere of radius $4\pi/\lambda$



with radius $4\pi/\lambda$ (see Fig. 4.6). Any deviation in the relative intensities of diffracted beams must, therefore, come from textured (preferred orientation) from the crystallographic planes among the alloy grains. In a real sample, further correction terms need be considered in the expression for the diffraction intensity of scattered photons: photon polarisation after diffraction (Lorentz factor), a variation of shape and size of scattering volume as reciprocal space is sampled, X-ray absorption, and the temperature-dependent Debye-Waller factor [222]

An important application of X-ray diffraction is the crystal structure identification of an unknown material, in particular, we describe the so-called powder diffractometry technique. In the powder diffractometry technique, we use a convergent and monochromatic (λ wavelength) beam of X-rays with a rotating sample stage ω axis and moving detector, known as Bragg-Brentano (see figure 4.7). The convergent and monochromatic X-rays are generated when 20–60kV electrons collide with a metallic target (Cu for example) to produce a divergent beam of characteristic and continuously energy distributed X-rays. Characteristic X-ray energy (K_α) is selected by the

Fig. 4.7.: The sample set up for powder diffractometry of a rotation sample about axis ω and moving detector. Figure adapted from [224]



use of monochromator crystals, the beam is then collimated with the aid of absorber and filters and the so-called Soller slits. The output data consist on numerical lists of N diffracted intensity values for each value of scattering angle measured $\{2\theta_i, I_i\}_{i=1,2,\dots,N}$. For phase identification purposes, the key feature to analyse from the data is to identify the $2\theta_i$ for maximum intensities. In particular, the program CMPR [223] can generate the list of $2\theta_i$ values for a given space group symmetry with given parameters (lattice constant for a cubic lattice) and a given wavelength of radiation $\lambda_{CuK\alpha} = 1.5396$ or 8.04 keV, the experimental position of can be compared with respect to the predicted values, and estimate the lattice spacing of the structure.

Diffraction analysis of x-ray or electron radiation by crystallographic planes (elastic scattering) affects the angular spread of the incident radiation. In particular, diffraction analysis with electron radiation, requires high energies to avoid electron absorption when compared to X-rays, the cause being inelastic scattering of the incident electron radiation with outermost electrons in matter, which broadens the energy distribution (loss of monochromaticity) and results in radiation stopping; At the typical energies of photons in X-ray diffractometers (8 keV for Cu $\lambda_{K\alpha}$) and electrons in transmission electron microscopes (200 keV) for example in Al ($Z=13$) specimens, the absorption probabilities of electrons are approximately 3500 times greater than for X-rays (total collision cross-section is approximately given by 4.0

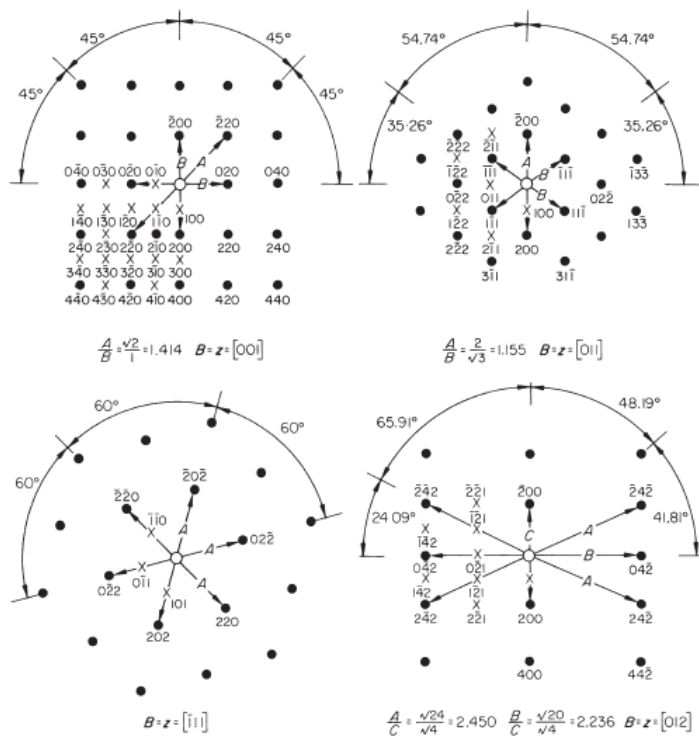
10^{-22} m^2 , see relativistic expression for absorption cross-section in [225]) and photons (due to photoelectric effect, $1.6 \cdot 10^{-25} \text{ m}^2$, see attenuation of photons in [155]). In practice, the absorption issues mean that penetration depths of X-rays in the matter are typically fractions of millimetres and for electrons fractions of microns [43]. For intermediately thin crystalline samples, inelastically scattered electron radiation can undergo elastic scattering, in a process known as Kikuchi diffraction [226].

The thin specimens, $t \sim 10 \text{ nm}$, required for penetration of electron radiation and for doing electron diffraction analysis cause the diffraction spots to become finite rods (size $1/t$) instead of infinitesimally small points associated with infinitely large samples. The finite size of the diffraction spots limits the accuracy of electron diffraction for doing lattice spacing measurements to more preferred X-ray diffraction methods. Furthermore, the high energies and small wavelength of electrons mean that the radius of curvature of the Ewald sphere is enormous compared to the distance between reciprocal lattice sites. Probing several diffraction beams by intersecting reciprocal lattice sites with the Ewald sphere becomes difficult, and can only be achieved through carefully tilting of the specimen in a transmission electron microscope (TEM) fitted with a rotation stage. Regarding the orientation condition for imaging thin samples the TEM there are two only orientations routinely used to study microstructural features: the two-beam condition (for imaging distortions in one plane) and the zone axis condition (for acquiring a diffraction pattern of a structure). A depiction of the diffraction conditions is indicated in Fig. 4.9.

The analysis of diffraction patterns obtained from a zone axis condition can be achieved either by means of look-up standard low-index diffraction patterns (FCC, BCC or HCP) in textbooks (see figure 4.8) or by comparing a experimental diffraction patterns with diffraction patterns calculated from a given CIF (crystallographic information file) file by a computer software,

Fig. 4.8.: Common diffraction patterns for the lowest order zones. Figure adapted from [227]. 4.9(a) for FCC diffraction patterns in zone axis condition of zone directions: [001], [011], [$\bar{1}11$], [012]; 4.9(b) for BCC diffraction patterns in zone axis condition of zone directions: [001], [011], [$\bar{1}11$], [012]

(a)



(b)

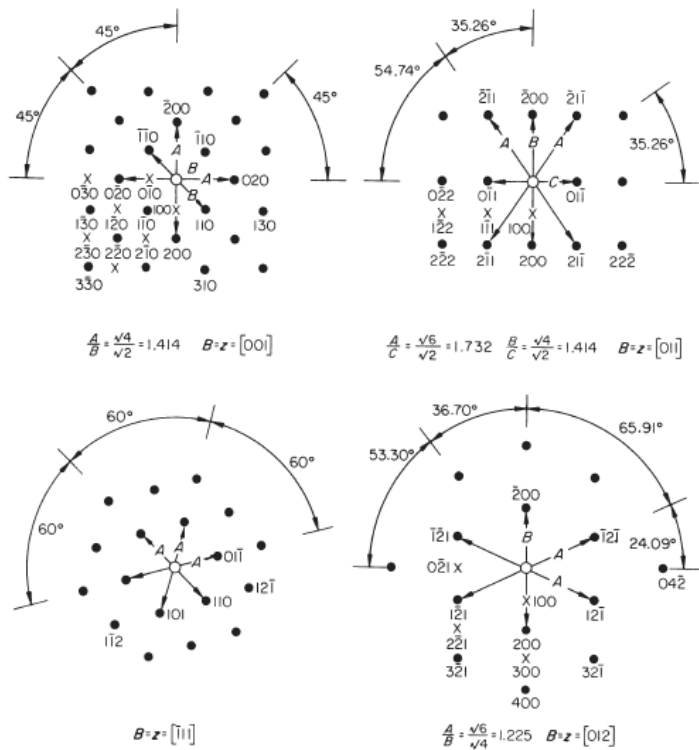


Fig. 4.9.: The most important diffraction conditions for TEM work: on the left-hand side we see the two-beam condition, useful for imaging distortions in a given $g = (hkl)$ -plane, where only one beam g meets the Bragg condition; here the g -relrod intersects the Ewald sphere at its centre. On the right-hand side, the so-called zone axis condition, which is used for acquiring diffraction patterns from a selected area of material, the diffraction spots in the horizontal plane are uniformly illuminated; this is achieved in practice by intersecting the top tip of the relrods by the Ewald sphere. The deviation parameter for the zone axis condition is negative and equal to $s = -|g|^2\lambda/2$, where $\delta\theta = -\theta$ is the angle of deviation between the reflecting planes (hkl) and the exact Bragg angle. Figure adapted from [228]

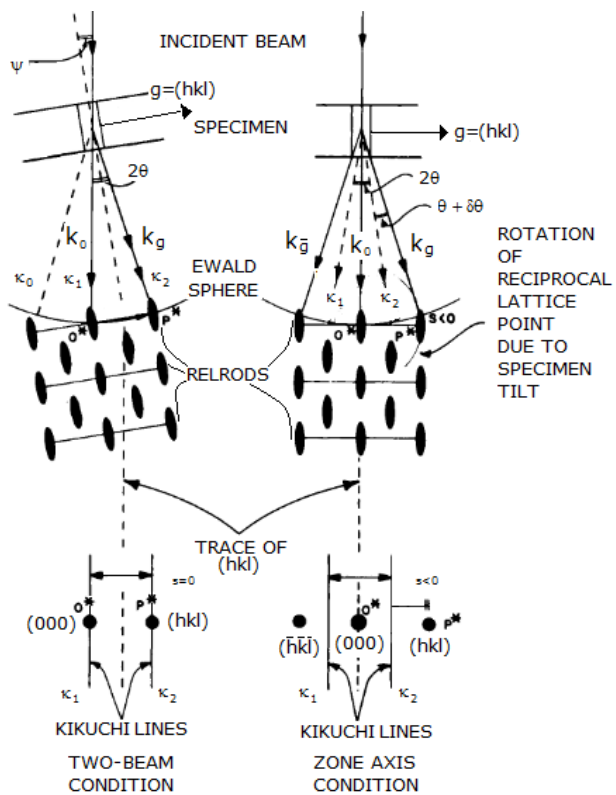
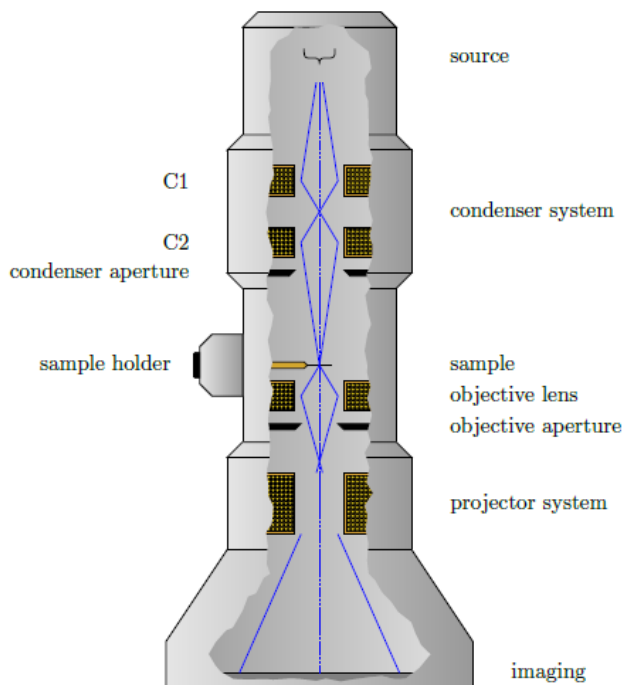


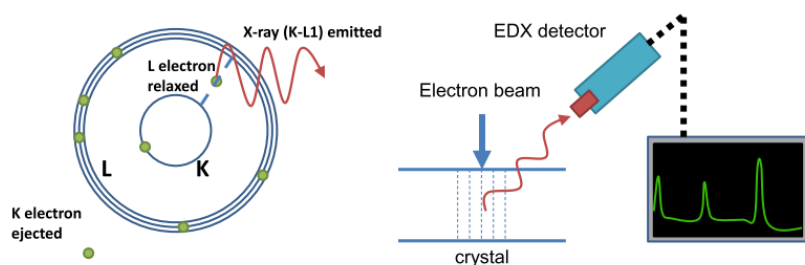
Fig. 4.10.: Conventional transmission electron microscope showing the source of electrons at the top followed by the illumination system of condensers, the specimen located in a rotating holder, the objective lens for focusing the electron image and the project lenses to increase magnification. Figure reproduced from <http://www.texample.net/tikz/examples/transmission-electron-microscope/>



in particular JEMS [229] for more intricate crystallographic phases. In practice, the CIF files can be obtained from databases such as the COD (Crystallographic Open Database) [230] and then simulate the diffraction pattern for a wide range of orientations with the JEMS software.

A conventional TEM (see Fig. 4.10) has a filament, a condenser with an aperture, an objective with an aperture, an extra aperture for the selection of areas of interest for diffraction, a set of intermediate lenses to magnify the image and a screen and camera. For two-beam condition imaging, the objective aperture is used to select a given plane; for diffraction, the objective aperture is removed and instead, the selected area diffraction aperture is inserted to scatter electrons from a particular region in the specimen.

Fig. 4.11.: Depiction of the atomic transition leading to the generation of X-rays. A high energy electron impacts and ejects an inner shell K-electron, subsequently electronic relaxation from the L shell occupies the vacancy at K shell, emitting the excess energy of the transition as an X-ray. Each X-ray has characteristic energy that allows to uniquely identify the atomic species involved in its generation.



Many excitations are resulting from electron interaction with matter including backscattered electrons, secondary electrons both of which are of relevance for the scanning electron microscope (SEM), heat and the generation of characteristic X-rays. X-rays are particularly useful for the determination of specimen composition if the signal is appropriately corrected.

4.4 Defect characterisation with TEM

The TEM specimens were prepared by grinding with P2000 and P4000 grit size SiC abrasive paper of the recrystallised samples in order to reduce the thickness from 500 μm to 50–80 μm . Small discs of 3 mm were punched from the ground specimens for thinning by electro-polishing. The thinning process was performed in a twinjet electro-polish Tenupol machine with a solution of 10 % HClO_4 + 90% CH_3OH at -40 °C. The prepared discs were observed in Tecnai G2-F20, and a TALOS operated at accelerating voltage of 200 kV.

TEM samples were also prepared using the focused ion beam technique, in particular, the DCF irradiated specimens due to the 1.5 μm Ni irradiated

thin layer. The cleaning-polishing was performed with a final step at 2 kV to ensure that FIB damage was kept to a minimum. The resulting micrographs displaying the degree of polishing are provided in Chapter 7.

Fast electrons at accelerating voltages of a few hundreds of kV's travel at very high speeds (70 % of the speed of light at 200 kV which is typical in Transmission electron microscope - TEM). The relativistic expression for the speed of light in terms of the accelerating voltage (E), elementary charge (e), electron rest mass (m_0), and speed of light (c) is $\frac{c}{1+\omega}\sqrt{(1+\omega)^2-1}$, where $\omega = eE/m_0c$ (see [231]) The interaction between fast electrons and atomistic internal structure of materials for imaging in the TEM necessitates quantum mechanical description. For this purpose, it is necessary to introduce the wavelength of the electron, given by De Broglie's expression $\lambda = h/p$, where the momentum, p is given by $p = m_0(1+\omega)v$. For the accelerating voltage range 100-1000 kV, the electron wavelength is of the order of a few pm's, approaching 1 pm at 800 kV. The dynamics of a relativistic electron interacting with a crystal lattice by the potential $U[\mathbf{r}]$ can be described by the scalar version of the Dirac equation (see Eq. 4.5), the so-called Klein-Gordon equation [231]. The general solution of the dynamical diffraction equation is a Bloch wave (represented by $B^j[\mathbf{r}]$ in Eq. 4.5)i.e. a weighted sum over transmitted plane wave (wavevector \mathbf{k}_0^j) and diffracted plane waves (wavevector $\mathbf{k}_0^j + \mathbf{g}$, where \mathbf{g} is a reciprocal lattice vector). The relative angular orientation between the diffracted and transmitted plane waves is given by Bragg's law (see subsection 4.3 later in this chapter). Alternatively, the travelling electron wavefunction solution in the crystal can be expanded in Darwin form i.e. a weighted sum of plane waves over transmitted plane

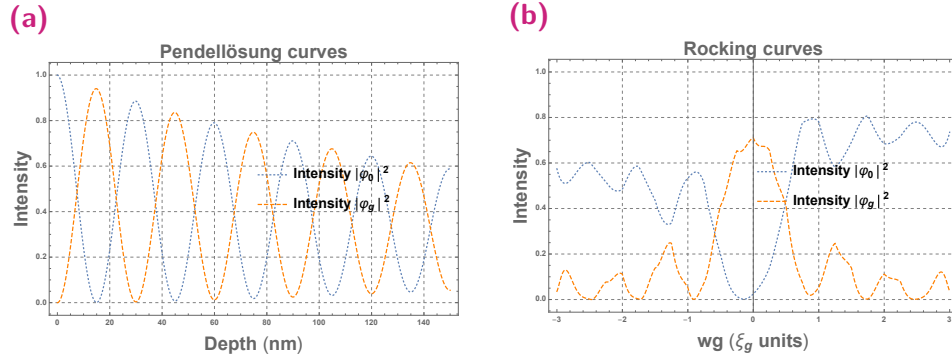
wave (wavevector \mathbf{k}_0) and diffracted plane waves (wavevector $\mathbf{k}_0 + \mathbf{g}$). The weights being the beam amplitudes, $\phi_{\mathbf{g}}[\mathbf{r}]$.

$$\begin{aligned}\Delta\Psi[\mathbf{r}] + 4\pi^2 k_0^2 \Psi[\mathbf{r}] &= -4\pi^2 U[\mathbf{r}] \Psi[\mathbf{r}] \\ \Psi[\mathbf{r}] &= \sum_{\mathbf{g}} \phi_{\mathbf{g}}[\mathbf{r}] e^{2\pi i (\mathbf{k}_0 + \mathbf{g}) \cdot \mathbf{r}} \\ \Psi[\mathbf{r}] &= \sum_j \psi^j B^j[\mathbf{r}] \\ (B^j[\mathbf{r}] &= \sum_{\mathbf{g}} C_{\mathbf{g}}^j e^{2\pi i (\mathbf{k}_0^j + \mathbf{g}) \cdot \mathbf{r}})\end{aligned}\tag{4.5}$$

The lattice constant of pure FCC Ni (see Chapter 2 Table 2.13) described by lattice vectors is approximately equal to $a = 350$ pm, the reciprocal lattice of FCC is BCC, with $a_{rec} = 2/a = 0.0031/\text{pm}$, thus the nearest neighbour reciprocal lattice point has length of 0.005 1/pm. On the other hand, at 200 kV, the relativistic electron wavelength is approximately equal to 2.51 pm, thus the radius of the Ewald sphere is approximately equal to 0.41/pm. According to Bragg's law the diffraction angle for the wavelength and reciprocal lattice point is given 0.4 °, which results in almost 2 orders of magnitude smaller than if diffracted radiation were X-rays (diffraction angle is 22.3 ° at for $\lambda_{CuK\alpha}=0.15$ nm). In brief, the Ewald sphere appears approximately flat surface for the diffracted beams, more explicitly the ratio of Ewald sphere radius to the least diffracted beam is 81 i.e. $|\mathbf{k}_0| = 81|\mathbf{g}|$. In consequence, it is possible in practice to study dynamical diffraction in the two-beam condition i.e. with only a single excited diffracted beam, $\phi_{\mathbf{g}}[\mathbf{r}]$. The Equations for two-beam dynamical diffraction have been formulated from Darwin-Howie-Whelan equations [232].

The two-beam dynamical approximation has been applied for an example application to the perfect foils in Fig. 4.12.

Fig. 4.12.: The parameters used for the simulation where $Re[\xi_g]=30\text{nm}$, $Im[\xi_g]=1500\text{ nm}$, $Im[\xi_0]=1500\text{ nm}$. (a) for Profile of Pendellösung fringes computed from the two-beam theory with $w_g=0$, and $t = 5Re[\xi_g]$; (b) for Rocking curves computed from the two-beam theory with $t = 1.5Re[\xi_g]$



The dislocation contrast due to the presence of dislocation loop defects has been described in detail by Wilkens [233]. This is shown in Fig. 4.13.

4.5 Mechanical properties

Several indentations or impression tests have been developed to measure macroscopic mechanical properties from contact of known geometry including spherically shaped Brinell or Rockwell and diamond Vickers impressions [234]. On the other hand, for testing of mechanical properties at the microscale level nanoindentation has become the preferred technique [235]. Nanoindentation performs instrumented indentations commonly with a diamond tip of pyramidal shape (Berkovich indenter) employing sensors and actuators, rather than relying on visual examination of the imprint.

As the indenter is pressed into the surface of the material being tested to plastically deform it, the required load, as well as the displacement of the tip, is being recorded. The load-displacement curves corresponding to both the load and the unloading contain a wealth of information including elastic modulus, work hardening behaviour in the slope of unloading curves.

Fig. 4.13.: Black/white contrast in the imaging of dislocation loops in the two-beam dynamical approximation. Figure reproduced from [233].

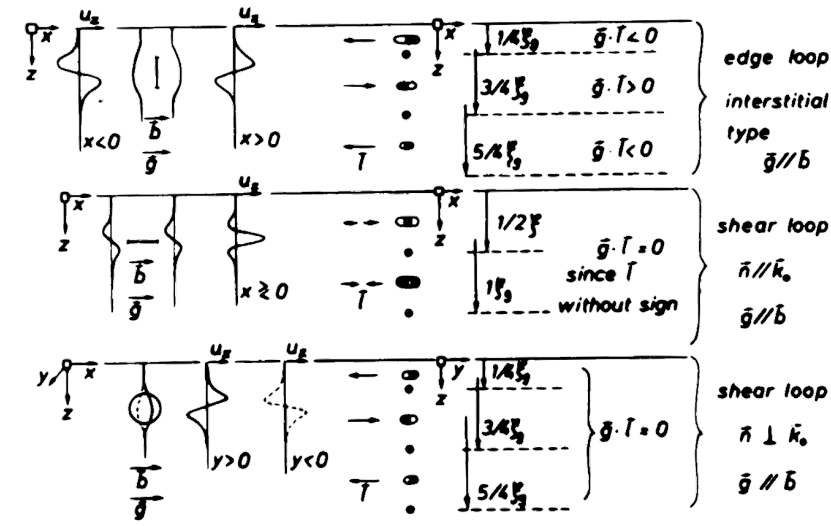


Fig. 4.14.: Schematic of nanoindenter equipment. Mechanical load is applied to the sample by electronically controlled actuators. Sensors are used to record the penetration of the tip into the surface of the material being tested. Figure reproduced from [234]

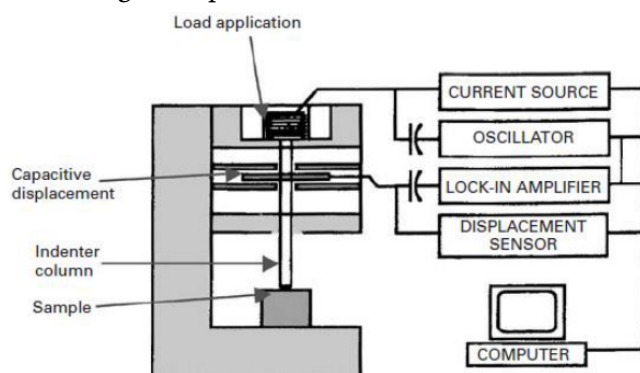
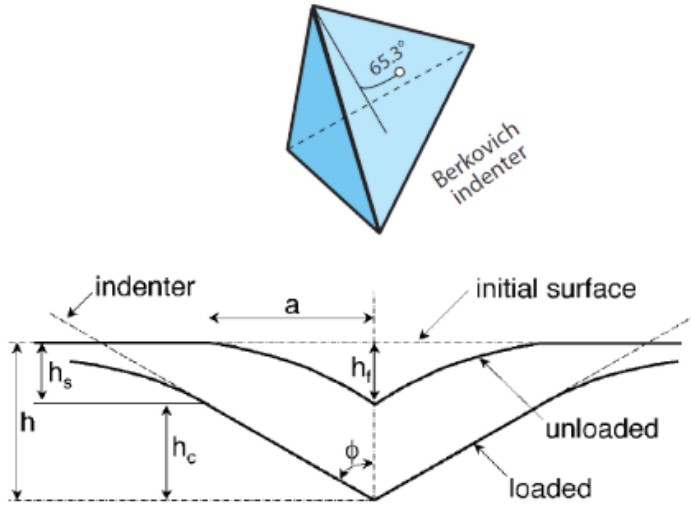


Fig. 4.15.: The recorded penetration of the indenter tip into the bulk sample, h , results in a plastic flow of material sideways to the tip (sink-in or pile-up). The correct contact area for the computation of the hardness is determined by the contact depth exposed to the tip at depth h_c . Figure reproduced from [236]



The area of indenter tip can in practice deviate from the geometrically sharp diamond tip for many reasons but typically due to wear, because hardness is the ratio of the load to the plastically deformed area, uncertainties in the area of the tip can propagate into the measurements of hardness values. To accurately compute hardness, calibration methods have been proposed. Specifically, the continuous stiffness method uses local measurements of the stiffness in a standard material such as fused silica to determine the contact area [236], A_c at contact depth h_c by

$$A_c[h_c] = \frac{\pi}{4} \frac{S^2[h_c]}{\beta E_{eff}^2} \quad (4.6)$$

where S represents the stiffness measured in force/length units; E_{eff} is the effective elastic constant for the frame and the calibration material; β is a correction in the terminology of Oliver and Pharr [236] that is approximately given by 1 for fused silica calibration material. Once a series of contact area values determined from expression at different contact depths 4.7 have been

obtained, the quantity of contact area can be fit into a polynomial expression of with 9 coefficients, c_n .

$$A_c[h_c] = \sum_{n=1}^9 c_n h_c^{2^n} \quad (4.7)$$

The polynomial function of contact depth 4.7 parametrised in terms of h_c , is characteristic of the tip of the intender and can be used to compute hardness in other materials by dividing the load by the value of the polynomial at the given contact depth of the material. Typically, the curves of hardness against contact depth present a sharp increase at small penetrations. This effect has been attributed to geometrically necessary dislocations, according to which hardness depends on the square root of the inverse of contact depth. The parameter H_0 represents the value that hardness achieves at bulk distances, and the parameter h_0 is related to the density of geometrically necessary dislocations and the geometry of tip [237].

$$H[h_c] = H_0 \sqrt{1 + h_0/h_c} \quad (4.8)$$

Short-Range Order in High Entropy Alloys: Theoretical Formulation and Application to Mo-Nb-Ta-V-W System

The complete author list for the published paper is provided in Chapter 1

Purpose of the paper and contributions from the authors

The purpose of this chapter is to show how first-principles modelling can be used to predict chemical ordering or segregation tendencies in HEAs at low temperatures, where entropy is not expected to stabilize the disordered random solid solution. Short-range order can indicate the existence of ordered domains in a microstructure. The general formalism is applied to the MoNbTaVW system, and it is predicted Mo-Ta ordering, which may derive into B2 phase precipitation.

This chapter is a verbatim copy of the publication: Fernández-Caballero, A., Wróbel, J. S., Mummery, P. M. and Nguyen-Manh, D. Short-Range Order in

High Entropy Alloys: Theoretical Formulation and Application to Mo-Nb-Ta-V-W System. *J. Phase Equilibria Diffus.* 38, 391–403 (2017).

Antonio Fernandez-Caballero conceived the idea, and performed the theoretical formulation for the MoNbTaVW system, and wrote the manuscript. Jan Wróbel and Duc Nguyen-Manh reviewed the paper. Antonio Fernandez-Caballero acknowledges Jan Wróbel for performing the Monte Carlo calculations and generating the figures nicely formatted. Antonio Fernandez-Caballero acknowledges Jan Wróbel, Duc Nguyen-Manh and Paul Mummery for their support, and suggestions in the elaboration of the manuscript.

Abstract

In high-entropy alloys (HEAs), the local chemical fluctuations from disordered solute solution state into segregation, precipitation and ordering configurations are complex due to a large number of elements. In this work, the cluster expansion (CE) Hamiltonian for multi-component alloy systems is developed to investigate the dependence of chemical ordering of HEAs as a function of temperature dependence due to derivation of configuration entropy from the ideal solute solution. Analytic expressions for Warren–Cowley short-range order (SRO) parameters are derived for a five-component alloy system. The theoretical formulation is used to investigate the evolution of the ten different SRO parameters in the MoNbTaVW and the sub-quaternary systems obtained by Monte-Carlo simulations within the combined CE and first-principles formalism. The strongest chemical SRO parameter is predicted for the first nearest-neighbour Mo-Ta pair that is in agreement with the high value of enthalpy of mixing in the B2 structure for this binary system. The prediction of B2 phase presence for Mo-Ta pairs in the considered bcc HEAs is reinforced by the positive contribution to the average SRO from the second nearest-neighbour shell. Interestingly, it is found that the average SRO pa-

parameter for the first and second nearest-neighbour shells of V-W pairs is also strongly negative in a comparison with the Mo-Ta pairs. This finding in the HEAs can be rationalized and discussed by the presence of the ordered-like B32 phase which has been predicted as the ground-state structure in binary bcc V-W system at the equimolar composition.

5.1 Introduction

Multi-principal element alloys, termed high entropy alloys (HEAs) with predominantly single solid solution phases have become an emerging field for alloy development with many basic concepts, including the origin of entropy effect on the interplay between thermodynamic analysis of complex, concentrated alloys and their microstructural properties [83, 13, 12]. This new class of materials, first brought to the attention in 2004 through the work of Cantor *et al.* [156] and Yeh *et al.* [11] is based around the concept that their high configurational entropy of mixing should stabilize simple solid-solution phases (such as fcc or bcc) relative to the formation of potentially-embrittling intermetallic ones. Recent experimental investigations cast doubts about the effect of entropic stabilization of solid solutions in different HEAs [15, 13, 91, 238]. In particular, the formation of two distinct types of Cr-rich precipitates ($M_{23}C_6$ and the σ phases) has been reported in the initially believed single fcc phase of the HEAs CrMnFeCoNi following long-term heat treatment [13].

Nevertheless, HEAs offer not only new and exciting approach to alloy design but also attract interest due to the discovery of alloys with unusual and attractive properties including physical, chemical, magnetic and mechanical properties [12, 238]. An example of exceptional mechanical property is having greater yield strength than any of its individual constituents in the bcc-structured refractory high entropy alloys MoNbTaVW. These HEAs

have high melting points and the excellent yield strength sustained to ultra-high temperatures has been usually attributed to solid solute strengthening mechanism and associated lattice strain [239]. In general, the HEAs are characterized not only by high values of entropy but also by high atomic-level stresses originating from the mixing of elements with different sizes [240, 241]. Therefore, there are still many fundamental questions that need to be addressed to understand the local atomic structure in the order and disorder of the terms of HEAs. Each element in HEAs will tend to occupy the position that minimizes its site energy and bond energies which in turn depend on preferred local chemical environments, interatomic interactions and atomic volumes of different constituent species. To experimentally determine the elemental distribution, several complementary techniques have been applied to ascertain the HEAs local structure include neutron scattering, high energy synchrotron x-ray diffraction, atom probe tomography and transmission electron microscopy coupled with x-ray energy dispersive spectroscopy (XEDS) [238, 242, 243].

In recent years, HEAs have attracted significant attention due to their superior radiation resistance compared to conventional single-phase Fe-Cr-Ni austenitic stainless steels making them potential candidates for high-temperature fission and fusion applications [20, 148]. Stability upon irradiation after cascade events may be attributed to the presence of high atomic level stresses resulted from the difference in atomic sizes in HEAs and their tendency for amorphization and recrystallization at high rates after irradiation-induced thermal spike [Egami2014]. It is worth mentioning that W based alloys are considered the preferred option for plasma-facing materials in magnetically confined fusion reactor designs [9]. Besides the high melting point, the reasons for the interest are high thermal conductivity, low activation, low tritium retention and low sputtering yield with regards to radiation damage for structural materials in nuclear fusion power plants [7, 244]. In the present work, a predictive model developed previously for

investigating phase stability in multi-component alloys [240, 245] has been employed in order to quantify short-range ordering of different atomic species for HEAs from first-principles calculations in a combination with the cluster expansion (CE) approach. The CE Hamiltonian can be used to describe both enthalpy and entropy contributions to free energy consistently not only for the solid solution but also for intermetallic phases in multicomponent alloy systems. In particular, by using thermodynamic integration via Monte-Carlo simulations with the effective cluster interactions (ECIs), it is shown that in general, the configurational entropy contribution depends strongly on temperature and therefore the entropy expression for ideal random solid solution phenomenologically adopted for HEAs is valid only at high-temperature limit [245]. The non-random configuration gives a tendency toward phase separation or chemical short-range ordering (SRO) and both of these trends decrease the configurational entropy from ideal estimates. This paper is organized as follows. In section 2, the CE formalism is introduced and developed for the Hamiltonian of the multicomponent system with a special focus on quinary alloys. In section 3, the mathematical expression of short-range order formulas is derived explicitly for five element alloy in terms of average pair correlation functions. In section 4, the SRO expressions are applied to the short-range order parameters for the specific HEAs MoNbTaVW and the corresponding five quaternary sub-systems. The second nearest-neighbour contributions into SRO properties are discussed in section 5. A summary of our results is given in section 6.

5.2 Cluster Expansion Hamiltonian for Multicomponent Alloys

The phase stability of multi-component alloys can be investigated using a combination of density functional theory (DFT) technique and lattice statisti-

cal simulations based on CE formalism [240, 245]. DFT calculations were performed using the projector augmented wave (PAW) method implemented in Vienna Ab-initio Simulation Package (VASP) [201, 202, 203, 204, 205, 206]. We use PAW potentials with semi-core p electron contribution with 11 electrons treated as valence for V, Nb, Ta and 12 electrons for Mo and W. Exchange and correlation interactions were treated in the generalized gradient approximation GGA-PBE [166]. The enthalpy of mixing for a five-component alloy, which can be evaluated using DFT, can be defined as:

$$\begin{aligned}\Delta H_{\text{Mixing}}(\vec{\sigma}) = & E_{\text{tot}}^{\text{lat}}(A_{c_A}B_{c_B}C_{c_C}D_{c_D}E_{c_E}, \vec{\sigma}) - c_A E_{\text{tot}}^{\text{lat}}(A) - c_B E_{\text{tot}}^{\text{lat}}(B) \\ & - c_C E_{\text{tot}}^{\text{lat}}(C) - c_D E_{\text{tot}}^{\text{lat}}(D) - c_E E_{\text{tot}}^{\text{lat}}(E)\end{aligned}\quad (5.1)$$

where c_A, c_B, c_C, c_D , and c_E are the average concentrations of alloy components A, B, C, D and E, respectively, and $E_{\text{tot}}^{\text{lat}}$ is the total energy per atom for considered structure. Here the vector $\vec{\sigma}$ defines the alloy configuration for a given lattice such as body-centered cubic (bcc). Within the cluster expansion formalism, [246, 200, 184, 247] the configurational enthalpy of mixing from Eq. 5.1 can be expressed in term of different cluster interaction energies by the following formula

$$\Delta H_{\text{Mixing}}(\vec{\sigma}) = \sum_{\omega} J_{\omega} m_{\omega} \langle \Gamma_{\omega'}(\vec{\sigma}) \rangle_{\omega} \quad (5.2)$$

where the summation in Eq. 5.2 is performed over all the clusters ω distinct under symmetry operations within the underlying lattice; m_{ω} denotes the multiplicities indicating the number of clusters equivalent to ω by symmetry and J_{ω} are the effective cluster interactions corresponding to cluster ω . $\langle \Gamma_{\omega'}(\vec{\sigma}) \rangle_{\omega}$ are the cluster functions defined as product of point functions of occupation variables, $\gamma_i(\sigma_p)$ specific cluster ω and averaged over the clusters

of atoms ω' that are equivalent to cluster ω' . The general expression for the cluster correlation function corresponding to an alloy configuration given by σ is given by:

$$\langle \Gamma_{|\omega|,m}^{(ijk\cdots)}(\vec{\sigma}) \rangle = \sum_{pqr\cdots} \gamma_i(\sigma_p) \gamma_j(\sigma_q) \gamma_k(\sigma_r) \cdots y_m^{pqr\cdots} \quad (5.3)$$

Here m is an integer corresponding to the configuration of the atomic labellings of the lattice points in the cluster shell. $y_m^{(pqr\cdots)}$ denotes the temperature-dependent probability of finding atomic species $pqr\cdots$ which are located at the atomic configuration in the shell specified by m . For general n -component systems, the orthogonal point functions γ_j are defined as in [184] by:

$$\gamma_{j,n}(\sigma_i) = \begin{cases} 1 & \text{if } j = 0, \\ -\cos\left(2\pi\lceil\frac{j}{2}\rceil\frac{\sigma_i}{n}\right) & \text{if } j > 0 \text{ and odd,} \\ -\sin\left(2\pi\lceil\frac{j}{2}\rceil\frac{\sigma_i}{n}\right) & \text{if } j > 0 \text{ and even,} \end{cases} \quad (5.4)$$

The direct relationship between $\langle \Gamma_{|\omega|,m}^{(ijk\cdots)}(\vec{\sigma}) \rangle$ and the probability of finding many-atom cluster configuration $y_m^{(pqr\cdots)}$ defined by Eqs. (3) and (4) demonstrates that this ensemble average are independent and consistent with CE Hamiltonian in Eq. 5.2. From Eqs. 5.3 and 5.4, the cluster correlation functions for point and pair clusters are given, respectively, by:

$$\langle \Gamma_{1,m}^{(i)}(\vec{\sigma}) \rangle = \sum_p \gamma_i(\sigma_p) y_m^p = \sum_p \gamma_i(\sigma_p) c_p \quad (5.5)$$

$$\left\langle \Gamma_{2,m}^{(ij)}(\vec{\sigma}) \right\rangle = \sum_{pq} \gamma_i(\sigma_p) \gamma_j(\sigma_q) y_m^{pq} \quad (5.6)$$

In Eq. 5.5 the average single-site cluster functions can be expressed in term of alloy concentration c_p . For the average pairwise cluster functions, Eq. 5.6, the index m denotes the mth nearest-neighbour pair which has probability $y_m^{(pq)}$ with the atom of type p sitting at the first site and atom of type q at the second site of the mth pair. Note that the pair probabilities $y_m^{(pq)}$ described in Eq. 5.6 are mutually independent and consistent with the CE formalism only if Hamiltonian Eq. 5.2 includes pair interactions. As it will be shown later from Table 5.1, it is found that the three-body interaction parameters are much smaller in their magnitudes in a comparison with those for the two-body interactions. Therefore, although the CE Hamiltonian includes three-body contributions, the pair probabilities play a dominant role in determining quasi-independent configurations for multi-component alloys in the present study. The effect of triple effective cluster interactions on short-range order analysis in Mo-Nb-Ta-V-W alloys will be discussed in Section IV and V.

Table 5.1.: Cluster size $|\omega|$, decoration (s), coordinates of points, multiplicity $m_{|\omega|,n}^{(s)}$ and ECIs parameters $J_{|\omega|,n}^{(s)}$ (in meV/atom) for the bcc quinary Mo-Nb-Ta-V-W alloys

Table 5.1					
$ \omega $	(s)	Coordinates	$m_{ \omega ,n}^{(s)}$	$J_{ \omega ,n}^{(s)}$	
1	(4,0)	(1/2,1/2,-1/2)	1	-0.045916	
1	(4,1)	(1/2,1/2,-1/2)	1	0.001268	
1	(4,2)	(1/2,1/2,-1/2)	1	-0.038125	
1	(4,3)	(1/2,1/2,-1/2)	1	0.064412	
1	(4,4)	(1/2,1/2,-1/2)	1	0.118137	
2	(4,1),(4,1)	(1/2,1/2,-1/2),(1,0,0)	4	-0.000908	
2	(4,2),(4,1)	(1/2,1/2,-1/2),(1,0,0)	8	0.002665	
2	(4,3),(4,1)	(1/2,1/2,-1/2),(1,0,0)	8	-0.000769	

Continuation of Table 5.1

$ \omega $	(s)	Coordinates	$m_{ \omega ,n}^{(s)}$	$J_{ \omega ,n}^{(s)}$
2	(4,4),(4,1)	(1/2,1/2,-1/2),(1,0,0)	8	-0.002685
2	(4,2),(4,2)	(1/2,1/2,-1/2),(1,0,0)	4	0.005604
2	(4,3),(4,2)	(1/2,1/2,-1/2),(1,0,0)	8	-0.011832
2	(4,4),(4,2)	(1/2,1/2,-1/2),(1,0,0)	8	-0.0055
2	(4,3),(4,3)	(1/2,1/2,-1/2),(1,0,0)	4	0.006763
2	(4,4),(4,3)	(1/2,1/2,-1/2),(1,0,0)	8	0.009787
2	(4,4),(4,4)	(1/2,1/2,-1/2),(1,0,0)	4	0.00569
2	(4,1),(4,1)	(1/2,1/2,-1/2),(1/2,1/2,1/2)	3	-0.005199
2	(4,2),(4,1)	(1/2,1/2,-1/2),(1/2,1/2,1/2)	6	-0.000308
2	(4,3),(4,1)	(1/2,1/2,-1/2),(1/2,1/2,1/2)	6	0.008523
2	(4,4),(4,1)	(1/2,1/2,-1/2),(1/2,1/2,1/2)	6	-0.000649
2	(4,2),(4,2)	(1/2,1/2,-1/2),(1/2,1/2,1/2)	3	-0.000075
2	(4,3),(4,2)	(1/2,1/2,-1/2),(1/2,1/2,1/2)	6	-0.003539
2	(4,4),(4,2)	(1/2,1/2,-1/2),(1/2,1/2,1/2)	6	-0.001434
2	(4,3),(4,3)	(1/2,1/2,-1/2),(1/2,1/2,1/2)	3	-0.001909
2	(4,4),(4,3)	(1/2,1/2,-1/2),(1/2,1/2,1/2)	6	0.008087
2	(4,4),(4,4)	(1/2,1/2,-1/2),(1/2,1/2,1/2)	3	0.00258
2	(4,1),(4,1)	(1/2,1/2,-1/2),(1/2,-1/2,1/2)	6	-0.000769
2	(4,2),(4,1)	(1/2,1/2,-1/2),(1/2,-1/2,1/2)	12	0.000442
2	(4,3),(4,1)	(1/2,1/2,-1/2),(1/2,-1/2,1/2)	12	0.000808
2	(4,4),(4,1)	(1/2,1/2,-1/2),(1/2,-1/2,1/2)	12	-0.000952
2	(4,2),(4,2)	(1/2,1/2,-1/2),(1/2,-1/2,1/2)	6	0.001056
2	(4,3),(4,2)	(1/2,1/2,-1/2),(1/2,-1/2,1/2)	12	-0.002441
2	(4,4),(4,2)	(1/2,1/2,-1/2),(1/2,-1/2,1/2)	12	-0.000852
2	(4,3),(4,3)	(1/2,1/2,-1/2),(1/2,-1/2,1/2)	6	0.001001
2	(4,4),(4,3)	(1/2,1/2,-1/2),(1/2,-1/2,1/2)	12	0.002171
2	(4,4),(4,4)	(1/2,1/2,-1/2),(1/2,-1/2,1/2)	6	0.000536
3	(4,1),(4,1),(4,1)	(1/2,1/2,-1/2),(0,0,0),(1/2,1/2,1/2)	12	0.000025
3	(4,2),(4,1),(4,1)	(1/2,1/2,-1/2),(0,0,0),(1/2,1/2,1/2)	24	0.000053

Continuation of Table 5.1

$ \omega $	(s)	Coordinates	$m_{ \omega ,n}^{(s)}$	$J_{ \omega ,n}^{(s)}$
3	(4,3),(4,1),(4,1)	(1/2,1/2,-1/2),(0,0,0),(1/2,1/2,1/2)	24	-0.000263
3	(4,4),(4,1),(4,1)	(1/2,1/2,-1/2),(0,0,0),(1/2,1/2,1/2)	24	-0.000124
3	(4,1),(4,2),(4,1)	(1/2,1/2,-1/2),(0,0,0),(1/2,1/2,1/2)	12	-0.000015
3	(4,2),(4,2),(4,1)	(1/2,1/2,-1/2),(0,0,0),(1/2,1/2,1/2)	24	-0.000016
3	(4,3),(4,2),(4,1)	(1/2,1/2,-1/2),(0,0,0),(1/2,1/2,1/2)	24	0.000139
3	(4,4),(4,2),(4,1)	(1/2,1/2,-1/2),(0,0,0),(1/2,1/2,1/2)	24	0.000106
3	(4,1),(4,3),(4,1)	(1/2,1/2,-1/2),(0,0,0),(1/2,1/2,1/2)	12	0.000124
3	(4,2),(4,3),(4,1)	(1/2,1/2,-1/2),(0,0,0),(1/2,1/2,1/2)	24	0.000139
3	(4,3),(4,3),(4,1)	(1/2,1/2,-1/2),(0,0,0),(1/2,1/2,1/2)	24	-0.00069
3	(4,4),(4,3),(4,1)	(1/2,1/2,-1/2),(0,0,0),(1/2,1/2,1/2)	24	-0.000284
3	(4,1),(4,4),(4,1)	(1/2,1/2,-1/2),(0,0,0),(1/2,1/2,1/2)	12	0.000355
3	(4,2),(4,4),(4,1)	(1/2,1/2,-1/2),(0,0,0),(1/2,1/2,1/2)	24	0.000079
3	(4,3),(4,4),(4,1)	(1/2,1/2,-1/2),(0,0,0),(1/2,1/2,1/2)	24	-0.000465
3	(4,4),(4,4),(4,1)	(1/2,1/2,-1/2),(0,0,0),(1/2,1/2,1/2)	24	-0.000304
3	(4,2),(4,1),(4,2)	(1/2,1/2,-1/2),(0,0,0),(1/2,1/2,1/2)	12	-0.000185
3	(4,3),(4,1),(4,2)	(1/2,1/2,-1/2),(0,0,0),(1/2,1/2,1/2)	24	0.000176
3	(4,4),(4,1),(4,2)	(1/2,1/2,-1/2),(0,0,0),(1/2,1/2,1/2)	24	-0.000101
3	(4,2),(4,2),(4,2)	(1/2,1/2,-1/2),(0,0,0),(1/2,1/2,1/2)	12	0.00056
3	(4,3),(4,2),(4,2)	(1/2,1/2,-1/2),(0,0,0),(1/2,1/2,1/2)	24	-0.000718
3	(4,4),(4,2),(4,2)	(1/2,1/2,-1/2),(0,0,0),(1/2,1/2,1/2)	24	-0.000358
3	(4,2),(4,3),(4,2)	(1/2,1/2,-1/2),(0,0,0),(1/2,1/2,1/2)	12	-0.000422
3	(4,3),(4,3),(4,2)	(1/2,1/2,-1/2),(0,0,0),(1/2,1/2,1/2)	24	0.00119
3	(4,4),(4,3),(4,2)	(1/2,1/2,-1/2),(0,0,0),(1/2,1/2,1/2)	24	0.000856
3	(4,2),(4,4),(4,2)	(1/2,1/2,-1/2),(0,0,0),(1/2,1/2,1/2)	12	-0.00018
3	(4,3),(4,4),(4,2)	(1/2,1/2,-1/2),(0,0,0),(1/2,1/2,1/2)	24	0.000766
3	(4,4),(4,4),(4,2)	(1/2,1/2,-1/2),(0,0,0),(1/2,1/2,1/2)	24	0.000347
3	(4,3),(4,1),(4,3)	(1/2,1/2,-1/2),(0,0,0),(1/2,1/2,1/2)	12	-0.000432
3	(4,4),(4,1),(4,3)	(1/2,1/2,-1/2),(0,0,0),(1/2,1/2,1/2)	24	-0.000359
3	(4,3),(4,2),(4,3)	(1/2,1/2,-1/2),(0,0,0),(1/2,1/2,1/2)	12	0.00121

Continuation of Table 5.1

$ \omega $	(s)	Coordinates	$m_{ \omega ,n}^{(s)}$	$J_{ \omega ,n}^{(s)}$
3	(4,4),(4,2),(4,3)	(1/2,1/2,-1/2),(0,0,0),(1/2,1/2,1/2)	24	0.00077
3	(4,3),(4,3),(4,3)	(1/2,1/2,-1/2),(0,0,0),(1/2,1/2,1/2)	12	-0.001927
3	(4,4),(4,3),(4,3)	(1/2,1/2,-1/2),(0,0,0),(1/2,1/2,1/2)	24	-0.001913
3	(4,3),(4,4),(4,3)	(1/2,1/2,-1/2),(0,0,0),(1/2,1/2,1/2)	12	-0.001353
3	(4,4),(4,4),(4,3)	(1/2,1/2,-1/2),(0,0,0),(1/2,1/2,1/2)	24	-0.001071
3	(4,4),(4,1),(4,4)	(1/2,1/2,-1/2),(0,0,0),(1/2,1/2,1/2)	12	0.000133
3	(4,4),(4,2),(4,4)	(1/2,1/2,-1/2),(0,0,0),(1/2,1/2,1/2)	12	0.000449
3	(4,4),(4,3),(4,4)	(1/2,1/2,-1/2),(0,0,0),(1/2,1/2,1/2)	12	-0.001004
3	(4,4),(4,4),(4,4)	(1/2,1/2,-1/2),(0,0,0),(1/2,1/2,1/2)	12	-0.00088

End of Table 5.1

The expression for the single-site correlation function for five-component alloy can be obtained by using Eq. 5.5 in terms of the average atomic concentration of all the elements present in the system as follows:

$$\langle \Gamma_{1,1}^0 \rangle = 1$$

$$\langle \Gamma_{1,1}^1 \rangle = \frac{1}{4} [\phi_- (c_B + c_E) + \phi_+ (c_C + c_D) - 4c_A]$$

$$\langle \Gamma_{1,1}^2 \rangle = \sqrt{\chi_-} (c_D - c_C) + \sqrt{\chi_+} (c_E - c_B) \quad (5.7)$$

$$\langle \Gamma_{1,1}^3 \rangle = \frac{1}{4} [\phi_- (c_C + c_D) + \phi_+ (c_B + c_E) - 4c_A]$$

$$\langle \Gamma_{1,1}^4 \rangle = \sqrt{\chi_-} (c_E - c_B) + \sqrt{\chi_+} (c_C - c_D)$$

where we used the following notation: $\phi_{\pm} = 1 \pm \sqrt{5}$, $\chi_{\pm} = 5/8 \pm \sqrt{5/8}$. From Eq.5.6, the expressions for the pairwise cluster functions can be expressed in terms of the pair probabilities, $y_m^{(pq)}$, as follows:

$$\begin{aligned}\langle \Gamma_{2,m}^{11} \rangle &= \frac{1}{16} \left[2\phi_{-}\phi_{+} (y_m^{BC} + y_m^{BD} + y_m^{CE} + y_m^{DE}) - 8\phi_{-} (y_m^{AB} + y_m^{AE}) \right. \\ &\quad + \phi_{-}^2 (y_m^{BB} + 2y_m^{BE} + y_m^{EE}) \\ &\quad \left. - 8\phi_{+} (y_m^{AC} + y_m^{AD}) + \phi_{+}^2 (y_m^{CC} + 2y_m^{CD} + y_m^{DD}) + 16y_m^{AA} \right] \\ \langle \Gamma_{2,m}^{12} \rangle &= \frac{1}{4} \left[\phi_{-}\sqrt{\chi_{+}} (y_m^{EE} - y_m^{BB}) + \sqrt{\chi_{-}}\phi_{+} (y_m^{DD} - y_m^{CC}) \right. \\ &\quad + 4\sqrt{\chi_{-}} (y_m^{AC} - y_m^{AD}) \\ &\quad + \sqrt{\chi_{-}}\phi_{-} (-y_m^{BC} + y_m^{BD} - y_m^{CE} + y_m^{DE}) + 4\sqrt{\chi_{+}} (y_m^{AB} - y_m^{AE}) \\ &\quad \left. + \sqrt{\chi_{+}}\phi_{+} (-y_m^{BC} - y_m^{BD} + y_m^{CE} + y_m^{DE}) \right] \\ \langle \Gamma_{2,m}^{13} \rangle &= \frac{1}{16} \left[\phi_{-}\phi_{+} (y_m^{BB} + 2y_m^{BE} + y_m^{CC} + 2y_m^{CD} + y_m^{DD} + y_m^{EE}) \right. \\ &\quad - 4\phi_{-} (y_m^{AB} + y_m^{AC} + y_m^{AD} + y_m^{AE}) \\ &\quad + \phi_{-}^2 (y_m^{BC} + y_m^{BD} + y_m^{CE} + y_m^{DE}) \\ &\quad - 4\phi_{+} (y_m^{AB} + y_m^{AC} + y_m^{AD} + y_m^{AE}) + \phi_{+}^2 (y_m^{BC} + y_m^{BD} + y_m^{CE} + y_m^{DE}) \\ &\quad \left. + 16y_m^{AA} \right] \\ \langle \Gamma_{2,m}^{14} \rangle &= \frac{1}{4} \left[\phi_{-}\sqrt{\chi_{+}} (y_m^{BC} - y_m^{DE}) + \sqrt{\chi_{-}}\phi_{+} (y_m^{DE} - y_m^{BC}) \right. \\ &\quad + (\phi_{-}\sqrt{\chi_{+}} + \sqrt{\chi_{-}}\phi_{+}) (y_m^{CE} - y_m^{BD}) + 4\sqrt{\chi_{-}} (y_m^{AB} - y_m^{AE}) \\ &\quad + \sqrt{\chi_{-}}\phi_{-} (y_m^{EE} - y_m^{BB}) \\ &\quad \left. - 4\sqrt{\chi_{+}} (y_m^{AC} - y_m^{AD}) + \sqrt{\chi_{+}}\phi_{+} (y_m^{CC} - y_m^{DD}) \right] \\ \langle \Gamma_{2,m}^{22} \rangle &= 2\sqrt{\chi_{-}\chi_{+}} (y_m^{BC} - y_m^{BD} - y_m^{CE} + y_m^{DE}) + \chi_{-} (y_m^{CC} - 2y_m^{CD} + y_m^{DD}) \\ &\quad + \chi_{+} (y_m^{BB} - 2y_m^{BE} + y_m^{EE})\end{aligned}$$

$$\begin{aligned}
\langle \Gamma_{2,m}^{23} \rangle = & \frac{1}{4} \left[(\phi_- \sqrt{\chi_+} + \sqrt{\chi_-} \phi_+) (y_m^{DE} - y_m^{BC}) + \phi_- \sqrt{\chi_+} (y_m^{CE} - y_m^{BD}) \right. \\
& + \sqrt{\chi_-} \phi_+ (y_m^{BD} - y_m^{CE}) + 4 \sqrt{\chi_-} (y_m^{AC} - y_m^{AD}) \\
& \left. + \sqrt{\chi_-} \phi_- (y_m^{DD} - y_m^{CC}) + 4 \sqrt{\chi_+} (y_m^{AB} - y_m^{AE}) + \sqrt{\chi_+} \phi_+ (y_m^{EE} - y_m^{BB}) \right] \\
\langle \Gamma_{2,m}^{24} \rangle = & \sqrt{\chi_- \chi_+} (y_m^{BB} - 2y_m^{BE} - y_m^{CC} + 2y_m^{CD} - y_m^{DD} + y_m^{EE}) \\
& + \chi_- (y_m^{BC} - y_m^{BD} - y_m^{CE} + y_m^{DE}) + \chi_+ (-y_m^{BC} + y_m^{BD} + y_m^{CE} - y_m^{DE}) \\
\langle \Gamma_{2,m}^{33} \rangle = & \frac{1}{16} \left[2\phi_- \phi_+ (y_m^{BC} + y_m^{BD} + y_m^{CE} + y_m^{DE}) - 8\phi_- (y_m^{AC} + y_m^{AD}) \right. \\
& + \phi_-^2 (y_m^{CC} + 2y_m^{CD} + y_m^{DD}) - 8\phi_+ \\
& \left. (y_m^{AB} + y_m^{AE}) + \phi_+^2 (y_m^{BB} + 2y_m^{BE} + y_m^{EE}) + 16y_m^{AA} \right] \\
\langle \Gamma_{2,m}^{34} \rangle = & \frac{1}{4} \left[\sqrt{\chi_-} \phi_+ (y_m^{EE} - y_m^{BB}) + \phi_- \sqrt{\chi_+} (y_m^{CC} - y_m^{DD}) + 4 \sqrt{\chi_-} (y_m^{AB} - y_m^{AE}) \right. \\
& + \sqrt{\chi_-} \phi_- (-y_m^{BC} - y_m^{BD} + y_m^{CE} + y_m^{DE}) \\
& \left. - 4 \sqrt{\chi_+} (y_m^{AC} - y_m^{AD}) + \sqrt{\chi_+} \phi_+ (y_m^{BC} - y_m^{BD} + y_m^{CE} - y_m^{DE}) \right] \\
\langle \Gamma_{2,m}^{44} \rangle = & \sqrt{\chi_- \chi_+} (-2y_m^{BC} + 2y_m^{BD} + 2y_m^{CE} - 2y_m^{DE}) + \chi_- (y_m^{BB} - 2y_m^{BE} + y_m^{EE}) \\
& + \chi_+ (y_m^{CC} - 2y_m^{CD} + y_m^{DD})
\end{aligned} \tag{5.8}$$

Rewriting Eq.5.2 in terms of average point and pair cluster functions given by Eqs. 5.7 it is found that the configurational enthalpy of mixing for quinary

alloys can be expressed as a function of concentration c_p and average pair probabilities y_m^{pq} by the following expression:

$$\begin{aligned}\Delta H_{\text{mix}}(\vec{\sigma}) = & J_{1,1}^0 \langle \Gamma_{1,1}^0(\vec{\sigma}) \rangle + J_{1,1}^1 \langle \Gamma_{1,1}^1(\vec{\sigma}) \rangle + J_{1,1}^2 \langle \Gamma_{1,1}^2(\vec{\sigma}) \rangle + J_{1,1}^3 \langle \Gamma_{1,1}^3(\vec{\sigma}) \rangle \\ & + J_{1,1}^4 \langle \Gamma_{1,1}^4(\vec{\sigma}) \rangle + \sum_{\text{m pairs}} \left[m_{2,\text{m}}^{11} J_{2,\text{m}}^{11} \langle \Gamma_{2,\text{m}}^{11}(\vec{\sigma}) \rangle + m_{2,\text{m}}^{12} J_{2,\text{m}}^{12} \langle \Gamma_{2,\text{m}}^{12}(\vec{\sigma}) \rangle \right. \\ & + m_{2,\text{m}}^{13} J_{2,\text{m}}^{13} \langle \Gamma_{2,\text{m}}^{13}(\vec{\sigma}) \rangle + m_{2,\text{m}}^{14} J_{2,\text{m}}^{14} \langle \Gamma_{2,\text{m}}^{14}(\vec{\sigma}) \rangle + m_{2,\text{m}}^{22} J_{2,\text{m}}^{22} \langle \Gamma_{2,\text{m}}^{22}(\vec{\sigma}) \rangle \\ & + m_{2,\text{m}}^{23} J_{2,\text{m}}^{23} \langle \Gamma_{2,\text{m}}^{23}(\vec{\sigma}) \rangle + m_{2,\text{m}}^{24} J_{2,\text{m}}^{24} \langle \Gamma_{2,\text{m}}^{24}(\vec{\sigma}) \rangle + m_{2,\text{m}}^{33} J_{2,\text{m}}^{33} \langle \Gamma_{2,\text{m}}^{33}(\vec{\sigma}) \rangle \\ & \left. + m_{2,\text{m}}^{34} J_{2,\text{m}}^{34} \langle \Gamma_{2,\text{m}}^{34}(\vec{\sigma}) \rangle + m_{2,\text{m}}^{44} J_{2,\text{m}}^{44} \langle \Gamma_{2,\text{m}}^{44}(\vec{\sigma}) \rangle \right] + \sum_{\text{triplets}} \dots\end{aligned}\quad (5.9)$$

The ECI $J_{(\omega, n)}^{(s)}$ parameters in five-component alloy MoNbTaVW system were obtained by mapping DFT energies calculated for 428 bcc-like structures from different binaries, ternaries, quaternaries into the CE Hamiltonian in Eq. 5.8 by using the structure inversion method (SIM) [186, 181]. The fitting procedure was carried out using the ATAT package [246] and the cross-validation error between DFT and CE energies was about 8 meV/atom. The values of 5 point, 30 pair and 40 triple ECIs parameters initially reported in [240] are given in Table 5.1.

It is found that the dominant contributions to the pairwise energies come from the first and second bcc nearest-neighbour interactions whereas the third nearest-neighbour pair interactions and the three-body interactions are significantly smaller. It is worth noting that the CE energy for multi-component alloy in Eq. 5.8 represents a generalization of the Ising-like Hamiltonian where the only nearest-neighbour interactions between different species are taken into account, for example, in the case of four-component HEAs MoNbTaW [248]. The CE Hamiltonian can be used to perform quasi-canonical Monte-Carlo simulations to investigate free energies of alloy formation from disorder to order phase transitions. The evaluations of the free energies involved thermo-

dynamic integration algorithm for computing the configurational entropies of alloys as it has been described in detail previously [245]. More importantly, the chemical short-range order (SRO) parameters describing the occupational derivations from the average random configuration at a local atomic scale can be evaluated from the CE free energies of mixing and compared with available experimental data.

5.3 Short Range Order Parameters for Multicomponent Alloy

In general, multi-component alloys can exhibit structural order over both short and medium length scales, the latter reaching 2 nm or so. Theoretically, the present CE Hamiltonian approach in a combination with Monte-Carlo simulations can allow to investigate medium-range order in HEAs via multi-body cluster probability functions $y_m^{(pqr\dots)}$ in Eq. 5.3. However, medium-range order is difficult to measure experimentally and to interpret unambiguously. Here we focus our study on chemical short-range order (SRO) analysis which has been successfully applied and compared with available experimental data for the ternary Fe-Cr-Ni alloy case [245]. The degree of chemical SRO influences both the configuration entropy and enthalpy of mixing in alloy complex. The chemical SRO is absent in ideal solid solutions where atom species occupy sites randomly. It is common to describe SRO in form of Warren-Cowley short-range order or pair-correlation parameters in the following formula [249]:

$$\alpha_{2,m}^{pq} = 1 - \frac{y_m^{pq}}{c_p c_q} \quad (5.10)$$

Here we use the notation for the average concentration c_p and the average pair probability for the m th nearest-neighbor shell as they have been defined from Eqs. 5.5 and 5.6, respectively. Note that $P_m^{pq} = y_m^{pq}/c_p$ is the conditional probability of finding atom q in the m th coordination shell surrounding the atom p. When $\alpha_{(2,m)}^{pq} = 0$ this describes random alloys namely in this case elements p and q in the pair configuration m are found in the alloy system with a probability equal to $c_p c_q$. In the case of $\alpha_{(2,m)}^{pq} \geq 0$ there is a tendency of clustering or segregation of p-p and q-q pairs and for $\alpha_{(2,m)}^{pq} \leq 0$ there is a tendency of unlike pairs ordering p-q.

Short range order parameters can be expressed in terms of average point and pair correlation functions. The expressions for the $y_{(2,m)}^{pq}$ in Eq. 5.11 can be obtained from the inversion of the equations 5.7 and 5.8. For a five component alloy system there are 10 distinct pair probability functions and their explicit formulas are below.

$$y_{2,m}^{\text{AB}} = \frac{1}{50} \left[-(\kappa + 3) \langle \Gamma_{1,1}^1 \rangle + \sqrt{2} \sqrt{\kappa + 5} (2 (\langle \Gamma_{2,m}^{12} \rangle + \langle \Gamma_{2,m}^{23} \rangle) - \langle \Gamma_{1,1}^2 \rangle) + \sqrt{10 - 2\kappa} (2 (\langle \Gamma_{2,m}^{14} \rangle + \langle \Gamma_{2,m}^{34} \rangle) - \langle \Gamma_{1,1}^4 \rangle) + (\kappa - 3) \langle \Gamma_{1,1}^3 \rangle + 2(\kappa - 1) \langle \Gamma_{2,m}^{11} \rangle - 4 \langle \Gamma_{2,m}^{13} \rangle - 2(\kappa + 1) \langle \Gamma_{2,m}^{33} \rangle + 2 \right]$$

$$y_{2,m}^{\text{AC}} = \frac{1}{50} \left[(\kappa - 3) \langle \Gamma_{1,1}^1 \rangle + \sqrt{10 - 2\kappa} (2 (\langle \Gamma_{2,m}^{12} \rangle + \langle \Gamma_{2,m}^{23} \rangle) - \langle \Gamma_{1,1}^2 \rangle) + \sqrt{2} \sqrt{\kappa + 5} (\langle \Gamma_{1,1}^4 \rangle - 2 (\langle \Gamma_{2,m}^{14} \rangle + \langle \Gamma_{2,m}^{34} \rangle)) - (\kappa + 3) \langle \Gamma_{1,1}^3 \rangle - 2(\kappa + 1) \langle \Gamma_{2,m}^{11} \rangle - 4 \langle \Gamma_{2,m}^{13} \rangle + 2(\kappa - 1) \langle \Gamma_{2,m}^{33} \rangle + 2 \right]$$

$$y_{2,m}^{\text{AD}} = \frac{1}{50} \left[(\kappa - 3) \langle \Gamma_{1,1}^1 \rangle + \sqrt{10 - 2\kappa} (\langle \Gamma_{1,1}^2 \rangle - 2 (\langle \Gamma_{2,m}^{12} \rangle + \langle \Gamma_{2,m}^{23} \rangle)) + \sqrt{2} \sqrt{\kappa + 5} (2 (\langle \Gamma_{2,m}^{14} \rangle + \langle \Gamma_{2,m}^{34} \rangle) - \langle \Gamma_{1,1}^4 \rangle) - (\kappa + 3) \langle \Gamma_{1,1}^3 \rangle - 2(\kappa + 1) \langle \Gamma_{2,m}^{11} \rangle - 4 \langle \Gamma_{2,m}^{13} \rangle + 2(\kappa - 1) \langle \Gamma_{2,m}^{33} \rangle + 2 \right]$$

$$y_{2,m}^{AE} = \frac{1}{50} \left[-(\kappa + 3) \langle \Gamma_{1,1}^1 \rangle + \sqrt{2} \sqrt{\kappa + 5} (\langle \Gamma_{1,1}^2 \rangle - 2 (\langle \Gamma_{2,m}^{12} \rangle + \langle \Gamma_{2,m}^{23} \rangle)) + \sqrt{10 - 2\kappa} (\langle \Gamma_{1,1}^4 \rangle - 2 (\langle \Gamma_{2,m}^{14} \rangle + \langle \Gamma_{2,m}^{34} \rangle)) + (\kappa - 3) \langle \Gamma_{1,1}^3 \rangle + 2(\kappa - 1) \langle \Gamma_{2,m}^{11} \rangle - 4 \langle \Gamma_{2,m}^{13} \rangle - 2(\kappa + 1) \langle \Gamma_{2,m}^{33} \rangle + 2 \right]$$

$$y_{2,m}^{BC} = \frac{1}{25} \left[\langle \Gamma_{1,1}^1 \rangle - \sqrt{2\kappa + 5} (\langle \Gamma_{1,1}^2 \rangle + \langle \Gamma_{2,m}^{14} \rangle) + \sqrt{5 - 2\kappa} (\langle \Gamma_{1,1}^4 \rangle - \langle \Gamma_{2,m}^{23} \rangle) + \langle \Gamma_{1,1}^3 \rangle - \langle \Gamma_{2,m}^{11} \rangle - \sqrt{10 - 2\kappa} (\langle \Gamma_{2,m}^{12} \rangle + 3 \langle \Gamma_{2,m}^{13} \rangle + \kappa \langle \Gamma_{2,m}^{22} \rangle - \kappa \langle \Gamma_{2,m}^{24} \rangle - \langle \Gamma_{2,m}^{33} \rangle) + \sqrt{2} \sqrt{\kappa + 5} \langle \Gamma_{2,m}^{34} \rangle - \kappa \langle \Gamma_{2,m}^{44} \rangle + 1 \right]$$

$$y_{2,m}^{BD} = \frac{1}{100} \left[4 \langle \Gamma_{1,1}^1 \rangle - 4 \sqrt{5 - 2\kappa} \langle \Gamma_{1,1}^2 \rangle + 4 \langle \Gamma_{1,1}^3 \rangle - 4 \sqrt{2\kappa + 5} \langle \Gamma_{1,1}^4 \rangle - 4 \langle \Gamma_{2,m}^{11} \rangle + \sqrt{2} \sqrt{\kappa + 5} (-4 \langle \Gamma_{2,m}^{12} \rangle + (\kappa - 3) \langle \Gamma_{2,m}^{14} \rangle + (\kappa + 1) \langle \Gamma_{2,m}^{23} \rangle) + 4 (3 \langle \Gamma_{2,m}^{13} \rangle - \kappa \langle \Gamma_{2,m}^{22} \rangle + \kappa \langle \Gamma_{2,m}^{24} \rangle - \langle \Gamma_{2,m}^{33} \rangle - \sqrt{10 - 2\kappa} \langle \Gamma_{2,m}^{34} \rangle + \kappa \langle \Gamma_{2,m}^{44} \rangle) + 4 \right]$$

$$y_{2,m}^{BE} = \frac{1}{50} \left[-2(\kappa - 1) \langle \Gamma_{1,1}^1 \rangle + 2(\kappa + 1) \langle \Gamma_{1,1}^3 \rangle - (\kappa - 3) \langle \Gamma_{2,m}^{11} \rangle - 4 \langle \Gamma_{2,m}^{13} \rangle - (\kappa + 5) \langle \Gamma_{2,m}^{22} \rangle - 4\kappa \langle \Gamma_{2,m}^{24} \rangle + (\kappa + 3) \langle \Gamma_{2,m}^{33} \rangle + (\kappa - 5) \langle \Gamma_{2,m}^{44} \rangle + 2 \right]$$

$$y_{2,m}^{CD} = \frac{1}{50} \left[2(\kappa + 1) \langle \Gamma_{1,1}^1 \rangle - 2(\kappa - 1) \langle \Gamma_{1,1}^3 \rangle + (\kappa + 3) \langle \Gamma_{2,m}^{11} \rangle - 4 \langle \Gamma_{2,m}^{13} \rangle + (\kappa - 5) \langle \Gamma_{2,m}^{22} \rangle + 4\kappa \langle \Gamma_{2,m}^{24} \rangle - (\kappa - 3) \langle \Gamma_{2,m}^{33} \rangle - (\kappa + 5) \langle \Gamma_{2,m}^{44} \rangle + 2 \right]$$

$$\begin{aligned}
y_{2,m}^{\text{CE}} = & \frac{1}{100} \left[4 \langle \Gamma_{1,1}^1 \rangle + 4\sqrt{5-2\kappa} \langle \Gamma_{1,1}^2 \rangle + 4 \langle \Gamma_{1,1}^3 \rangle + 4\sqrt{2\kappa+5} \langle \Gamma_{1,1}^4 \rangle \right. \\
& - 4 \langle \Gamma_{2,m}^{11} \rangle - \sqrt{2}\sqrt{\kappa+5} (-4 \langle \Gamma_{2,m}^{12} \rangle + (\kappa-3) \langle \Gamma_{2,m}^{14} \rangle + (\kappa+1) \langle \Gamma_{2,m}^{23} \rangle) \\
& + 4 (3 \langle \Gamma_{2,m}^{13} \rangle - \kappa \langle \Gamma_{2,m}^{22} \rangle + \kappa \langle \Gamma_{2,m}^{24} \rangle - \langle \Gamma_{2,m}^{33} \rangle + \sqrt{10-2\kappa} \langle \Gamma_{2,m}^{34} \rangle + \kappa \langle \Gamma_{2,m}^{44} \rangle) \\
& \left. + 4 \right] \\
y_{2,m}^{\text{DE}} = & \frac{1}{25} \left[\langle \Gamma_{1,1}^1 \rangle + \sqrt{2\kappa+5} (\langle \Gamma_{1,1}^2 \rangle + \langle \Gamma_{2,m}^{14} \rangle) \right. \\
& + \sqrt{5-2\kappa} (\langle \Gamma_{2,m}^{23} \rangle - \langle \Gamma_{1,1}^4 \rangle) + \langle \Gamma_{1,1}^3 \rangle - \langle \Gamma_{2,m}^{11} \rangle + \sqrt{10-2\kappa} \langle \Gamma_{2,m}^{12} \rangle \\
& + 3 \langle \Gamma_{2,m}^{13} \rangle + \kappa \langle \Gamma_{2,m}^{22} \rangle - \kappa \langle \Gamma_{2,m}^{24} \rangle - \langle \Gamma_{2,m}^{33} \rangle - \sqrt{2}\sqrt{\kappa+5} \langle \Gamma_{2,m}^{34} \rangle \\
& \left. - \kappa \langle \Gamma_{2,m}^{44} \rangle + 1 \right]
\end{aligned} \tag{5.11}$$

here $\kappa = \sqrt{5}$. Substituting Eqs. Eq. 5.11 into 5.10, the full set of ten different chemical SRO parameters $\alpha_{(2,m)}^{pq}$ can be calculated using both point and pair correlation functions generated by the Monte-Carlo simulations with the ECIs. The numerical value of each of the cluster correlation functions are obtained from the cluster expansion of the Hamiltonian in combination with Monte Carlo simulations as a function of temperature. The resulting Warren-Cowley SRO parameters: $\alpha_{(2,m)}^{AB}, \alpha_{(2,m)}^{AC}, \dots, \alpha_{(2,m)}^{ED}$ as a function of alloy temperature for equimolar HEAs Mo-Nb-Ta-V-W will be analyzed in the next section.

5.4 Application High Entropy Alloy Mo-Nb-Ta-V-W

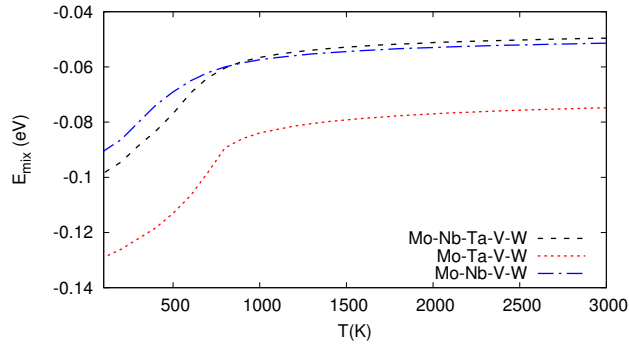
Using the effective cluster interactions (ECI) computed for quinary system Mo-Nb-Ta-V-W [240] the energetically favourable atomic configurations are investigated as a function temperature and alloy composition using quasi-canonical Monte-Carlo simulations. Fig. 5.1 shows the evolution of mixing enthalpy as a function of temperature from 3000 K for the equimolar quinary

Mo-Nb-Ta-V-W system as well as for the two quaternary sub-systems: Mo-Ta-V-W and W- Nb-V-W. These pre-melting configurations were generated by random numbers for the case of large systems whereas for the case of smaller simulation cell special quasi-random structures (SQSs) can be used [250]. Inflexion points from the temperature curve of enthalpy of mixing indicate order-disorder phase transformations from the solid solution phase into different non-random configurations. From Fig.5.1, at temperatures below 750 K, a partially ordered phase is thermodynamically more stable than the equimolar solid-solution random configuration. For the two sub-system alloys, it is found that the enthalpy of mixing for HEAs in the presence of Mo-Ta binaries, namely Mo-Ta-V-W, is significantly lower not only than the those for the Mo-Nb-V-W where Ta element is absent but also in a comparison with quinary Mo-Nb-Ta-V-W system.

The simulated structure of this alloy system is generated at T=400K and depicted in Fig. 5.2. Phase segregation or clustering of Nb (in green) around the edges of the atomic cell and V (in yellow) around the centre of the cell can be seen clearly from the presented configuration implying that there are no chemical attractive interactions between Nb and V atoms. The latter finding is consistent with our DFT calculations for bcc Nb-V alloy that the enthalpies of mixing for this binary are positive in all the composition range from our DFT calculations. On the contrary, the chemical ordering of Mo-Ta (red and blue) can be appreciated on the left-hand side face of the cubic cell that is in a full agreement with the strong negative enthalpy of mixing for the bcc binary Mo-Ta system. More detailed analysis of chemical SRO parameters will confirm the above observations.

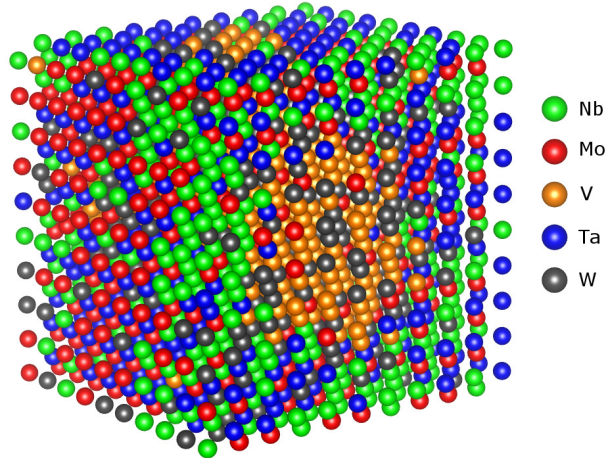
For the five-component alloy, the SRO formulation presented in the previous section can be applied to study order-disorder trends of the high-entropy Mo-Nb-Ta-V-W system as function composition and temperature. The temperature-dependent evolution of ten different SRO parameters for the

Fig. 5.1.: Enthalpy of mixing of the three equimolar HEAs: quinary Mo-Nb-Ta-V-W and quaternaries Mo-Ta-V-W, Mo-Nb-V-W, as a function of temperature



first nearest-neighbour (NN) shell for the equimolar composition is shown in Fig. 5.3. In the high-temperature limit, it can be seen clearly from Fig. 5.3 that all the SRO parameters trend to zero value corresponding to the presence of ideal randomly single phase of solid solution with the configuration entropy of mixing $\Delta S_{mix} = R \sum_p c_p \ln(c_p)$ where R is the gas constant). The latter expression is conventionally used in the definition of HEAs [12]. In the temperature region lower than 750K, from Fig. 5.3 it is found that the SRO parameter for Mo-Ta pair, $\alpha_{2,1}^{Mo-Ta}$, becomes the most negative one. This indicates a strong probability of having Ta atoms around a Mo atom in the first shell of the considered equimolar Mo-Ta-Ta-VW bcc alloy. The prediction of strong chemical SRO parameter for Mo-Ta pair is in a consistent agreement with the previous DFT study for the first nearest-neighbour Mo-Ta bonding interaction in the quaternary equimolar Mo-Nb-Ta-W system [248] and the present study of DFT database for the negative enthalpy of mixing in bcc binary Mo-Ta system. The next and strong negative SRO parameter has been predicted for V-W pair from our MC simulation and it is followed by the SRO parameter for Mo-Nb pair. Note that the negative SRO parameters for Mo-Ta, V-W and Mo-Nb are in agreement with the energetical phase stability trend of bcc binary systems between groups V and VI from the periodic table of elements [251]. It is interesting to find from Fig.5.3 that the SRO parameter for Mo-Nb pair becomes positive at very low temperature showing that there is competition between Nb and Ta atoms to occupy the first nearest-neighbour shell surrounding Mo atom in the five-component alloy. At low-temperature

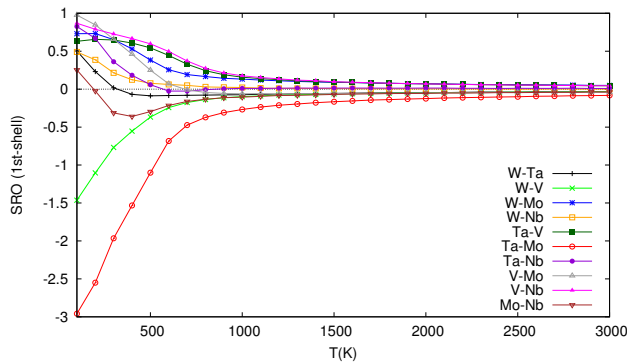
Fig. 5.2.: Atomistic configuration for equimolar Mo-Nb-V-Ta-W HEAs obtained from the present MC simulations at 400 K



region, there is a strong tendency of segregation with the positive values of $\alpha_{2,1}^{NbV}$, $\alpha_{2,1}^{MoW}$, and $\alpha_{2,1}^{TaV}$ namely for SRO parameters of the pairs between elements of the same groups V or VI.

Having said that it is worth mentioning here that the behaviour of first nearest-neighbour SRO parameter in the multi-component bcc-HEAs is much more complex than those predicted from the related binary system. For example, interpretation of the favourable V-W and unfavourable Ta-W 1NN chemical bonding obtained from Fig. 5.3 for the negative $\alpha_{2,1}^{VW}$ and positive $\alpha_{2,1}^{TaW}$ value, respectively, at very low temperature seems to be quite different to those predicted by the DFT calculations of the ground-state structure of B32 for V-W and B23 for Ta-W binary systems at equimolar composition [252]. It is known that the 1NN environment in B32 structure is not fully favourable for the chemical interaction in a comparison with those in the B2 or B23 structure. It is also important to emphasize again that the present study provides atomistic configurations which have been generated from a set of ECIs which include not only pair-wise interactions but also the triple effective cluster-expansion contributions in Eq. 5.9. This means that the enthalpy of mixing for five-component system Mo-Nb-V-Ta-W and therefore the configuration entropy as well as the free energy of mixing are certainly

Fig. 5.3.: Evolution of 1NN short-range-order parameters in equimolar HEAs Mo-Nb-Ta-V-W as a function temperature



determined beyond the simple Ising model with first nearest-neighbour interaction parameter from the ten constituent binary systems. It can be seen from Fig. 5.3 that the SRO parameters $\alpha_{2,1}^{TaW}$, $\alpha_{2,1}^{NbW}$, and $\alpha_{2,1}^{MoV}$ are positive whereas the enthalpy of mixing for the corresponding binaries are negative but smaller than those of the dominant Mo-Ta binary alloys. The complex behaviour of the interplay between the ten SRO parameters as a function of temperature can be explained by the many-body effects of cluster interactions in stabilizing the multi-component HEAs.

In order to cross-check the consistency of SRO expressions for the five component system, in particular, the competition between transition metal elements Nb and Ta from group V in the quinary Mo-Nb-Ta-V-W, the SRO parameters for the equimolar and quaternary sub-systems Mo-Ta-V-W and Mo-Nb-V-W are calculated and depicted in Fig. 5.4 and Fig. 5.5, respectively. Mathematical derivation of the SRO parameters for a quaternary system (A-B-C-D) is carried out by inverting formulas for the correlation functions to get the average pair probabilities (see Eq.10) in a similar fashion as for the five component system.

For a four-component system the explicit results in $\alpha_{2,m}^{AB}, \alpha_{2,m}^{AC}, \dots, \alpha_{2,m}^{CD}$ are as follows:

$$\begin{aligned}
\alpha_{2,m}^{AB} &= 1 - \frac{-2(\langle \Gamma_{1,1}^1 \rangle + \langle \Gamma_{1,1}^2 \rangle - 2\langle \Gamma_{2,m}^{12} \rangle + \langle \Gamma_{2,m}^{13} \rangle - \langle \Gamma_{2,m}^{23} \rangle) - \langle \Gamma_{2,m}^{33} \rangle + 1}{(-2\langle \Gamma_{1,1}^1 \rangle - \langle \Gamma_{1,1}^3 \rangle + 1)(-2\langle \Gamma_{1,1}^2 \rangle + \langle \Gamma_{1,1}^3 \rangle + 1)} \\
\alpha_{2,m}^{AC} &= 1 - \frac{-2\langle \Gamma_{1,1}^3 \rangle - 4\langle \Gamma_{2,m}^{11} \rangle + \langle \Gamma_{2,m}^{33} \rangle + 1}{(1 - \langle \Gamma_{1,1}^3 \rangle)^2 - 4(\langle \Gamma_{1,1}^1 \rangle)^2} \\
\alpha_{2,m}^{AD} &= 1 - \frac{-2(\langle \Gamma_{1,1}^1 \rangle - \langle \Gamma_{1,1}^2 \rangle + 2\langle \Gamma_{2,m}^{12} \rangle + \langle \Gamma_{2,m}^{13} \rangle + \langle \Gamma_{2,m}^{23} \rangle) - \langle \Gamma_{2,m}^{33} \rangle + 1}{(-2\langle \Gamma_{1,1}^1 \rangle - \langle \Gamma_{1,1}^3 \rangle + 1)(2\langle \Gamma_{1,1}^2 \rangle + \langle \Gamma_{1,1}^3 \rangle + 1)} \\
\alpha_{2,m}^{BC} &= 1 - \frac{2(\langle \Gamma_{1,1}^1 \rangle - \langle \Gamma_{1,1}^2 \rangle - 2\langle \Gamma_{2,m}^{12} \rangle + \langle \Gamma_{2,m}^{13} \rangle + \langle \Gamma_{2,m}^{23} \rangle) - \langle \Gamma_{2,m}^{33} \rangle + 1}{(2\langle \Gamma_{1,1}^1 \rangle - \langle \Gamma_{1,1}^3 \rangle + 1)(-2\langle \Gamma_{1,1}^2 \rangle + \langle \Gamma_{1,1}^3 \rangle + 1)} \\
\alpha_{2,m}^{BD} &= 1 - \frac{2\langle \Gamma_{1,1}^3 \rangle - 4\langle \Gamma_{2,m}^{22} \rangle + \langle \Gamma_{2,m}^{33} \rangle + 1}{(\langle \Gamma_{1,1}^3 \rangle + 1)^2 - 4(\langle \Gamma_{1,1}^2 \rangle)^2} \\
\alpha_{2,m}^{CD} &= 1 - \frac{2(\langle \Gamma_{1,1}^1 \rangle + \langle \Gamma_{1,1}^2 \rangle + 2\langle \Gamma_{2,m}^{12} \rangle + \langle \Gamma_{2,m}^{13} \rangle - \langle \Gamma_{2,m}^{23} \rangle) - \langle \Gamma_{2,m}^{33} \rangle + 1}{(2\langle \Gamma_{1,1}^1 \rangle - \langle \Gamma_{1,1}^3 \rangle + 1)(2\langle \Gamma_{1,1}^2 \rangle + \langle \Gamma_{1,1}^3 \rangle + 1)}
\end{aligned} \tag{5.12}$$

By using Eq.5.12, the evolution of six SRO parameters in equimolar Mo-Ta-V-W sub-system is represented in Fig. 5.4. It is found that the most favourable chemical bonding between the Mo-Ta and V-W pairs in this quaternary sub-system Fig. 5.3 are consistent with the results obtained for the corresponding SRO parameters in equimolar Mo-Nb-Ta-V-W system. Here the tendency of phase separation between Mo and W as well as Ta and V in the quaternary Mo-V-Ta-W alloy at the low-temperature region ($T < 750$ K) is also demonstrated by positive values of the corresponding parameters $\alpha_{2,1}^{MoW}, \alpha_{2,1}^{TaV}$. Again the SRO parameters $\alpha_{2,1}^{TaW}$ and $\alpha_{2,1}^{MoV}$ become also positive at the low temperature that is in agreement with the previous discussion for the quinary Mo-Nb-V-Ta-W alloys. Importantly, the opposite feature between 1NN SRO parameters $\alpha_{2,1}^{VW}$ and $\alpha_{2,1}^{TaW}$ in a comparison with those found in the ground state of B32 and B23 structure for VW and TaW binary, respectively, discussed previously in the quinary system remains the same in the quaternary Mo-Ta-V-W.

Fig. 5.4.: Dependence of 1NN short range order parameters for quaternary subsystem without Nb as a function of temperature

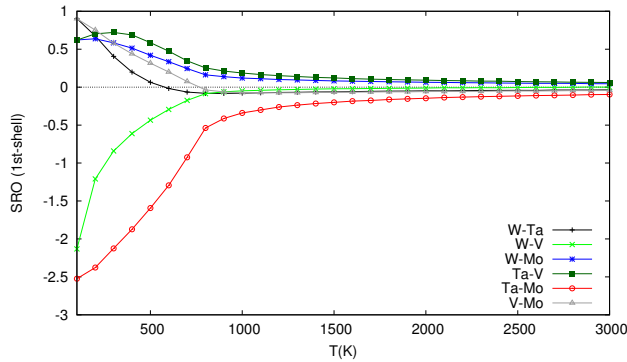
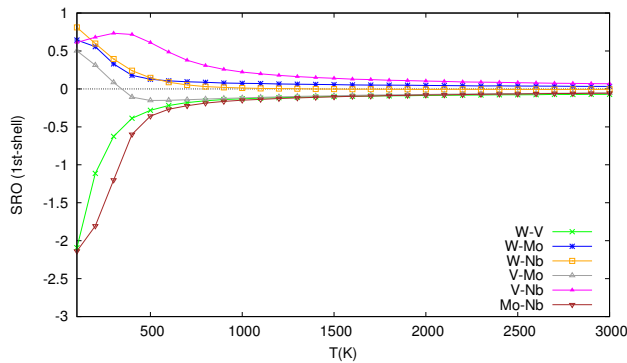


Fig. 5.5.: Dependence of 1NN short range order parameters for quaternary subsystem without Ta as a function of temperature



In the absence of Ta, the six SRO parameters in the quaternary Mo-Nb-V-W sub-system are represented in Fig. 5.5. The most interesting result from this figure is that the chemical SRO between Mo and Nb $\alpha_{2,1}^{MoNb}$ is now dominantly negative and in strong competition with $\alpha_{2,1}^{VW}$, instead of those for the Mo-Ta pair. This finding indicates the preferred ordering between the Mo-Nb pairs that are different behaviour in a comparison with quinary Mo-Nb-V-Ta-W and quaternary Mo-Ta-V-W alloys where it becomes positive at lower temperatures than 200K. On the other hand, the SRO for V-W pair is also negative as in previously considered cases for the quinary and the quaternary HEAs. Finally, the SRO parameter for Nb-V pair, $\alpha_{2,1}^{NbV}$, remains strongly positive for the quaternary Mo-Nb-V-W system in a consistent with its behaviour for the initial five-component alloy.

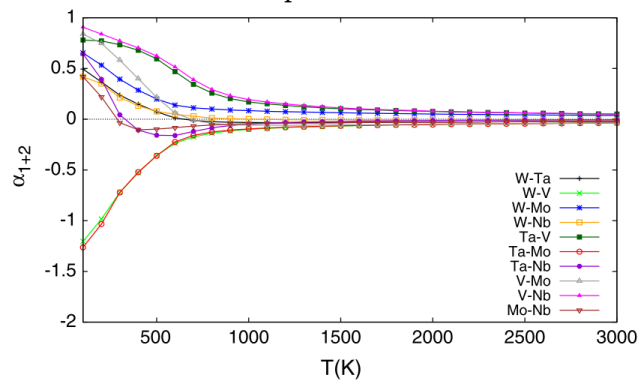
5.5 Second Nearest-Neighbor SRO Effects

Figs. 5.3, 5.4, and 5.5 represent SRO parameters in the first nearest-neighbor shell of the three considered HEAs. For a bcc alloy where the first and second NN distances are very close to each other, the average SRO parameter corresponding to the grouped shell of coordination $z_1 + z_2$ is defined as:

$$\alpha_{1+2}^{pq} = \frac{z_1\alpha_{2,1}^{pq} + z_2\alpha_{2,2}^{pq}}{z_1 + z_2} \quad (5.13)$$

where $z_1 = 8$ and $z_2 = 6$. Note that the average SRO parameter can be deduced experimentally with good confidence from diffuse-neutron scattering measurements [253]. Figs. 5.6, 5.7, and 5.8 show the dependence of all average SRO parameters calculated for the equimolar HEAs Mo-Nb-Ta-V-W, Mo-Ta-V-W and Mo-Nb-V-W, respectively. Comparing the results obtained from Fig. 5.6 for the average SRO parameters for both 1NN and 2NN, α_{1+2}^{pq} , with those presented in Fig. 5.3 for the first shell only, it is found a significant change in the SRO parameter for Mo-Ta pair in the quinary HEAs. The second NN contribution to SRO parameter for the Mo-Ta pair becomes positive and the resulting average SRO parameter, α_{1+2}^{MoTa} , is now reduced in the low-temperature region in a comparison with the 1NN SRO parameter, α_{1+2}^{MoTa} . This confirms that in equimolar Mo-Nb-Ta-V-W HEAs, the presence of the B2 phase where the 2NN shell contains only atoms of the same chemical species for Mo-Mo or Ta-Ta pairs are very favourable from the short-range order consideration. A similar reduction in average SRO parameter for the Mo-Ta pair is also consistently predicted in the quaternary alloys without the presence of Nb element (see Fig. 5.7).

Fig. 5.6.: Dependence of the average short-range-order parameters for quinary system as a function of temperature



Another interesting result found by comparing Figs. 5.6 and 5.3 is that when the 2NN contribution is taken into consideration, the average SRO parameters for the V-W pair become more dominant and comparable with the corresponding values for Mo-W. By analyzing separately the contributions from the 1NN and 2NN, it is found that the 2NN SRO parameter α_{1+2}^{VW} for V-W pair is negative in a large range of temperatures and only becomes positive at very low temperatures smaller than 100K. Therefore unlike Mo-Ta binary, the formation of B2-like phase for V-W bcc-binary systems in the considered quinary HEA system is only favourable at the low-temperature phase transition. For temperatures higher than 100K the negative value of the SRO parameter indicates the presence of unlike V-W pairs in the 2NN. The latter finding seems to support the local chemical environment of the ordered B32 phase which is the ground-state structure predicted by DFT calculations in the equimolar binary system [252]. A similar analysis for average SRO parameter for V-W pair in the two quaternary sub-systems without Nb and Ta (see Fig. 5.7 and 5.8, respectively) shows that the phase transition from the ordered-like B32 configuration to B2-like structure occurs at the temperatures smaller than 200K.

Finally, by including the 2NN effects, the average SRO α_{1+2}^{TaV} for Ta-V (see Fig. 5.7) and α_{1+2}^{NbV} – for Nb-V pair (see Fig. 5.8) are now clearly positive at the very low-temperature region of quaternary HEAs Mo-Ta-V-W and Mo-Nb-

Fig. 5.7.: Dependence of the average short-range-order parameters for quaternary subsystem without Nb as a function of temperature

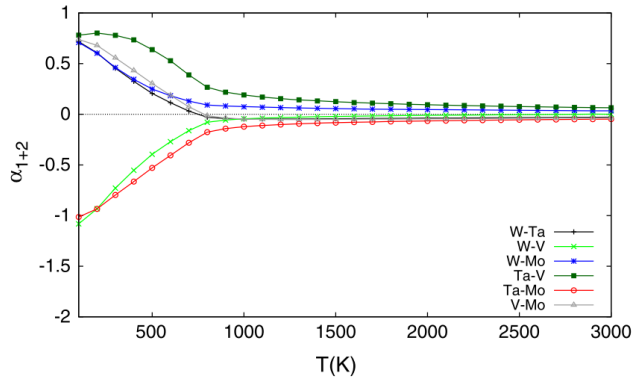
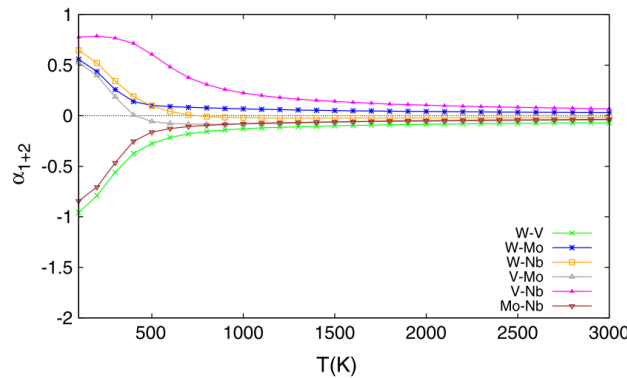


Fig. 5.8.: Dependence of average short-range-order parameters for quaternary subsystem without Ta as a function of temperature



V-W, respectively. Both of these SRO parameters remain strongly positive in quinary Mo-Nb-Ta-V-W system (see (6)) showing the segregation trend between Ta and V as well as between Nb and V. This predicted trend is consistent with atomic configuration visualized in Fig. 5.2

5.6 Conclusion

A theoretical formulation for the Warren–Cowley short-range order parameters has been systematically developed for the five and four-component alloy systems. Their analytical expressions are written in terms of correlation functions which can be computed from many-body cluster-expansion Hamiltonian in a combination with Monte Carlo simulations using ECIs. As an application

of the formulation, the dependence of SRO as a function of temperature has been analyzed consistently for the equimolar quinary Mo-Nb-Ta-V-W and two of its quaternary sub-systems (Mo-Nb-V-W and Mo-Ta-V-W) in bcc lattice. It is found that below temperatures of 750 K there is an order-disorder phase transition from the high-temperature limit of ideal solutions to a non-random distribution of different chemical species where the excess of configuration entropy terms come from non-zero values of SRO parameters. In general, the SRO exists in HEAs structures that show a preference of a particular pair of atoms to occur as first neighbours. In the present study, a strong negative SRO parameter has been predicted for Mo-Ta pair in quinary Mo-Nb-Ta-V-W and quaternary Mo-Ta-V-W HEAs. The origin of this phenomenon comes from the negative enthalpy of mixing and therefore the effective first-nearest neighbour interaction between Mo and Ta in the bcc binary system in our DFT database calculations for the CE Hamiltonian. It is also in an agreement with previous ab-initio analysis for the phase transition between the disordered (A2) to the ordered (B2) phases [248] as well as electronic structure calculations for the quaternary Mo-Nb-Ta-W system [254]. For the case of quaternary Mo-Nb-V-W HEAs where there are no Ta atoms, it is found that the chemical preference for a Mo-Nb pair becomes dominant in the first nearest neighbour and therefore its SRO is strongly negative at low temperature. For all the three considered HEAs, the chemical SRO parameter for W and V pair is also predicted to be strongly negative and consistently preferable in the first neighbour of the bcc lattice. It is important to note that the values of three SRO parameters, $\alpha_{2,1}^{MoTa}$; $\alpha_{2,1}^{MoNb}$; $\alpha_{2,1}^{WV}$, represent the chemical bonding of transition metals between the group V and VI in the periodic table of elements and their negative values can be understood from the analysis of mixing enthalpy in the corresponding binary systems.

The analytically calculated Warren–Cowley SRO parameters for other pairs in the equimolar quinary and quaternary systems are positive at low temperature showing different degrees of phase segregation between them in first nearest

neighbours. While the positive values of $\alpha_{2,1}^{MoW}$; $\alpha_{2,1}^{NbTa}$; $\alpha_{2,1}^{NbV}$ and $\alpha_{2,1}^{TaV}$ can be explained from the fact that thermodynamically the chemical bonding is not favourable for bcc binary between transition metal elements from the same group V or VI, the separation between Nb-W, Ta-W and Mo-V pairs in HEAs are not directly related to the mixing enthalpy values of their binaries. The complex trend of SRO parameters in multi-component alloys, therefore, can only be explained from the cluster-expansion Hamiltonian model which goes beyond the nearest-neighbour pair-wise approximation in the present study.

A further investigation of SRO parameters by including the 2NN shell in bcc alloys confirms the formation of favourable B2 phase for the Mo-Ta binaries in both quinary and quaternary systems. The investigation for the V-W pair shows that the average SRO parameter becomes comparably negative to those for Mo-Ta pair. The formation of B2-like, where the 1NN and 2NN SRO parameters have the opposite signs, is only favourable for the V-W in the considered HEAs at very the low temperatures, namely lower than 100 K for the quinary and 200 K for the quaternary systems. At higher temperatures, both 1NN and 2NN SRO parameters for V-W pair are found to be negative indicating a similar local environment of the ground-state B32 phase which has been predicted previously in the corresponding bcc binary system. The average SRO parameters for both 1NN and 2NN pairs confirm a clear trend of segregation between Nb and V (or Ta and V) elements from the group V of bcc transition metal series.

Finally, it is noted that the SRO phenomenon considered in this work describes the degree of local deviation from the average on a local scale in term of chemical occupation. The off-lattice expansion effect at elevated temperatures on atomic configurations has not been properly taking into account in the present Monte-Carlo simulations on a rigid lattice. A hybrid Monte-Carlo/Molecular Dynamic simulation would certainly help to overcome this

problem by investigating SRO via partial radial distribution functions [248]. There is, however, a limitation to perform the ab-initio molecular dynamic technique for a large atomic cell whereas for classical molecular dynamics simulation there is still a great challenge to find accurate interatomic potentials for multicomponent alloy system [255]. The displacive deviation due to atomic size effects is not considered here although a generalized theory of SRO from first-principles calculations can be taken into account [240, 256, 257]. In particular, as it has been shown in our previous study [240] that the lattice distortion produced by the interaction of the different atomic species in Mo-Nb-Ta-V-W alloys can be evaluated accurately with mean error in predicted atomic coordinates within the order of 1-2 pm in a comparison with fully related DFT calculations over all compositions and temperatures considered. It would be very desirable to compare the present theoretical data for SRO in Mo-Nb-Ta-V-W with a detailed experimentally detectable analysis of local chemical order, for example, from neutron diffraction experiment first produced in reference [258].

5.7 Acknowledgements

This work has been carried out within the framework of the EUROfusion Consortium and has received funding from the Euratom research and training programme 2014-2018 under Grant Agreement No. 633053 and funding from the RCUK Energy Programme [Grant Number EP/P012450/1]. The views and opinions expressed herein do not necessarily reflect those of the European Commission. AFC acknowledges financial support from EPSRC (EP/ L01680X/1) through the Materials for Demanding Environments Centre for Doctoral Training. JSW acknowledges the financial support from the Foundation of Polish Science grant HOMING (No. Homing/2016-1/12). The HOMING programme is co-financed by the European Union under the European Regional Development Fund. The simulations were partially carried

out by JSW with the support of the Interdisciplinary Centre for Mathematical and Computational Modelling (ICM), University of Warsaw, under grant no GA65-14. DNM would like to acknowledge the support from Marconi-Fusion, the High-Performance Computer at the CINECA headquarters in Bologna (Italy) for its provision of supercomputer resources.

Configurational Entropy in Multicomponent Alloys: Matrix Formulation from ab initio based Hamiltonian and Application to FCC Cr-Fe-Mn-Ni Alloys

The complete author list for the published paper is provided in Chapter 1

Purpose of the paper and contributions from the authors

The purpose of this chapter is to generalize the formulation found in the previous chapter 5 for multi-body probabilities which can hint at the precipitation of equilibrium structures consisting on more than require more than 2 lattice sites that SRO employs. These multi-body probabilities are also used to compute temperature-dependent configuration entropies, this is done to complement another methodology to evaluate configuration entropy, namely the thermodynamic integration, that generally is more computationally demanding due to the need to evaluate thermodynamic equilibrium configurations in a finer temperature grid. The general formalism is applied

in particular to the FCC Cr-Fe-Mn-Ni to show that $L1_2\text{CrFe}_3$ and $L1_0\text{-MnNi}$ are particularly stable at low temperatures.

Antonio Fernandez-Caballero and Duc Nguyen-Manh conceived the idea. Antonio Fernandez-Caballero developed the theoretical formalism and applied the formulation to the CrFeMnNi system. Antonio Fernandez-Caballero wrote the manuscript, and Duc Nguyen-Manh and Jan Wróbel and Paul Mummery reviewed it and contributed to check English. Mark Fedorov and Jan Wróbel provided the calculations of DFT-based semi canonical Monte Carlo simulations for the CrFeMnNi system. All the authors made comments on the final version before its submission.

This chapter is a verbatim copy of the publication: A. Fernández-Caballero, M. Fedorov, J. Wróbel, P. Mummery, and D. Nguyen-Manh, Entropy 21, 68 (2019). (Feature paper in Special Issue on New Advances in High-Entropy Alloys)

Abstract

Configuration entropy is believed to stabilize disordered solid solution phases in multicomponent systems at elevated temperatures over intermetallic compounds by lowering the Gibbs free energy. Traditionally the increment of configuration entropy with temperature was computed by time-consuming thermodynamic integration methods. In this work, a new formalism based on a hybrid combination of the Cluster Expansion (CE) Hamiltonian and Monte Carlo simulations is developed to predict the configuration entropy as a function of temperature from multi-body cluster probability in a multi-component system with arbitrary average composition. The multi-body probabilities are worked out by explicit inversion and direct product of a matrix formulation within orthonormal sets of point functions in the clus-

ters obtained from symmetry independent correlation functions. The matrix quantities are determined from semi canonical Monte Carlo simulations with Effective Cluster Interactions (ECIs) derived from Density Functional Theory (DFT) calculations. The formalism is applied to analyze the four-body cluster probabilities for the quaternary system Cr-Fe-Mn-Ni as a function of temperature and alloy concentration. It is shown that for two specific compositions ($\text{Cr}_{25}\text{Fe}_{25}\text{Mn}_{25}\text{Ni}_{25}$ and $\text{Cr}_{18}\text{Fe}_{27}\text{Mn}_{27}\text{Ni}_{28}$) the high value of probabilities for Cr-Fe-Fe-Fe and Mn-Mn-Ni-Ni are strongly correlated with the presence of the ordered phases $\text{L}1_2\text{-CrFe}_3$ and $\text{L}1_0\text{-MnNi}$, respectively. These results are in an excellent agreement with predictions of these ground-state structures by ab-initio calculations. The general formalism is used to investigate the configuration entropy as a function of temperature and for 285 different alloy compositions. It is found that our matrix formulation of cluster probabilities provides an efficient tool to compute configuration entropy in multi-component alloys in a comparison with the result obtained by the thermodynamic integration method. At high temperatures, it is shown that many-body cluster correlations still play an important role in understanding the configuration entropy before reaching the solid solution limit of high-entropy alloys (HEAs).

6.1 Introduction

Multicomponent systems, termed as High Entropy Alloys (HEAs), are crystalline solids that form predominantly in a single phase. These systems were brought to wider attention through the work of Cantor et al [156] and Yeh et al [11]. At or near the equiatomic ratio of compositions the configuration entropy is maximized and given by the formula $S_{config}/R = \ln K$ where R the ideal gas constant, and K the total number of different components. It has been proposed to define $K = 4$ as the minimum number of components

at or near equiatomic composition for these systems to be called HEAs [15, 259, 147].

There are various sources of entropy in a system in addition to configuration entropy including vibration, electronic and magnetic contributions. The co-existence of multiple phases in the equilibrium state of a chemical system with a given overall composition at a specified temperature is found by minimizing the Gibbs free energy of the whole system. When the system undergoes a phase transition of either order-disorder or spinodal decomposition, the relative differences of configurational entropy are dominant in comparison to those contributions from vibration and magnetic terms in FeCoCrNi [260] where the relative difference of configuration entropy dominates or is of similar magnitude to vibration entropy. These multicomponent alloys have transition metals Co, Cr, Fe, and Ni that exhibit magnetic behaviour and have magnetic phase transitions characterized by Curie temperatures sensitive to concentrations [238].

In general, the formulation of configuration entropy given by the expression $S_{config}/R = \ln K$ only holds for disordered alloys with equiatomic composition at temperatures near their melting point (See appendix B for a derivation of this formula under the assumption of the ergodic hypothesis in statistical physics). On the other hand at low temperatures, the lowest free energy structures can be ordered intermetallic phases or partially ordered structures. In the intermediate temperature range, there exists short-range order, which is related to the nature of the chemical environment of each atomic species, containing ordering or segregation preferences especially at low temperatures, because random disordering is favoured at the high temperatures. The importance of short-range order (SRO) was manifested in diffuse X-ray scattering measurements of alloys containing ordered superstructure domains. The SRO effect is also seen to significantly affect electrical resistivity properties [261, 262], and to influence the alloy strength by hindering dislocation

motion [263] in concentrated alloys. Recently, it has been demonstrated how short-range order can be predicted from ab initio based Hamiltonian in combination with Monte Carlo simulations [96] in multi-component Mo-Nb-Ta-V-W systems. The study predicted that a strong SRO parameter may lead to the formation of Mo-Ta ordering in the B2 structure after quenching down from temperatures as high as 3,000 K. HEAs such as $\text{Al}_{1.3}\text{CoCrCuFeNi}$ have been reported to be susceptible to complex phase transitions including segregation, precipitation, chemical ordering and spinodal decomposition into a complex microstructure containing regions of BCC, FCC and B2 phases [242]. Physical models have been successfully applied to predict the formation of these phases based on the average number of valence electrons [91].

The prediction of equilibrium thermodynamic properties (free energies, and phase diagrams) is one of the goals of computational materials science. Lattice statistical models involving an Ising-like Hamiltonian developed from ab initio enthalpies of mixing have become an important tool in the computation of the thermodynamic properties of alloy systems. In particular, the cluster expansion method [264, 265, 184] expands the Hamiltonian into contributions from an optimized set of clusters, each term weighted by Effective Cluster Interactions. The thermodynamic properties at temperature are obtained from the ECIs by computing the free energies from semi-canonical Monte Carlo simulations in a combination with thermodynamic integration technique [245].

The CVM formalism [266, 196] expresses the free energy in terms of enthalpies of mixing and configuration entropies as a function of the temperature dependence for a specific set of clusters by minimizing the free energy from variational principles. The correlation function parameters in terms of which configuration entropy and enthalpy of mixing are expressed grow exponentially with the component number K and the size of the maximal cluster ω . Due to this, the CVM has been commonly applied to clusters consisting of

four sites in a regular tetrahedron or the so-called tetrahedron-octahedron in the FCC lattice [267, 268], or the four sites in an irregular tetrahedron in the BCC lattice [269]. Within the tetrahedron approximation, the CVM calculations for the FCC involve the empty lattice, isolated points, first nearest neighbour pair, triangle and tetrahedron [267]. It is generally accepted that the integrated Monte Carlo method is more accurate, but the calculations are time-consuming due to the need for many passes to obtain free energies at any given temperature from the disordered high-temperature configuration. A hybrid approach taking the Monte Carlo calculated correlation functions at temperature and computing the configuration entropy value from analytic CVM expression has been used in a binary FCC lattice model[270]. It is shown that accurate free energy can be obtained for ordered and disordered phases at arbitrary chemical concentration and temperature without thermodynamic integration provided that use is made of high-order CVM entropy expressions. However, the clusters optimized from the CE method reported in the literature do not often match those used for the CVM. More importantly, calculations of the configuration entropy for multi-component systems represent a very serious challenge for computational materials science. In this work, we close this gap by developing a new methodology based on matrix formulation to calculate analytically the cluster probabilities for arbitrary K -component alloys from the correlation functions obtained by the hybrid Monte Carlo and CE Hamiltonian. We apply our method to the FCC four-component CrFeMnNi system for investigating configuration entropy as a function of temperature and alloy composition. Two specific compositions are chosen to illustrate the importance of many-body cluster probability functions in multicomponent systems. The first one is equiatomic composition $Cr_{25}Fe_{25}Mn_{25}Ni_{25}$ which is of great interest for the HEA community. The second one is $Cr_{18}Fe_{27}Mn_{27}Ni_{28}$ which has been used recently to design radiation-tolerant materials for advanced nuclear reactor systems. This alloy has been studied in preference to Cantor's one [156] due to the removal of

Co, which can cause activation by transmutation of ^{60}Co isotope in nuclear reactors [20].

This paper is organized as follows. In section 2, a new matrix formulation for a K-component system based on the orthonormal sets of cluster expansion initially introduced within the Alloy Theoretic Automated Toolkit (ATAT) program [265, 184] is presented. This formulation provides a rigorous link of cluster correlation functions obtained from Monte Carlo simulations with multi-body probabilities. The notation is developed to treat as general as possible arbitrary cluster sizes, ω , number of components, K , and temperature. In section 3, the hybrid method is illustrated to calculate four-body cluster probabilities as a function of temperature for the two specific compositions of equiatomic $\text{Cr}_{25}\text{Fe}_{25}\text{Mn}_{25}\text{Ni}_{25}$ and also the composition $\text{Cr}_{18}\text{Fe}_{27}\text{Mn}_{27}\text{Ni}_{18}$ from [20]. Here the connection with the tetrahedron approximation in CVM is discussed due to the presence of a first nearest-neighbour four-body cluster interaction within the investigated CE Hamiltonian. In section 4, configuration entropy is discussed at two temperatures between 1000 and 3000 K for different cluster decorations obtained from the CE method and compared with the integrated Monte Carlo results. The changes in configuration entropy are attributed to the presence of ordered phases that are more stable at low temperatures and the complementary tendency towards the disordered random solution of the alloy at the given average composition. The main conclusions of this work are given in section 5.

6.2 Methods

6.2.1 Matrix formulation of cluster expansion

Let us consider an alloy system with an arbitrary number, K , of components and crystalline lattice symmetry, in which the disordered phase is described by space group, G . The CE Hamiltonian at $T = 0$ K of the alloy can be found from enthalpies of mixing, $\Delta H_{DFT}^{Mixing}[\vec{\sigma}]$, of derivative alloy structures [189, 184] denoted by varying length arrays of spin-like variables $\vec{\sigma}_i$ taking values from 0 to $K - 1$. In general a derivative structure of the alloy has non-zero atomic concentrations for each of $p = 1, \dots, K$ different chemical elements forming it i.e. $x[\vec{\sigma}]_p \neq 0$. For each member structure, the reference energy in the calculation of the enthalpy of mixing is the pure element total energy, $E_{total}[p]$, with the same crystallographic symmetry. The alloy enthalpy of mixing is defined as follows:

$$\Delta H_{DFT}^{Mixing}[\vec{\sigma} \equiv \{\sigma_1, \sigma_2, \dots\}] = E_{total}[\vec{\sigma} \equiv \{\sigma_1, \sigma_2, \dots\}] - \sum_{p=1, \dots, K} x_p[\vec{\sigma}] E_{total}[p] \quad (6.1)$$

The enthalpies of mixing are calculated from the total energies $E_{total}[\vec{\sigma}]$ and $E_{total}[p]$ of alloy and pure element, respectively, by density functional theory for the underlying lattice. In the CE the $\Delta H_{DFT}^{mixing}[\vec{\sigma}]$ of an arbitrary structure $\vec{\sigma}$ is expanded into a sum of reference clusters, $\Delta H_{CE}^{Mixing}[\vec{\sigma}]$ and can be written in the following formula [265, 184, 245]:

$$\Delta H_{CE}^{Mixing}[\vec{\sigma} \equiv \{\sigma_1, \sigma_2, \dots\}] = \sum_{\omega, n, (s)} m_{\omega, n}^{(s)} J_{\omega, n}^{(s)} \langle \Gamma_{\omega', n'}^{(s')} [\vec{\sigma} \equiv \{\sigma_1, \sigma_2, \dots\}] \rangle_{\omega, n, (s)} \quad (6.2)$$

In Eq. 6.2 each reference cluster is characterized by three labels ω , n and (s) . The label ω denotes the total number sites; n is an auxiliary label that refers to highest order coordination shell contained in the reference cluster; and finally the label $(s) = (j_1, j_2, \dots, j_\omega)$, denotes decoration of the cluster by point functions with dimension equal to ω and j_i taking values $0, \dots, K - 1$. For each reference cluster, there is an associated effective cluster interaction $J_{\omega,n}^{(s)}$, and multiplicity per lattice site, $m_{\omega,n}^{(s)}$. The term $\langle \Gamma_{\omega',n'}^{(s')}[\vec{\sigma}] \rangle_{\omega,n,(s)}$ used in the definition of enthalpy of mixing in Eq. 6.2 is the thermally averaged cluster correlation function over all clusters $\omega', n', (s')$ which are equivalent to a space group symmetry element of the disordered phase within the reference decorated cluster defined by $\omega, n, (s)$. Overall the triple product of multiplicity, ECI and correlation function, $m_{\omega,n}^{(s)} J_{\omega,n}^{(s)} \langle \Gamma_{\omega',n'}^{(s')}[\vec{\sigma}] \rangle_{\omega,n,(s)}$ gives the energetic contribution per lattice site of the reference cluster ω, n and (s) to the enthalpy of mixing of the particular structure configuration given by $\vec{\sigma}$.

For multicomponent systems, the choice of a set of basis functions is important for the matrix formulation of the CE method [264]. The simplest set consists of the successive $K - 1$ powers of the pseudo-spin configuration variable $\{\sigma\}$ as was originally suggested by Taggart [271]. In this work, the correlation function is defined as the product of point functions initially proposed in the ATAT program [265, 184]. Configurational average of the correlation functions is then given by the following formula:

$$\begin{aligned} \langle \Gamma_{\omega',n'}^{(s')}[\vec{\sigma}] \rangle_{\omega,n,(s)} &= \langle \gamma_{j_1,K}[\sigma_1] \gamma_{j_2,K}[\sigma_2] \cdots \gamma_{j_\omega,K}[\sigma_\omega] \rangle \\ &= \frac{1}{\Omega[\omega, n]} \sum_{u=1}^{\Omega[\omega, n]} \gamma_{j_1,K}[\sigma_{\overrightarrow{(\omega,n)}_{u_1}}] \gamma_{j_2,K}[\sigma_{\overrightarrow{(\omega,n)}_{u_2}}] \cdots \gamma_{j_\omega,K}[\sigma_{\overrightarrow{(\omega,n)}_{u_\omega}}] \end{aligned} \quad (6.3)$$

where the point function is written as:

$$\gamma_{j,K}[\sigma_i] = \begin{cases} 1 & \text{if } j = 0, \\ -\cos\left(2\pi\lceil\frac{j}{2}\rceil\frac{\sigma_i}{K}\right) & \text{if } j > 0 \text{ and odd,} \\ -\sin\left(2\pi\lceil\frac{j}{2}\rceil\frac{\sigma_i}{K}\right) & \text{if } j > 0 \text{ and even,} \end{cases} \quad (6.4)$$

In Eq. 6.3 the correlation function of the system is averaged over the arbitrary crystal structure of the alloy system with configuration $\vec{\sigma}$ over all the set of $\Omega[\omega, n]$ clusters, $\{\overleftrightarrow{(\omega, n)_u}\}_{u=1,2,\dots,\Omega[\omega,n]}$ where each cluster labeled by u contains ω sites, each site denoted by the vector, $\overrightarrow{(\omega, n)}_{u_i}$. The i -union of the ω vectors, $\overrightarrow{(\omega, n)}_{u_i}$, composes the cluster of vectors, $(\overrightarrow{(\omega, n)}_{u_1}, \overrightarrow{(\omega, n)}_{u_2}, \dots, \overrightarrow{(\omega, n)}_{u_\omega}) \equiv \overleftrightarrow{(\omega, n)_u}$. The $u_1, u_2, \dots, u_\omega$ are numeric labels referring to the values taken by variable u in Eq. 6.3 that serve to enumerate the vectors making up the u cluster of vectors $\{\overleftrightarrow{(\omega, n)_u}\}$. The clusters $\overleftrightarrow{(\omega, n)_u}$ are symmetrically equivalent to the reference cluster (ω, n) sites by a symmetry operation and are enumerated by an index taking values $1, 2, \dots, \Omega[\omega, n]$. $\Omega[\omega, n]$ is defined as the number of times the reference cluster (ω, n) is contained in a structural configuration which can be obtained from Monte Carlo simulation. The sites in the cluster $\{\overleftrightarrow{(\omega, n)_u}\}$ can allocate all of the possible decoration values $\in (s)$ which we express as $(s) = (j_1, j_2, \dots, j_\omega)$. These integer indexes corresponding to the decorated cluster are parameters for the point functions in Eq. 6.4.

For an arbitrary ω -sites cluster and K components, the number of ω -tuples formed with integer entries running from $0 \dots K - 1$ can be calculated. For $\omega = 2$, the formula calculates the number of symmetrically unique decorations (s) for a two-point cluster $\langle \Gamma_{\omega',n'}^{(s')}[\vec{\sigma}'] \rangle_{\omega=2,n,(s)}$ and K component alloy system reduces to $(K + 1)K/2$ [96], where K is the number of components. For higher order clusters, the total number of decorations depend on the cluster coordinates and the space group symmetry G of the high temperature

disordered phase i.e. FCC or BCC and can not be simply expressed in terms of K (in general there could be less than $\binom{\omega+K-1}{K-1} = \frac{(\omega+K-1)!}{(K-1)!(\omega)!}$ number of symmetrically unique correlation functions). ATAT [265, 184] numerically works out all the number of symmetrically unique decorated clusters $\omega', n', (s')$ equivalent to $\omega, n, (s)$ and uses one correlation function per set of equivalent decorated clusters $\langle \Gamma_{\omega',n'}^{(s')}[\vec{\sigma}] \rangle_{\omega,n,(s')}$. For convenience in notation, from now on we will use $\langle \Gamma_{\omega,n}^{(s)}[\vec{\sigma}] \rangle = \langle \Gamma_{\omega',n'}^{(s')}[\vec{\sigma}] \rangle_{\omega,n,(s)}$. In general, two decorations (s) and (s') are symmetrically equivalent if there is at least one element in the space group symmetry $g \in G$ that transforms the sites $\{\vec{\tau}_1, \vec{\tau}_2, \dots, \vec{\tau}_\omega\} \subset (\omega, n)$ into $\{\vec{\tau}_{g[1]}, \vec{\tau}_{g[2]}, \dots, \vec{\tau}_{g[\omega]}\} \subset (\omega, n)$ as the permutation connecting the decorations $(s) = (1, 2, \dots, \omega) \subset \{(s)_{(\omega,n)}\}$ and $(s') = (g[1], g[2], \dots, g[\omega]) \subset \{(s)_{(\omega,n)}\}$. This is given by the following equation:

$$g\{\vec{\tau}_1, \vec{\tau}_2, \dots, \vec{\tau}_\omega\} = \{\vec{\tau}_{g[1]}, \vec{\tau}_{g[2]}, \dots, \vec{\tau}_{g[\omega]}\} \quad (6.5)$$

With the symmetry relations between decorations (s) and (s') in any given cluster, we are able to retrieve all K^ω possible ω -tuples from the set of unique symmetries corresponding to an ω cluster. The point functions $\gamma_{j,K}[\sigma_i]$ used to define the general correlation functions are related to the multi-body cluster probabilities (see below in Eq. 6.9) by direct products of a linear [182] transformation τ_K

$$(\tau_K)_{ji} \equiv \gamma_{j,K}[\sigma_i] \quad (6.6)$$

where the new matrix τ is constructed from these point functions, $\gamma_{j,K}[\sigma_i]$. It can be trivially shown that the inverse of Van der Monde matrices with complex entries equal to roots of unity, is its complex conjugate. The inverse of the τ_K matrix can be obtained from the complex conjugate matrix of τ_K

by taking the real and imaginary part and riffling their rows. From Eq. 6.4, the following expression results for a system with K components:

$$(\tau_K^{-1})_{ij} = \begin{cases} \frac{1}{K} & \text{if } j = 0, \\ -\frac{2}{K} \cos(2\pi \lceil \frac{j}{2} \rceil \frac{\sigma_i}{K}) & \text{if } j > 0 \text{ and } j < K - 1 \text{ and } j \text{ odd}, \\ -\frac{2}{K} \sin(2\pi \lceil \frac{j}{2} \rceil \frac{\sigma_i}{K}) & \text{if } j > 0 \text{ and } j \text{ even,} \\ -\frac{1}{K} \cos(2\pi \lceil \frac{j}{2} \rceil \frac{\sigma_i}{K}) & \text{if } j = K - 1 \text{ and } j \text{ odd,} \end{cases} \quad (6.7)$$

To the best of our knowledge, Eq. 6.7 represents a new formulation for the inverse of τ_K matrix to ensure that the basis set defined by Eq. 6.4 is rigorously orthonormal. The size of τ_K matrix is $K \times K$, where K is the number of components. It is convenient to perform the matrix multiplications with all K^ω decorations formed from ω -tuples with integer elements running from 0 to $K-1$. In particular, for the case of four component, $K = 4$ these matrices, τ become by applying Eqs. 6.4 and 6.7 for the inverse τ_K^{-1} :

$$\tau_4 = \begin{pmatrix} 1 & 1 & 1 & 1 \\ -1 & 0 & 1 & 0 \\ 0 & -1 & 0 & 1 \\ -1 & 1 & -1 & 1 \end{pmatrix} \quad \tau_4^{-1} = \frac{1}{4} \begin{pmatrix} 1 & -2 & 0 & -1 \\ 1 & 0 & -2 & 1 \\ 1 & 2 & 0 & -1 \\ 1 & 0 & 2 & 1 \end{pmatrix} \quad (6.8)$$

We duplicate the symmetrically unique decorations (s) whenever two decorations are connected by the symmetry of the disordered structure. For relating two equivalent decorations we find it convenient to use a permutation representation of the space group operator as permutations of ω -site tuples. We use the property of invariance of the cluster expansion to obtain probability distributions from correlation functions [191]. As a consequence

of the compact formalism and by using Eqs. 6.4 and 6.7, the expression of correlation functions can be rewritten into a matrix form:

$$\langle \Gamma_{\omega,n}^{(ij\dots)}[\vec{\sigma}] \rangle = \sum_{\forall[(pq\dots)]}^{K^\omega} \gamma_{i,K}[\vec{\sigma}_p] \gamma_{j,K}[\vec{\sigma}_q] \dots y_{\omega,n}^{(pq\dots)}[\vec{\sigma}] \equiv \overbrace{(\tau_K \otimes \dots \otimes \tau_K)}^{\omega}_{ij\dots, pq\dots} y_{\omega,n}^{(pq\dots)}[\vec{\sigma}] \quad (6.9)$$

With the aid of the matrix formulation from Eq. 6.9 and the generalized form of the inverse matrix τ_K^{-1} in Eq. 6.7, one can express the ω -cluster probabilities into a matrix form:

$$y_{\omega,n}^{(pq\dots)}[\vec{\sigma}] = \overbrace{(\tau_K^{-1} \otimes \dots \otimes \tau_K^{-1})}^{\omega}_{pq\dots, ij\dots} \langle \Gamma_{\omega,n}^{(ij\dots)}[\vec{\sigma}] \rangle \quad (6.10)$$

where we have used the notation for direct product of matrices $\overbrace{(\tau_K^{-1} \otimes \dots \otimes \tau_K^{-1})}^{\omega}_{pq\dots, ij\dots} = (\tau_K)_{p,i}(\tau_K)_{q,j} \dots$. And we also implied summation over repeated indexes on the right hand side of Eq. D.7. Note that the size of these matrices increases exponentially with cluster size ω , $K^\omega \times K^\omega$; in particular for $\omega = 4$ the matrices have 256x256 entries. The cluster probabilities are normalized as expressed in Eq. 6.11

$$\sum_{\forall[(pq\dots)]}^{K^\omega} y_{\omega,n}^{(pq\dots)}[\vec{\sigma}] = 1 \quad (6.11)$$

As a consequence of the normalization of the cluster probabilities, it is possible to separate probabilities of the decorated sub-clusters from the probabilities of the maximal cluster by partial summations over all possible decorations for

the sites that belong to the maximal cluster ω, n but not the i -th sub-cluster ω_i, n_i .

$$\sum_{(pq\cdots) \in \{(pq\cdots)_{\omega_i, n_i}\}} y_{\omega_i, n_i}^{(pq\cdots)}[\vec{\sigma}] = y_{\omega, n}^{(pq\cdots)}[\vec{\sigma}] \quad (6.12)$$

From Eq. D.7 and for the case with $\omega=2$, it follows that the generalized expression for SRO of species p and q at the n th shell, $\alpha_{2,n}^{(pq)}[\vec{\sigma}] (p \neq q)$, can be interpreted as the tendency to order or segregate species p and q with respect the disordered random probability given by the product of their elemental, p , bulk concentration $x_p[\vec{\sigma}]$. For the four component Cr-Fe-Mn-Ni system, there are 6 chemically distinct SRO parameters: $\alpha_{2,n}^{(01)}[\vec{\sigma}]$ for Cr-Fe; $\alpha_{2,n}^{(02)}[\vec{\sigma}]$ for Cr-Mn; $\alpha_{2,n}^{(03)}[\vec{\sigma}]$ for Cr-Ni; $\alpha_{2,n}^{(12)}[\vec{\sigma}]$ for Fe-Mn; $\alpha_{2,n}^{(13)}[\vec{\sigma}]$ for Fe-Ni; and $\alpha_{2,n}^{(23)}[\vec{\sigma}]$ for Mn-Ni. The SRO allows a quantitative description of the interactions between atoms as a function of temperature to predict order-disorder transition temperatures [251, 96]. In particular the matrix formalism from Eqs. 6.7 and D.7 allows one to generalize the SRO treatment for an arbitrary number of components, K :

$$y_{2,n}^{(pq)}[\vec{\sigma}] = x_p[\vec{\sigma}]x_q[\vec{\sigma}] (1 - \alpha_{2,n}^{(pq)}[\vec{\sigma}]) \quad (6.13)$$

6.2.2 Configuration entropy in the matrix formulation

In general, a thermodynamical system in state $\vec{\sigma}$ and with enthalpy of mixing given by the CE Hamiltonian $\Delta H_{CE}^{Mixing}[\vec{\sigma}]$ is described by a set of symmetry unique probability distributions $y_{\omega, n}^{(pq\cdots)}[\vec{\sigma}]$ characterized by decorations of a chosen maximal ω, n cluster. In practice the chosen maximal cluster ω, n

contains few points. As a mean field approximation [182], the CVM can be rationalized as a factorization of the probability distributions of the ω, n maximal cluster into integer powers $\eta_{\omega_1, n_1}, \eta_{\omega_2, n_2} \dots, \eta_{\omega_s[\omega, n], n_s[\omega, n]}$ of the probability distributions of the sub-clusters $(\omega_i, n_i) \subseteq (\omega, n); i = 1, \dots, [\omega, n]$ [196] with decorations $(pq \dots)_{\omega_i, n_i}$ corresponding to the components $(pq \dots)_{\omega_i, n_i}$ of all decorations $(pq \dots) \in \{(pq \dots)_{(\omega, n)}\}$ occupied by sites of the ω_i, n_i sub-cluster

$$y_{\omega, n}^{(pq \dots)}[\vec{\sigma}] = (y_{\omega_1, n_1}^{(pq \dots)_{\omega_1, n_1}}[\vec{\sigma}])^{\eta_{\omega_1, n_1}} (y_{\omega_2, n_2}^{(pq \dots)_{\omega_2, n_2}}[\vec{\sigma}])^{\eta_{\omega_2, n_2}} \dots (y_{\omega_s[\omega, n], n_s[\omega, n]}^{(pq \dots)_{\omega_s[\omega, n], n_s[\omega, n]}}[\vec{\sigma}])^{\eta_{\omega_s[\omega, n], n_s[\omega, n]}} \quad (6.14)$$

The following expression, a consequence of the CVM factorization scheme, can be derived from [196] and is the reason why the disordered configuration at high temperature is reproduced from multi-body probabilities $\sum_{i=1}^{[\omega, n]} \omega_i \eta_{\omega_i, n_i} = -1$. This occurs because at the high-temperature limit the CVM probabilities tend to products of the composition of the species involved in the decorations of the cluster:

$$y_{\omega_i, n_i}^{(pq \dots)_{\omega_i, n_i}}[\vec{\sigma}] \xrightarrow{T \rightarrow \infty} \prod_{j=1}^{\omega_i} y_{1,1}^{((pq \dots)_j)_{\omega_i, n_i}}[\vec{\sigma}] = \prod_{j=1}^{\omega_i} x_{((pq \dots)_j)_{\omega_i, n_i}}[\vec{\sigma}] \quad (6.15)$$

where $y_{1,1}^{((pq \dots)_j)_{\omega_i, n_i}}[\vec{\sigma}] = x_{((pq \dots)_j)_{\omega_i, n_i}}[\vec{\sigma}]$ is the concentration of the $(pq \dots)_j$ equal to one of the integers $0, 1, \dots, K - 1$ in the disordered state of the alloy. A natural consequence of the factorization scheme chosen for the

CVM multi-body probabilities is that the configuration entropy assumes the formulation

$$S_{\omega,n}[\vec{\sigma}] \equiv \sum_{i=1}^{s[\omega,n]} \eta_{\omega_i,n_i} \tilde{S}_{\omega_i,n_i}[\vec{\sigma}] = \sum_{i=1}^{s[\omega,n]} \eta_{\omega_i,n_i} \sum_{\forall[(pq\dots)_{\omega_i,n_i}]}^{K^{\omega_i}} k_B y_{\omega_i,n_i}^{(pq\dots)_{\omega_i,n_i}}[\vec{\sigma}] \ln(y_{\omega_i,n_i}^{(pq\dots)_{\omega_i,n_i}}[\vec{\sigma}]) \quad (6.16)$$

where \tilde{S}_{ω_i,n_i} , is the entropy contribution to cluster (ω, n) from the sub-cluster (ω_i, n_i) :

$$\tilde{S}_{\omega_i,n_i}[\vec{\sigma}] = \sum_{\forall(pq\dots)_{\omega_i,n_i}}^{K^{\omega_i}} k_B y_{\omega_i,n_i}^{(pq\dots)_{\omega_i,n_i}}[\vec{\sigma}] \ln(y_{\omega_i,n_i}^{(pq\dots)_{\omega_i,n_i}}[\vec{\sigma}]) \quad (6.17)$$

The set of integers $\eta_{\omega_1,n_1}, \eta_{\omega_2,n_2}, \dots, \eta_{\omega_{s[\omega,n]},n_{s[\omega,n]}}$ are the mean field integer coefficients associated with the partition function of the alloy system. In the theory of regular mixtures, the coefficients can be found from the recursive heuristic expression after Kikuchi, [195], Barker [197] and whose formulation was explicitly derived by using group theoretic methods by Gratias et al. [272]. It requires the determination of two quantities: the site multiplicity N_{ω_i,n_i} and the sub-cluster multiplicity N_{ω_i,n_i}^β . The site multiplicity can be determined by calculating the number of symmetry operators, $\mathcal{N}_{\omega_i,n_i}$, that stabilize the ω_i, n_i cluster i.e. $g \in G$ such that the application of g into the set of cluster positions $\{\vec{\tau}_1, \vec{\tau}_2, \dots, \vec{\tau}_\omega\}$ results in a permutation of the set. Then $N_{\omega_i,n_i} = \frac{|G|}{|\mathcal{N}_{\omega_i,n_i}|}$ where $|G|$ is the order of the point group associated to the space group G and $|\mathcal{N}_{\omega_i,n_i}|$ is the order of the group $\mathcal{N}_{\omega_i,n_i}$. The sub-cluster

multiplicity N_{ω_i, n_i}^β is just the frequency of the cluster β that is contained in the cluster ω_i, n_i

$$\eta_{\omega_i, n_i} = -N_{\omega_i, n_i} - \sum_{(\omega_i, n_i) \subset \beta \subseteq (\omega, n)} N_{\omega_i, n_i}^\beta \eta_\beta \quad (6.18)$$

In particular the formulation applied to a point cluster retrieves the Bragg-Williams approximation for the maximal cluster ($\omega = 1, n = 1$), i.e a site cluster, giving the entropy weight of $\eta_{\omega_1=1, n_1=1} = -1$ and for a two body cluster ($\omega = 2, n$) in the n^{th} coordination shell, we get $\eta_{\omega_2, n_2} = -N_{2,n}$ and $\eta_{\omega_1, n_1} = 2N_{2,n} - 1$, where $N_{2,n}$ is site multiplicity of the cluster $(2, n)$ calculated from the sites in this cluster and the space group G .

In this work, the above matrix formulation is applied in the hybrid CE-Monte Carlo method which performs the free energy minimization from the CE Hamiltonian in a combination with Monte Carlo simulations. Within the process, the Monte Carlo method produces the correlation functions for the equilibrium configurations found at each of the temperatures investigated. The hybrid approach uses these correlation functions in the analytic expressions for configuration entropy.

There is an alternative to the hybrid approach for the entropy calculation where the thermodynamic integration method can be used. Here entropy is calculated from the configuration contribution to the specific heat at constant volume, C_{conf} derived from the fluctuations of enthalpy of mixing at temperature values in a fine grid of temperature values:

$$S_{conf}[T] = \int_0^T \frac{C_{conf}}{T'} dT' = \int_0^T \frac{\langle \Delta H_{CE}^{Mixing} \rangle^2 - \langle \Delta H_{CE}^{Mixing} \rangle^2}{T'^3} dT' \quad (6.19)$$

where $\langle \Delta H_{CE}^{Mixing} \rangle^2$ and $\langle \Delta H_{CE}^{Mixing^2} \rangle$ are the square of the mean and mean square enthalpies of mixing, respectively, calculated by averaging over all the MC steps at the accumulation stage for a given temperature. The accuracy of the evaluation of configuration entropy depends on the size of the temperature integration step and the number of MC steps performed at the accumulation stage [273]. The integration of specific heat is performed from 0 K to the temperature T . To calculate the configuration entropy at a given temperature the value for specific heats at lower temperatures is thus required. For example, assuming that the chosen temperature step is equal to 5 K, to evaluate configuration entropy numerically at 3000 K would need to compute the specific heat at 600 smaller temperatures. In contrast, using Eq.(6.17) the configuration entropy can be computed analytically from the correlation functions at any given temperature and alloy composition. Our experiences show that the computational time using the hybrid method can be of two orders faster than those by the thermodynamic integration.

6.2.3 Computational details

The DFT enthalpies of mixing given by Eq. 6.1 were calculated from fully relaxed spin-polarized DFT total energy calculations performed using the projector augmented wave (PAW) method [274] implemented in VASP [275, 276, 277, 278, 279]. Exchange and correlation were treated in the generalized gradient approximation GGA-PBE [280]. The core configurations of Fe, Cr, Mn and Ni in PAW potentials are [Ar]3d⁷4s¹, [Ar]3d⁵4s¹, [Ar]3d⁶4s¹ and [Ar]3d⁹4s¹, respectively. The total energies were calculated using the Monkhorst-Pack [281] mesh of 12x12x12 k-point for a four-atom FCC cubic cell. The plane wave cut-off energy used in the calculations was 400 eV. The total energy convergence criterion was set to 10^{-6} eV/cell, and force components were relaxed to 10^{-3} eV/nm.

In the semi-canonical Monte Carlo calculations performed the temperature range and temperature steps are important. The accuracy of the thermodynamic integration method to calculate configuration entropy generally requires a smaller temperature integration step, $\Delta T = 5$ K and also depends on the number of Monte Carlo passes [273]. In particular, we use a cell containing 2048 atoms distributed into a 8x8x8 primitive unit cell, and average compositions for the ensemble given by $\text{Cr}_{18}\text{Fe}_{27}\text{Mn}_{27}\text{Ni}_{28}$ and equiatomic $\text{Cr}_{25}\text{Fe}_{25}\text{Mn}_{25}\text{Ni}_{25}$. The Monte Carlo simulations were performed from random configurations at high temperature (3,000 K) where the configuration entropy at the high-temperature limit is given by $k_B \ln(4)$ for equiatomic and $-k_B \{0.18 * \ln(0.18) + 2 * 0.27 * \ln(0.27) + 0.28 * \ln(0.28)\}$ for $\text{Cr}_{18}\text{Fe}_{27}\text{Mn}_{27}\text{Ni}_{28}$ [200]. By quenching down systematically with the temperature step of $\Delta T = 5$ K, various equilibrium configurations were obtained at lower temperatures. For thermodynamic integration calculation of configuration entropy, we integrated numerically the specific heat at constant volume using the theoretical formula (6.19) starting from the lowest temperature value 0 K to 3,000 K.

6.3 Cluster probability functions in fcc

Cr-Fe-Mn-Ni alloys

We apply the matrix formulation of cluster expansion outlined in sub-section 2.1 to the FCC CrFeMnNi system for investigating the temperature and composition-dependent cluster probability distribution functions and the configuration entropy.

6.3.1 Cluster Expansion Hamiltonian for FCC CrFeMnNi

The DFT enthalpies of mixing for the FCC CrFeMnNi system were used to map iteratively into the cluster expansion Hamiltonian given by Eq. 6.2 using the ATAT package [184]. The mapping has been performed systematically from the 6 binary and 4 ternary constituent subsystems of the considered quaternary. The database of structures for the cluster expansion consisted of 835 structures categorized by the difference of local environments in binaries (structures with two chemical elements: 58 CrFe, 55 CrMn, 77 CrNi, 58 FeMn, 54 FeNi and 52 MnNi), ternaries (structures with three chemical elements: 89 CrFeMn, 85 CrFeNi, 46 FeMnNi, and 66 CrMnNi); and 191 quaternaries CrFeMnNi. More information about the type of binary and ternary structures used in our DFT database has been detailed in our previous work [245]. Their structures are typically ordered ones with their composition ranged for each constituent element from 5% to 95%. It is important to stress here that in difference with other studies of HEAs, our DFT database for constructing the CE Hamiltonian didn't include randomly distributed structures such as the so-called special quasi-random structures (SQSs). The latter, however, can be generated within the present approach from Monte-Carlo simulations after obtaining the reliable ECIs. The set of clusters which have minimized the cross-validation score of 12.95 meV/atom, consists of 6 two-body, 2 three-body and 1 four-body ECIs. In the present work, the clusters with the same sizes and relative positions have been included consistently in the considered subsystems. The prediction of the corresponding ground-state intermetallic phases is in a good agreement with the experimental binary phase diagrams available (for example, the ferromagnetic $FeNi_3$ in $L1_2$ structure and anti-ferromagnetic $MnNi$ in $L1_0$ structure) as well as with the previous theoretical study for the ternary and ferrimagnetic $CrFe_2Ni$ phase in $NiCu_2Zn$ structure [245]. A new intermetallic phase $FeCr_2MnNi_4$ is

predicted for the quaternary system and full results of magnetic properties in CrFeMnNi system will be discussed in a separate work.

The CE Hamiltonian for the quaternary system CrFeMnNi consists in total of 83 different decorated clusters distributed among 10 different non-decorated clusters: 4 decorated clusters for the point cluster, $\omega = 1, n = 1$; 6 decorated clusters for each pair cluster $\omega = 2, n = 1, \dots, 6$; 10 decorated clusters for the non-decorated cluster $\omega = 3, n = 1$; 18 decorated clusters for the non-decorated cluster $\omega = 3, n = 2$; and 15 decorated clusters for the non-decorated cluster $\omega = 4, n = 1$. The decoration labels, (s) required to specify the clusters, are listed in Tab. 6.1. Each non-decorated cluster is defined by the coordinates (specified with respect to the standard Cartesian coordinate system in units of lattice spacing) of the lattice sites that it includes. The decorations define the chemical species allocated to each site in strictly the same order i.e. for $\omega = 2, n = 1$ cluster the decoration $(2, 3)$ means that species 2 is allocated for site with coordinates $(1, 1, 1)$ and species 3 is allocated for site with coordinates $(1/2, 3/2, 3/2)$.

6.3.2 Full set of cluster decorations

In general the set of temperature dependent decorated cluster correlation functions, $\langle \Gamma_{\omega,n}^{(s)}[\vec{\sigma}] \rangle$, constitute a set of K^ω quantities for a given maximal cluster (ω, n) in the CE. From each of the K^ω temperature dependent decorated cluster correlation functions, the matrix formalism described in section 6.2.1 generates the set of temperature dependent multi-body probability functions describing the temperature dependent behavior associated with the maximal cluster (ω, n) . The symmetry unique decorations for all of the clusters in the CE, $\forall(\omega, n)$, are reported in the ATAT clusters.out file and here they are listed in Tab. 6.1. If one cluster is included into another, it becomes a sub-cluster $(\omega_i, n_i) \in (\omega, n)$; these sub-clusters have been classified according to their

inclusion into maximal clusters, and are listed in Tab. 6.2. If the sub-cluster (ω_i, n_i) is included in the maximal cluster, $(\omega_i, n_i) \in (\omega, n)$, then the decorations from the sub-cluster $(s)_{(\omega_i, n_i)}$ can be transferred into the decorations of the maximal cluster, $(s)_{(\omega, n)}$, by using the intrinsic space group symmetry of the parent lattice. In general any given sub-cluster (ω_i, n_i) can be found several times within the cluster (ω, n) . For convenience, symmetry of the cluster decorations is implemented by means of permutation operators in Tab. 6.2 including X for the empty site. The full set of decorated cluster correlation functions, $\langle \Gamma_{\omega, n}^{(s)}[\vec{\sigma}] \rangle$, corresponding to the maximal cluster (ω, n) , is generated by studying which of the decorations $(s)_{\omega_i, n_i}$ form the sub-clusters (ω_i, n_i) in (ω, n) that have decorations with empty cluster, i.e. at least one integer entry in $0 \subseteq (s)_{\omega_i, n_i}$.

For the case of the maximal cluster $(\omega = 2, n = 1)$ consisting of sites $\{(1, 1, 1)\}, \{(1, 3/2, 3/2)\}$, see Tab. 6.1, we have a full set of $4^2 = 16$ 2-tuples of decorations, each associated to a temperature dependent decorated cluster correlation function. It can be noted that the cluster $\{(1, 1, 1)\}, \{(1, 3/2, 3/2)\}$ contains two sub-clusters: the point cluster $\{(1, 1, 1)\}$ that has decorations $\{(0), (1), (2), (3)\}$; and the cluster itself which has decorations $\{(1, 1), (2, 1), (3, 1), (2, 2), (2, 3), (3, 3)\}$. To each of these decorations there are corresponding decorated cluster correlation functions. In this case the point cluster is contained twice: once in $(1, 1, 1) \subset \{(1, 1, 1)\}, \{(1, 3/2, 3/2)\}$ and also in $(1, 3/2, 3/2) \subset \{(1, 1, 1), (1, 3/2, 3/2)\}$. Similarly the cluster itself $\{(1, 1, 1), (1, 3/2, 3/2)\}$ is contained once. Thus a point cluster decorated by $(s) = (3)$ is transferred to $\omega = 2$ -tuples notation in the maximal cluster as $(3, 0)$ or $(0, 3)$. This can be captured by the permutation operators $\{(1, X), (X, 1)\}$ (see Tab. 6.2) where X stands for an empty cluster where a 0 should be placed. Similarly the decorations denoted by $(s) = (1, 2)$ in the 2-tuples notation are equivalent to the symmetry equivalent decorations $(s) = (1, 2)$ and $(s') = (2, 1) \equiv (1, 2)$. The symmetry effect can again be captured by permutation operators $\{(1, 2), (2, 1)\}$, where X no longer appears,

since the $\omega_i = 2$ -tuples have the same order ($\omega = \omega_i$) as the $\omega = 2$ -tuples from the maximal cluster ($\omega = 2, n = 1$). The analysis outlined above for the two body cluster $\{(1, 1, 1), (1, 3/2, 3/2)\}$ with $K = 4$ components can be extended to the remaining ($\omega = 2, n > 1$) maximal clusters. The permutation operators that carry out the appropriate decorations $(s)_{\omega_i, n_i}$ of sub-clusters (ω_i, n_i) into (ω, n) cluster ω -tuples notation are detailed in Tab. 6.2. It should be noted that for any two body cluster, the point and corresponding pair sub-clusters add up forming $4 + 6 = 10$ symmetrically unique correlation functions $\langle \Gamma_{\omega, n}^{(ij)}[\vec{\sigma}] \rangle$.

Referring to the maximal cluster ($\omega = 3, n = 1$), from Tab. 6.2 there are 3 contained sub-clusters $(\omega_1 = 1, n_1 = 1)$, $(\omega_2 = 2, n_2 = 1)$ and $(\omega_3 = 3, n_3 = 1)$ within the maximal cluster ($\omega = 3, n = 1$). The point sub-cluster ($\omega_1 = 1, n_1 = 1$) has, according to Tab. 6.1, 4 decorations associated with it; the two body cluster ($\omega_2 = 2, n_2 = 1$) has 6 decorations associated with itself; and finally the sub-cluster ($\omega_3 = 3, n_3 = 1$) has 10 decorations associated with itself. The total number of symmetry unique decorated cluster correlation functions, which is smaller than $K^\omega = 4^3 = 64$, but can nevertheless fully describe cluster ($\omega = 3, n = 1$) with $K = 4$ components is therefore given by $4 + 6 + 10 = 20$ decorated cluster correlation functions. From these 20 symmetry unique decorated cluster correlations, it is possible to generate a total of 64 decorated cluster correlation functions by using the permutation operators in Tab. 6.2. The number of permutation operators to transfer decorations from sub-cluster $(\omega_1 = 1, n_1 = 1)$ to $(\omega = 3, n = 1)$, is 3; from $(\omega_2 = 2, n_2 = 1)$, 6 permutation operators ,and from the cluster itself $(\omega_3 = 3, n_3 = 1)$ there are 3 permutation operators. The total number of permutation operators is therefore $3 + 6 + 6 = 15$. The remaining decorations, which are not listed in Tab. 6.1, add up to $64 - 20 = 44$ and are obtained by using appropriately the 15 permutation operators corresponding to the maximal cluster ($\omega = 3, n = 1$). Similarly the maximal cluster ($\omega = 3, n = 2$) has 34 symmetrically unique decorations and 12 permutation operators; and

$(\omega = 4, n = 1)$ has 35 symmetry unique decorations with 64 permutation operators (all possible permutations for $K = 4$).

Table 6.1: ω , highest coordination shell n , decoration (s) and coordinates of points in the relevant clusters on FCC lattice. The coordinates are referred to as the simple cubic Bravais lattice. Index (s) is the same as the sequence of points in the relevant cluster. The canonical order for decoration indexes, $(s)_i$, is 0,1,2 and 3 is Cr, Fe, Mn and Ni. All values of the Effective Cluster Interactions (ECIs) obtained from the present CE study are shown in the last column.

Table 6.1				
ω	n	(s)	Coordinates	ECI (meV/atom)
1	1	(0)	(1,1,1)	+0.00
		(1)		+0.11
		(2)		-0.04
		(3)		-0.01
2	1	(1,1)	(1,1,1)	+9.40
		(2,1)	(1,3/2,3/2)	-0.10
		(3,1)		+3.40
		(2,2)		+0.40
		(3,2)		+1.30
		(3,3)		+6.00
2	2	(1,1)	(1,1,1)	-9.20
		(2,1)	(1,1,0)	+0.40
		(3,1)		-4.40
		(2,2)		-11.60
		(3,2)		-3.50
		(3,3)		-8.80
2	3	(1,1)	(1,1,1)	0.90
		(2,1)	(2,3/2,3/2)	2.60
		(3,1)		3.50
		(2,2)		1.60
		(3,2)		-0.30

Continuation of Table 6.1				
ω	n	(s)	Coordinates	ECI (meV/atom)
(3,3)				0.10
2	4	(1,1)	(1,1,1)	-0.40
		(2,1)	(2,1,2)	2.40
		(3,1)		1.20
		(2,2)		0.50
		(3,2)		0.60
		(3,3)		-0.80
2	5	(1,1)	(1,1,1)	-1.00
		(2,1)	(1,3/2,-1/2)	-3.50
		(3,1)		-2.00
		(2,2)		0.20
		(3,2)		0.90
		(3,3)		0.40
2	6	(1,1)	(1,1,1)	0.80
		(2,1)	(2,2,0)	2.10
		(3,1)		1.00
		(2,2)		-2.70
		(3,2)		-1.30
		(3,3)		0.50
3	1	(1,1,1)	(1,1,1)	+0.20
		(2,1,1)	(3/2,1,1/2)	+0.90
		(3,1,1)	(1,3/2,1/2)	+1.60
		(2,2,1)		-3.40
		(3,2,1)		-0.50
		(3,3,1)		+1.20
		(2,2,2)		+0.20
		(3,2,2)		+2.00
		(3,3,2)		-0.50

Continuation of Table 6.1

ω	n	(s)	Coordinates	ECI (meV/atom)
(3,3,3)				+0.00
3	2	(1,1,1)	(1,1,1)	-0.60
		(2,1,1)	(1,3/2,1/2)	+1.00
		(3,1,1)	(1,1,0)	+0.90
		(1,2,1)		-1.80
		(2,2,1)		+2.30
		(3,2,1)		-0.70
		(1,3,1)		-2.10
		(2,3,1)		-0.30
		(3,3,1)		-0.60
		(2,1,2)		-6.30
		(3,1,2)		-1.20
		(2,2,2)		-0.60
		(3,2,2)		-0.10
		(2,3,2)		+1.60
		(3,3,2)		+0.60
		(3,1,3)		-2.00
		(3,2,3)		+0.30
(3,3,3)				-1.40
4	1	(1,1,1,1)	(1,1,1)	-3.30
		(2,1,1,1)	(3/2,3/2,1)	+2.00
		(3,1,1,1)	(3/2,1,1/2)	+0.70
		(2,2,1,1)	(1,3/2,1/2)	-2.90
		(3,2,1,1)		+0.60
		(3,3,1,1)		+0.70
		(2,2,2,1)		-0.60
		(3,2,2,1)		-1.10
		(3,3,2,1)		+1.30
		(3,3,3,1)		+2.60

Continuation of Table 6.1

ω	n	(s)	Coordinates	ECI (meV/atom)
		(2,2,2,2)		-0.50
		(3,2,2,2)		+4.90
		(3,3,2,2)		+1.00
		(3,3,3,2)		-1.60
		(3,3,3,3)		-1.70

End of Table 6.1

6.3.3 Four-body probability functions from Monte Carlo simulations

After performing semi-canonical Monte Carlo simulations for alloy compositions $\text{Cr}_{18}\text{Fe}_{27}\text{Mn}_{27}\text{Ni}_{28}$ and equiatomic $\text{Cr}_{25}\text{Fe}_{25}\text{Mn}_{25}\text{Ni}_{25}$, we use the correlation functions calculated at each of the temperatures to study the temperature dependent probabilities of decorated clusters corresponding to the equilibrium configuration $[\vec{\sigma}]$ of the Monte Carlo super-cell following the formalisms described in the Methods section. For each non-decorated cluster ω, n and temperature we generate the corresponding τ^{-1} matrices with dimension $K^\omega \times K^\omega$ and a vector formed by all the decorated correlation cluster functions, $\langle \Gamma_{\omega,n}^{(ij\dots)} [\vec{\sigma}] \rangle$ with dimension K^ω . The Monte Carlo simulations output only the symmetrically unique correlation functions (see Tab. 6.1), which are less than the K^ω required for matrix operation. In order to generate the full set of K^ω from the symmetrically unique correlation functions we devise a set of permutation operators g_i (see Tab. 6.2) that indicate how an arbitrary decoration ω -tuple of integers is obtained from the symmetrically unique decorations belonging to the non-decorated cluster or one of its sub-clusters (see the third column of Tab. 6.2 for identifying the

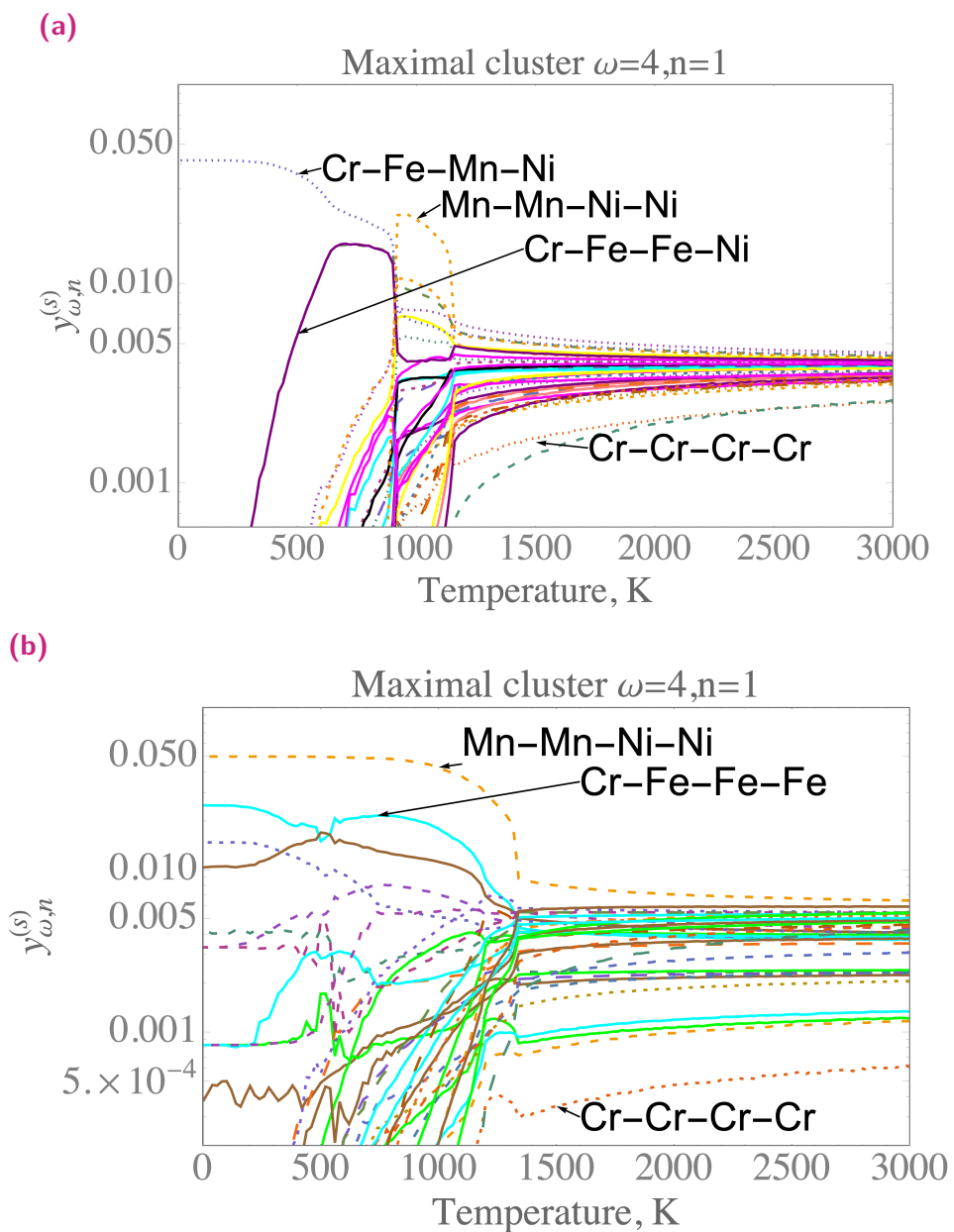
cluster-sub-cluster relation). Tab. 6.2 contains all the operators necessary to generate cluster probabilities, $y_{\omega,n}^{(s)}$, for any possible decoration, (s) , of 10 non-decorated clusters employed in the cluster expansion Hamiltonian.

As an important case of study, we chose the maximal cluster given by $\omega = 4, n = 1$ to obtain the four-body configuration probabilities. Figs. 6.1 a-b, shows the plot of 35 symmetrically unique probabilities for the four-body maximal cluster defined by the set of lattice sites $((1, 1, 1), (3/2, 3/2, 1), (3/2, 1, 1/2), (1, 3/2, 1/2))$ as a function of temperature.

The most important four-body bonding configurations in the temperature range from 0 to 3000 K for the two alloy systems (the equiatomic $\text{Cr}_{25}\text{Fe}_{25}\text{Mn}_{25}\text{Ni}_{25}$ and $\text{Cr}_{18}\text{Fe}_{27}\text{Mn}_{27}\text{Ni}_{28}$) are highlighted in Figs. 6.1 a-b. It should be noted that for both compositions the cluster configuration referred to as Cr-Cr-Cr-Cr appears as the least probable of all the cluster configurations. This finding is consistent with the fact that Cr has the BCC ground-state and therefore the probability of finding a Cr cluster in the FCC lattice is negligible, in particular in the low-temperature region.

For the equiatomic composition, the probability of Cr-Fe-Mn-Ni is particularly very high at temperatures between 0-900 K. The presence of four-body Cr-Fe-Mn-Ni clusters at low temperature demonstrates the relationship with our DFT/CE prediction of the new ordered phase $\text{FeCr}_2\text{MnNi}_4$ in the quaternary system. Furthermore, in the temperature range below 900 K, the cluster configuration Cr-Fe-Fe-Ni shows as the second most probable configuration. This configuration is directly correlated with the ordered Fe_2CrNi structure predicted in our earlier study of phase stability in the ternary Fe-Cr-Ni system [245]. In the temperature region between 900K and 1200K, an increase of probability of Mn-Mn-Ni-Ni cluster is significantly important. Beyond 1200 K, all of the cluster configuration probabilities tend to the solid solution or random configuration.

Fig. 6.1.: Four-body probabilities obtained from the hybrid CE-Monte Carlo calculations: (a) All the four-body probabilities for the equiatomic composition $\text{Cr}_{25}\text{Fe}_{25}\text{Mn}_{25}\text{Ni}_{25}$ as a function of temperature; (b) The same as in (a) but for the composition $\text{Cr}_{18}\text{Fe}_{27}\text{Mn}_{27}\text{Ni}_{28}$.



For the system with average composition Cr₁₈Fe₂₇Mn₂₇Ni₂₈, the cluster probability of decorations given by Mn-Mn-Ni-Ni appears to dominate until 1300 K, where the solid solution or random configuration begins. Furthermore, the second most probable cluster configuration in the temperature range 500-1200 K appears to be Cr-Fe-Fe-Fe. Again, these findings are remarkable and the origin of these clusters would need a more detailed discussion.

Table 6.2.: List of permutation operators for generating the full set of decorations represented by K^ω dimensional integer arrays with entries taking values from 0 to $K - 1$. The symmetry operators (see Eq. 6.5) here represented in permutation form in column 2 act on the set of 83 symmetry unique decorations indicated under the (s) column in Tab. 6.1 by permuting the entries in (s) or by introducing the empty cluster X for sub-clusters belong to a given cluster; examples with discussion are provided in subsection 6.3.2. The space group of the disordered FCC structure, $g \in O_h^5$, is implicitly assumed in order to convolute the symmetry unique into the full set of decorations. The last four columns represent (ω_i, n_i) i^{th} sub-cluster of the maximal cluster (ω, n) ; N_{ω_i, n_i} site multiplicity of (ω_i, n_i) ; $N_{\omega, n}^{\omega_i, n_i}$ sub-cluster multiplicity of the cluster $(\omega_i, n_i) \in (\omega, n)$; and η_{ω_i, n_i} , the sub-cluster (ω_i, n_i) contribution to configuration entropy expression corresponding to the maximal cluster (ω, n)

Table 6.2

Maximal cluster	Permutation operators	Sub-cluster $\{\omega_i, n_i\}$	N_{ω_i, n_i}	$N_{\omega, n}^{\omega_i, n_i}$	η_{ω_i, n_i}
$\omega = 1, n = 1$	{(1)}	$\omega_1 = 1, n_1 = 1$	1	1	-1
$\omega = 2, n = 1$	{(1,X),(X,1)}	$\omega_1 = 1, n_1 = 1$	1	2	11
	{(1,2),(2,1)}	$\omega_2 = 2, n_2 = 1$	6	1	-6
$\omega = 2, n = 2$	{(1,X),(X,1)}	$\omega_1 = 1, n_1 = 1$	1	2	5
	{(1,2),(2,1)}	$\omega_2 = 2, n_2 = 2$	3	1	-3
$\omega = 2, n = 3$	{(1,X),(X,1)}	$\omega_1 = 1, n_1 = 1$	1	2	23
	{(1,2),(2,1)}	$\omega_2 = 2, n_2 = 3$	12	1	-12
$\omega = 2, n = 4$	{(1,X),(X,1)}	$\omega_1 = 1, n_1 = 1$	1	2	11
	{(1,2),(2,1)}	$\omega_2 = 2, n_2 = 4$	6	1	-6
$\omega = 2, n = 5$	{(1,X),(X,1)}	$\omega_1 = 1, n_1 = 1$	1	2	23
	{(1,2),(2,1)}	$\omega_2 = 2, n_2 = 5$	12	1	-12
$\omega = 2, n = 6$	{(1,X),(X,1)}	$\omega_1 = 1, n_1 = 1$	1	2	7
	{(1,2),(2,1)}	$\omega_2 = 2, n_2 = 6$	4	1	-4

Continuation of Table 6.2

Maximal cluster	Permutation operators	Sub-cluster $\{\omega_i, n_i\}$	N_{ω_i, n_i}	$N_{\omega, n}^{\omega_i, n_i}$	η_{ω_i, n_i}
$\omega = 3, n = 1$	$\{(1,X,X), (X,X,1), (X,1,X)\}$ $\{(1,2,X), (2,1,X), (2,X,1),$ $(1,X,2), (X,1,2), (X,2,1)\}$ $\{(1,3,2), (3,2,1), (2,1,3),$ $(3,1,2), (2,3,1), (1,2,3)\}$	$\omega_1 = 1, n_1 = 1$ $\omega_2 = 2, n_2 = 1$ $\omega_3 = 3, n_3 = 1$	1 6 8	3 3 1	-13 18 -8
$\omega = 3, n = 2$	$\{(1,X,X), (X,X,1), (X,1,X)\}$ $\{(2,1,X), (1,2,X)\}$ $\{(1,X,2), (2,X,1),$ $(X,1,2), (X,2,1)\}$ $\{(3,1,2), (1,3,2), (1,2,3)\}$	$\omega_1 = 1, n_1 = 1$ $\omega_2 = 2, n_2 = 2$ $\omega_3 = 2, n_3 = 1$ $\omega_4 = 3, n_4 = 2$	1 1 6 12	3 1 2 1	-19 9 18 -12
$\omega = 4, n = 1$	$\{(1,X,X,X), (X,X,X,1),$ $(X,X,1,X), (X,1,X,X)\}$ $\{(X,X,1,2), (X,X,2,1),$ $(1,2,X,X), (2,1,X,X)$ $(X,1,X,2), (X,2,X,1),$ $(2,X,1,X), (1,X,2,X)$ $(1,X,X,2), (2,X,X,1),$ $(X,1,2,X), (X,2,1,X)\}$ $\{(1,3,2,X), (3,1,X,2),$ $(2,X,1,3), (X,2,3, 1)$ $(3,2,1,X), (1,X,3,2),$ $(X,1,2,3), (2,3,X,1)$ $(2,1,3,X), (X,3,1,2),$ $(1,2,X,3), (3,X,2,1)$ $(2,X,3, 1), (X,2,1,3),$ $(1,3, X,2), (3,1,2,X)$ $(1,X,2,3), (3,2,X,1),$ $(2,3,1,X), (X,1,3,2)$ $(3,X,1,2), (1,2,3,X),$ $(X,3,2,1), (2,1,X,3)\}$	$\omega_1 = 1, n_1 = 1$ $\omega_2 = 2, n_2 = 1$ $\omega_3 = 3, n_3 = 1$ $\omega_4 = 3, n_4 = 1$	1 6 8 4	4 6 4 0	-5 6 -5 0

Continuation of Table 6.2

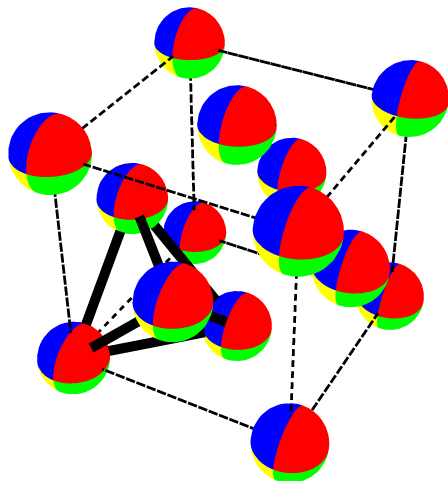
Maximal cluster	Permutation operators	Sub-cluster $\{\omega_i, n_i\}$	N_{ω_i, n_i}	$N_{\omega, n}^{\omega_i, n_i}$	η_{ω_i, n_i}
	$\{(1,4,3,2), (4,1,2,3),$ $(3,2,1,4), (2,3,4,1)$ $(4,3,1,2), (1,2,4,3),$ $(2,1,3,4), (3,4,2,1)$ $(3,1,4,2), (2,4,1,3)$ $(1,3,2,4), (4,2,3,1)$ $(3,2,4,1), (2,3,1,4),$ $(1,4,2,3), (4,1,3,2)$ $(1,2,3,4), (4,3,2,1),$ $(3,4,1,2), (2,1,4,3)$ $(4,2,1,3), (1,3,4,2),$ $(2,4,3,1), (3,1,2,4)\}$	$\omega_4 = 4, n_4 = 1$	2	1	-2

End of Table 6.2

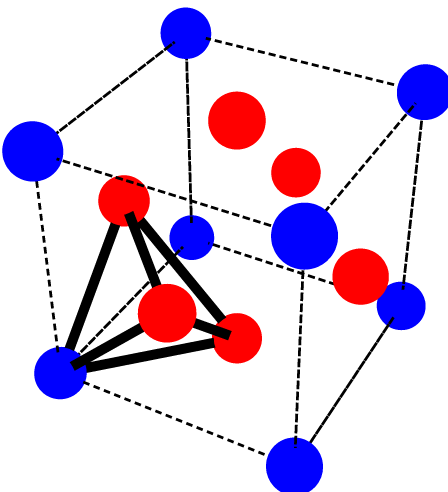
The prediction of the high probabilities for Mn-Mn-Ni-Ni and Cr-Fe-Fe-Fe clusters in $\text{Cr}_{18}\text{Fe}_{27}\text{Mn}_{27}\text{Ni}_{28}$ alloy composition shown in Fig. 6.1 b can be explained by the decoration of the first nearest neighbour four-atom cluster interaction obtained from the CE Hamiltonian. It is important to stress that in this case, the CE method reproduces the well-known result from the tetrahedron approximation in the CVM [266, 196]. The configuration Mn-Mn-Ni-Ni is understood to be related to L1_0 structure in Strukturbericht notation with Mn and Ni atoms, whereas the composition Cr-Fe-Fe-Fe is related the L1_2 structure in Strukturbericht notation with Cr and Fe atoms. Both of these structures are depicted in Fig. 6.2 and they are in a full agreement with our first-principles investigations. Indeed, the MnNi-L1_0 structure is predicted by both the DFT and CE Hamiltonian to be one of the ground-state structures

Fig. 6.2.: (a) Most probable phase at high temperature (disordered structure); (b) and (c): two most probable ordered phases at low temperature in the equiatomic $\text{Cr}_{25}\text{Fe}_{25}\text{Mn}_{25}\text{Ni}_{25}$ and $\text{Cr}_{18}\text{Fe}_{27}\text{Mn}_{27}\text{Ni}_{28}$ HEAs compositions. Cr, Fe, Mn and Ni are illustrated in blue, red, yellow and green respectively.

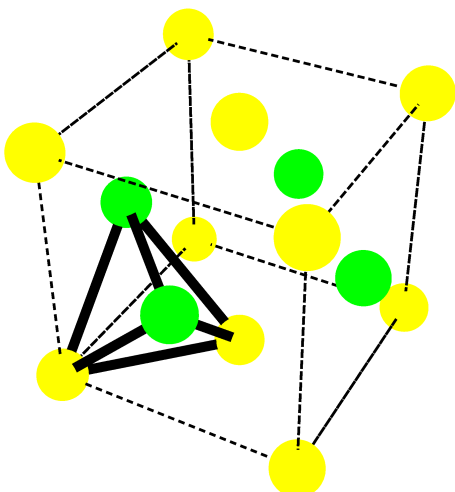
(a)



(b)



(c)



not only for the binary Mn-Ni system but also for the quaternary Fe-Cr-Mn-Ni one. The $CrFe_3-L1_2$ structure has also been found as the lowest-energy binary structure in the previous study of the phase stability of Fe-Cr binary in the FCC lattice (see Fig. 2a from [245]). In particular, the latter structure has also been found to be stable due to the strong anti-ferromagnetic interaction between Cr and Fe from the magnetic cluster expansion (MCE) performed for the ternary CrFeNi system [282]. In that work, Monte Carlo simulations using MCE indicated that ordered magnetic structures in the Ni-rich corner (ferromagnetic) of the $FeCrNi$ system persists until temperatures of 600 K and that for the atomic compositions between $CrFe_2$ and $CrFe_3$ the anti-ferromagnetic order was retained beyond 500 K.

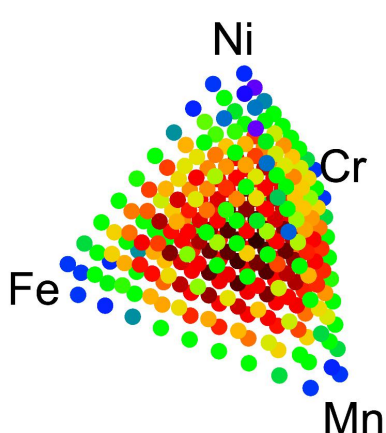
6.4 Configuration entropy in Cr-Fe-Mn-Ni system

For each temperature value in the range 0-3000 K the configuration probabilities corresponding to cluster $\omega = 4, n = 1$ are used in Eq. 6.17 to obtain the quantities $\tilde{S}_{\omega_i, n_i}[\vec{\sigma}]$. There is one quantity $\tilde{S}_{\omega_i, n_i}[\vec{\sigma}]$ and a corresponding weight η_{ω_i, n_i} for each of the ω_i, n_i sub-clusters : $\omega = 1, n = 1, \omega = 2, n = 1; \omega = 3, n = 1$; and $\omega = 4, n = 1$ included in the maximal cluster $\omega = 4, n = 1$. The total configuration entropy, $S_{\omega, n}[\vec{\sigma}]$, is calculated by adding the η_{ω_i, n_i} weighted quantities $\tilde{S}_{\omega_i, n_i}[\vec{\sigma}]$. By applying the same arguments developed for the cluster $\omega = 4, n = 1$, the total configuration entropy for each of the 10 different maximal clusters can be calculated. The sub-clusters and the permutation operators contained in each of the 10 maximal clusters appearing in the cluster expansion are detailed in Tab. 6.2.

Composition dependent entropies at fixed temperatures 1000 K and 3000 K are shown in Fig. 6.3 a-b. At each of these temperature values, any of

Fig. 6.3.: Composition dependent entropies obtained from Monte Carlo simulations in CE. (a) for composition dependent entropy at fixed temperature 1,000 K; (b) the same as in 6.4(a) but at fixed temperature 3,000 K

(a)



(b)

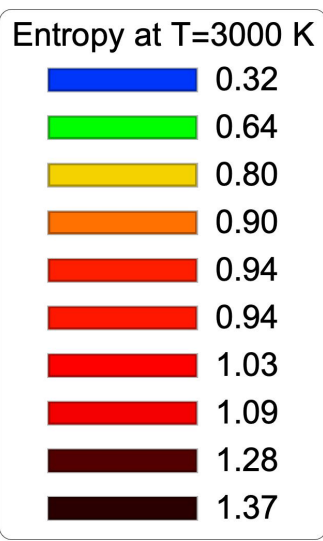
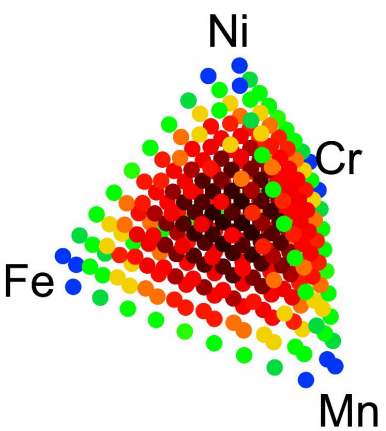
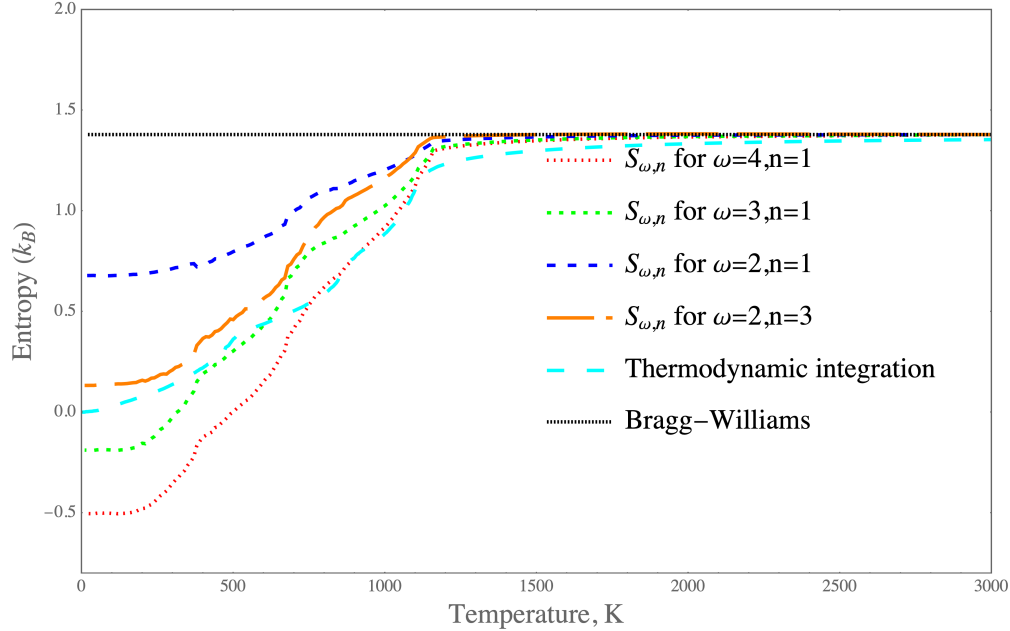


Fig. 6.4.: Temperature dependence of configuration entropy evaluated at various levels of cluster approximations and compared with the thermodynamic integration result at the equiatomic composition Cr₂₅Fe₂₅Mn₂₅Ni₂₅

EQUIATOMIC CrFeMnNi



the configuration entropy expressions from Tab. 6.2 provides approximately the same value. At 3000 K, the entropy is maximized in the centre of the tetrahedron namely at the equiatomic composition to $1.37 k_B$, and it is decreased upon lowering the temperature at all of the composition points. The variation of configuration entropy is too complex to be captured in the fixed temperature plots, therefore we use specifically the equiatomic composition and calculate the configuration entropy as a function of temperature in Fig. 6.4. Regarding the high-temperature limit value of entropy in Figs. 6.4 , we use as a maximal cluster that from the four body, three body and two body in the nearest neighbour cluster probabilities. Above 1200 K, the cluster approximation for the configuration entropy approaches the high-temperature limit of the disordered solute solution ($-k_B \sum_p^4 x_p[\vec{\sigma}] \ln(x_p[\vec{\sigma}])$) much more rapidly than the thermodynamic integration. The reason the high temperature limit is preserved can be clearly seen from the factorization of the CE expression that resulted from analytical derivation in Eq. 6.15. It is important to stress that within the high-temperature limit, our theoretical prediction recovers the

ideal configuration entropy of mixing for solution phase as it has been originally proposed by the phenomenological guidelines in designing high-entropy alloys using thermodynamic and topological parameters of the constituent elements [12].

It is worth mentioning that the entropy increase (Fig. 6.3) as a function of temperature for the equiatomic alloy composition can thus be understood by the corresponding decrease in probabilities (Figs. 6.1) of the ordered state of the structures $L1_0$ towards the disorder configuration $A1$ in Fig. 6.2. Similarly, in the alloy with composition $Cr_{18}Fe_{27}Mn_{27}Ni_{28}$, the increase of configuration entropy is correlated with the decrease in the high probability of the configurations of Cr-Fe-Fe-Fe and Mn-Mn-Ni-Ni clusters originally related to the ordered fcc-like $L1_2$ - $CrFe_3$ and $L1_0$ - $MnNi$ structure, respectively.

For the cluster $\omega = 4, n = 1$, the calculated configuration entropy in Fig. 6.4 appears to be negative at low temperature for the positive values correctly predicted by the thermodynamic integration method. This demonstrates clearly that this maximum cluster within the tetrahedron approximation conventionally adopted within the CVM is only valid to describe the configuration entropy for the four-component Cr-Fe-Mn-Ni system in the high-temperature limit. It is shown from Fig. 6.4 that the first nearest-neighbour triangle cluster ($\omega = 3, n = 1$) which plays an important role within the tetrahedron approximation, also gives physically incorrect and negative entropy contribution at low temperature. As it has been discussed in the Introduction, in a difference to the CVM tetrahedron approximation, besides to the first nearest-neighbour cluster contributions, the present CE results include also other pair clusters up to the sixth nearest neighbours and the next nearest-neighbour triangle cluster contributions. For example, in Fig. 6.4, the third nearest-neighbour pair cluster ($\omega = 2, n = 3$) gives the significantly positive contribution to configuration entropy in all the range of temperature. These additional cluster contributions, in turn, ensure the correct behaviour of the configuration

entropy obtained from the thermodynamic integration. Therefore, from a statistical physics point of view, the hybrid technique combining Monte Carlo simulations with the CE method can be considered to be more advanced than the mean-field approach advocated within the CVM.

6.5 Conclusions

In this work, we develop a matrix formalism to study multi-body ordering probabilities beyond pair approximation previously used for investigating the SRO and configuration entropy in multi-component alloys by using a hybrid combination of CE and Monte Carlo methods. The cluster probabilities are worked out by explicit inversion within the orthonormal sets of the point functions adopted in the ATAT package and direct product of a matrix formulation obtained from symmetrically independent correlation functions. The correlation functions are determined from semi-canonical Monte Carlo simulations and ECIs derived from DFT calculations. We apply our method to the quaternary FCC Cr-Fe-Mn-Ni system by considering 285 different alloy compositions covering the compositional space of the quaternary alloy as a function of temperature. To further assess our formulated expressions for configuration entropy, focus is put on two alloy compositions, equiatomic $\text{Cr}_{25}\text{Fe}_{25}\text{Mn}_{25}\text{Ni}_{25}$ and $\text{Cr}_{18}\text{Fe}_{27}\text{Mn}_{27}\text{Ni}_{28}$, to obtain cluster probabilities and understand the variation in configuration entropy with temperature due to the lowering of the ordering probability corresponding to the ordered configuration. The cluster probability plots against temperature show that for the composition $\text{Cr}_{18}\text{Fe}_{27}\text{Mn}_{27}\text{Ni}_{28}$ there is high probability of formation of the L1_0 MnNi phase at low temperatures below 1300 K and for the L1_2 CrFe_3 phase in the temperature range 500-1200 K. Similarly for the equiatomic composition the L1_0 MnNi phase appears stable in the temperature range 900-1200 K, while the lower temperature region is preferred for the configuration Cr-Fe-Mn-Ni. The configuration Cr-Cr-Cr-Cr was found to be the least

probable configuration at all temperature ranges for both compositions of the Cr-Fe-Mn-Ni system. Furthermore, the configuration entropy as a function of temperature was derived from these probabilities: the high-temperature limit is in accordance with random solid solution approximation; but at low temperatures, the entropy is seen to be reduced due to ordering or segregation tendencies which are in turn determined by multi-body probability functions including chemical short-range order.

We believe that the present study will help to promote further understanding of derivative phases as a function of temperature and multi-component alloy composition from disordered solid solutions in the phenomenological description of HEAs. By applying the formalism to the Cr-Fe-Mn-Ni system, it will also serve as a benchmarking example in designing radiation-tolerant materials for advanced nuclear reactor systems by using the ab initio based CE method. The composition $\text{Cr}_{18}\text{Fe}_{27}\text{Mn}_{27}\text{Ni}_{28}$ multicomponent system has been studied for advanced nuclear applications due to promising irradiation resistance with regards to void swelling.

6.6 Acknowledgements

This work has been carried out within the framework of the EUROfusion Consortium and has received funding from the Euratom research and training programme 2014-2018 and 2019-2020 under Grant Agreement No. 633053 and funding from the RCUK Energy Programme [Grant Number EP/P012450/1]. The views and opinions expressed herein do not necessarily reflect those of the European Commission. AFC acknowledges financial support from EPSRC (EP/L01680X/1) through the Materials for Demanding Environments Center for Doctoral Training. MF and JSW acknowledge the financial support from the Foundation for Polish Science grant HOMING (No.Homing/2016-1/12). The HOMING programme is co-financed by the European Union under the Eu-

ropean Regional Development Fund. The simulations were partially carried out by MF with the support of the Interdisciplinary Centre for Mathematical and Computational Modelling (ICM), University of Warsaw, under grant no GA65-14. DNM and JSW acknowledge the support from high-performance computing facility MARCONI (Italy) provided by the EUROfusion. DNM also acknowledges the support from the Institute of Materials Science at Los Alamos via the funding for IMS Rapid Response 2018 visit to the LANL.

High-dose ion irradiation damage in $\text{Fe}_{27}\text{Ni}_{28}\text{Mn}_{27}\text{Cr}_{18}$ HEA characterised by TEM and nanoindentation

This paper is to be submitted.

Purpose of the paper and contributions from the authors

The purpose of this chapter was to characterize the microstructures of recrystallised and irradiated FeNiMnCr HEAs.

D. Nguyen-Manh was critical in providing the samples through his collaboration with the University of Sheffield by introducing the author into the Accelerated Metallurgy project. The author performed the specimen heat treatments partly at Manchester and partly at the University of Sheffield. The sample preparation before the irradiation experiment with the aid of E. J. Pickering and M. B. Burke. S. M. Shubeita, P. T. Wady, Y. Gu, R. Krishna and O. Ciucă aided with beam time during irradiation experiment by helping with beam set up, sample loading and doing several overnight shifts at Dalton Cumbrian Facility. E. J. Pickering and M. G. Burke helped with to prepare

TEM specimens by electropolishing and FIB lift out. The author performed most TEM microscopy work in Tecnai F20 and Phillips CM20. E. Bousser significantly helped with calibrating nanoindentation measurements. E. J. Pickering helped to obtain STEM-EDX maps with the TALOS TEM (Figs. 7.11 (d) through (i)). The author wrote the entire manuscript. M. G. Burke and P. M. Mummery guided all of the stages of the work.

Abstract

One of the key challenges for the development of high-performance fusion materials is to design materials capable of maintaining mechanical and structural integrity under the extreme levels of displacement damage, high temperature and transmutation rates. The use of ion irradiations to mimic displacement damage typical of future fusion reactors combined with post-mortem TEM characterisation of defects and nanoindentation methods are well-developed techniques at the nanoscale. Since their conception in 2004 after Cantor et al. and Yeh et al., HEAs (high-entropy alloys) have attracted attention. Pioneering investigations of radiation damage in $\text{Fe}_{27}\text{Ni}_{28}\text{Mn}_{27}\text{Cr}_{18}$ at doses as high as 10 dpa by Kumar et al. brought about the interest of the community of HEAs into irradiation damage studies. In this work, we study $\text{Fe}_{27}\text{Ni}_{28}\text{Mn}_{27}\text{Cr}_{18}$ HEA with irradiation doses as high as 20 dpa. We find the presence of Cr rich bcc precipitates in both the non-irradiated and in the irradiated condition, and the presence of dislocation loops only in the irradiated state. We argue that $\text{Fe}_{27}\text{Ni}_{28}\text{Mn}_{27}\text{Cr}_{18}$ may not be as stable against irradiation or thermomechanical processing as previously believed. We correlate the features found with irradiation hardening by the continuous stiffness method (CSM) nano-indentation technique and see that the change in the bulk stiffness increases significantly at 20 dpa for temperatures 300 and 450 °C.

7.1 Introduction

Alloys containing four or more elements in nearly equal atomic concentration or with more than 5 % concentration crystallising into fcc, bcc or hcp structures have been referred as high entropy alloys (HEAs) after Yeh et al. [11, 283] or as multi-component alloys (MCPs) after Cantor [156]. The high number of different combinations of elements in HEAs can make possible the discovery of materials properties that can not be achieved in conventional alloys, which only contain one-element as principal. The interest of HEAs as high-temperature structural materials for nuclear industries has been motivated by some reports of their attractive mechanical properties at elevated temperatures including hardness, strength, ductility, wear, and corrosion resistance [12]

The structural materials for fusion reactors plants will experience very demanding environments in terms of high temperatures (300-800 °C) and intense 14 MeV neutron irradiation fluxes [284] posing potential challenges to mechanical strength, fracture toughness and ductility and dimensional changes due to void swelling and creep [285]. The development of high-performance materials that are radiation resistant is critical for advanced nuclear reactor systems. In particular, HEAs could be potential candidates for fuel cladding of Generation IV reactors and pressure vessels [12]. Due to their chemical complexity, different atomic sizes and charge transfer among the elements in the random solid solution, atomic-level stresses have been rationalised as the cause for reduced number densities of vacancy or interstitial defect clusters due to enhanced vacancy-interstitial recombination of defect clusters in the cascade following the thermal spike [16, 286, 18].

Recently, attention has been drawn to multicomponent alloys, in particular, HEAs containing light transition metal elements Co, Cr, Fe, Ni, and Mn that form predominantly a single phase with secondary phase precipitates that

can form after prolonged heat treatments [212, 13]. It is interesting to note that strength and ductility studies in the CrMnFeCoNi HEA showed excellent low-temperature dependent behaviour with ductility and strength not being inversely proportional as usually occurs for conventional alloys [15, 14]. Nevertheless, for some of the alloys belonging to the family of CrMnFeCoNi HEA but without Co, mechanical tensile tests have indicated that these alloys can become brittle due to the presence of the hard and brittle σ phase [13, 287]. The embrittlement studies motivated the study of particular alloy composition, specifically Cr content controlled to narrow down selection to composition $\text{Fe}_{27}\text{Ni}_{28}\text{Mn}_{27}\text{Cr}_{18}$ [151]. The composition of $\text{Fe}_{27}\text{Ni}_{28}\text{Mn}_{27}\text{Cr}_{18}$ has also been pointed out as favoured for nuclear applications due to the removal of Co. If Co is exposed to intense high energy neutron fluxes, it can transmute into ^{60}Co long-lived radioactive isotope [21].

In previous work [20], the microstructure and hardness of 5.8 MeV Ni irradiated $\text{Fe}_{27}\text{Ni}_{28}\text{Mn}_{27}\text{Cr}_{18}$ HEA was studied up to doses of 10 dpa and temperatures of 700 °C by TEM and by nanoindentation. In the study, the HEA was reported to be a single-phase solid solution and remain stable during irradiation. The essential radiation-induced features were high-density dislocation loop formation, reduced grain boundary Cr segregation compared to FeCrNi austenitic stainless steels irradiated to similar doses, and lack of void formation. The authors rationalised the small size, and high number density of dislocation loops in comparison to equivalent irradiated FeCrNi austenitic stainless steels as being due to a reduced point defect recombination in this HEA.

Heavy-ion irradiations have been used as simulation experiments for neutron damage in structural materials since they are amenable to flexible environmental conditions, including control of temperature and displacement per atom rate [288]. These parameters are not so easily controlled during in-reactor irradiation experiments. Furthermore, the high rates of displacement

per atom from heavy ion irradiations, which are several orders of magnitude higher than for neutron irradiations, speed up the accumulation of radiation damage [288]. The drawbacks of heavy ion irradiation are mainly the few μm ranges of implanted damage that makes difficult sample preparation for microscopy.

Irradiation hardening is one of the main degradation issues for structural materials in fusion reactor components of the blanket. The nanoindentation technique was first applied to study irradiation hardening in irradiated CuZr alloy [289]. Since then, nanoindentation has been used as a tool to probe the change in mechanical behaviour (elastic modulus and plasticity) of thin layers typically a few microns exposed to light particle or heavy ion radiations [290, 291, 292, 293, 294, 295, 296, 297]

This current work aimed to assess the irradiation behaviour of the $\text{Fe}_{27}\text{Ni}_{28}\text{Mn}_{27}\text{Cr}_{18}$ alloy in detail at high doses to further elucidate mechanisms for irradiation resistance. The structure of this paper is as follows: $\text{Fe}_{27}\text{Ni}_{28}\text{Mn}_{27}\text{Cr}_{18}$ is characterized in non-irradiated state by TEM ; the microstructure of the 5 MeV Ni irradiated $\text{Fe}_{27}\text{Ni}_{28}\text{Mn}_{27}\text{Cr}_{18}$ is characterized by TEM; and hardening is studied from nanoindentation measurements.

7.2 Experimental methods

7.2.1 Thermo-mechanical processing and sample preparation

The $\text{Fe}_{27}\text{Ni}_{28}\text{Mn}_{27}\text{Cr}_{18}$ HEA specimens were prepared by arc melting in a Ti-gettered high-purity argon atmosphere at the University of Sheffield, U.K by mixing high purity (99.9%) elemental Cr, Mn, Fe and Ni in the concentra-

tion of 18%-27%-27%-28% at. % respectively. To cross-check the average chemical composition of the as-cast HEA SEM-EDX analysis was conducted over 10 regions of the approximate area given by 100 μm by 100 μm . The resulting analysis is shown in Table 7.1, which agrees reasonably well with the expected composition values, thus indicating that no relative depletion of alloy element in bulk occurred in the manufacturing process.

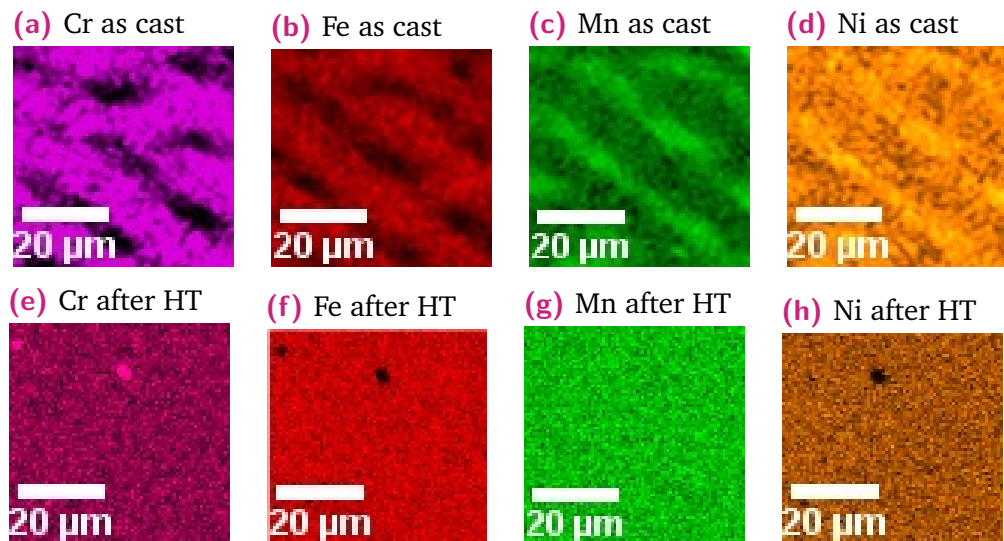
Table 7.1.: Chemical composition of $\text{Fe}_{27}\text{Ni}_{28}\text{Mn}_{27}\text{Cr}_{18}$ HEA for this work, measured with SEM-EDX

Element	at.% ([20])	at.% (this work)
Cr	18.00	18.0 ± 0.1
Mn	27.00	26.0 ± 0.6
Fe	27.00	28.1 ± 0.3
Ni	28.00	27.9 ± 0.3

More detailed analysis performed with a FEI SEM with EDX (Scanning electron microscopy-energy dispersive X-rays) revealed micro-segregation at the μm scale with the presence of dendrite-like structures of approximately 20 μm separated see Figs. 7.1 a-d. To homogenise and anneal possible sinks for irradiation defects in the microstructure we performed a homogenization heat treatment at 1200 °C for 48 hr and water quench, then cold forging to a thickness reduction of 40 %. And finally a re-crystallisation heat treatment at 900 °C for 4 hr followed by furnace cooling. The results are shown in Figs. 7.1e-h. The heat treatment was performed to reproduce work by Kumar et al. [20], which resulted in an fcc recrystallised structure (see Fig. 7.2) with the lattice spacing of 3.64 nm.

Thermomechanically processed specimens were electro-discharge machined into square blocks of approximate size 10 mm and thickness between 0.5 and 1 mm. Grinding and polishing were performed on an automatic spinner platen with abrasive SiC paper P800, P1200, P2400 and P4000, then followed by polishing with 1 μm polycrystalline diamond suspension in a cloth, and finally the specimens were OPS polished until grain boundaries appeared slightly etched in the optical microscope Zeiss Axio. The mean grain size in

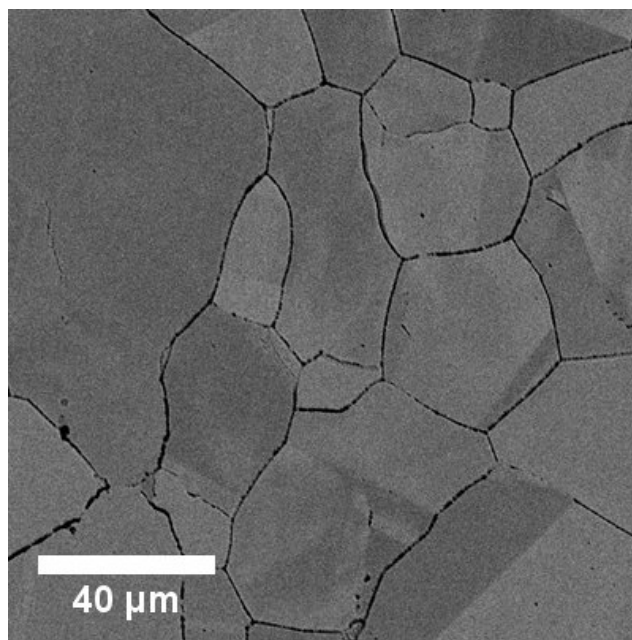
Fig. 7.1.: Representative SEM EDX maps of Cr, Fe, Mn and Ni before (a)-(d) and after (e)-(h) homogenisation heat treatment in as cast $\text{Fe}_{27}\text{Ni}_{28}\text{Mn}_{27}\text{Cr}_{18}$ HEA at 1200 °C for 48 hrs. During the heat treatment MnCr oxide inclusions appeared, these are shown in the heat treated maps as black dots.



the recrystallised condition was found to be approximately 45 μm by simple linear intercept method from the SEM micrograph in Fig. 7.2

The recrystallised condition was characterised by X-ray diffraction (XRD) to ascertain that our microstructure is face-centred cubic (fcc) and to find the lattice spacing. The powder diffractometer used for this work was a Phillips XRD5 PANalytical X'Pert Pro using a combined characteristic radiation of $\text{CuK}\alpha_1$ and $\text{CuK}\alpha_2$ X-rays with a Nickel foil to remove β X-ray radiation and a graphite monochromator to reduce fluorescence effects that can mask the diffraction peaks in samples containing transition metal elements (our sample has Fe, Cr, Mn and Ni). This diffractometer uses $\theta - \theta$ Bragg-Brentano geometry, and the sample is spun along the normal to its planar surface. The working voltage of the diffractometer was 40 kV, and the operating current was 40 mA. The scanning region ranged from 35 ° to 110 °, in steps of 0.05°

Fig. 7.2.: SEM Backscattered electron micrograph of the recrystallised microstructure indicating the grain structure after etching with metallographic etchant of nitric acid and ethanol



7.2.2 Self-ion irradiation experiment

For the irradiation experiment, the recrystallised specimens were mounted on the sample end-stage at the 30° beamline from Dalton Cumbrian Facility [217]. The beam was focused and operated in rastering mode. The last beam slits were adjusted to trim the beam to irradiate an area uniformly of 7 by 7 mm^2 area for all of the samples reported in this study. The sample temperature was monitored continuously throughout the irradiation experiment by using camera recordings of infrared and visible radiation calibrated according to a Black-body energy emission formulation to measure the temperature increase due to the combined beam heating and external heaters (see Fig. 7.4). The real beam current on the sample was monitored through the continuous reading of charge deposited at the end-stage by a data acquisition system implemented with LabView. Corrections were applied to measured current on the sample to compensate for the spurious secondary electron emission from the sample upon the impact of the heavy ions.

Table 7.2.: Irradiations performed at Dalton Cumbrian Facility [217] with Nickel ions (excitation state +3) at 5 MeV under different conditions. The dose rate (dpa/s) was 2.4E-04 for all but the 2nd sample in the Table for which was 4.40E-04

Ion fluence (ion/cm ²)	Dose (dpa)	Temperature (°C)	Exposure (time)
8.00E+14	2	300	2 h 19 min
8.00E+15	20	300	12 h 37 min
8.00E+15	20	450	23 h 9 min
8.00E+14	2	450	2 h 19 min

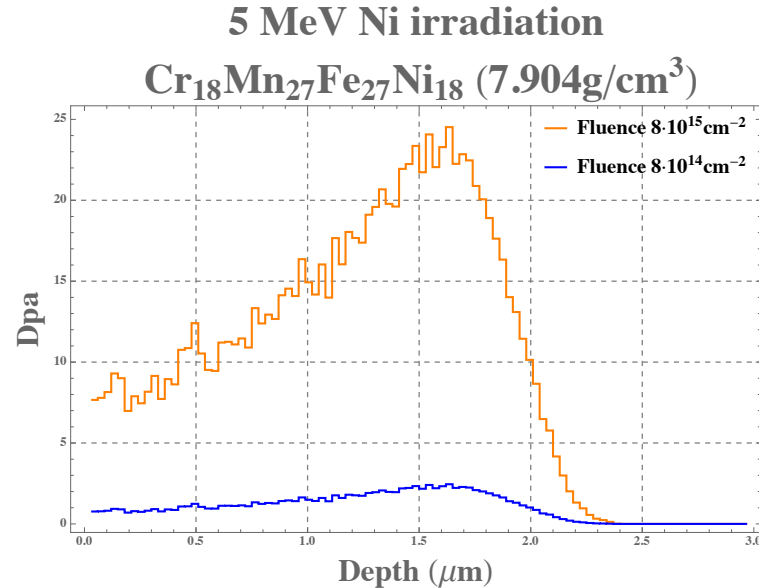
The displacements per atom (dpa) were estimated from SRIM (2008 version) [298] code and at 80% depth of the Bragg peak for 5 MeV Nickel ions with +3 charge state. To make consistent our ion irradiation doses with potential future neutron irradiations we set up the SRIM simulation with lattice and surface binding energies of the Cr, Mn, Fe and Ni atoms equal to zero and we choose the Kinchin-Pease calculation mode following findings from [56]. For the displacement energies of the lattice atoms Cr, Fe, Mn and Ni 40 eV was used. The peak dpa is estimated from SRIM dpa per fluence and the estimated fluence of the ion irradiation deposited charge corrected on each of our specimens (see Fig. 7.3).

7.2.3 Nanoindentation methods

For carrying out depth-sensing nanoindentation, we used MTS Nano Indenter XP equipped with a Berkovich indenter. The maximum allowed drift rate was set to 0.15 nm/s and a surface approach velocity for the tip of 10 nm/s. The penetration depth range examined in the irradiated specimens ranged from 0 to 2000 nm with a maximum load of 200 mN (see Fig. 7.5). The average hardness values were determined from averaging 25 hardness values each being derived from a continuous load-displacement curve by using the continuous stiffness method (CSM). The 25 impressions were spread in

Fig. 7.3.: Displacement per atom (Dpa) (a) and Nickel (atomic %) implantation profile (b) in $\text{Fe}_{27}\text{Ni}_{28}\text{Mn}_{27}\text{Cr}_{18}$ for the two fluences considered in Table 7.2. Calculation with SRIM [298]

(a)



(b)

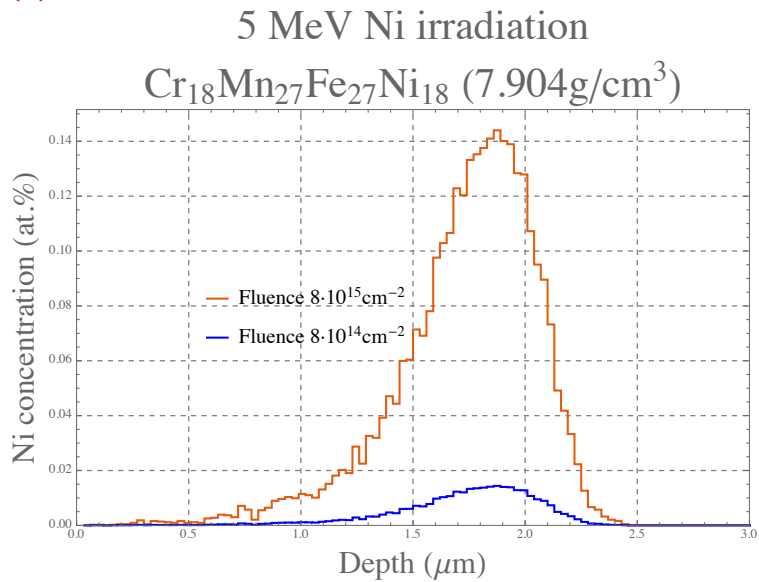


Fig. 7.4.: Sample set up for irradiation experiment at beamline of Dalton Cumbrian Facility. An approximate area of 7 by 7 mm² delimited by scintillator quartz crystal is irradiated uniformly by the ion beam. The irradiation temperature is controlled by the heaters below the specimen and a chiller circulating continuously. The tantalum shield prevents the structural material of the stage from becoming activated by the incident radiation

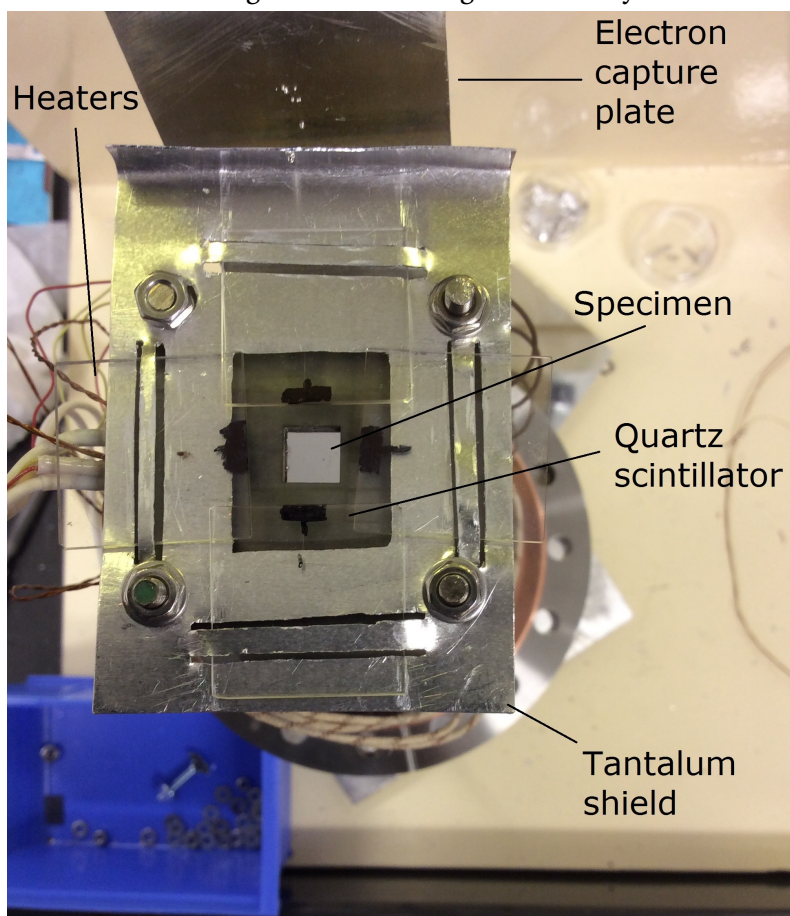
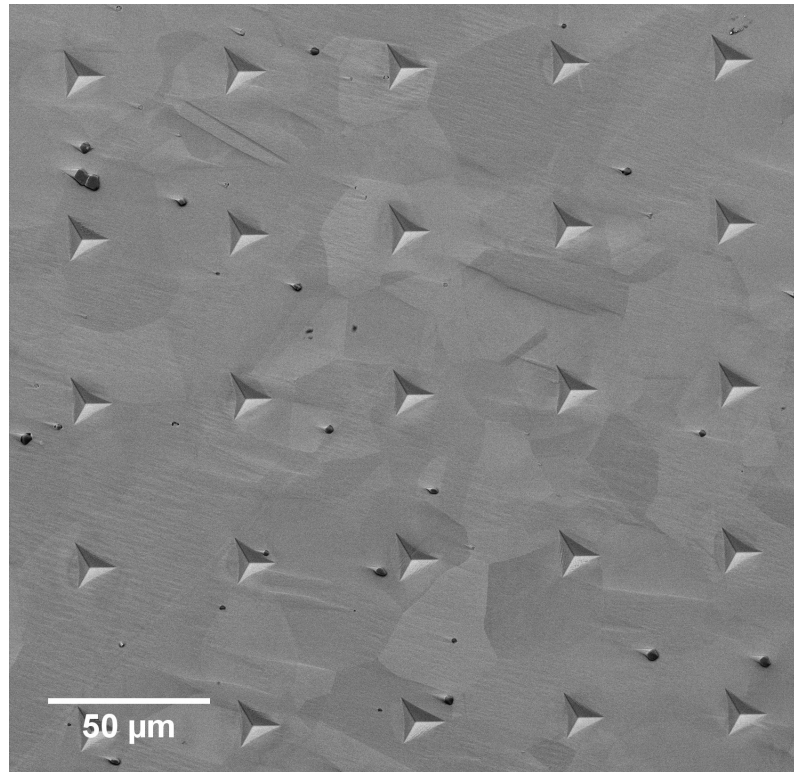


Fig. 7.5.: Representative SEM image of array nanoindenter impressions after the test. The impressions are spaced approximately $50 \mu\text{m}$ apart and were performed on a sample irradiated at 300°C and 20 dpa



an array of points separated by $50 \mu\text{m}$ to avoid interference effects due to localised plastic zones among the indents.

To calibrate the area of tip truncation or bluntness from the Berkovich-type indenter fused silica (FS) reference specimen was used. The method developed by [236] for contact area calibration from local stiffness measurements were used to obtain the correct functional form of the contact area under the tip of the indenter as a function of the contact depth, h_c

Using fused silica test sample, we generate values of experimental contact area from the model formula that depends on the material stiffness which can

be estimated from effective stiffness after removing the frame contribution, i.e. $1/S_{eff} = 1/S_f + 1/S$:

$$A_c = \frac{\pi}{4} \frac{S^2}{(\beta E_{eff})^2} \quad (7.1)$$

We assume the validity of the contact area, A_c , formula to be applicable down until the regime of forces similar to adhesion forces (μN), below which we assume the formulation to be invalid. In the regime where expression 7.1 holds uncertainties in the material and frame stiffness contribute into the best estimate for the contact area as $\sigma_{A_c} = aA_c$, where a is a constant (presumably dependent on the frame stiffness) and to be optimised at a later stage for finding the best fit. The contact area is parametrised by the contact depth, which for materials with no pile-up (such as fused silica) requires subtraction of these effects from the total measured depth

$$h_c = h - \epsilon \frac{P}{S} \quad (7.2)$$

Following work by Oliver and Pharr for calibration using fused silica samples [236] we use $E_{eff}=69.9$ GPa, $\beta=1.034$ and $\epsilon=0.75$. The parametrisation of contact area formula for fitting purposes is assumed to be given by the full polynomial formed by powers of contact depth ranging from 2 down to 1/128; i.e.

$$\begin{aligned} A_c[h_c] &= \sum_{n=1}^9 C_n h_c^{2^{-n}} = C_1 h_c^2 + C_2 h_c + C_3 h_c^{1/2} + C_4 h_c^{1/4} + C_5 h_c^{1/8} \\ &\quad + C_6 h_c^{1/16} + C_7 h_c^{1/32} + C_8 h_c^{1/64} + C_9 h_c^{1/128} \end{aligned} \quad (7.3)$$

Table 7.3.: Polynomial coefficients after fitting. The units of the parameter values are used to give the contact area, A_c , in units of nm² when substituted into contact area expression 7.3.

Parameter	C_i	σ_{C_i}
h_c^2	$+1.02 \cdot 10^{02}$	$1.35 \cdot 10^{01}$
h_c	$-1.91 \cdot 10^{06}$	$2.35 \cdot 10^{05}$
$h_c^{1/2}$	$+1.40 \cdot 10^{09}$	$1.90 \cdot 10^{08}$
$h_c^{1/4}$	$-1.43 \cdot 10^{11}$	$2.04 \cdot 10^{10}$
$h_c^{1/8}$	$+3.96 \cdot 10^{12}$	$5.81 \cdot 10^{11}$
$h_c^{1/16}$	$-3.96 \cdot 10^{13}$	$5.87 \cdot 10^{12}$
$h_c^{1/32}$	$+1.06 \cdot 10^{14}$	$2.39 \cdot 10^{13}$
$h_c^{1/64}$	$-2.58 \cdot 10^{14}$	$3.86 \cdot 10^{13}$
$h_c^{1/128}$	$+1.33 \cdot 10^{14}$	$2.00 \cdot 10^{13}$

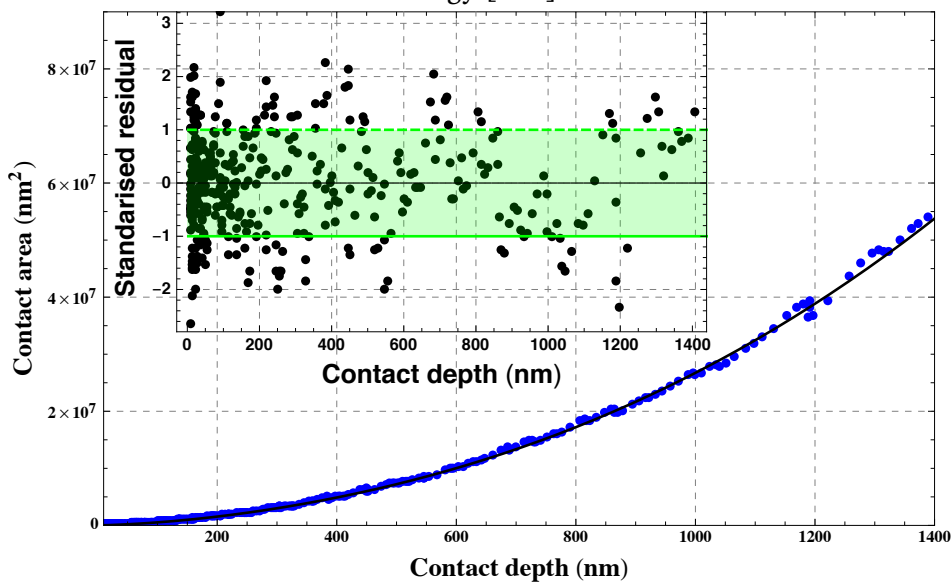
Data at contact depths less than 10 nm was removed due to atomic surface effects in the determination of the contact area. In the regime of contact depths less than 10 nm, the measured loads were at least as high as the adhesion force, approximately found to be 40 μN . Only data belonging to the loading profile is considered in this work.

The uncertainties for depths less than 1100 nm we take $\sigma_{A_c} = 24 \cdot 10^{-3} A_c$ where $a = 24 \cdot 10^{-3}$ and for areas at depths greater than 1100 nm we take $\sigma_{A_c} = 4.5 \mu\text{m}^2$. For these uncertainties the fit is good by the χ^2 test. The best parameters estimates are written in Table 7.3.

The standardised residuals agree reasonably well with the assumption of errors normally distributed and are plotted in a green colour band from Fig. 7.6.

We fitted a formula for contact area in the approximate contact depth range 0-1400 nm. We tested the goodness of the fit by using $R^2=0.99$ and $\chi^2_r=1.04$ criteria. The area function is characteristic of the tip of the indenter and

Fig. 7.6.: Experimental fit of contact area with contact depth for fused silica using Oliver and Pharr methodology [236]



can be used to compute hardness in other materials, provided the loads and contact displacements are known.

Bulk equivalent hardness in irradiated specimens, H_0 , is computed from fitting the contact depth-dependent hardness $P[h_c]/A[h_c]$ according to a formulation in terms of parameters h_0 and H_0 similar to well known indentation size effect (ISE), $H[h_c] = H_0\sqrt{1 + h_0/h_c}$. This formulation has previously been applied for irradiated specimens by [291]. Bulk equivalent irradiation hardening is then estimated by subtracting the equivalent bulk hardness of the non-irradiated specimens from the each of the bulk-equivalent hardness in the irradiated samples. Irradiation hardening can then be studied as a function of dose and irradiation temperature.

7.2.4 TEM sample preparation

TEM lamellae for characterising the $1 \mu\text{m}$ thin irradiated layer were prepared by the FIB lift-out method using Ga ions in a Quanta 3D operated at 30 kV. Final cleaning-polishing was performed at 2 kV to minimise Ga ions induced

damage on the microstructure until lamellae were electron transparent. The lamellae were mounted in a Cu TEM grid. The lamellae were observed in Tecnai F20, and a TALOS with TEM and STEM-EDX modes both operated at the accelerating voltage of 200 kV.

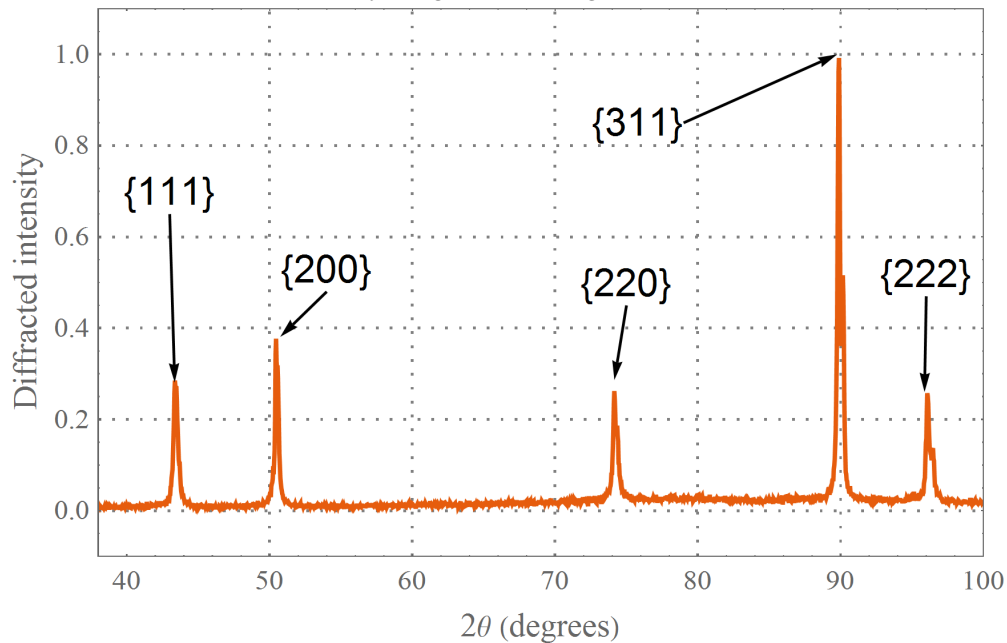
7.3 Results and discussion

7.3.1 Microstructural characterization in the non-irradiated condition

The XRD pattern from the recrystallised microstructure indicates that the fcc structure is the main phase within the detection limits of the signal-to-noise ratio (Fig. 7.7). The single-phase stability of $\text{Fe}_{27}\text{Ni}_{28}\text{Mn}_{27}\text{Cr}_{18}$ HEA is in agreement with the chemical homogeneity colour maps of Cr, Mn, Fe and Ni in the SEM-EDX results after annealing (see Fig. 7.1). We use the CMPR software [223] to investigate the parameters of the structure by predicting the angular location for the diffracted intensities from basic crystallographic information and optimise the lattice constants to fit the experimental intensity peak positions. The refined lattice parameter was found to be 3.61 \AA in space group O_h^5 .

SEM-EDX maps 7.1 and TEM selected area diffraction from the matrix (Fig. 7.11 a) material confirmed the XRD predictions of fcc homogeneous solid solution phase except for oxide inclusions abundant in Mn and Cr associated to the spinel structure. Their presence could be related to the oxygen impurities in the raw materials or contamination in the manufacturing process in the arc melter, as has been found for Cantor alloy [79, 13].

Fig. 7.7.: XRD diffraction pattern as obtained from recrystallised $\text{Fe}_{27}\text{Ni}_{28}\text{Mn}_{27}\text{Cr}_{18}$ HEA. The secondary peaks to the right of the main peaks are due to diffraction caused by longer wavelength of $\text{CuK}\alpha_2$ radiation.



We find significant dislocation pile-up and dislocation arrays in Figs. 7.8 a)-b) in the recrystallised microstructure, indicating a build-up of stress at the phase boundaries between fcc grains or fcc-bcc boundaries. This is likely to occur from the sample preparation procedure of electropolishing.

Recrystallised CrMnFeNi HEAs were analysed with the TEM to find precipitates. The precipitates found are shown in Fig. 7.11 c-i, where the structure of these precipitates is consistent to be consistent with the bcc symmetry. The precipitate is shown to lay along the grain boundary of the fcc matrix, but we also found precipitates within the recrystallised grains in the samples. By calculating the distance between diffraction spots along with the (200) directions (7.11(a)), the lattice constant of the bcc phase is approximately given by 2.9 \AA . The findings of a bcc phase of similar lattice constant as Cr has been reported in previous works for CrMnFeCoNi Cantor alloy [299]. The bcc precipitates are seen to be rich in Cr and depleted in Mn, Fe and Ni as shown in STEM-EDX maps in Fig. 7.11

Fig. 7.8.: TEM micrographs of the recrystallised condition. (a) for pile up of dislocations; (b) for slip band of dislocations

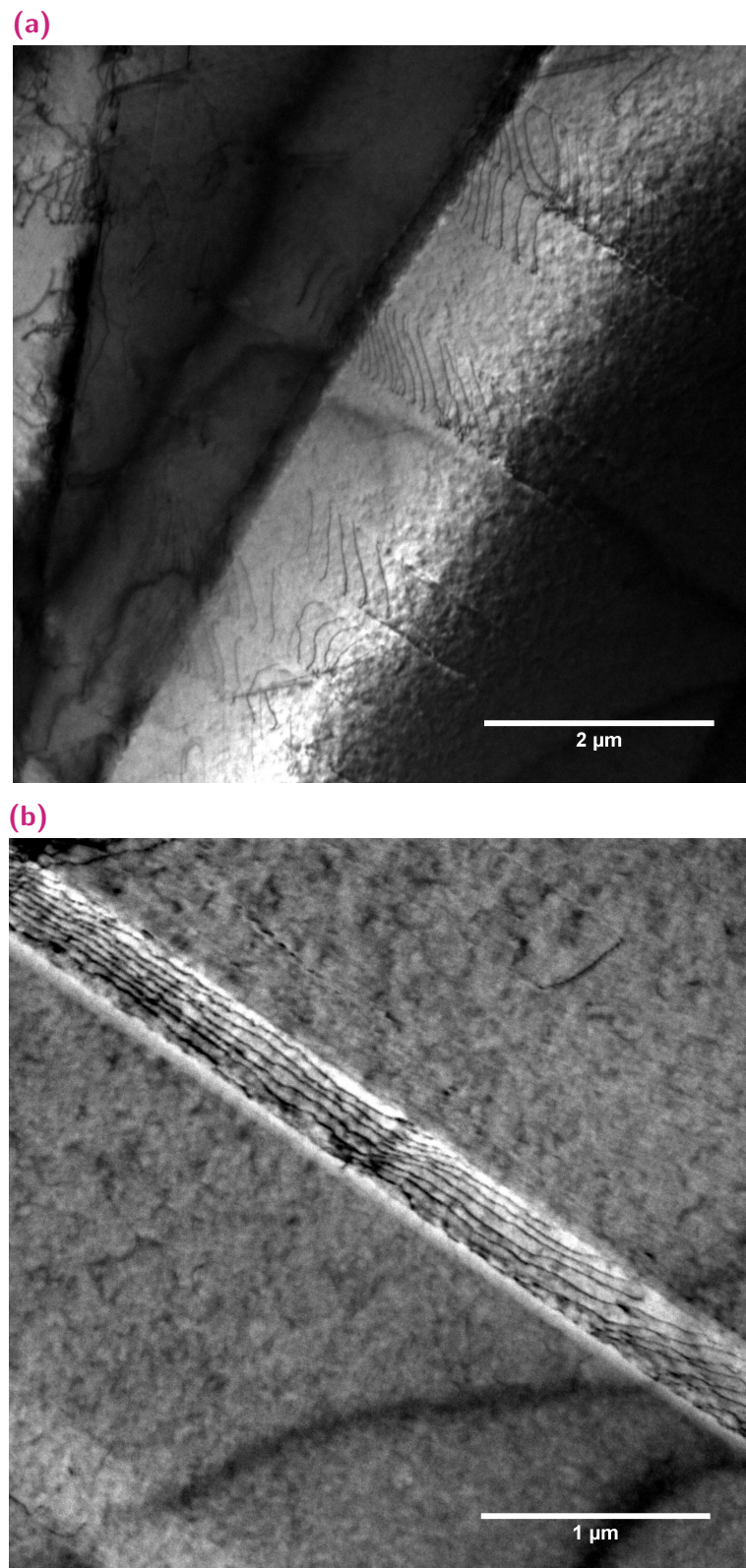
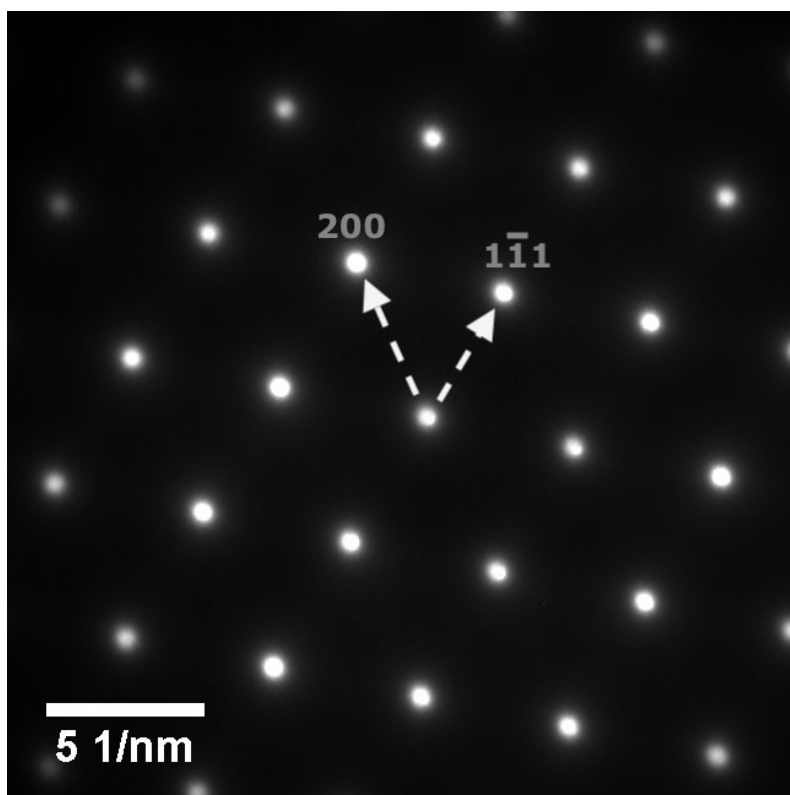


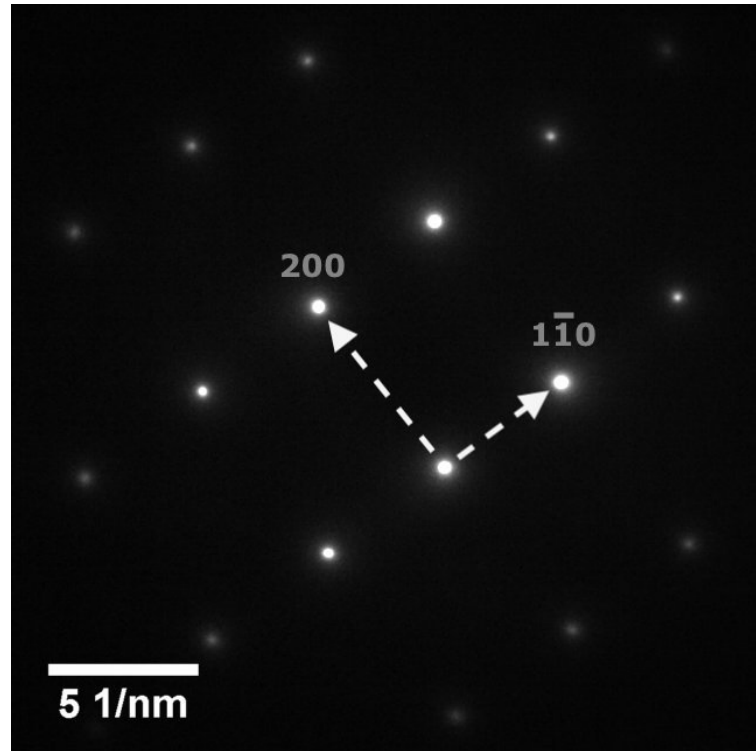
Fig. 7.9.: TEM selected area diffraction (the zone axis is [011] crystallographic direction for fcc matrix



The presence of the bcc phase in the fcc matrix was not reported in previous studies [20]. The presence of the bcc phase can be rationalized by the empirical VEC (Valence Electron Concentration) model [92]. In the VEC model, the average electronic concentration is worked out from the composition weighted electronic ground state configuration in the s, p, d orbitals of the alloy's constituent elements. According to the VEC model [92], single bcc phase was attributed to $3 < VEC < 6$, and single fcc phase for $8 < VEC < 11$. In the $\text{Fe}_{27}\text{Ni}_{28}\text{Mn}_{27}\text{Cr}_{18}$ HEA, application of the empirical VEC model gives 7.93, which lays in between the bcc, and fcc regions $6 < VEC < 8$; consequently mixed bcc and fcc phases are expected.

Fig. 7.10.: TEM selected area diffraction (the zone axis is [011] crystallographic direction for bcc phases (a)) and Dark Field Micrographs (b)

(a) Cr precipitate



(b) Dark field

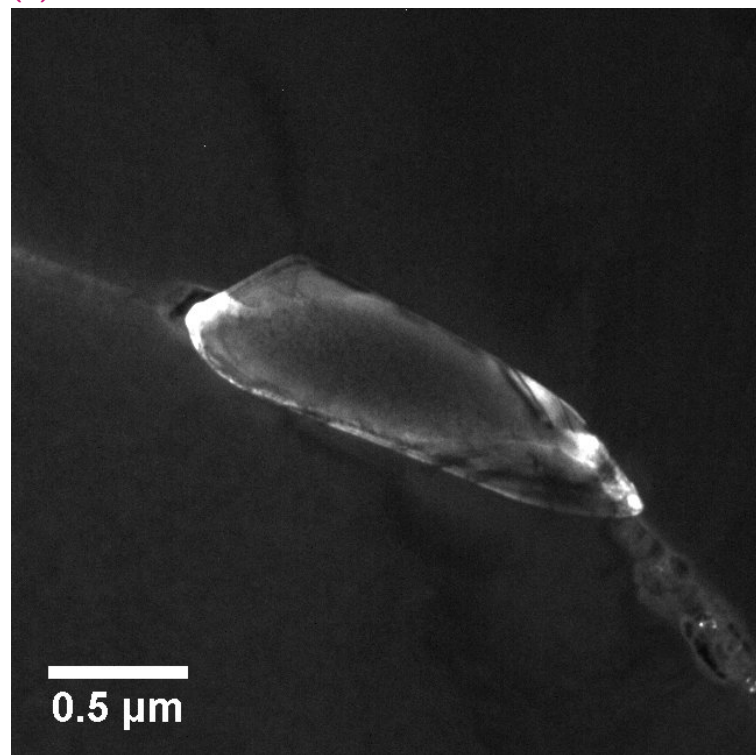
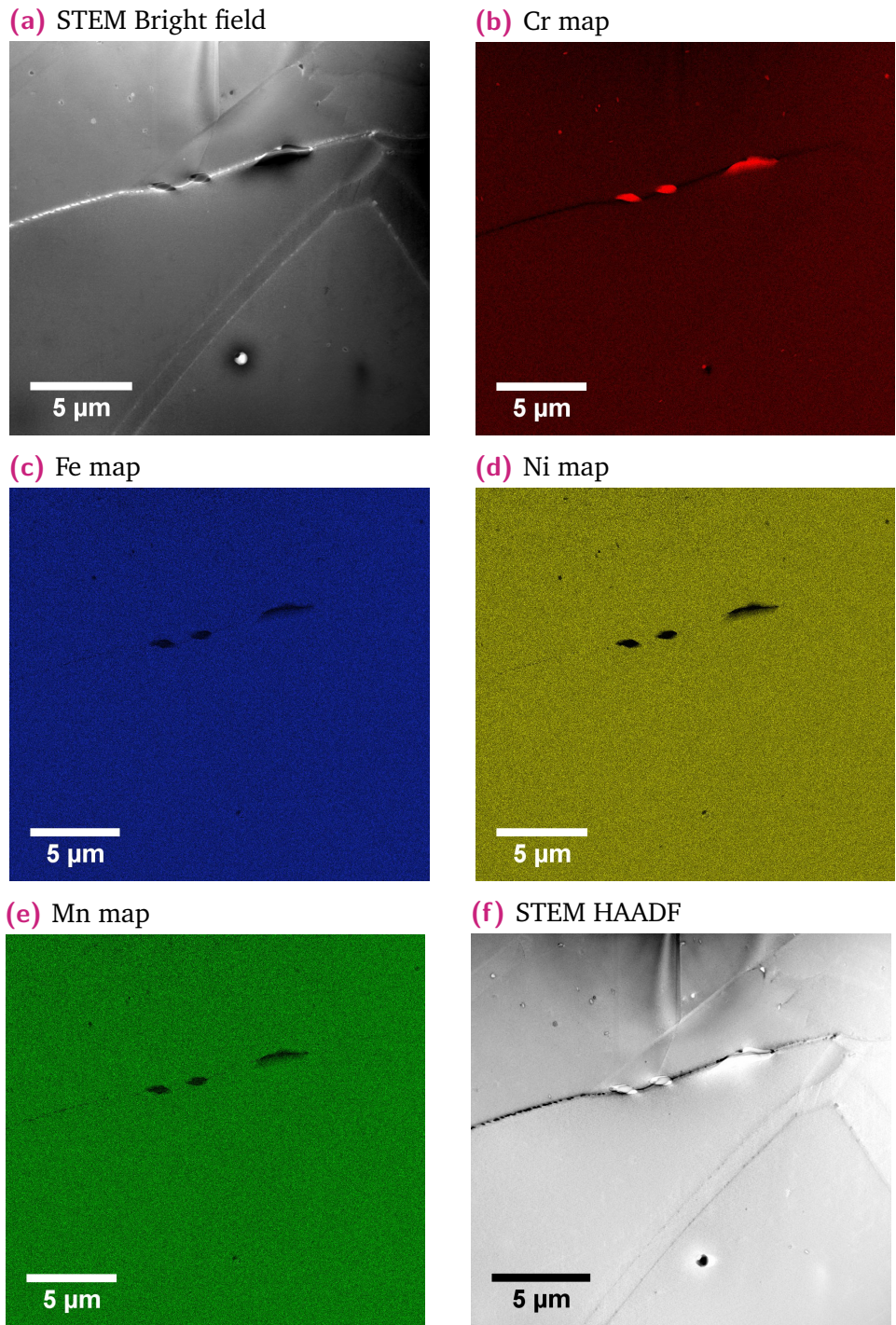


Fig. 7.11.: STEM Bright Field (a) and high angle annular dark field (f), and STEM energy dispersive X-ray maps of Cr (b), Fe (c), Mn (e), and Ni (d)



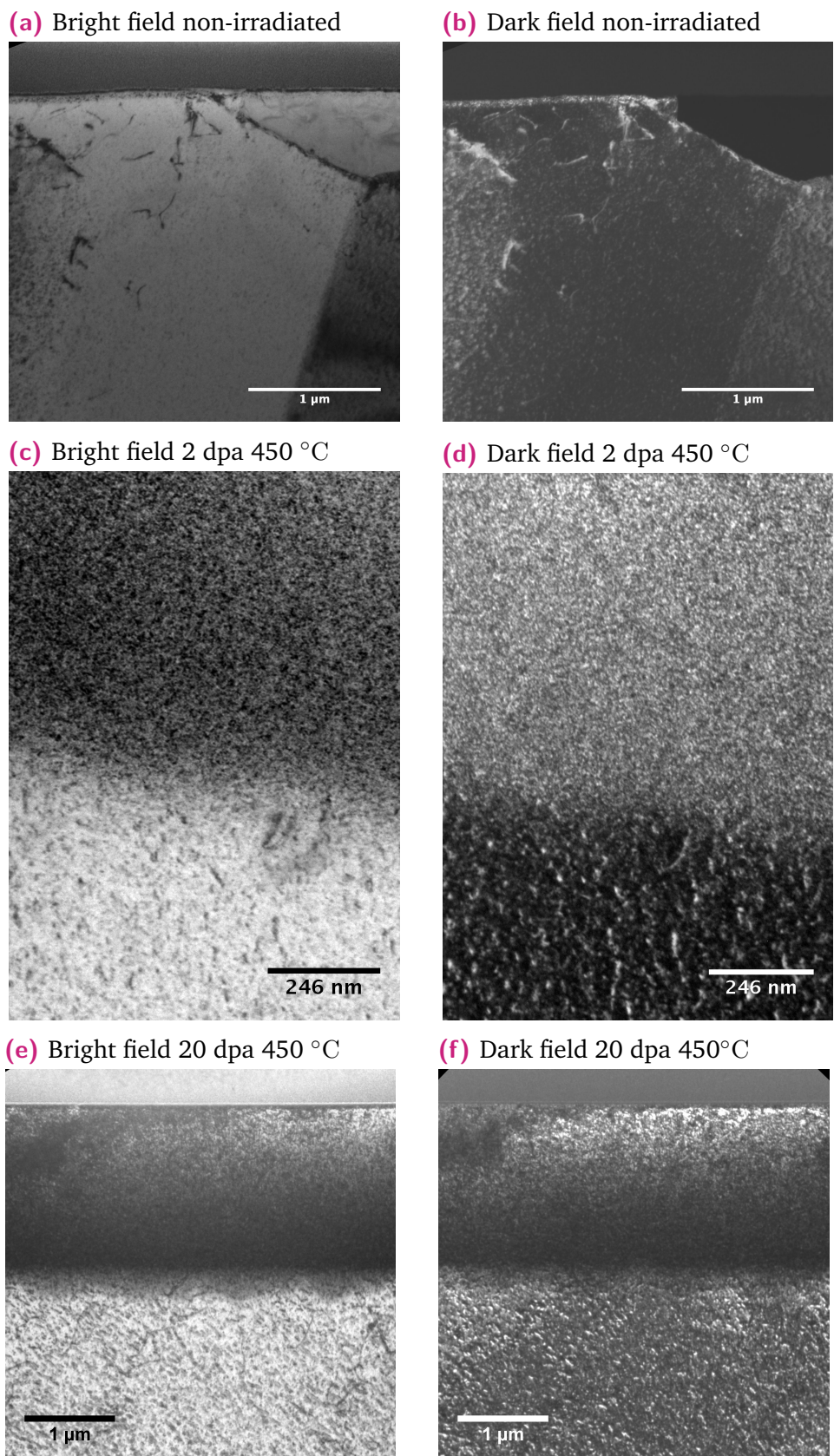
7.3.2 Microstructural characterization in the irradiated condition

The Bragg peak corresponding to the Ni irradiation was found at the approximate depth of $1.6 \mu\text{m}$, which according to our SRIM estimations from Fig. 7.3 is separated from the Ni implantation peak which is at $1.9 \mu\text{m}$. The peak dose achieved was approximately 20 dpa, and the peak Ni implantation was approximately 0.14 at.%, as indicated in Figs. 7.3 (a), and 7.3 (b) respectively. The values for the main parameters fluence, dose, irradiation temperature, exposure time and dose are detailed in Table 7.2.

Radiation damage produces individual point defects in the form of vacancies and interstitials as well as clusters of point defects. In fcc materials, the vacancies and interstitials can form dislocation loops of vacancy or interstitial types as well as voids. In situations where vacancy mobility is low due to an operating temperature less than approximately half of the melting temperature, vacancy dislocation loops are known [149] to be unstable due to the higher capture radius of dislocation for interstitial than vacancy point defects. Thus resulting in the annihilation of vacancy loops by diffusing interstitial point defects and leaving the only interstitial loops stable. In Fig. 7.12 (e)-(f), we show dislocation loop contrast corresponding to Frank loops by using the two-beam condition. Based on the dislocation bias argument we reason that the loops are of interstitial-type faulting.

Preparation of TEM lamellae using Ga ions with the FIB technique can produce ripple-shaped contrast and black dot contrast [300]. The non-irradiated specimens shown in Figs. 7.12 a)-b) are prepared to reduce FIB damage by following a careful 2 kV final cleaning-polishing; there is no damaged layer in the non-irradiated samples when compared to remaining Figs. 7.12 c)-f). The Frank loops may be attributed to the Ni 5 MeV

Fig. 7.12.: Micrographs of irradiated HEAs Lamella prepared by the FIB lift-out method. In the lamellae, the platinum layer of protection is found at the top of the images. The platinum location indicates the entry direction of the ion irradiation as it penetrated the bulk of the recrystallised specimen.



irradiation field and not from the FIB preparation work. The depth of the observed damage layer in the irradiated sample in Fig. 7.13(f) has a varying depth between 1.9 and 2.1 μm is consistent with SRIM 5 MeV Ni implantation and dpa simulations as shown in Figs. 7.4(a) and 7.4(b)

7.3.3 Irradiation hardening from nanoindentation tests

Mechanical properties are affected by radiation damage. In materials that do not suffer from brittle fracture, the yield point marks the onset for free movement of dislocations in glide planes. During irradiation, defects are introduced in these glide planes and these obstacles inhibit the passing of dislocations through them. The yield strength can increase with irradiation dose at low temperatures when dislocations can not climb.

To understand the effects of dislocation loops in the irradiated specimens, we choose nanoindentation to quantify the effect of damage on the mechanical strength after the ion irradiations. In particular, we choose to indent from the top of the irradiated surface rather than from the cross-section due to the fragile irradiated layer.

For studying irradiation hardening, we repeat the analysis undertaken for the non-irradiated samples with the irradiated samples and apply the irradiation hardening model from [291] based on an extension from geometrically necessary dislocations of Nix and Gao [301] between the depth range between 100 nm and the inflection point of the hardness squared curves. We estimate the irradiation hardening $\Delta H_{\text{irr}} = H_0^{\text{irr}} - H_0^{\text{nonirr}}$ for each of the irradiated samples and report the results in table 7.4; and find that hardness increases with dose up to 4 GPa at all irradiation temperatures, furthermore we find

Fig. 7.13.: Example load displacement curve averaged across 25 indents for the non-irradiated specimen 7.14(a), and 2dpa irradiated specimen 7.14(b).

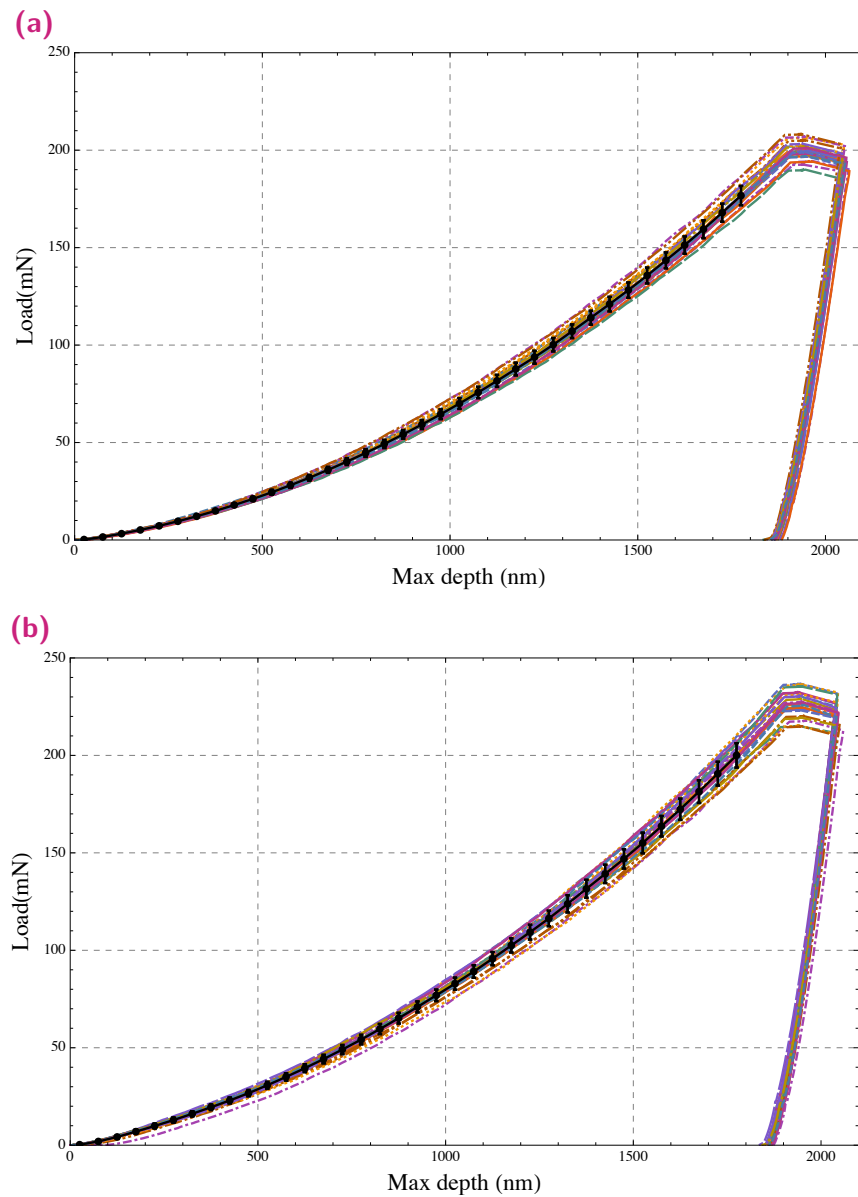


Table 7.4.: Irradiation hardening (in GPa units) concerning non-irradiate condition as obtained from this work (first two rows), and previous work [20] (last two columns).

Irradiation temperature	Low dose (0.2 dpa)	Medium dose (2 dpa)	High dose (20 dpa)
300° C		2.5±0.9	3.7±0.4
450° C	0.5±0.5	0.3±0.2	4.4±0.7
	Low dose (0.3 dpa)	Medium dose (3 dpa)	
25° C	2.31 ([20])		
500° C	0.33 ([20])	0.47 ([20])	

that irradiation temperature effects from 300 and 450 °C are no significant differences.

Previous work [20] reported room temperature and 500 °C nanoindentation results in ion-irradiated CrMnFeNi. We have compared their data to ours in Table 7.4. In this work, we explored high doses to 20 dpa, and find that the increase in hardness after irradiation at 450 °C is 4.4 GPa, which expands the knowledge of the irradiation behaviour of this alloy after the hardness increase value of 0.47 GPa reported in [20] after 3 dpa of irradiation.

7.4 Conclusion

In the non-irradiated condition, we find Cr-rich bcc precipitates in the fcc- $\text{Fe}_{27}\text{Ni}_{28}\text{Mn}_{27}\text{Cr}_{18}$ HEA matrix, this is in contrast to previously reported work in this alloy [20], which found no precipitates in any condition. In the irradiated state we find that dislocation loops of interstitial-type occur under irradiation, but in very high number densities difficulting quantitative analysis. The TEM experimental observation of a damaged layer with depth varying between 1.9 and 2.1 μm is consistent with SRIM 5 MeV Ni implantation and dpa simulations. To understand the implications of these radiation-induced

defects in HEAs we use a hardening model based on previous work to convert measured nanoindentation hardness in the damaged layer of thickness 1400 nm to bulk equivalent hardness. Change in hardness is measured at 0.2, 2, and 20 dpa and at irradiation temperatures of 300 °C and 450 °C. The findings of this work suggest that irradiation hardening at 20 dpa is as high as 4 GPa, indicating significant hardening in contrast to previous works.

Conclusion and future work

“ If a man knows not to which port he sails,
no wind is favorable.

— Seneca the Younger

8.1 Conclusion

In this thesis, the following findings were made concerning the thermodynamical equilibrium of HEAs and also concerning their irradiation behaviour.

1. A general formulation for treating short-range order for 4 or 5 component HEAs was developed from first-principles electronic structure calculations.
2. Application of the short-range formulation to quinary Mo-Nb-Ta-V-W HEA and two of its quaternary sub-systems (Mo-Nb-V-W and Mo-Ta-V-W) in the BCC lattice. In the Ta containing systems, it is predicted that Mo-Ta is particular stable binding due to very negative short-range order parameter for the Mo-Ta pair. This result is rationalized by the tendency of the A2 disordered phase to precipitate into the B2 Mo-Ta ordered phase. Furthermore, B2 ordered phase is consistent with a very negative enthalpy of mixing. For the quaternary Mo-Nb-V-W HEAs chemical preference between Mo-Nb pair is found to be dominant.

For the remaining chemical pairs, segregation is expected due to the predicted value for their short-range order parameters.

3. Development of a matrix formalism to study arbitrary multi-body ordering probabilities, short-range order and configuration entropy for an arbitrary number of alloy elements from first-principles electronic structure calculations.
4. Application of the matrix formalism to the Cr-Fe-Mn-Ni system at two compositions $\text{Cr}_{25}\text{Fe}_{25}\text{Mn}_{25}\text{Ni}_{25}$ and $\text{Cr}_{18}\text{Fe}_{27}\text{Mn}_{27}\text{Ni}_{28}$. For the composition $\text{Cr}_{18}\text{Fe}_{27}\text{Mn}_{27}\text{Ni}_{28}$ high probabilities of formation of the L1_0 MnNi phase at low temperatures below 1300 K and for the L1_2 CrFe_3 phase at the temperature range 500-1200 K were found. Similarly, for the equiatomic composition the L1_0 MnNi phase appears stable at temperature range 900-1200 K, the lower temperature region is preferred for the configuration Cr-Fe-Mn-Ni. The configuration Cr-Cr-Cr-Cr was found to be the least probable at all temperature ranges for both compositions of the Cr-Fe-Mn-Ni system. Furthermore, configuration entropy as a function of temperature was derived from these probabilities, the high-temperature limit is following the random solid solution approximation, but at low temperatures, the entropy is seen to be reduced due to the ordering or segregation tendencies.
5. Cr-rich BCC precipitates were found in FCC- $\text{Cr}_{18}\text{Fe}_{27}\text{Mn}_{27}\text{Ni}_{28}$ HEA indicating that this alloy is not stable after thermomechanical processing consisting in homogenisation, cold rolling and recrystallisation. This finding is in contradiction with phase stability claims reported by [20]. The finding of Cr-rich BCC precipitates in FCC- $\text{Cr}_{18}\text{Fe}_{27}\text{Mn}_{27}\text{Ni}_{28}$ HEA is consistent with similar findings of Cr-rich precipitates observed after 500 days annealed at 500 °C CrMnFeCoNi equiatomic alloy by Otto et al. [299].

6. Calibrated hardness values from nanoindentation tests in Ni self-ion irradiated specimens to 20 dpa indicated a 4 GPa increase at the irradiation temperature of 450 °C. The increase in hardening is attributed to a dense presence of irradiation-induced dislocation loops potentially of interstitial type.

8.2 Experimental future work

Three main directions for further research seem natural extensions and at the same time realistic to the work presented in this thesis:

Void swelling and helium pre-implantation Void swelling, an irradiation-induced defect that CrFeMnNi appears to resist, in general, can nucleate at locations where helium bubbles exist [149]. Recent studies in ferritic/martensitic steels [302] have shown that increased amounts of pre-implanted helium lead to higher void number densities after self-ion irradiations. The exploration of the behaviour of CrFeMnNi in-situ with α -particle irradiations combined with TEM observations could shed light into the resistance to void swelling of HEAs under more realistic fusion like conditions.

WTaVCr HEAs Explore the implications of W-based HEAs, specifically system containing low activation elements V, Cr, and Ta. Alloys within the compositional space spanned by W, Ta, V and Cr look promising due to their low activation materials properties (nuclear waste classification <100 years of half-life) [21], but have not yet been investigated as far as the author knows (a paper published in November 2018 has published irradiation resistant properties of a WTaVCr alloys [22]). The manufacturing of these HEAs could probably be successfully achieved in a conventional arc melter by using the fine powder form (<1 micron)

for W, which has the highest melting point in the periodic table. This new concept of W HEAs could be useful for solving current irradiation embrittlement issues associated with pure W, the leading candidate for armour material in modern fusion tokamak devices [285].

8.3 Modelling future work

In an environment of 14 MeV neutrons, W is expected to transmute into Re, Os, He, and H within years of exposure [303, 53, 304]. As a result of transmutation, the average bulk composition may change by a few per cent, including the production of gases such as H, and He. The modification of bulk composition can lead to secondary phase precipitation in the body-centred cubic W crystal structure: σ -phase, and Re/Os segregation. The modified microstructure, particularly with the secondary phases can result in hardening and embrittlement.

In nuclear fusion research, degradation of material microstructure and nanosstructure by radiation damage is of interest both from experimentally and modelling perspectives. Modelling from first principles can be used to rationalize mechanisms behind degradation phenomena caused by the simplest type of damage produced by radiation: vacancies and interstitials and their clusters. Recent studies found that density functional theory and kinetic Monte Carlo can be used to investigate radiation-induced segregation and precipitation [303] incorporating both vacancy and interstitial into Ising-like ABVI model Hamiltonian [303]. The kinetic processes of solute transport both by vacancies and interstitials can be captured by a Hamiltonian parametrised by bond energies and derived from DFT.

The interaction at the temperature of atomistic defects produced by irradiation predicted by Molecular Dynamics simulations is limited by a time

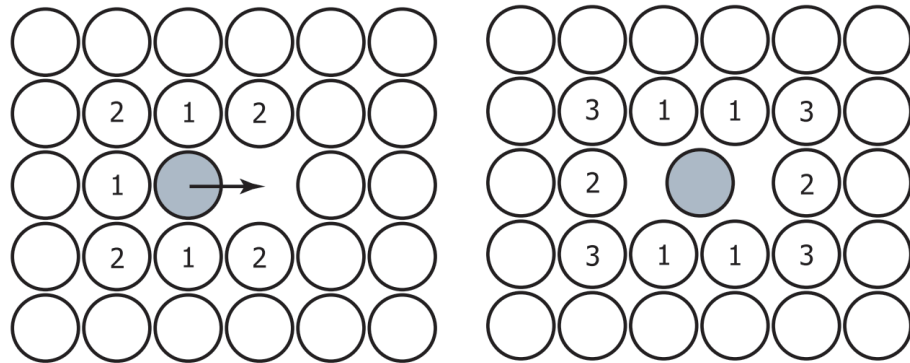
scale problem to microseconds, despite longer time scale processes such as diffusion. This is because picoseconds are required for the dynamical evolution of a system of thousands or millions of atoms, where at the initial time, there is only the PKA which is at high velocity. Atomistic kinetic Monte Carlo (AKMC) attempts to solve the time-scale problem from Molecular Dynamics simulations by treating directly state to state diffusive jumps. The diffusive jumps are treated utilizing a probability distribution for the first escape time from a state "i" to a state "j", $p_{ij}(t)$, which depend parametrically on the rate constant k_{ij} characterising the state transition.

$$p_{ij} = k_{ij} e^{-k_{ij} t} \quad (8.1)$$

The fundamental AKMC algorithms for time-evolution of the system have been reviewed comprehensively in [305]. The temperature-dependent rate constants can be determined from the theories Harmonic state transition theory, and lattice gas models, $k = v e^{-E_{\text{static}}/(k_B T)}$. In the lattice gas models, the static barrier height can be determined by using the principle of additive energy interactions, such as in the cluster expansion. The evaluation of the static energy barrier can be done by considering the saddle state configuration and the initial state configuration as depicted in Fig. 8.1. The number of nearest neighbours (1), and their interaction energy are represented by n_1 and E_1 , similarly for the next nearest neighbours. An extra subindex is added to indicate whether the energies refer to the saddle state or the initial state configuration.

$$E_{\text{static}} = E_{\text{saddle}} - E_i = E_{\text{saddle}}^0 - E_i^0 + n_{s1}E_{s1} + n_{s2}E_{s2} - n_{i1}E_{i1} - n_{i2}E_{i2} \quad (8.2)$$

Fig. 8.1.: Nearest, and next-nearest neighbour atoms in the lattice gas model of a square lattice for predicting the rate constant of a diffusional jump of a vacancy. On the left is the minimum, and the right is the saddle state. Figure reproduced from [305]



Future work developments for immediate application are the W-Re-Vac system, and the present status of work is provided in Appendix D

Appendix

A.1 Principles of superlattice structure construction for HEAs.

From an initial database of 30 structures reported in previous works [245] (from now on labelled from 0-29) by space group symmetry analysis, we can find that the least symmetrical structure can be described by 4 Wyckoff sites for a maximal space group compatible. This structure corresponds to number 8 following nomenclature from [245]. Similarly, it can be shown that the remaining structures all have 3 or less Wyckoff sites.

The methodology presented above leads to reach the following conclusion regarding compositional space. Structures with 1 Wyckoff site can allocate at most unary systems, 2 Wyckoff sites can allocate at most binary structures, 3 Wyckoff sites can allocate at most ternaries and finally, with 4 Wyckoff sites we can at most reach Quaternary systems see table A.1

The range of compositional values for the derivative structures depends also on the multiplicity of the Wyckoff sites. For example for 2 Wyckoff sites

Table A.1.: Summary of derivative structures. Note that we do not include the structures 15-29, because they have the same symmetry as those in the range 0-14, and therefore do not lead to new derivative structures

Compositional system	Generate derivative structures from	Wyckoff sites
Unary	0-14	1 or more
Binary	1-14	2 or more
Ternary	1,2,3,4,5 and 7	3 or more
Quaternary	8	4 or more

Fig. A.1.: Application of the methodology to extract the possible magnetic configurations.

Binary Structure number	Space group no.	No. of Wyckoff sites	Wyckoff positions	Total count of derived magnetic structures
1	139	3	{(A, 8h), (A, 8l), (B, 2a)}	24
2	225	3	{(A, 24d), (A, 4b), (B, 4a)}	24
3	123	3	{(A, 2h), (A, 1h), (B, 1a)}	24
4	12	3	{(A, 4i), (A, 2d), (B, 2a)}	24
5	47	3	{(A, 2p), (A, 1e), (B, 1a)}	24
6	221	2	{(A, 3c), (B, 1a)}	4
7	139	3	{(A, 2b), (A, 4d), (B, 2a)}	24
8	139	4	{(A, 4c), (A, 4e), (A, 4d), (B, 4e)}	112
9	164	2	{(A, 2d), (B, 1a)}	4
10	139	2	{(A, 4e), (B, 2b)}	4
11	71	2	{(A, 4e), (B, 2a)}	4
12	129	2	{(A, 2c), (B, 2c)}	4
13	166	2	{(A, 3b), (B, 3a)}	4
14	59	2	{(A, 2a), (B, 2a)}	4
...	Total 14 structures (15-28 are derived from the pure binary set of 14)
...	Total of 284 structures for each binary with generic species A and B and magnetic moments $m_A = \pm T_A \mu_B$ and $m_B = \pm T_B \mu_A$

one with multiplicity 1 and the other with multiplicity 2, the maximal compositional system is binary with compositions A_2B or AB_2 .

The magnetic configurational space is even more complex, and we can not generally constraint the values of the magnetic moment of the unit cell. We can nevertheless classify magnetic structures according to the unit cell magnetic moment and the relative orientation of the local magnetic moments. The family of positions equivalent to a Wyckoff position from space group symmetry can in principle be split into sets of distinct magnetic sites, thus splitting the symmetry of the structure. In a most simplistic scenario, we can assign the same magnetic moment to each of the images of the Wyckoff positions found from space group theory. However, magnetic symmetry breakdown at the Wyckoff sites can occur after electronic structure calculations. This is illustrated in Fig. A.2.

An in-depth analysis of the symmetry of the 0-29 structures leads to a total count of 284 possible magnetic configurations spanning 24 possible chemically distinct configurations. The list of symmetrically distinct structures is illustrated in Fig. A.3.

Fig. A.2.: Depiction of derivative magnetic structure in the FeMn binary system. The spins up/down are illustrated before and after electronic structure calculation with VASP. The Mn spin up/down after VASP indicates symmetry breakdown at the Mn Wyckoff sites.

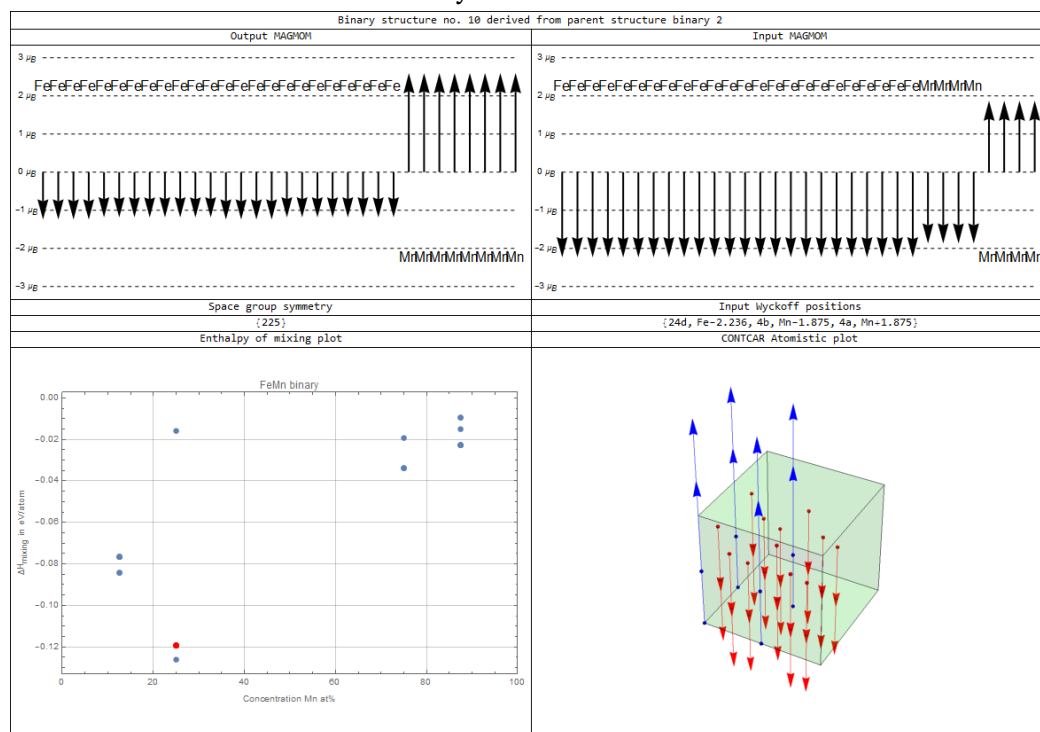
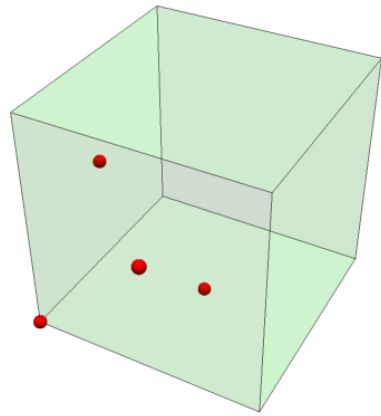
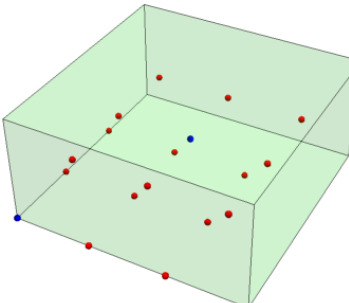


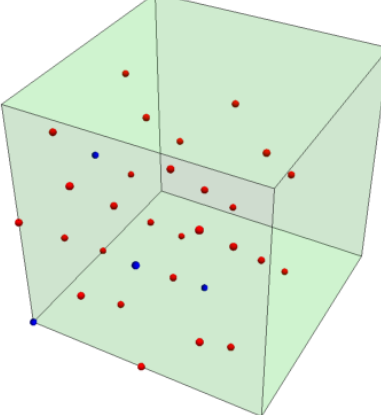
Fig. A.3.: The crystallographic information of each of the initial 0 to 14 structures considered for this work. All of these structures have a space group which is a subgroup of the fcc (no. 225) space group, structure here represented by 0, for which we assume a fcc lattice of 3.55 Å

Atomistic picture	Species/Wyckoff pos	Space group no.	Lattice (a, b, c) (α, β, γ)
	{A, 4a}	{225}	{3.55, 3.55, 3.55} {90., 90., 90.}

(a) Structure 0

Atomistic picture	Species/Wyckoff pos	Space group no.	Lattice (a, b, c) (α, β, γ)
	{A, 8h} {A, 8i} {B, 2a}	{139}	{7.53069, 7.53069, 3.55} {90., 90., 90.}

(b) Structure 1

Atomistic picture	Species/Wyckoff pos	Space group no.	Lattice (a, b, c) (α, β, γ)
	{A, 24d} {A, 4b} {B, 4a}	{225}	{7.1, 7.1, 7.1} {90., 90., 90.}

(c) Structure 2

Atomistic picture	Species/Wyckoff pos	Space group no.	Lattice (a,b,c) (α , β , γ)
	{A, 2h} {A, 1b} {B, 1a}	{123}	{2.51023, 2.51023, 7.1} {90., 90., 90.}

(d) Structure 3

Atomistic picture	Species/Wyckoff pos	Space group no.	Lattice (a,b,c) (α , β , γ)
	{A, 4i} {A, 2d} {B, 2a}	{12}	{8.32549, 2.51023, 4.34784} {90., 79.975, 90.}

(e) Structure 4

Atomistic picture	Species/Wyckoff pos	Space group no.	Lattice (a,b,c) (α , β , γ)
	{A, 2p} {A, 1e} {B, 1a}	{47}	{3.55, 5.02046, 2.51023} {90., 90., 90.}

(f) Structure 5

Atomistic picture	Species/Wyckoff pos	Space group no.	Lattice (a,b,c) (α , β , γ)
	{A, 3c} {B, 1a}	{221}	{3.55, 3.55, 3.55} {90., 90., 90.}

(g) Structure 6

Atomistic picture	Species/Wyckoff pos	Space group no.	Lattice (a,b,c) (α , β , γ)
	{A, 2b} {A, 4d} {B, 2a}	{139}	{3.55, 3.55, 7.1} {90., 90., 90.}

(h) Structure 7

Atomistic picture	Species/Wyckoff pos	Space group no.	Lattice (a,b,c) (α , β , γ)
	{A, 4c} {A, 4e} {A, 4d} {B, 4e}	{139}	{3.55, 3.55, 14.2} {90., 90., 90.}

(i) Structure 8

Atomistic picture	Species/Wyckoff pos	Space group no.	Lattice (a,b,c) (α , β , γ)
	{A, 2d} {B, 1a}	{164}	{2.51023, 2.51023, 6.14878} {90., 90., 120.}

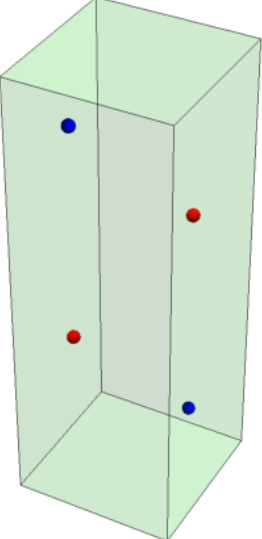
(j) Structure 9

Atomistic picture	Species/Wyckoff pos	Space group no.	Lattice (a,b,c) (α , β , γ)
	{A, 4e} {B, 2b}	{139}	{2.51023, 2.51023, 10.65} {90., 90., 90.}

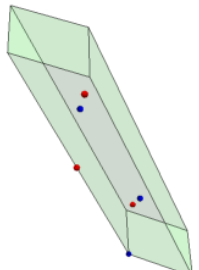
(k) Structure 10

Atomistic picture	Species/Wyckoff pos	Space group no.	Lattice (a,b,c) (α , β , γ)
	{A, 4e} {B, 2a}	{71}	{7.53069, 3.55, 2.51023} {90., 90., 90.}

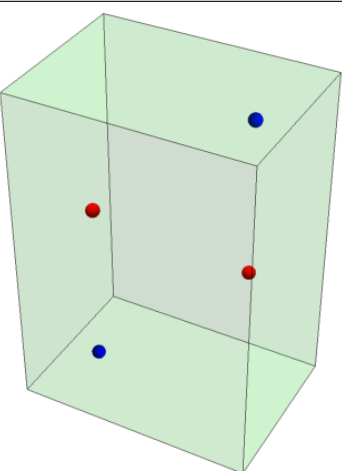
(l) Structure 11

Atomistic picture	Species/Wyckoff pos	Space group no.	Lattice (a,b,c) (α , β , γ)
	{A, 2c} {B, 2c}	{129}	{2.51023, 2.51023, 7.1} {90., 90., 90.}

(m) Structure 12

Atomistic picture	Species/Wyckoff pos	Space group no.	Lattice (a,b,c) (α , β , γ)
	{A, 3b} {B, 3a}	{166}	{2.51023, 2.51023, 12.2976} {90., 90., 120.}

(n) Structure 13

Atomistic picture	Species/Wyckoff pos	Space group no.	Lattice (a,b,c) (α , β , γ)
	{A, 2a} {B, 2a}	{59}	{3.55, 2.51023, 5.02046} {90., 90., 90.}

Appendix

B.1 Ergodicity, broken-ergodicity and configuration entropy in high-entropy alloys

The configurational entropy in the Boltzmann definition, S_B is given in Eq. B.1. Where Ω is the number of compatible microstates with a given macrostate. The Boltzmann formula can be applied to an alloy system with components A, and B assuming completely random distributions of the atoms in the lattice sites, the entropy per atom from Eq. B.1 takes the form $S_B = k_B \ln \Omega$, where the number of microstates, $\Omega = \frac{(N_A + N_B)!}{N_A! N_B!}$, can be simplified by using Stirling's approximation [306] for large interger N values, $\ln N! = N \ln N - N$. Thus, the entropy per atom reduces to $S_G = -k_B \sum_{i=A,B} p_i \ln p_i$, where $p_i = N_i/N$ is the probability of component i in any given site. The formula can be generalised to arbitrary number of alloy components, K as expressed in Eq. B.1. For equiatomic concentration, all the $p_i = 1/K$ are equal, and the configuration entropy of a completely random distribution of K different atoms results in $k_B \ln K$

$$S_B = k_B \ln \Omega = -k_B \sum_{i=1}^K p_i \ln p_i \quad (\text{B.1})$$

Ergodicity in statistical physics refers to the equivalence of the time and ensemble averages of the properties of a system. In high-entropy alloy

systems, the question of ergodicity depends on two-time scales: an internal relaxation time scale τ_{int} on which the system loses “memory” of its preceding states, and an external observation time scale τ_{obs} on which properties are measured. The ratio of internal to external time scales defines the transition from ergodic to the non-ergodic system: when $D < 1$, the system is said to be ergodic; and $D > 1$ implies a nonergodic system. The transition occurs at $D = 1$ is referred to as a partitioning process [307]. A partitioning process results in a loss of configurational entropy because the system, due to the limiting observation time, can only probe a subset or component of configurational phase space. In terms of Boltzmann’s definition of entropy, the macrostate of a non-random alloy system is determined by a fewer number of microstates compared to the macrostate of a random distribution of atoms in an alloy system. The statistical mechanics of broken ergodicity systems was developed by Palmer in the 1980s [308]. The configurational entropy of a broken ergodic system can be calculated by applying the definition of entropy within each component α -accessible atomic distribution states in the alloy system.

$$S_\alpha = -k_B \sum_{i \in \alpha} \frac{p_i}{P_\alpha} \ln \left(\frac{p_i}{P_\alpha} \right) \quad (\text{B.2})$$

The configurational entropy of the system as a whole is simply a weighted sum of the Gibbs entropies of the individual components

$$S = \sum_{\alpha} S_\alpha P_\alpha = -k_B \sum_{\alpha} \sum_{i \in \alpha} p_i \ln \left(\frac{p_i}{P_\alpha} \right) = -k_B \sum_{\alpha} \sum_i p_i \ln(p_i) + k_B \sum_{\alpha} P_\alpha \ln(P_\alpha) \quad (\text{B.3})$$

At low temperatures below the melting point of the alloy systems, the state of completely random distribution of atoms will not be valid. Segregation and precipitation may occur, restricting the accessible microstates of atomic

distributions of atoms from the set of microstates of completely random distribution of atoms. For example, suppose that in a 2-component alloys system, at low temperature the alloy system is a partition in two states: 30 % of the system segregates into one component, but the remaining 70 % retains in the state of the completely random binary distribution of atoms. Entropy will be reduced by a maximum amount equal to $k_B(0.3\ln 0.3 + 0.7\ln 0.7)$.

Appendix

C.1 Kinematics of two-body scattering

The projectile particle is denoted by its mass, m . The recoil particle is denoted by its mass, M . The reduced mass, which represents an effective particle that simplifies expressions of energies to a single particle problem, is given in terms of the particle masses by $M_r = \frac{mM}{m + M}$.

Under an elastic collision, the total kinetic energy and the momentum are conserved. These are expressed in Laboratory frame of reference as:

$$\frac{mv_0^2}{2} = \frac{mv^2}{2} + \frac{mV^2}{2} \quad (\text{C.1})$$

$$mv_0 = mv\cos(\vartheta) + MV\cos(\theta) \quad (\text{C.2})$$

$$0 = mv\sin(\vartheta) - MV\sin(\theta) \quad (\text{C.3})$$

The kinetic energy of the projectile and target particles can be obtained by solving for v and V for the above systems of Eqs. C.1, C.2, and C.3: solving for V in terms of v from Eq. C.3, then substituting into Eq. C.1, and solving for both v , and ϑ in the resulted previous step. As a result, the following expressions are obtained:

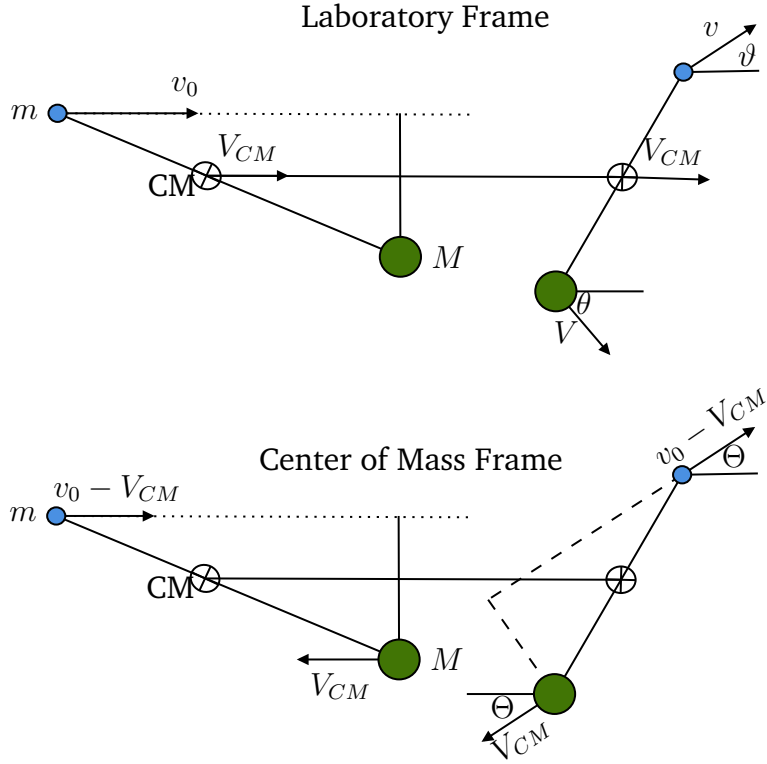


Fig. C.1.: Asymptotic views of elastic collision in the Laboratory and Center of Mass frames of reference. See text for description of the variables

$$v^2 = v_0^2 \left(1 - \frac{4M_r^2 \cos(\theta)^2}{mM}\right) \quad (\text{C.4})$$

$$V^2 = v_0^2 \frac{4M_r^2 \cos(\theta)^2}{M^2} \quad (\text{C.5})$$

The recoil particle kinetic energy is computed in terms of the scattering angle, θ and the squared speed V^2 given by Eq. C.5. Alternatively, the recoil energy can be expressed in terms of the CM scattering angle Θ by using the angular relationship $\theta = \frac{\pi - \Theta}{2}$ (which can be derived from Fig. C.1) The result is given in Eq. C.6.

$$T = \frac{MV^2}{2} = \frac{4mM}{(m+M)^2} \cos(\theta)^2 E_m = \frac{2mM}{(m+M)^2} (1 - \cos(\Theta)) E_m \quad (\text{C.6})$$

where for simplicity $E_m = \frac{mv_0^2}{2}$.

For inelastic scattering, the conservation energy equation Eq. C.1 needs to be modified by adding an extra energy term, Q . Q represents the energy retained by the struck particle, M after the inelastic interaction.

Appendix

D.1 Derivation of the ABVI model

hamiltonian from cluster expansion in the pair interaction

In the ABVI model, there are 6 components: A (solvent), B (solute), V (vacancy), I (interstitials) which include three possible configurations A-A, A-B, and B-B. Therefore, the point defects in the ABVI model consist of four types V, A-A, A-B, and B-B. The Hamiltonian of the system has been written [303] in terms of bonding energies, ϵ , and an average number of bonds per atom, n , in the system. The ABVI hamiltonian has been expressed as a sum over bond types over the supercell.

$$\Delta H_{mix} = \sum_i \sum_{\alpha,\beta} n_{\alpha,\beta}^i \epsilon_{\alpha,\beta}^i \quad (\text{D.1})$$

where i specifies the type of nearest neighbour i.e. 1 for the shell corresponding to the nearest neighbour, 2 for the next shell and so on. Similarly, $\alpha, \beta = \{A, B, V, A - A, A - B, B - B\}$ indicate the atomic configuration of the $n_{\alpha,\beta}$ bond.

Applying the definition of scalar product in the cluster expansion formalism of energy, $E(\sigma)$ (see chapter 6, and [245]) to relate to the effective cluster interactions, $J_{\omega,n}^{(s)}$:

$$J_{\omega,n}^{(s)} = \langle \Gamma_{\omega,n}^{(s)}(\vec{\sigma}), E(\vec{\sigma}) \rangle = \rho_0^{(s)} \sum_{\sigma} \Gamma_{\omega,n}^{(s)}(\vec{\sigma}) E(\vec{\sigma}) \quad (\text{D.2})$$

The set of K point functions, $\{\gamma_{i,K}[\sigma]\}_{i=0,\dots,K-1}$, form a set of orthorgonal functions by defining the scalar product between cluster functions, $\langle \Gamma_{\omega,n}^{(\alpha)}, \Gamma_{\omega,n}^{(\beta)} \rangle$, written explicitly in index notation where $(\alpha) = (\alpha_1, \dots, \alpha_{\omega})$, and $(\beta = \beta_1, \dots, \beta_{\omega})$ as in Eq. D.3. By introducing a normalisation constant, $\rho_0^{(\alpha)}$, the set of point functions can be normalised [309]

$$\begin{aligned} \langle \Gamma_{\omega,n}^{(\alpha)}, \Gamma_{\omega,n}^{(\beta)} \rangle &= \rho_0^{(\alpha)} \sum_{\forall \sigma_i} \left(\prod_{i=1}^{\omega} \gamma_{\alpha_i, K}[\sigma_i] \gamma_{\beta_i, K}[\sigma_i] \right) \\ &= \rho_0^{(\alpha)} \sum_{\forall \sigma_i} \left(\prod_{i=1}^{\omega} (\tau_K)_{\alpha_i, i} (\tau_K)_{\beta_i, i} \right) \\ &= \prod_{i=1}^{\omega} \delta_{\alpha_i, \beta_i} \end{aligned} \quad (\text{D.3})$$

The normalisation constant, $\rho_0^{(pq\dots)}$, (where $(s) = (pq\dots)$ for simplicity in notation) is found after imposing the orthonormality condition for cluster functions $\Gamma_{\omega,n}^{(s)}$ [245], which is expressed here in Eq. D.3. To develop an expression for $\rho_0^{(s)}$, two sums need be evaluated $\sum_{\sigma=0}^{K-1} \cos^2 \left(2\pi \lceil s/2 \rceil \frac{\sigma}{K} \right)$, and $\sum_{\sigma=0}^{K-1} \sin^2 \left(2\pi \lceil s/2 \rceil \frac{\sigma}{K} \right)$. These two sums can be rewritten as geomet-

ric series by substituting the trigonometric functions by their complex exponential functions. The result of the sums is simplified to Eq. D.4:

$$\rho_0^{(s)} = \prod_{j=(s)_1}^{(s)_\omega} \frac{1}{\varsigma_{j,K}} \quad (\text{D.4})$$

where $\varsigma_{j,K}$ is given by:

$$\varsigma_{j \geq 0, K} = \begin{cases} K & j = 0 \\ \frac{1}{2} \left(\cos \left(\frac{2\pi}{3}(j+1) \right) + \cos \left(\frac{4\pi}{3}(j+1) \right) + K+1 \right) & j \text{ odd} \\ -\frac{1}{2} \left(\cos \left(\frac{2\pi j}{3} \right) + \cos \left(\frac{4\pi j}{3} \right) - K+1 \right) & j \text{ even} \end{cases} \quad (\text{D.5})$$

Note that the normalisation constant $\rho_0^{(s)}$ is related to the Kronecker product of τ_K matrices and the transpose τ_K^T matrix, $(\tau_K \otimes \cdots \otimes \tau_K)$, as shown in Eq. D.6.

$$\sum_{j=1}^{K^\omega} \overbrace{(\tau_K \otimes \cdots \otimes \tau_K)}^{\omega}_{i,j} \overbrace{(\tau_K^T \otimes \cdots \otimes \tau_K^T)}^{\omega}_{j,k} = \frac{\delta_{i,k}}{\rho_0^{(i)}} \quad (\text{D.6})$$

For example, in case of $K = 3$ and for the pair interaction, by applying Eq. D.4 we reproduce explicitly the values for the normalisation constants $\rho_0^{(0,0)} = \frac{1}{9}$, $\rho_0^{(0,1)} = \frac{2}{9}$, $\rho_0^{(0,2)} = \frac{2}{9}$, $\rho_0^{(1,0)} = \frac{2}{9}$, $\rho_0^{(1,1)} = \frac{4}{9}$, $\rho_0^{(1,2)} = \frac{4}{9}$, $\rho_0^{(2,0)} = \frac{2}{9}$, $\rho_0^{(2,1)} = \frac{4}{9}$, $\rho_0^{(2,2)} = \frac{4}{9}$. Note that for decorations (11), (12), (21) and (22), we get the factor 4/9 in agreement with Eq. 15 from the reference [245].

Eq. D.2 can be put in the matrix formulation in terms of the τ_K matrices to give:

$$J_{\omega,n}^{(s)} = \sum_{i=1}^{K^\omega} \rho_0^{(s)} \overbrace{(\tau_K \otimes \cdots \otimes \tau_K)}^{\omega}_{s,i} E_{\omega,n}^{(i)}, \quad (\text{D.7})$$

And similarly after using Eq. D.6 in Eq. D.7

$$E_{\omega,n}^{(s)} = \sum_{i=1}^{K^\omega} \overbrace{(\tau_K^T \otimes \cdots \otimes \tau_K^T)}^{\omega}_{s,i} J_{\omega,n}^{(i)}, \quad (\text{D.8})$$

More explicitly Eq. D.8 applied to a cluster with two sites ($\omega = 2$) results in the matrix relationship Eq. D.9 with dimensions 6 by 6, after reducing symmetric entries from the non-symmetrized matrix with dimensions of 9 by 9 by removing rows and columns of the full matrix.

D.2 Two-body Hamiltonian interaction

The formulation in the previous section can be applied to the simplified ABV model with three components namely A (solvent), B(solute), and V (vacancy).

Applying Eq. D.8 to ABV model ($K = 3$), and performing a symmetry reduction, the matrix relationship between the $E_{2,n}^{(s)}$ and $J_{1,1}^{(s)}, J_{2,n}^{(s)}$ reads:

$$\begin{pmatrix} E_{2,n}^{(A,A)} \\ E_{2,n}^{(A,B)} \\ E_{2,n}^{(A,V)} \\ E_{2,n}^{(B,B)} \\ E_{2,n}^{(B,V)} \\ E_{2,n}^{(V,V)} \end{pmatrix} = \begin{pmatrix} 1 & -1 & 0 & 1 & 0 & 0 \\ 1 & \frac{1}{2} & -\frac{\sqrt{3}}{2} & -\frac{1}{2} & \frac{\sqrt{3}}{2} & 0 \\ 1 & \frac{1}{2} & \frac{\sqrt{3}}{2} & -\frac{1}{2} & -\frac{\sqrt{3}}{2} & 0 \\ 1 & \frac{1}{2} & -\frac{\sqrt{3}}{2} & \frac{1}{4} & -\frac{\sqrt{3}}{4} & \frac{3}{4} \\ 1 & \frac{1}{2} & \frac{\sqrt{3}}{2} & \frac{1}{4} & \frac{\sqrt{3}}{4} & -\frac{3}{4} \\ 1 & \frac{1}{2} & \frac{\sqrt{3}}{2} & \frac{1}{4} & \frac{\sqrt{3}}{4} & \frac{3}{4} \end{pmatrix} \cdot \begin{pmatrix} J_{1,1}^{(0)} \\ 2J_{1,1}^{(1)} \\ 2J_{1,1}^{(2)} \\ J_{2,n}^{(1,1)} \\ 2J_{2,n}^{(1,2)} \\ J_{2,n}^{(2,2)} \end{pmatrix} \quad (\text{D.9})$$

Bibliography

- [1]World Nuclear Association. *Heat Values of Various Fuels*. 2018 (cit. on p. 14).
- [2]J. Huth. “Relativistic Theory of Rocket Flight With Advanced Propulsion Systems”. In: *ARS Journal* 30.3 (1960), pp. 250–253 (cit. on pp. 14, 29).
- [3]U.S. Department of the Interior. *U.S. Geological Survey, Mineral Commodity Summaries 2000*. 2000 (cit. on pp. 16, 36, 37).
- [4]A. V. Nero. “A Guidebook to Nuclear Reactors”. In: *Nuclear Technology* 58.3 (1982), pp. 554–555 (cit. on p. 16).
- [5]D. Campbell. “6 Magnetic confinement fusion: tokamak”. In: *Nuclear Energy*. Berlin/Heidelberg: Springer-Verlag, 2006, pp. 369–417 (cit. on pp. 17, 33).
- [6]S. J. Zinkle and N. M. Ghoniem. “Operating temperature windows for fusion reactor structural materials”. In: *Fusion Eng. Des.* 51-52 (2000), pp. 55–71 (cit. on pp. 18, 19, 55).
- [7]S. J. Zinkle and J. T. Busby. “Structural materials for fission & fusion energy”. In: *Mater. Today* 12.11 (2009), pp. 12–19 (cit. on pp. 18, 132).
- [8]S.J. Zinkle and L.L. Snead. “Designing Radiation Resistance in Materials for Fusion Energy*”. In: *Annu. Rev. Mater. Res.* 44.1 (2014), pp. 241–267 (cit. on pp. 19, 71).
- [9]D. Stork, P. Agostini, J. L. Boutard, et al. “Developing structural, high-heat flux and plasma facing materials for a near-term DEMO fusion power plant: The EU assessment”. In: *J. Nucl. Mater.* 455.1-3 (2014), pp. 277–291 (cit. on pp. 19, 57, 58, 132).
- [10]P.J. Maziasz and J.T. Busby. “Properties of Austenitic Steels for Nuclear Reactor Applications”. In: *Compr. Nucl. Mater.* Vol. 2. Elsevier, 2012, pp. 267–283 (cit. on pp. 19, 58, 75).
- [11]J.W. Yeh, S.K. Chen, S.J. Lin, et al. “Nanostructured high-entropy alloys with multiple principal elements: Novel alloy design concepts and outcomes”. In: *Adv. Eng. Mater.* 6.5 (2004), pp. 299–303 (cit. on pp. 19, 27, 59, 131, 162, 202).

- [12]Y. Zhang, T.T. Zuo, Z. Tang, et al. “Microstructures and properties of high-entropy alloys”. In: *Prog. Mater. Sci.* 61.October 2013 (2014), pp. 1–93 (cit. on pp. 19, 131, 148, 196, 202).
- [13]E. J. Pickering and N. G. Jones. “High-entropy alloys: a critical assessment of their founding principles and future prospects”. In: *Int. Mater. Rev.* 61.3 (2016), pp. 183–202 (cit. on pp. 19, 63, 104, 131, 203, 215).
- [14]Z. Li, K.G. Pradeep, Y. Deng, et al. “Metastable high-entropy dual-phase alloys overcome the strength-ductility trade-off”. In: *Nature* 534.7606 (2016), pp. 227–230 (cit. on pp. 20, 203).
- [15]A. Gali and E.P. George. “Tensile properties of high- and medium-entropy alloys”. In: *Intermetallics* 39 (2013), pp. 74–78 (cit. on pp. 20, 60, 131, 163, 203).
- [16]C. Lu, L. Niu, N. Chen, et al. “Enhancing radiation tolerance by controlling defect mobility and migration pathways in multicomponent single-phase alloys”. In: *Nat. Commun.* 7 (2016), p. 13564 (cit. on pp. 20, 72, 202).
- [17]T. Egami, W. Guo, P. D. Rack, et al. “Irradiation Resistance of Multicomponent Alloys”. In: *Metall. Mater. Trans. A* 45.1 (2014), pp. 180–183 (cit. on p. 20).
- [18]T. Egami, M. Ojha, O. Khorgolkhuu, et al. “Local Electronic Effects and Irradiation Resistance in High-Entropy Alloys”. In: *Jom* 67.10 (2015), pp. 2345–2349 (cit. on pp. 20, 202).
- [19]M W. Ullah, D S. Aidhy, Y Zhang, et al. “Damage accumulation in ion-irradiated Ni-based concentrated solid-solution alloys”. In: *Acta Mater.* 109 (2016), pp. 17–22 (cit. on p. 20).
- [20]N.A.P.K. Kumar, C. Li, K.J. Leonard, et al. “Microstructural stability and mechanical behavior of FeNiMnCr high entropy alloy under ion irradiation”. In: *Acta Mater.* 113 (2016), pp. 230–244 (cit. on pp. 20, 22, 68, 74, 76, 105, 132, 166, 203, 205, 218, 225, 228).
- [21]E.E. Bloom, R.W. Conn, J.W. Davis, et al. “Low activation materials for fusion applications”. In: *J. Nucl. Mater.* 122.1-3 (1984), pp. 17–26 (cit. on pp. 20, 72, 203, 229).
- [22]Z. Li, S. Zhao, R. O Ritchie, et al. “Mechanical properties of high-entropy alloys with emphasis on face-centered cubic alloys”. In: *Progress in Materials Science* 102.March 2018 (2019), pp. 296–345 (cit. on pp. 21, 229).
- [23]International Energy Agency. *Key world energy statistics. Also available on smartphones and tablets.* Tech. rep. 2018 (cit. on pp. 28, 29).
- [24]W. Petri. “4.5.1 Rocket propulsion”. In: *Astronomy and Astrophysics*. Berlin/Heidelberg: Springer-Verlag, pp. 215–216 (cit. on p. 29).

- [25]J. P. Holdren. “Population and the Energy Problem”. In: *Popul. Environ. A J. Interdiscip. Stud.* 12.3 (1991) (cit. on p. 29).
- [26]Culham Centre for fusion energy. *Introduction to fusion*. 2019 (cit. on p. 30).
- [27]Jet Team. *Fusion energy production from a deuterium-tritium plasma in the JET tokamak*. Tech. rep. 1992, p. 187 (cit. on pp. 30, 54).
- [28]K.S. Krane. *Introductory Nuclear Physics*. John Wiley & Sons, Inc., 1988 (cit. on pp. 30, 33).
- [29]IAEA Nuclear Data Section. *Live chart of nuclides*. 2019 (cit. on p. 30).
- [30]H.-S Bosch and G. M. Hale. “Improved formulas for fusion cross-sections and thermal reactivities The behaviour of fast ions in tokamak experiments IMPROVED FORMULAS FOR FUSION CROSS-SECTIONS AND THERMAL REACTIVITIES”. In: *Nuclear Fusion* 32.4 (1992), pp. 611 –631 (cit. on pp. 32, 34).
- [31]S. Zheng, D. Ward, R. Pampin, et al. “Preliminary evaluation of decay heat in a HCPB DEMO fusion reactor”. In: *Progress in Nuclear Science and Technology* 4 (2014), pp. 126–129 (cit. on p. 33).
- [32]M. Keilhacker. “Fusion physics progress on the Joint European Torus (JET)”. In: *Plasma Physics and Controlled Fusion* 41.SUPPL. 12B (1999) (cit. on p. 33).
- [33]A.M. Bradshaw, T. Hamacher, and U. Fischer. “Is nuclear fusion a sustainable energy form?” In: *Fusion Eng. Des.* 86.9-11 (2011), pp. 2770–2773 (cit. on p. 34).
- [34]A. Fernandez-Caballero. *Personal notes taken from the course Introduction to Nuclear Fusion - Master of Science Physics and Technology of Nuclear Reactors imparted by S. Lilley from Applied Radiation Physics, Culham Centre for Fusion Energy*. Birmingham, UK: University of Birmingham, School of Physics and Astronomy, 2013 (cit. on p. 35).
- [35]World Nuclear Association. *Reactor Database*. 2019 (cit. on p. 35).
- [36]E. Rebhan, D. Reiter, R. Weynants, et al. “5 Controlled nuclear fusion: general aspects”. In: *Nuclear Energy*. Berlin/Heidelberg: Springer-Verlag, 2006, pp. 304–368 (cit. on pp. 36, 37).
- [37]A. Fernandez-Caballero. *Personal notes taken from the course Radiation detectors - Master of Science Physics and Technology of Nuclear Reactors imparted by T. Leadbeater from School of Physics and Astronomy*. Birmingham, UK: University of Birmingham, School of Physics and Astronomy, 2013 (cit. on p. 38).
- [38]L. W. Alvarez and F. Bloch. “A quantitative determination of the neutron moment in absolute nuclear magnetons”. In: *Physical Review* 57.2 (1940), pp. 111–122 (cit. on p. 39).

- [39]Y. A. Alexandrov. “2 The neutron as an elementary particle”. In: *Low Energy Neutrons and their Interaction with Nuclei and Matter. Part 1*. Vol. 2. 2. Berlin/Heidelberg: Springer-Verlag, 1932, pp. 1–17 (cit. on p. 39).
- [40]A. Fernandez-Caballero. *Personal notes taken from the course Radiation transport - Master of Science Physics and Technology of Nuclear Reactors imparted by P. Norman from School of Physics and Astronomy*. Birmingham, UK: University of Birmingham, School of Physics and Astronomy, 2013 (cit. on p. 39).
- [41]H. Ullmaier. “3.2.1 (n, alpha)-reactions”. In: *Atomic Defects in Metals*. Vol. 1. Berlin/Heidelberg: Springer-Verlag, 1991, pp. 385–386 (cit. on p. 40).
- [42]M. Nastasi and J.W. Mayer. *Ion Implantation and Synthesis of Materials*. Berlin, Heidelberg: Springer Berlin Heidelberg, 2006, pp. 1–263 (cit. on pp. 41, 45, 51).
- [43]A. Guinier. “General Review of the Experimental Methods for the Determination of Atomic Structures”. In: *Diffraction and Imaging Techniques in Material Science* (1978), pp. 3–6 (cit. on pp. 41, 118).
- [44]J. Ayache, L. Beaunier, J. Boumendil, et al. *Sample Preparation Handbook for Transmission Electron Microscopy*. New York, NY: Springer New York, 2010 (cit. on p. 41).
- [45]R. B. Firestone. “Appendix 3 - Stopping power and range for nuclei”. In: *Table of Isotopes - 1999 update with CD-ROM*. Ed. by S.Y. Frank Chu and Coral M. Baglin. Eight edition. Wiley-VCH, 1999, p. 224 (cit. on p. 41).
- [46]M. Inokuti. “Inelastic Collisions of Fast Charged Particles with Atoms and Molecules—The Bethe Theory Revisited”. In: *Reviews of Modern Physics* 43.3 (1971), pp. 297–347 (cit. on p. 43).
- [47]P. Jung. “1.7 Production of atomic defects in metals by irradiation”. In: *Atomic Defects in Metals*. Berlin/Heidelberg: Springer-Verlag, pp. 6–7 (cit. on p. 44).
- [48]K. G. Dedrick. “Kinematics of High-Energy Particles”. In: *Reviews of Modern Physics* 34.3 (1962), pp. 429–442 (cit. on p. 45).
- [49]G.P. Mueller. “Total cross-section corresponding to the differential cross-section of lindhard, nielsen and scharff”. In: *Radiation Effects* 21.4 (1974), pp. 253–254 (cit. on pp. 45, 47).
- [50]M.W. Thompson and S.B. Wright. “A new damage function for predicting the effect of reactor irradiation on graphite in different neutron spectra”. In: *Journal of Nuclear Materials* 16.2 (1965), pp. 146–154 (cit. on pp. 46, 48).
- [51]M. I. Norgett and M. T. Robinson and I. M. Torrens. “A proposed method of calculating displacement dose rates”. In: *Nuclear Engineering and Design* 33 (1975), pp. 50–54 (cit. on pp. 46, 48).

- [52]X-5 Monte Carlo Team. “MCNP - A General Monte Carlo N-Particle Transport Code, Version 5”. In: *Los Alamos Nuclear Laboratory I* (2005), pp. 2–71 –2–80 (cit. on p. 46).
- [53]M.R. Gilbert, J. Marian, and J.-Ch. Sublet. “Energy spectra of primary knock-on atoms under neutron irradiation”. In: *J. Nucl. Mater.* 467 (2015), pp. 121–134 (cit. on pp. 47, 50, 230).
- [54]T. Diaz de la Rubia, R. S. Averback, Horngming Hsieh, et al. “Molecular dynamics simulation of displacement cascades in Cu and Ni: Thermal spike behavior”. In: *Journal of Materials Research* 4.03 (1989), pp. 579–586 (cit. on p. 50).
- [55]M. I. Norgett and M. T. Robinson and I. M. Torrens. “A proposed method of calculating displacement dose rates”. In: *Nucl. Eng. Des.* 33 (1975), pp. 50–54 (cit. on pp. 48, 50).
- [56]R.E. Stoller, M.B. Toloczko, G.S. Was, et al. “On the use of SRIM for computing radiation damage exposure”. In: *Nucl. Instruments Methods Phys. Res. Sect. B Beam Interact. with Mater. Atoms* 310 (2013), pp. 75–80 (cit. on pp. 50, 110, 111, 208).
- [57]P. Ehrhart. “2.1.3.5 Defect reactions and annealing stages”. In: *Atomic Defects in Metals*. Berlin/Heidelberg: Springer-Verlag, 2005, pp. 100–102 (cit. on p. 52).
- [58]W. Schilling and H. Ullmaier. “Physics of Radiation Damage in Metals”. In: *Materials Science and Technology*. Vol. 31. 1-2. Weinheim, Germany: Wiley-VCH Verlag GmbH & Co. KGaA, 2006, pp. 83–110. arXiv: arXiv:1011.1669v3 (cit. on p. 53).
- [59]F. Garner. “Irradiation Performance of Cladding and Structural Steels in Liquid Metal Reactors”. In: *Materials Science and Technology*. American Cancer Society, 2006. eprint: <https://onlinelibrary.wiley.com/doi/pdf/10.1002/9783527603978.mst0110> (cit. on p. 54).
- [60]ITER. *Building ITER*. 2019 (cit. on p. 54).
- [61]N. J. Fisch, J. L. Peterson, and A. Cohen. “Material requirements for controlled nuclear fusion”. In: *Fundam. Mater. Energy Environ. Sustain.* Ed. by David S. Ginley and David Cahen. Cambridge: Cambridge University Press, 2011, pp. 194–204 (cit. on p. 54).
- [62]D. Maisonnier, D. Campbell, I. Cook, et al. “Power plant conceptual studies in Europe”. In: *Nucl. Fusion* 47.11 (2007), pp. 1524–1532 (cit. on p. 54).
- [63]B. Riccardi R. Lässer, N. Baluc, J.-L. Boutard, E. Diegele, S. Dudarev, M. Gasparotto, A. Möslang, R. Pippal and B. Van Der Schaaf. “Structural Materials for DEMO: Development, Testing and Modelling”. In: *24th SOFT, 11th-15th Sept. Warsaw*. 2006, p. 36 (cit. on p. 55).

- [64] S. M. González De Vicente, J. L. Boutard, S. J. Zinkle, et al. “Materials testing facilities and programmes for fission and ion implantation damage”. In: *Nuclear Fusion* 57.9 (2017) (cit. on pp. 55, 56).
- [65] J. Knaster. “An assessment of the available alternatives for fusion relevant neutron sources”. In: *Nuclear Fusion* 58.9 (2018), p. 095001 (cit. on p. 56).
- [66] E. Surrey, M. Porton, A. Caballero, et al. “FAFNIR: Strategy and risk reduction in accelerator driven neutron sources for fusion materials irradiation data”. In: *Fusion Engineering and Design* 89.9-10 (2014), pp. 2108–2113 (cit. on p. 56).
- [67] R. Lindau, A. Möslang, M. Rieth, et al. “Present development status of EUROFER and ODS-EUROFER for application in blanket concepts”. In: *Fusion Eng. Des.* 75-79 (2005), pp. 989–996 (cit. on pp. 56, 58, 60).
- [68] M.R. Gilbert, J.-Ch. Sublet, and R. A. Forrest. “Handbook of activation, transmutation, and radiation damage properties of the elements simulated using FISPACT-II & TENDL-2014; Magnetic Fusion Plants”. In: December (2015) (cit. on p. 57).
- [69] F. A. Garner, H. R. Brager, and R. A. Dodd. “Ion-induced spinodal-like decomposition of Fe-Ni-Cr Invar Alloys”. In: *Nucl. Instruments Methods Phys. Res. B* 16 (1986), pp. 244–250 (cit. on p. 57).
- [70] S. J. Zinkle. “Radiation-induced effects on microstructure”. In: *Compr. Nucl. Mater.* Vol. 1. 2012, pp. 65–98 (cit. on pp. 57, 58).
- [71] E. Gaganidze, C. Petersen, E. Materna-Morris, et al. “Mechanical properties and TEM examination of RAFM steels irradiated up to 70dpa in BOR-60”. In: *J. Nucl. Mater.* 417.1-3 (2011), pp. 93–98 (cit. on pp. 57, 58).
- [72] D.A. McClintonck, M.A. Sokolov, D.T. Hoelzer, et al. “Mechanical properties of irradiated ODS-EUROFER and nanocluster strengthened 14YWT”. In: *J. Nucl. Mater.* 392.2 (2009), pp. 353–359 (cit. on p. 58).
- [73] G.R. Odette, M.J. Alinger, and B.D. Wirth. “Recent Developments in Irradiation-Resistant Steels”. In: *Annu. Rev. Mater. Res.* 38.1 (2008), pp. 471–503 (cit. on p. 58).
- [74] M. J. Gorley and Ccfe. *Critical Assessment: Prospects for Reduced Activation Steel for Fusion Plant*. Tech. rep. 2015, pp. 975–980 (cit. on p. 58).
- [75] O.K. Chopra and A.S. Rao. “A review of irradiation effects on LWR core internal materials – Neutron embrittlement”. In: *J. Nucl. Mater.* 412.1 (2011), pp. 195–208 (cit. on p. 58).
- [76] D. L. Smith, R. F. Mattas, and Michael C. Billone. “Fusion Reactor Materials”. In: *Materials Science and Technology*. American Cancer Society, 2006. eprint: <https://onlinelibrary.wiley.com/doi/pdf/10.1002/9783527603978.mst0114> (cit. on p. 60).

- [77]A. Haglund, M. Koehler, D. Catoor, et al. “Polycrystalline elastic moduli of a high-entropy alloy at cryogenic temperatures”. In: *Intermetallics* 58 (2015), pp. 62–64 (cit. on p. 60).
- [78]T. J. Dolan. *Fusion research: Principles, Experiments and Technology*. Pergamon press, 1982, pp. 1–937 (cit. on p. 60).
- [79]F. Otto, A. Dlouhý, Ch Somsen, et al. “The influences of temperature and microstructure on the tensile properties of a CoCrFeMnNi high-entropy alloy”. In: *Acta Materialia* 61.15 (2013), pp. 5743–5755 (cit. on pp. 60, 215).
- [80]F. Otto, A. Dlouhý, C. Somsen, et al. “The influences of temperature and microstructure on the tensile properties of a CoCrFeMnNi high-entropy alloy”. In: *Acta Materialia* 61.15 (2013), pp. 5743–5755 (cit. on p. 60).
- [81]G. Laplanche, P. Gadaud, O. Horst, et al. “Temperature dependencies of the elastic moduli and thermal expansion coefficient of an equiatomic, single-phase CoCrFeMnNi high-entropy alloy”. In: *Journal of Alloys and Compounds* 623 (2015), pp. 348–353 (cit. on p. 60).
- [82]M. H. Tsai. “Physical properties of high entropy alloys”. In: *Entropy* 15.12 (2013), pp. 5338–5345 (cit. on pp. 60, 64, 73, 75).
- [83]D.B. Miracle and O.N. Senkov. “A critical review of high entropy alloys and related concepts”. In: *Acta Mater.* 122 (2017), pp. 448–511. arXiv: 1507.02142 (cit. on pp. 59, 131).
- [84]D.B. Miracle and O.N. Senkov. “A critical review of high entropy alloys and related concepts”. In: *Acta Materialia* 122 (2017), pp. 448–511 (cit. on pp. 59, 61, 64, 66).
- [85]S. Gorsse, M.H. Nguyen, O.N. Senkov, et al. “Database on the mechanical properties of high entropy alloys and complex concentrated alloys”. In: *Data in Brief* 21. December (2018), pp. 2664–2678 (cit. on pp. 61, 62).
- [86]MatWeb Material Property Data. *Material Category Search*. 2019 (cit. on p. 61).
- [87]O. N. Senkov, D. B. Miracle, K. J. Chaput, et al. “Development and exploration of refractory high entropy alloys—A review”. In: *Journal of Materials Research* 33.19 (2018), pp. 3092–3128 (cit. on p. 61).
- [88]K. J. Laws, C. Crosby, A. Sridhar, et al. “High entropy brasses and bronzes – Microstructure, phase evolution and properties”. In: *Journal of Alloys and Compounds* 650 (2015), pp. 949–961 (cit. on p. 62).
- [89]C. Zhang and M. C. Gao. *High-Entropy Alloys*. Ed. by Michael C. Gao, Jien-Wei Yeh, Peter K. Liaw, et al. Cham: Springer International Publishing, 2016, pp. 399–444 (cit. on p. 62).

- [90]M.J. de Oliveira. *Equilibrium Thermodynamics*. Graduate Texts in Physics. Berlin, Heidelberg: Springer Berlin Heidelberg, 2017, pp. 17–25, 172–179 (cit. on p. 63).
- [91]Z. Leong, J. S. Wróbel, S. L. Dudarev, et al. “The Effect of Electronic Structure on the Phases Present in High Entropy Alloys”. In: *Scientific Reports* 7.1 (2017), p. 39803 (cit. on pp. 63, 131, 164).
- [92]S. Guo, C. Ng, J. Lu, et al. “Effect of valence electron concentration on stability of fcc or bcc phase in high entropy alloys”. In: *Journal of Applied Physics* 109.10 (2011), p. 103505 (cit. on pp. 63, 64, 218).
- [93]A. P. Cracknell. “Appendix - Bravais and reciprocal lattices, unit cells, first Brillouin zones”. In: *Electron States and Fermi Surfaces of Elements*. Berlin/Heidelberg: Springer-Verlag, 2005, pp. 451–462 (cit. on p. 64).
- [94]N.G. Jones, R. Izzo, P.M. Mignanelli, et al. “Phase evolution in an Al0.5CrFeCoNiCu High Entropy Alloy”. In: *Intermetallics* 71 (2016), pp. 43–50 (cit. on p. 64).
- [95]B. Predel. “Cu-Pd (Copper-Palladium)”. In: *Cr-Cs – Cu-Zr*. Vol. 5D. Berlin/Heidelberg: Springer-Verlag, 1994, pp. 1–9 (cit. on p. 65).
- [96]A. Fernández-Caballero and J. and S. Wróbel and P. M. Mummery and D. Nguyen-Manh. “Short-Range Order in High Entropy Alloys: Theoretical Formulation and Application to Mo-Nb-Ta-V-W System”. In: *Journal of Phase Equilibria and Diffusion* 38.4 (2017), pp. 391–403 (cit. on pp. 65, 96, 164, 169, 173).
- [97]A. Fernández-Caballero, M. Fedorov, J. Wróbel, et al. “Configurational Entropy in Multicomponent Alloys: Matrix Formulation from Ab Initio Based Hamiltonian and Application to the FCC Cr-Fe-Mn-Ni System”. In: *Entropy* 21.1 (2019), p. 68 (cit. on p. 65).
- [98]C. Varvenne, A. Luque, and W. A. Curtin. “Theory of strengthening in fcc high entropy alloys”. In: *Acta Materialia* 118 (2016), pp. 164–176 (cit. on p. 65).
- [99]F. X. Zhang, S. Zhao, K. Jin, et al. “Local Structure and Short-Range Order in a NiCoCr Solid Solution Alloy”. In: *Physical Review Letters* 118.20 (2017), p. 205501 (cit. on pp. 65, 68).
- [100]P. Cenedese, F. Bley, and S. Lefebvre. “Diffuse scattering in disordered ternary alloys: neutron measurements of local order in a stainless steel Fe 0 . 56 Cr 0 . 21 Ni 0 . 23”. In: *Acta Crystallographica Section A Foundations of Crystallography* 40.3 (1984), pp. 228–240 (cit. on p. 65).
- [101]A. Z. Menshikov, C. Dimitrov, and A. E. Teplykh. “Local Atomic Redistribution Under Irradiation in γ -NiFeCr Alloys”. In: *Journal de Physique III* 7.10 (1997), pp. 1899–1908 (cit. on p. 65).

- [102]A. Bhaduri. *Mechanical Properties and Working of Metals and Alloys*. Vol. 264. Springer Series in Materials Science 4. Singapore: Springer Singapore, 2018, p. 310 (cit. on p. 66).
- [103]G. Laplanche, J. Bonneville, C. Varvenne, et al. “Thermal activation parameters of plastic flow reveal deformation mechanisms in the CrMnFeCoNi high-entropy alloy”. In: *Acta Materialia* 143 (2018), pp. 257–264 (cit. on p. 66).
- [104]D. Chen, Y. Tong, J. Wang, et al. “Microstructural response of He+ irradiated FeCoNiCrTi0.2 high-entropy alloy”. In: *Journal of Nuclear Materials* 510 (2018), pp. 187–192 (cit. on pp. 67, 68, 74).
- [105]T. J. Dolan. *Magnetic Fusion Technology*. Ed. by T. J. Dolan. Vol. 19. Lecture Notes in Energy. London: Springer London, 2013 (cit. on pp. 67, 68).
- [106]P. G. Klemens and G. Neuer. “3.1.2 Estimation method for alloys”. In: *Thermal Conductivity of Pure Metals and Alloys*. Berlin/Heidelberg: Springer-Verlag, 2005, pp. 126–129 (cit. on p. 68).
- [107]B. Predel. “Al-Co (Aluminum-Cobalt)”. In: *Ac-Au – Au-Zr*. Vol. 17. 4. Berlin/Heidelberg: Springer-Verlag, 1996, pp. 1–6 (cit. on p. 69).
- [108]B. Predel. “Al-Cr (Aluminum-Chromium)”. In: *Ac-Au – Au-Zr*. Vol. 5. 1. Berlin/Heidelberg: Springer-Verlag, pp. 1–6 (cit. on p. 69).
- [109]B. Predel. “Co-Cr (Cobalt-Chromium)”. In: *Ca-Cd – Co-Zr*. Berlin/Heidelberg: Springer-Verlag, pp. 1–6 (cit. on p. 69).
- [110]B. Predel. “Al-Cu (Aluminum-Copper)”. In: *Ac-Au – Au-Zr*. Berlin/Heidelberg: Springer-Verlag, pp. 1–9 (cit. on p. 69).
- [111]B. Predel. “Co-Cu (Cobalt-Copper)”. In: *Ca-Cd – Co-Zr*. Berlin/Heidelberg: Springer-Verlag, pp. 1–5 (cit. on p. 69).
- [112]B. Predel. “Cr-Cu (Chromium-Copper)”. In: *Cr-Cs – Cu-Zr*. Berlin/Heidelberg: Springer-Verlag, pp. 1–5 (cit. on p. 69).
- [113]B. Predel. “Al-Fe (Aluminum-Iron)”. In: *Ac-Au – Au-Zr*. Berlin/Heidelberg: Springer-Verlag, pp. 1–10 (cit. on p. 69).
- [114]B. Predel. “Co-Fe (Cobalt-Iron)”. In: *Ca-Cd – Co-Zr*. Berlin/Heidelberg: Springer-Verlag, pp. 1–13 (cit. on p. 69).
- [115]B. Predel. “Cr-Fe (Chromium-Iron)”. In: *Cr-Cs – Cu-Zr*. Berlin/Heidelberg: Springer-Verlag, pp. 1–10 (cit. on p. 69).
- [116]B. Predel. “Cu-Fe (Copper-Iron)”. In: *Cr-Cs – Cu-Zr*. Berlin/Heidelberg: Springer-Verlag, pp. 1–7 (cit. on p. 69).
- [117]B. Predel. “Al-Mn (Aluminum-Manganese)”. In: *Ac-Au – Au-Zr*. Vol. 2. Berlin/Heidelberg: Springer-Verlag, pp. 1–7 (cit. on p. 69).

- [118]B. Predel. “Co-Mn (Cobalt-Manganese)”. In: *Ca-Cd – Co-Zr*. Berlin/Heidelberg: Springer-Verlag, pp. 1–8 (cit. on p. 69).
- [119]B. Predel. “Cr-Mn (Chromium-Manganese)”. In: *Cr-Cs – Cu-Zr*. Vol. 2. Berlin/Heidelberg: Springer-Verlag, pp. 1–6 (cit. on p. 69).
- [120]B. Predel. “Cu-Mn (Copper-Manganese)”. In: *Cr-Cs – Cu-Zr*. Berlin/Heidelberg: Springer-Verlag, 1994, pp. 1–10 (cit. on p. 69).
- [121]B. Predel. “Fe-Mn (Iron-Manganese)”. In: *Dy-Er – Fr-Mo*. Berlin/Heidelberg: Springer-Verlag, pp. 1–8 (cit. on p. 69).
- [122]B. Predel. “Al-Ni (Aluminum-Nickel)”. In: *Ac-Au – Au-Zr*. Berlin/Heidelberg: Springer-Verlag, pp. 1–7 (cit. on p. 69).
- [123]B. Predel. “Co-Ni (Cobalt-Nickel)”. In: *Ca-Cd – Co-Zr*. Berlin/Heidelberg: Springer-Verlag, pp. 1–5 (cit. on p. 69).
- [124]B. Predel. “Cr-Ni (Chromium-Nickel)”. In: *Cr-Cs – Cu-Zr*. Cd. Berlin/Heidelberg: Springer-Verlag, pp. 1–7 (cit. on p. 69).
- [125]B. Predel. “Cu-Ni (Copper-Nickel)”. In: *Cr-Cs – Cu-Zr*. Vol. 2. Berlin/Heidelberg: Springer-Verlag, 1958, pp. 1–7 (cit. on p. 69).
- [126]B. Predel. “Fe-Ni (Iron-Nickel)”. In: *Dy-Er – Fr-Mo*. Berlin/Heidelberg: Springer-Verlag, pp. 1–12 (cit. on p. 69).
- [127]B. Predel. “Mn-Ni (Manganese-Nickel)”. In: *Li-Mg – Nd-Zr*. Vol. 2. Berlin/Heidelberg: Springer-Verlag, pp. 1–7 (cit. on p. 69).
- [128]B. Predel. “Al-Ti (Aluminum-Titanium)”. In: *Ac-Au – Au-Zr*. Berlin/Heidelberg: Springer-Verlag, 1983, pp. 1–8 (cit. on p. 69).
- [129]B. Predel. “Ni-Ti (Nickel-Titanium)”. In: *Ni-Np – Pt-Zr*. Berlin/Heidelberg: Springer-Verlag, pp. 1–5 (cit. on p. 69).
- [130]B. Predel. “Cr-Ti (Chromium-Titanium)”. In: *Cr-Cs – Cu-Zr*. Berlin/Heidelberg: Springer-Verlag, pp. 1–8 (cit. on p. 69).
- [131]B. Predel. “Cu-Ti (Copper-Titanium)”. In: *Cr-Cs – Cu-Zr*. Berlin/Heidelberg: Springer-Verlag, pp. 1–7 (cit. on p. 69).
- [132]B. Predel. “Fe-Ti (Iron-Titanium)”. In: *Dy-Er – Fr-Mo*. Berlin/Heidelberg: Springer-Verlag, 2006, pp. 1–7 (cit. on p. 69).
- [133]B. Predel. “Mn-Ti (Manganese-Titanium)”. In: *Li-Mg – Nd-Zr*. Berlin/Heidelberg: Springer-Verlag, pp. 1–2 (cit. on p. 69).
- [134]B. Predel. “Ni-Ti (Nickel-Titanium)”. In: *Ni-Np – Pt-Zr*. Berlin/Heidelberg: Springer-Verlag, pp. 1–5 (cit. on p. 69).
- [135]B. Predel. “Al-V (Aluminum-Vanadium)”. In: *Ac-Au – Au-Zr*. Berlin/Heidelberg: Springer-Verlag, pp. 1–6 (cit. on p. 69).

- [136]B. Predel. “Cr-V (Chromium-Vanadium)”. In: *Cr-Cs – Cu-Zr*. Berlin/Heidelberg: Springer-Verlag, pp. 1–4 (cit. on p. 69).
- [137]B. Predel. “Cu-V (Copper-Vanadium)”. In: *Cr-Cs – Cu-Zr*. Berlin/Heidelberg: Springer-Verlag, pp. 1–3 (cit. on p. 69).
- [138]B. Predel. “Fe-V (Iron-Vanadium)”. In: *Dy-Er – Fr-Mo*. l. Berlin/Heidelberg: Springer-Verlag, pp. 1–6 (cit. on p. 69).
- [139]B. Predel. “Mn-V (Manganese-Vanadium)”. In: *Li-Mg – Nd-Zr*. Berlin/Heidelberg: Springer-Verlag, pp. 1–2 (cit. on p. 69).
- [140]B. Predel. “Ni-V (Nickel-Vanadium)”. In: *Ni-Np – Pt-Zr*. Vol. 3. V. Berlin/Heidelberg: Springer-Verlag, pp. 1–3 (cit. on p. 69).
- [141]B. Predel. “Ti-V (Titanium-Vanadium)”. In: *Pu-Re – Zn-Zr*. Berlin/Heidelberg: Springer-Verlag, pp. 1–4 (cit. on p. 69).
- [142]L. Yang, H. Ge, J. Zhang, et al. “High He-ion irradiation resistance of CrMnFe-CoNi high-entropy alloy revealed by comparison study with Ni and 304SS”. In: *Journal of Materials Science & Technology* 35.3 (2019), pp. 300–305 (cit. on p. 68).
- [143]Y. Lu, H. Huang, X. Gao, et al. “A promising new class of irradiation tolerant materials: Ti₂ZrHfV_{0.5}Mo_{0.2} high-entropy alloy”. In: *Journal of Materials Science & Technology* 35.3 (2019), pp. 369–373 (cit. on p. 68).
- [144]S. Sun, N. Qiu, K. Zhang, et al. “Segregation of Al_{1.5}CrFeNi high entropy alloys induced by vacancy-type defects”. In: *Scripta Materialia* 161 (2019), pp. 40–43 (cit. on p. 68).
- [145]C.M. Barr, J.E. Nathaniel, K.A. Unocic, et al. “Exploring radiation induced segregation mechanisms at grain boundaries in equiatomic CoCrFeNiMn high entropy alloy under heavy ion irradiation”. In: *Scripta Materialia* 156 (2018), pp. 80–84 (cit. on p. 68).
- [146]T. Yang, S. Xia, S. Liu, et al. “Precipitation behavior of Al_xCoCrFeNi high entropy alloys under ion irradiation”. In: *Scientific Reports* 6.1 (2016), p. 32146 (cit. on pp. 68, 71).
- [147]S. Xia, M. C. Gao, T. Yang, et al. “Phase stability and microstructures of high entropy alloys ion irradiated to high doses”. In: *Journal of Nuclear Materials* 480 (2016), pp. 100–108 (cit. on pp. 68, 163).
- [148]F. Granberg, K. Nordlund, Mohammad W. Ullah, et al. “Mechanism of Radiation Damage Reduction in Equiatomic Multicomponent Single Phase Alloys”. In: *Phys. Rev. Lett.* 116.13 (2016), p. 135504 (cit. on pp. 68, 132).
- [149]D. Olander. *Fundamental aspects of nuclear reactor fuel elements*. 1976, p. 602 (cit. on pp. 68, 73, 76, 221, 229).

- [150]M. Caro, L.K. Béland, G.D. Samolyuk, et al. “Lattice thermal conductivity of multi-component alloys”. In: *J. Alloys Compd.* 648 (2015), pp. 408–413 (cit. on pp. 72, 75).
- [151]Z. Wu and H. Bei. “Microstructures and mechanical properties of compositionally complex Co-free FeNiMnCr 18 FCC solid solution alloy”. In: *Mater. Sci. Eng. A* 640 (2015), pp. 217–224 (cit. on pp. 72, 203).
- [152]H.R. Higgy and F.H. Hammad. “EFFECT OF FAST-NEUTRON IRRADIATION ON MECHANICAL PROPERTIES OF STAINLESS STEELS : AISI TYPES 304 , 316 AND 347 Several types of stainless steels are widely considered as cladding and structural materials in nuclear reactors because of their excellent co”. In: *Journal of Nuclear Materials* 55 (1975), pp. 177–186 (cit. on p. 74).
- [153]C. Lu, T. Yang, K. Jin, et al. “Radiation-induced segregation on defect clusters in single-phase concentrated solid-solution alloys”. In: *Acta Materialia* 127 (2017), pp. 98–107 (cit. on p. 74).
- [154]C. Lu, T. Yang, K. Jin, et al. “Enhanced void swelling in NiCoFeCrPd high-entropy alloy by indentation-induced dislocations”. In: *Materials Research Letters* 6.10 (2018), pp. 584–591 (cit. on p. 74).
- [155]National Physical Laboratory. *Tables of Physical and Chemical Constants*. 2018 (cit. on pp. 75, 118).
- [156]B. Cantor, I.T.H. Chang, P. Knight, et al. “Microstructural development in equiatomic multicomponent alloys”. In: *Mater. Sci. Eng. A* 375-377 (2004), pp. 213–218 (cit. on pp. 76, 131, 162, 165, 202).
- [157]L. H. Thomas. “The calculation of atomic ells”. In: *Mathematical Proceedings of the Cambridge Philosophical Society* 23.5 (1927), pp. 542–548 (cit. on p. 79).
- [158]E. Fermi. “Eine statistische Methode zur Bestimmung einiger Eigenschaften des Atoms und ihre Anwendung auf die Theorie des periodischen Systems der Elemente”. In: *Zeitschrift für Physik* 48.1-2 (1928), pp. 73–79 (cit. on p. 79).
- [159]J. D. Walecka. *Introduction to modern physics: theoretical foundations*. 2008th ed. World Scientific Publishing (cit. on pp. 79, 80).
- [160]T. A. Carlson, C.W. Nestor, N. Wasserman, et al. “Calculated ionization potentials for multiply charged ions”. In: *Atomic Data and Nuclear Data Tables* 2 (1970), pp. 63 –99 (cit. on pp. 80, 81).
- [161]E. H. Lieb and B. Simon. “Thomas-Fermi theory revisited”. In: *Physical Review Letters* 31.11 (1973), pp. 681–683 (cit. on p. 81).
- [162]E. H. Lieb and B. Simon. “The Hartree-Fock theory for coulomb systems”. In: *Communications in Mathematical Physics* 53 (1977), pp. 185–194 (cit. on p. 81).

- [163]F. Giustino. *Materials Modelling using Density Functional Theory: Properties and Predictions*. 2014th ed. Oxford University Press (cit. on pp. 81, 85).
- [164]P. Hohenberg and W. Kohn. “Inhomogeneous electron gas”. In: *Physical Review B* 136.3B (1964), pp. 864–871 (cit. on p. 82).
- [165]J. E. Harriman. “Orthonormal orbitals for the representation of an arbitrary density”. In: *Physical Review A* 24.2 (1981), pp. 680–682 (cit. on p. 82).
- [166]J. P. Perdew and K. Burke and M. Ernzerhof. “Generalized gradient approximation made simple”. In: *Physical Review Letters* 77.18 (1996), pp. 3865–3868 (cit. on pp. 82, 85, 97, 134).
- [167]W. Kohn and L. J. Sham. “Self-Consistent Equations Including Exchange and Correlation Effects”. In: *Phys. Rev.* 140.4A (1965), A1133–A1138 (cit. on p. 82).
- [168]A. Zunger J. P. Perdew. “Self-interaction correction to density-functional approximations for many-electron systems”. In: *Physical Review B* 23.10 (1981), pp. 5048–5079 (cit. on p. 83).
- [169]D. M. Ceperley and B. J. Alder. “Ground State of the Electron Gas by a Stochastic Method f”. In: *Physical Review Letters* 45.7 (1980), pp. 566–569 (cit. on p. 83).
- [170]F. Bloch. “Über die Quantenmechanik der Elektronen in Kristallgittern”. In: *Zeitschrift für Physik* 52.7-8 (1929), pp. 555–600 (cit. on p. 84).
- [171]L. D. Landau and E.M. Lifshitz. *Statistical Physics: Part I*. 2013th ed. Butterworth-Heinemann (cit. on p. 84).
- [172]I. M. Gelfand. *Lectures on Linear Algebra*. 1989th ed. Dover Publications (cit. on p. 84).
- [173]G. N. Lewis. “The atom and the molecule”. In: *Journal of the American Chemical Society* 38.4 (1916), pp. 762–785 (cit. on p. 85).
- [174]U. von Barth and L. Hedin. “A local exchange-correlation potential for the spin polarized case: I”. In: *J. Phys. C: Solid State Phys.* 5.Hedin (1972), pp. 1629–1642 (cit. on p. 85).
- [175]H. Hellmann. “Zur Rolle der kinetischen Elektronenenergie für die zwischenatomaren Kräfte”. In: *Zeitschrift für Physik* 85.3-4 (1933), pp. 180–190 (cit. on p. 85).
- [176]R. P. Feynman. “Forces in molecules”. In: *Physical Review* 56.4 (1939), pp. 340–343 (cit. on p. 86).
- [177]Wikipedia. *List of quantum chemistry and solid-state physics software*. 2018 (cit. on p. 86).

- [178]J. G. Lee. *Computational materials science: An introduction*. CRC Press Taylor & Francis Group, 2012 (cit. on pp. 86, 87).
- [179]A. van de Walle. “Methods for first-principles alloy thermodynamics”. In: *The Journal of The Minerals, Metals & Materials Society* 65.11 (2013), pp. 1523–1532 (cit. on pp. 87, 88).
- [180]F. Ducastelle. *Order Phase Stability Alloys*. Vol. 3. Cohesion and Structure. North Holland, 1991 (cit. on p. 88).
- [181]J. W. D. Connolly and A. R. Williams. “Density-functional theory applied to phase transformations in transition-metal alloys”. In: *Physical Review B* 27.8 (1983), pp. 5169–5172 (cit. on pp. 88, 90, 98, 142).
- [182]P. Cenedese and D. Gratias. “Multicomponent formalism in the mean-field approximation: a geometric interpretation of Chebychev polynomials”. In: *Physica A: Statistical Mechanics and its Applications* 179.2 (1991), pp. 277–287 (cit. on pp. 88, 170, 174).
- [183]C. Wolverton and D. de Fontaine. “Cluster expansions of alloy energetics in ternary intermetallics”. In: *Physical Review B* 49.13 (1994), pp. 8627–8642 (cit. on p. 89).
- [184]A. van de Walle. “Multicomponent multisublattice alloys, nonconfigurational entropy and other additions to the Alloy Theoretic Automated Toolkit”. In: *Calphad: Computer Coupling of Phase Diagrams and Thermochemistry* 33.2 (2009), pp. 266–278 (cit. on pp. 89, 97, 134, 135, 164, 166–168, 170, 179).
- [185]M. Asta, C. Wolverton, D. de Fontaine, et al. “Effective cluster interactions from cluster-variation formalism. I”. In: *Physical Review B* 44.10 (1991), pp. 4907–4913 (cit. on p. 89).
- [186]J. M. Sanchez, F. Ducastelle, and D. Gratias. “Generalized cluster description of multicomponent systems”. In: *Physica A: Statistical Mechanics and its Applications* 128.1-2 (1984), pp. 334–350 (cit. on pp. 90, 98, 142).
- [187]J. M. Sanchez. “Cluster expansion and the configurational theory of alloys”. In: *Physical Review B - Condensed Matter and Materials Physics* 81.22 (2010), pp. 1–13 (cit. on p. 90).
- [188]S. V. Barabash, V. Blum, S. Müller, et al. “Prediction of unusual stable ordered structures of Au-Pd alloys via a first-principles cluster expansion”. In: *Physical Review B - Condensed Matter and Materials Physics* 74.3 (2006), pp. 1–22 (cit. on p. 90).
- [189]G. L. W. Hart and R. W. Forcade. “Algorithm for generating derivative structures”. In: *Physical Review B - Condensed Matter and Materials Physics* 77.22 (2008), pp. 224115–1–224115–12 (cit. on pp. 91, 167).

- [190]G. Inden and W. Pitsch. 9. *Atomic ordering*. Vol. Materials Science and Technology: A comprehensive Treatment. Volume 5. VCH Publishers, 2012 (cit. on p. 91).
- [191]M. H. F. Sluiter and Y. Kawazoe. “Invariance of truncated cluster expansions for first-principles alloy thermodynamics”. In: *Physical Review B - Condensed Matter and Materials Physics* 71.21 (2005), pp. 1–2 (cit. on pp. 92, 171).
- [192]N. A. Zarkevich and D. D. Johnson. “Reliable first-principles alloy thermodynamics via truncated cluster expansions”. In: *Physical Review Letters* 92.25 I (2004), pp. 1–4 (cit. on p. 92).
- [193]J. Boutard, M. J. Caturla, S. L. Dudarev, et al. *Strategic Objectives for Fusion Materials Modelling and Experimental Validation (2010-2015)*. Tech. rep. March 2009. 2009, pp. 1–15 (cit. on p. 92).
- [194]“3d, 4d and 5d Elements, Alloys and Compounds”. In: 19a (1986), pp. 3–5 (cit. on p. 93).
- [195]R. Kikuchi. “A theory of cooperative phenomena”. In: *Physical Review* 81.6 (1951), pp. 988–1003 (cit. on pp. 94, 175).
- [196]A. Finel. “The cluster variation method and some applications”. In: *Proceedings of NATO Advanced Study Institute on Statics and Dynamics of Alloy Phase Transformations*. Ed. by P. E. A. Turchi and A. Gonis. Rhodes, Greece: Springer, 1992, pp. 495–540 (cit. on pp. 94, 164, 174, 191).
- [197]J. A. Barker. “Methods of Approximation in the Theory of Regular Mixtures”. In: *Proceedings of the Royal Society A: Mathematical, Physical and Engineering Sciences* 216.1124 (1953), pp. 45–56 (cit. on pp. 94, 175).
- [198]N. Metropolis and A. W. Rosenbluth and M. N. Rosenbluth and A. W. Rosenbluth and M. N. Rosenbluth and A. H. Teller and E. Teller. “Equation of state calculations by fast computing machines”. In: *The Journal of Chemical Physics* 21.6 (1953), pp. 1087–1092 (cit. on pp. 94, 95).
- [199]K. Binder. *Phase Transitions and Critical Phenomena, Vol. 5 b*. Academic Press, 1976 (cit. on p. 96).
- [200]A. van de Walle and M. Asta. “Self-driven lattice-model Monte Carlo simulations of alloy thermodynamic properties and phase diagrams”. In: *Modelling Simul. Mater. Sci. Eng* 10.02 (2002), pp. 521–538 (cit. on pp. 96, 97, 134, 178).
- [201]G. Kresse and J. Hafner. “Ab initio molecular dynamics for liquid metals”. In: *Phys. Rev. B* 47.1 (1993), pp. 558–561. arXiv: 0927 – 0256(96) 00008 [10.1016] (cit. on pp. 97, 134).

- [202]G. Kresse and J. Hafner. “Ab initio molecular-dynamics simulation of the liquid-metal–amorphous–semiconductor transition in germanium”. In: *Phys. Rev. B* 49.20 (1994), pp. 14251–14269. arXiv: 0927–0256(96)00008 [10.1016] (cit. on pp. 97, 134).
- [203]G. Kresse, J. Furthmüller, and J Furthmüller B’. “Efficiency of ab-initio total energy calculations for metals and semiconductors using a plane-wave basis set”. In: *Comput. Mater. Sci.* 6.1 (1996), pp. 15–50. arXiv: 0927–0256(96)00008 [10.1016] (cit. on pp. 97, 134).
- [204]G. Kresse and J. Furthmüller. “Efficient iterative schemes for ab initio total-energy calculations using a plane-wave basis set”. In: *Phys. Rev. B* 54.16 (1996), pp. 11169–11186. arXiv: 0927–0256(96)00008 [10.1016] (cit. on pp. 97, 134).
- [205]P. E. Blöchl. “Projector augmented-wave method”. In: *Phys. Rev. B* 50.24 (1994), pp. 17953–17979. arXiv: arXiv:1408.4701v2 (cit. on pp. 97, 134).
- [206]G. Kresse and D. Joubert. “From ultrasoft pseudopotentials to the projector augmented-wave method”. In: *Phys. Rev. B* 59.3 (1999), pp. 1758–1775. arXiv: 0927–0256(96)00008 [10.1016] (cit. on pp. 97, 134).
- [207]G. Ya Lyubarskii. *The Application of Group Theory in Physics*. Pergamon Press, 1960 (cit. on p. 98).
- [208]A. Vos T. Hahn. *Guide to the use of space group tables*. Ed. by T. Hahn. D. Reidel Publishing Company, 1985 (cit. on p. 99).
- [209]M. A. Jaswon and M. A. Rose. *Crystal Symmetry: Theory of Colour Crystallography*. Ellis Horwood Limited, 1983 (cit. on p. 99).
- [210]C. Zhang, F. Zhang, S. Chen, et al. “Computational Thermodynamics Aided High-Entropy Alloy Design”. In: *JOM* 64.7 (2012), pp. 839–845 (cit. on p. 105).
- [211]Z. Wu, H. Bei, F. Otto, et al. “Recovery, recrystallization, grain growth and phase stability of a family of FCC-structured multi-component equiatomic solid solution alloys”. In: *Intermetallics* 46 (2014), pp. 131–140 (cit. on p. 105).
- [212]B. Cantor, I.T.H. Chang, P. Knight, et al. “Microstructural development in equiatomic multicomponent alloys”. In: *Mater. Sci. Eng. A* 375-377 (2004), pp. 213–218 (cit. on pp. 105, 203).
- [213]Y. Ma, Q. Wang, C. Li, et al. “Chemical short-range orders and the induced structural transition in high-entropy alloys”. In: *Scr. Mater.* 144 (2018), pp. 64–68 (cit. on p. 105).
- [214]Q. Yang, Y. Tang, Y. Wen, et al. “Microstructures and properties of CoCrCuFeN-iMox high-entropy alloys fabricated by mechanical alloying and spark plasma sintering”. In: *Powder Metall.* 61.2 (2018), pp. 115–122 (cit. on p. 105).

- [215]M. C. Flemings. “Solidification Processing”. In: *Materials Science and Technology*. American Cancer Society, 2006. eprint: <https://onlinelibrary.wiley.com/doi/pdf/10.1002/9783527603978.mst0173> (cit. on p. 105).
- [216]J.; Ayache, L.; Beaunier, J.; Boumendil, et al. *Sample Preparation Handbook for Transmission Electron Microscopy: Techniques*. 2009, p. 360 (cit. on p. 107).
- [217]P.T. Wady, A. Draude, S.M. Shubeita, et al. “Accelerated radiation damage test facility using a 5 MV tandem ion accelerator”. In: *Nucl. Instruments Methods Phys. Res. Sect. A Accel. Spectrometers, Detect. Assoc. Equip.* 806 (2016), pp. 109–116 (cit. on pp. 109, 207, 208).
- [218]K. Nordlund, A. E. Sand, F. Granberg, et al. *Primary Radiation Damage in Materials. Review of Current Understanding and Proposed New Standard Displacement Damage Model to Incorporate in Cascade Defect Production Efficiency and Mixing Effects*. Tech. rep. 2015, p. 87 (cit. on p. 113).
- [219]Cowley, J. M. *Diffraction Physics*. 3rd edition. North-Holland Personal Library, 1995, p. 481 (cit. on p. 115).
- [220]A. Guinier. *Advances in X-Ray and Neutron Diffraction Techniques*. Ed. by R. Gevers S. Amelinckx and J. van Landuyt. North-Holland Publishing Company, 1978 (cit. on p. 115).
- [221]L. M. Peng, G. Ren, S. L. Dudarev, et al. “Robust parameterization of elastic and absorptive electron atomic scattering factors”. In: *Acta Crystallographica Section A: Foundations of Crystallography* 52.2 (1996), pp. 257–276 (cit. on p. 115).
- [222]Fultz, B. and Howe, J. *Transmission Electron Microscopy and Diffractometry of Materials*. Ed. by H. E. Stanley W. T. Rhodes and R. Needs. 4th Edition. Graduated Text in Physics: Springer-Verlag, 2013, p. 775 (cit. on p. 116).
- [223]B. Toby. *Program CMPR*. version 1.34. NIST. 2005 (cit. on pp. 117, 215).
- [224]U. König, R. S. Angélica, N. Norberg, et al. “Rapid X-ray diffraction (XRD) for grade control of bauxites”. In: *ICSOBA 2012*. November 2012. 2012, p. 11 (cit. on p. 117).
- [225]R. P. Saxon M. Inokuti and J. L. Dehmer. “Total cross-sections for inelastic scattering of charged particles by atoms and molecules-VIII systematics for atoms in the first and second row”. In: *International Journal for Radiation Physics and Chemistry* 7.2-3 (1975), pp. 109–120 (cit. on p. 118).
- [226]S. Nishikawa and S. Kikuchi. “Diffraction of Cathode Rays by Mica”. In: *Nature* 121 (1928), pp. 1019–1020 (cit. on p. 118).
- [227]J. W. Edington. *4. Typical Electron Microscope Investigations*. Eindhoven: Palgrave, London, 1976, pp. 1–112 (cit. on p. 119).

- [228]G. Thomas. “KIKUCHI ELECTRON DIFFRACTION AND APPLICATIONS”. In: *Diffraction Imaging Tech. Mater. Sci.* Second Edition. Elsevier, 1978, pp. 399–427 (cit. on p. 120).
- [229]P. Stadelmann. *Simulation of diffraction patterns and high resolution images using jems Installation on WindowsXP*. Lausanne, Switzerland, 2006 (cit. on p. 121).
- [230]“Crystallography Open Database (COD): an open-access collection of crystal structures and platform for world-wide collaboration”. In: *Nucleic Acids Research* 40.D1 (2012), pp. D420–D427 (cit. on p. 121).
- [231]M. De Graef. *2. Basic quantum mechanics, Bragg’s Law, and other tools*. 2014, pp. 79–135 (cit. on p. 123).
- [232]M.J. Whelan. *Dynamical Theory of Electron Diffraction*. Second Edition. NORTH-HOLLAND PUBLISHING COMPANY, 1978, pp. 43–106 (cit. on p. 124).
- [233]M. Wilkens. “IDENTIFICATION OF SMALL DEFECT CLUSTERS IN PARTICLE-IRRADIATED CRYSTALS BY MEANS OF TRANSMISSION ELECTRON MICROSCOPY”. In: *Diffraction and Imaging Techniques in Material Science*. Elsevier, 1978, pp. 185–215 (cit. on pp. 125, 126).
- [234]K. K. Meyers, M. A.; Chawla. *Mechanical Behaviour of Materials*. 1st edition. Cambridge University Press, 2009 (cit. on pp. 125, 126).
- [235]C. A. Schuh. “Nanoindentation studies of materials”. In: *Mater. Today* 9.5 (2006), pp. 32–40 (cit. on p. 125).
- [236]W.C. Oliver and G.M. Pharr. “Measurement of hardness and elastic modulus by instrumented indentation: Advances in understanding and refinements to methodology”. In: *J. Mater. Res.* 19.01 (2004), pp. 3–20 (cit. on pp. 127, 211, 212, 214).
- [237]G. M. Pharr, E. G. Herbert, and Y. Gao. “The Indentation Size Effect: A Critical Examination of Experimental Observations and Mechanistic Interpretations”. In: *Annu. Rev. Mater. Res.* 40.1 (2010), pp. 271–292 (cit. on p. 128).
- [238]M. Calvo-Dahlborg, J. Cornide, J. Tobola, et al. “Interplay of electronic, structural and magnetic properties as the driving feature of high-entropy CoCr-FeNiPd alloys”. In: *J. Phys. D. Appl. Phys.* 50.18 (2017), p. 185002 (cit. on pp. 131, 132, 163).
- [239]O.N. Senkov, G.B. Wilks, D.B. Miracle, et al. “Refractory high-entropy alloys”. In: *Intermetallics* 18.9 (2010), pp. 1758–1765 (cit. on p. 132).
- [240]I. Toda-Caraballo, J.S. Wróbel, S.L. Dudarev, et al. “Interatomic spacing distribution in multicomponent alloys”. In: *Acta Mater.* 97 (2015), pp. 156–169 (cit. on pp. 132–134, 142, 146, 158).

- [241] R. Kozak, A. Sologubenko, and W. Steurer. “Single-phase high-entropy alloys – an overview”. In: *Zeitschrift für Krist. - Cryst. Mater.* 230.1 (2015), pp. 55–68 (cit. on p. 132).
- [242] L. J Santodonato, Y. Zhang, M. Feygenson, et al. “Deviation from high-entropy configurations in the atomic distributions of a multi-principal-element alloy”. In: *Nat. Commun.* 6.1 (2015), p. 5964 (cit. on pp. 132, 164).
- [243] R. E. A. Williams, B. Welk, B. D. Esser, et al. “Characterizing Sub-lattice Occupancies in B2 Phases in High Entropy Metallic Alloys using Atomic Resolution STEM-XEDS Mapping”. In: *Microsc. Microanal.* 20.S3 (2014), pp. 116–117 (cit. on p. 132).
- [244] D. Nguyen-Manh, M. Yu Lavrentiev, M. Muzyk, et al. “First-principles models for phase stability and radiation defects in structural materials for future fusion power-plant applications”. In: *J. Mater. Sci.* 47.21 (2012), pp. 7385–7398 (cit. on p. 132).
- [245] J. S. Wróbel, D. Nguyen-Manh, M. Y. Lavrentiev, et al. “Phase stability of ternary fcc and bcc Fe-Cr-Ni alloys”. In: *Phys. Rev. B* 91.2 (2015), p. 024108. arXiv: 1410.0548 (cit. on pp. 133, 134, 143, 164, 167, 179, 187, 193, 233, 248, 249).
- [246] A. Walle and G. Ceder. “Automating first-principles phase diagram calculations”. In: *J. Phase Equilibria* 23.4 (2002), pp. 348–359. arXiv: 0201511 [cond-mat] (cit. on pp. 134, 142).
- [247] G. L. W. Hart and R. W. Forcade. “Generating derivative structures from multilattices: Algorithm and application to hcp alloys”. In: *Phys. Rev. B* 80.1 (2009), p. 014120 (cit. on p. 134).
- [248] W.P. Huhn and M. Widom. “Prediction of A2 to B2 Phase Transition in the High-Entropy Alloy Mo-Nb-Ta-W”. In: *JOM* 65.12 (2013), pp. 1772–1779. arXiv: 1306.5043 (cit. on pp. 142, 148, 156, 158).
- [249] D. de Fontaine. “The number of independent pair-correlation functions in multicomponent systems”. In: *J. Appl. Crystallogr.* 4.1 (1971), pp. 15–19 (cit. on p. 143).
- [250] Zunger, Wei, Ferreira, et al. “Special quasirandom structures.” In: *Phys. Rev. Lett.* 65.3 (1990), pp. 353–356. arXiv: 1011.1669 (cit. on p. 147).
- [251] V. Blum and A. Zunger. “Prediction of ordered structures in the bcc binary systems of Mo, Nb, Ta, and W from first-principles search of approximately 3,000,000 possible configurations”. In: *Phys. Rev. B* 72.2 (2005), p. 020104 (cit. on pp. 148, 173).
- [252] M. Muzyk, D. Nguyen-Manh, K. J. Kurzydłowski, et al. “Phase stability, point defects, and elastic properties of W-V and W-Ta alloys”. In: *Phys. Rev. B* 84.10 (2011), p. 104115 (cit. on pp. 149, 154).

- [253]I. Mirebeau, M. Hennion, and G. Parette. “First Measurement of Short-Range-Order Inversion as a Function of Concentration in a Transition Alloy”. In: *Phys. Rev. Lett.* 53.7 (1984), pp. 687–690 (cit. on p. 153).
- [254]F. Körmann and M. Sluiter. “Interplay between Lattice Distortions, Vibrations and Phase Stability in NbMoTaW High Entropy Alloys”. In: *Entropy* 18.8 (2016), p. 403 (cit. on p. 156).
- [255]I. Toda-Caraballo, J. S. Wróbel, D. Nguyen-Manh, et al. “Simulation and Modeling in High Entropy Alloys”. In: *JOM* 69.11 (2017), pp. 2137–2149 (cit. on p. 158).
- [256]C. Wolverton, V. Ozolins, and A. Zunger. “First-principles theory of short-range order in size-mismatched metal alloys: Cu-Au, Cu-Ag, and Ni-Au”. In: *Phys. Rev. B* 57.8 (1998), pp. 4332–4348 (cit. on p. 158).
- [257]M. Widom. “Entropy and Diffuse Scattering: Comparison of NbTiVZr and CrMoNbV”. In: *Metall. Mater. Trans. A* 47.7 (2016), pp. 3306–3311. arXiv: 1505.0243 (cit. on p. 158).
- [258]O.N. Senkov, G.B. Wilks, J.M. Scott, et al. “Mechanical properties of Nb₂₅Mo₂₅Ta₂₅W₂₅ and V₂₀Nb₂₀Mo₂₀Ta₂₀W₂₀ refractory high entropy alloys”. In: *Intermetallics* 19.5 (2011), pp. 698–706 (cit. on p. 158).
- [259]R. Carroll, C. Lee, C. W. Tsai, et al. “Experiments and Model for Serration Statistics in Low-Entropy, Medium-Entropy, and High-Entropy Alloys”. In: *Scientific Reports* 5.October (2015), pp. 1–12 (cit. on p. 163).
- [260]M. S. Lucas, L. Mauger, J. A. Muñoz, et al. “Magnetic and vibrational properties of high-entropy alloys”. In: *Journal of Applied Physics* 109.7 (2011), pp. 0–3 (cit. on p. 163).
- [261]P. L. Rossiter and P. Wells. “The dependence of the electrical resistivity on short-range order”. In: *Journal of Physics C: Solid State Physics* 4 (1971), pp. 354 –363 (cit. on p. 163).
- [262]J. E. Spruiell and E. E. Stansbury. “X-Ray study of short-range order in nickel alloys containing 10.7 and 20.0 at. % Molybdenum”. In: *Journal of Physics and Chemistry of Solids* 26.5 (1965), pp. 811–822 (cit. on p. 163).
- [263]J. C. Fisher. “On the strength of solid solution alloys”. In: *Acta Metallurgica* 2.1 (1954), pp. 9–10 (cit. on p. 164).
- [264]de Fontaine D. “Cluster Approach to Order-Disorder Transformations in Alloys”. In: *Solid State Physics* 47.18 (1994), pp. 33–176 (cit. on pp. 164, 168).
- [265]A. Van de Walle, M. Asta, and G. Ceder. “The Alloy Theoretic Automated Toolkit: A User Guide”. In: *Calphad: Computer Coupling of Phase Diagrams and Thermochemistry* 26.2 (2002), pp. 539–553 (cit. on pp. 164, 166–168, 170).

- [266] J. M. Sanchez and D. de Fontaine. “The fcc Ising model in the cluster variation approximation”. In: *Physical Review B* 17.7 (1978), pp. 2926–2936 (cit. on pp. 164, 191).
- [267] Z. W. Lu, S. H. Wei, A. Zunger, et al. “First-principles statistical mechanics of structural stability of intermetallic compounds”. In: *Physical Review B* 44.2 (1991), pp. 512–544 (cit. on p. 165).
- [268] F. Lechermann, M. Fähnle, and J. M. Sanchez. “First-principles investigation of the Ni-Fe-Al system”. In: *Intermetallics* 13.10 (2005), pp. 1096–1109 (cit. on p. 165).
- [269] H. Ackermann, G. Inden, and R. Kikuchi. “Tetrahedron approximation of the cluster variation method for b.c.c. alloys”. In: *Acta Metallurgica* 37.1 (1989), pp. 1–7 (cit. on p. 165).
- [270] P.D. Tepesch, M. Asta, and G. Ceder. “Computation of configurational entropy using Monte Carlo probabilities in cluster-variation method entropy expressions”. In: *Modelling and Simulation in Materials Science and Engineering* 6.6 (1998), pp. 787–797 (cit. on p. 165).
- [271] G. B. Taggart. “Generalized Flinn operators with applications to multi-component alloys”. In: *Journal of Physics and Chemistry of Solids* 34.18 (1973), pp. 1917–1925 (cit. on p. 168).
- [272] D. Gratias, J. M. Sanchez, and D. de Fontaine. “Application of group theory to the calculation of the configurational entropy in the cluster variation method”. In: *Physica A: Statistical Mechanics and its Applications* 113.1-2 (1982), pp. 315–337 (cit. on p. 175).
- [273] J. S. Wróbel, D. Nguyen-Manh, K. J. Kurzydłowski, et al. “A first-principles model for anomalous segregation in dilute ternary tungsten-rhenium-vacancy alloys”. In: *Journal of Physics: Condensed Matter* 29.14 (2017), p. 145403 (cit. on pp. 177, 178).
- [274] P. E. Blöchl. “Projector augmented-wave method”. In: *Phys. Rev. B* 50.24 (1994), pp. 17953–17979 (cit. on p. 177).
- [275] G. Kresse and J. Hafner. “Ab initio molecular-dynamics simulation of the liquid-metal–amorphous–semiconductor transition in germanium”. In: *Phys. Rev. B* 49.20 (1994), pp. 14251–14269 (cit. on p. 177).
- [276] G. Kresse and D. Joubert. “From ultrasoft pseudopotentials to the projector augmented-wave method”. In: *Phys. Rev. B* 59.3 (1999), pp. 1758–1775 (cit. on p. 177).
- [277] G. Kresse and J. Hafner. “Ab initio molecular dynamics for liquid metals”. In: *Phys. Rev. B* 47.1 (1993), pp. 558–561 (cit. on p. 177).

- [278]G. Kresse and J. Furthmüller. “Efficient iterative schemes for ab initio total-energy calculations using a plane-wave basis set”. In: *Phys. Rev. B* 54.16 (1996), pp. 11169–11186 (cit. on p. 177).
- [279]G. Kresse, J. Furthmüller, and J Furthmüller B’. “Efficiency of ab-initio total energy calculations for metals and semiconductors using a plane-wave basis set”. In: *Comput. Mater. Sci.* 6.1 (1996), pp. 15–50 (cit. on p. 177).
- [280]J. P. Perdew, K. Burke, and M. Ernzerhof. “Generalized Gradient Approximation Made Simple”. In: *Phys. Rev. Lett.* 77.18 (1996), pp. 3865–3868 (cit. on p. 177).
- [281]H. J. Monkhorst and J. D. Pack. “Special points for Brillouin-zone integrations”. In: *Phys. Rev. B* 13.12 (1976), pp. 5188–5192 (cit. on p. 177).
- [282]M. Y. Lavrentiev, J. S. Wróbel, D. Nguyen-Manh, et al. “Magnetic cluster expansion model for random and ordered magnetic face-centered cubic Fe-Ni-Cr alloys”. In: *J. Appl. Phys.* 120.4 (2016), p. 043902 (cit. on p. 193).
- [283]M. C. Troparevsky, J. R. Morris, M. Daene, et al. “Beyond Atomic Sizes and Hume-Rothery Rules: Understanding and Predicting High-Entropy Alloys”. In: *JOM* 67.10 (2015), pp. 2350–2363 (cit. on p. 202).
- [284]S.J. Zinkle and G.S. Was. “Materials challenges in nuclear energy”. In: *Acta Mater.* 61.3 (2013), pp. 735–758 (cit. on p. 202).
- [285]D. Stork and S.J. Zinkle. “Introduction to the special issue on the technical status of materials for a fusion reactor”. In: *Nucl. Fusion* 57.9 (2017), p. 092001 (cit. on pp. 202, 230).
- [286]T. Egami, W. Guo, P. D. Rack, et al. “Irradiation Resistance of Multicomponent Alloys”. In: *Metall. Mater. Trans. A* 45.1 (2014), pp. 180–183 (cit. on p. 202).
- [287]N. D. Stepanov, D. G. Shaysultanov, M. A. Tikhonovsky, et al. “Tensile properties of the Cr-Fe-Ni-Mn non-equiautomic multicomponent alloys with different Cr contents”. In: *Mater. Des.* 87 (2015), pp. 60–65 (cit. on p. 203).
- [288]C. Abromeit. “Aspects of simulation of neutron damage by ion irradiation”. In: *J. Nucl. Mater.* 216 (1994), pp. 78–96 (cit. on pp. 203, 204).
- [289]S. J. Zinkle and W. C. Oliver. “Mechanical property measurements on ion-irradiated copper and Cu-Zr”. In: *J. Nucl. Mater.* 141-143.PART 1 (1986), pp. 548–552 (cit. on p. 204).
- [290]P. P. Liu, F. R. Wan, and Q. Zhan. “A model to evaluate the nano-indentation hardness of ion-irradiated materials”. In: *Nucl. Instruments Methods Phys. Res. Sect. B Beam Interact. with Mater. Atoms* 342 (2015), pp. 13–18 (cit. on p. 204).

- [291]R. Kasada, Y. Takayama, K. Yabuuchi, et al. “A new approach to evaluate irradiation hardening of ion-irradiated ferritic alloys by nano-indentation techniques”. In: *Fusion Eng. Des.* 86.9-11 (2011), pp. 2658–2661 (cit. on pp. 204, 214, 223).
- [292]R. Chaouadi, T. Hirai, J. Linke, et al. “A radiation hardening model of 9%Cr-martensitic steels including dpa and helium”. In: *J. Nucl. Mater.* 386-388.C (2009), pp. 544–549 (cit. on p. 204).
- [293]Z. Zhang, E. Hasenhuettl, K. Yabuuchi, et al. “Evaluation of helium effect on ion-irradiation hardening in pure tungsten by nano-indentation method”. In: *Nucl. Mater. Energy* 9 (2016), pp. 539–546 (cit. on p. 204).
- [294]Z. N. Ding, C. H. Zhang, Y. T. Yang, et al. “Hardening of ODS ferritic steels under irradiation with high-energy heavy ions”. In: *J. Nucl. Mater.* 493 (2017), pp. 53–61 (cit. on p. 204).
- [295]C. Heintze, F. Bergner, S. Akhmadaliev, et al. “Ion irradiation combined with nanoindentation as a screening test procedure for irradiation hardening”. In: *J. Nucl. Mater.* 472 (2016), pp. 196–205 (cit. on p. 204).
- [296]C. Heintze, F. Bergner, and M. Hernández-Mayoral. “Ion-irradiation-induced damage in Fe-Cr alloys characterized by nanoindentation”. In: *J. Nucl. Mater.* 417.1-3 (2011), pp. 980–983 (cit. on p. 204).
- [297]D.E.J. Armstrong, X. Yi, E. A. Marquis, et al. “Hardening of self ion implanted tungsten and tungsten 5-wt% rhenium”. In: *J. Nucl. Mater.* 432.1-3 (2013), pp. 428–436 (cit. on p. 204).
- [298]J. F. Ziegler, M.D. Ziegler, and J.P. Biersack. “SRIM – The stopping and range of ions in matter (2010)”. In: *Nuclear Instruments and Methods in Physics Research Section B: Beam Interactions with Materials and Atoms* 268.11-12 (2010), pp. 1818–1823 (cit. on pp. 208, 209).
- [299]F. Otto, A. Dlouhý, K. G. Pradeep, et al. “Decomposition of the single-phase high-entropy alloy CrMnFeCoNi after prolonged anneals at intermediate temperatures”. In: *Acta Mater.* 112 (2016), pp. 40–52 (cit. on pp. 216, 228).
- [300]H.-H. Jin, C. Shin, and J. Kwon. “Fabrication of a TEM sample of ion-irradiated material using focused ion beam microprocessing and low-energy Ar ion milling”. In: *J. Electron Microsc. (Tokyo)*. 59.6 (2010), pp. 463–468 (cit. on p. 221).
- [301]W. D. Nix and H. Gao. “INDENTATION SIZE EFFECTS IN CRYSTALLINE MATERIALS : A LAW FOR STRAIN GRADIENT PLASTICITY”. In: *J. Mech. Phys. Solids* 46.3 (1998), pp. 41–425 (cit. on p. 223).
- [302]X. Wang, A. M. Monterrosa, F. Zhang, et al. “Void swelling in high dose ion-irradiated reduced activation ferritic-martensitic steels”. In: *J. Nucl. Mater.* 462 (2015), pp. 119–125 (cit. on p. 229).

- [303]C. H. Huang and J. Marian. “A generalized Ising model for studying alloy evolution under irradiation and its use in kinetic Monte Carlo simulations”. In: *J. Phys. Condens. Matter* 28.42 (2016). arXiv: 1602.02470 (cit. on pp. 230, 247).
- [304]M. R. Gilbert and J.-Ch. Sublet. “Neutron-induced transmutation effects in W and W-alloys in a fusion environment”. In: *Nuclear Fusion* 51.4 (2011) (cit. on p. 230).
- [305]K. E. Sickafus, E. A. Kotomin, and B. P. Uberuaga, eds. *Radiation Effects in Solids*. Vol. 235. NATO Science Series. Dordrecht: Springer Netherlands, 2007, p. 593 (cit. on pp. 231, 232).
- [306]E. W. Weisstein. *Stirling's Approximation. From MathWorld—A Wolfram Web Resource.* (Cit. on p. 241).
- [307]J. C. Mauro, R. J. Loucks, and S. Sen. “Heat capacity, enthalpy fluctuations, and configurational entropy in broken ergodic systems”. In: *Journal of Chemical Physics* 133.16 (2010) (cit. on p. 242).
- [308]R. G. Palmer. “Broken ergodicity”. In: *Advances in Physics* 31.6 (1982), pp. 669–735 (cit. on p. 242).
- [309]D. De Fontaine. “Cluster Approach to Order-Disorder Transformations in Alloys”. In: *Solid State Physics - Advances in Research and Applications* 47 (1994), pp. 33–176 (cit. on p. 248).